Spatial fractionation of the dose in charged particle therapy

Cécile Peucelle

NNT : 2016SACLS363

THESE DE DOCTORAT
DE L'UNIVERSITE PARIS-SACLAY
PREPAREE A
L' UNIVERSITE PARIS-SUD

ECOLE DOCTORALE N° 576
Particules hadrons énergie et noyau :
instrumentation, image, cosmos et simulation (PHENIICS)

Spécialité de doctorat : Radio et hadron-thérapies

Par

Mme Cécile Peucelle

Spatial fractionation of the dose in charged particle therapy

Thèse présentée et soutenue à Orsay, le 4 novembre 2016:

Composition du Jury :

M. Elias Khan	Professeur, Université Paris-Saclay	Président
M. Jacques Balosso	Professeur, Université Joseph Fourier	Rapporteur
M. Faustino Gomez	Professeur, Universidade Santiago de Compostela	Rapporteur
M. Stephan Brons	Physicien médical, Heidelberg Ion Therapy Center	Examinateur
M. Marc Labalme	Maître de conférences, Université de Caen Normandie	Examinateur
Mme Yolanda Prezado	Chargée de recherches, CNRS	Directrice de thèse
Mme Immaculada Martínez-Rovira	Chercheuse, Universitat Autònoma de Barcelona	Co-encadrante de thèse

Acknowledgements

I would like to truly thank everyone who contributed directly or indirectly to the accomplishment of the work compiled in this manuscript.

En premier lieu, je remercie Yves Charon pour m'avoir accueillie au sein du laboratoire IMNC dont il était le directeur à mon arrivée en thèse. Merci également à Philippe Lanièce qui a pris sa suite.

Je tiens ensuite à remercier tous les membres du jury pour l'intérêt qu'ils ont porté à mes travaux de thèse. Tout d'abord, merci à Monsieur Elias Khan pour m'avoir fait l'honneur de présider ce jury. Je remercie ensuite Messieurs Jacques Balosso et Faustino Gomez pour la lecture attentive de mon manuscrit. Je remercie également Messieurs Stephan Brons et Marc Labalme d'avoir accepté d'être membres de ce jury. Je tiens à exprimer ma gratitude à Yolanda Prezado et Immaculada Martínez-Rovira pour avoir encadré cette thèse et guidé mon travail durant ces trois années. Je leur suis particulièrement reconnaissante pour leur encadrement scientifique de qualité, leurs enseignements, et leurs conseils pertinents et constructifs qui m'ont permis de découvrir le domaine de la recherche en physique médicale. Je les remercie également de m'avoir donné l'opportunité de publier et de présenter mes résultats dans plusieurs conférences internationales.

Je remercie également les autres membres (passés ou actuels) de l'équipe NARA avec qui j'ai eu la chance de collaborer pour ce travail, notamment Morgane Dos Santos, Rémy Salmon, Wilfredo Gonzalez-Infantes et Consuelo Guardiola. Merci également à l'équipe du CPO avec qui j'ai eu le plaisir de travailler, notamment Catherine Nauraye, Annalisa Patriarca, Eric Hierso et Ludovic De Marzi. Enfin, je tiens à remercier toutes les personnes au sein du laboratoire IMNC qui m'ont apporté leur aide à un moment ou un autre durant ces trois années. En particulier, je remercie Alexandre Liège pour les aspects informatiques, Albertine Dubois pour ses conseils avec GATE, Marc-Antoine Verdier pour m'avoir initié aux joies de Python et Vincent Vandenbussche pour m'avoir sauvé des obscurités de ROOT.

Je tiens à présent à remercier toutes les personnes qui m'ont soutenue et accompagnée durant ces longues études. Tout a commencé à Marseille, à l'université de Provence. Ma première année de licence pendant laquelle Yann et Olivier, entre deux TD d'Astro, m'ont initiée aux délices du café et aux joies de la contrée, restera l'une des plus belles de ma vie étudiante. Notre périple à l'OHPluie, les frasques de Super Petit (... Robert) et les problèmes médicaux de tonton Fabrice resteront à jamais dans ma mémoire!

Le temps de passer de l'amphi Fabry à la colline aux oiseaux, je me dirigeais déjà vers Luminy pour rejoindre la famille des GBM à l'ESIL. Parmi eux, je remercie Anaïs d'avoir été présente à mes côtés dès le premier jour. Le temps d'un stage à Sydney, j'ai été accueillie à bras ouverts par l'équipe de physique du Prince of Wales Hospital. J'y ai notamment rencontré Stéphanie Corde-Tehei que je remercie pour

avoir été la première à me donner l'envie d'entreprendre une thèse. Le temps de quelques soirées au Side Bar avec Céline et Lucie (trop de nostalgie!) et il était déjà temps de repartir pour la France.

Atterrissage à Lyon, accompagnée de mes deux acolytes ESILiens Anaïs et Chris. Ils furent tous deux d'un grand soutien durant cette année de concours, pendant laquelle nous nous consolions les soirs de démotivation avec des pizz' à 5 euros (la pince!) et des "papy". Merci également à Paulette, Coline et aux autres collègues du Master pour les bons moments partagés durant cette période délicate.

Quelques mois plus tard me voici rejoignant Orsay, où j'ai été chaleureusement accueillie par toute l'équipe du CPO. Durant mes quelques mois de stage, Ludovic et Catherine m'ont fait découvrir les basiques de la protonthérapie et ont su éveiller chez moi un grand intérêt pour cette technique. Je les remercie pour leurs enseignements et leur bonne humeur. J'ai partagé mon bureau avec Edouard, Gary et Virgile, qui sont très vite devenus "les coupaings". Merci pour votre folie (ah za), les souvenirs de cette période me décrochent à coup sûr un grand sourire!

Vint la période du stage de DQPRM à l'hôpital Tenon avec Coline, avec qui nous avons formé le binôme de choc des "cocottes chéries". Je tiens à remercier très chaleureusement, Jean-Noël, Katia, Paul, Alex, Thibaud, Lyliane et Romain pour le temps qu'ils nous ont accordé pendant cette année de stage, se rendant toujours disponibles pour répondre à nos questions de futures physiciennes. Je suis également très reconnaissante pour les très nombreux bons moments partagés avec eux. Je garderai toujours de cette année un excellent souvenir!

Enfin, mon parcours étudiant s'achève au sein du laboratoire IMNC que j'ai eu la chance d'intégrer au début de ma thèse. Je remercie l'ensemble des équipes et des personnels techniques et administratifs du laboratoire pour leur gentillesse et leur accueil. Plus particulièrement, Sara et Amandine, mes co-thésardes, ont été d'un immense soutien durant cette thèse. Toujours présentes pour les moments de réconfort (tu veux du chocolat?) ou plus légers, elles ont été mes piliers au laboratoire durant ces trois années. Un grand merci également à Morgane pour les moments cafés du matin, pour son soutien et son amitié, qui ont perduré même après son départ. C'est ensuite Emilie (mon p'tit Twinours) qui a pris la relève pour les cafés matinaux. Un grand merci pour ton écoute, ton réconfort et ton rire contagieux qui a égayé mes journées! I also would like to thank the post-doctoral fellows of the NARA team, Wilfredo, Consuelo and Judith, for their kindness. A special thank goes to Consuelo for reassuring me with my (continuous) doubts and for pushing me again and again to continue researching. I really appreciated working with you and I wish you all the best for the future. Je souhaite également la bienvenue à Rachel au sein de l'équipe. Merci à Olivier d'avoir accepté d'être mon parrain au laboratoire, de m'avoir beaucoup fait rire (are you neuneu?) et de m'avoir sauvé la vie avec le rétroprojecteur! Merci également à Albertine pour nos longues discussions qui m'ont fait beaucoup de bien. Je remercie la "team CESFO", en particulier Albertine et Marc-Antoine pour ne citer que les irréductibles, pour avoir rendu mes pause déjeuners très agréables. Je n'oublie pas les stagiaires et doctorants passés et présents du laboratoire que je n'ai pas encore cités, pour les bons moments partagés:

Vincent, Rémy, Yann, Fanny O., Julie, Fanny P., Luis, Haleh, Enzo et Carlotta. Je leur souhaite à tous bon courage pour la suite. Je termine par remercier l'ensemble des personnes présentes à ma soutenance de thèse et ceux qui étaient au rendez-vous pour célébrer mon doctorat comme il se doit!

En parallèle de mon activité de recherche, j'ai eu la chance de pouvoir enseigner au sein de l'UFR de pharmacie de Chatenay Malabry. Je remercie toute l'équipe pédagogique pour leur accueil, et en particulier Nicolas pour ses conseils et sa disponibilité, ainsi que Wafa et François-Xavier pour leur bonne humeur.

Enfin, je termine ces remerciement en citant les "intemporels", ceux qui ont toujours été et seront toujours là: Emilie, Hélène, Morgane et les "filles de la gym": Annabelle, Cot, Katia, Laure, Marine et Paupau. Un clin d'oeil spécial à Laure qui a vécu l'expérience de la thèse en simultané. Votre amitié et vos encouragements ont toujours été une grande force pour moi. Merci à Maxime pour son immense soutien durant ces nombreuses années. Je remercie également ma famille pour leur compréhension et leurs encouragements tout au long de ce parcours. Ma reconnaissance va à mes parents et à ma soeur qui m'ont toujours soutenue, et ont su me donner les moyens d'entreprendre ces longues études. Vous êtes les piliers de ma vie et j'espère vous rendre fiers. Pour terminer, mes infinis remerciements vont à Romain qui a "vécu" la thèse avec moi. Merci pour ta patience, tes encouragements, ton soutien et ton amour qui m'ont permis d'avancer chaque jour un peu plus.

Je dédie ce travail à ma grand mère, qui me manque énormément.

Abstract

Despite recent breakthroughs, radiotherapy (RT) treatments remain unsatisfactory: the tolerance of normal tissues to radiations still limits the possibility of delivering high (potentially curative) doses in the tumour. To overcome these difficulties, new RT approaches using distinct dose delivery methods are being explored. Among them, the synchrotron minibeam radiation therapy (MBRT) technique has been shown to lead to a remarkable normal tissue resistance to very high doses, and a significant tumour growth delay. MBRT allies sub-millimetric beams to a spatial fractionation of the dose. The combination of the more selective energy deposition of charged particles (and their biological selectivity) to the well-established normal tissue sparing of MBRT could lead to a further gain in normal tissue sparing. This innovative strategy was explored in this *Ph.D.* thesis. In particular, two new avenues were studied: proton MBRT (pMBRT) and very heavy ion MBRT. First, the experimental proof of concept of pMBRT was performed at a clinical facility (Institut Curie, Orsay, France). In addition, pMBRT setup and minibeam generation were optimised by means of Monte Carlo (MC) simulations. In the second part of this work, a potential renewed use of very heavy ions (neon and heavier) for therapy was evaluated in a MC study. Combining such ions to a spatial fractionation could allow profiting from their high efficiency in the treatment of hypoxic radio-resistant tumours, one of the main challenges in RT, while reducing at maximum their side effects. The promising results obtained in this thesis support further explorations of these two novel avenues. The dosimetry knowledge acquired will serve to guide the biological experiments.

Keywords: spatial fractionation, charged particle therapy, dosimetry, Monte Carlo simulations

Contents

Acknowledgements **i**

Abstract **v**

1 Introduction **1**
1.1 Cancer incidence and management . . . 1
1.2 Radiotherapy: fundamentals and techniques . . . 2
1.2.1 Brachytherapy . . . 4
1.2.2 Radiometabolic therapy . . . 5
1.2.3 Intraoperative radiotherapy . . . 5
1.2.4 External beam radiotherapy . . . 6
1.3 Charged particle therapy . . . 9
1.3.1 Physical aspects . . . 11
1.3.2 Technical aspects . . . 17
1.3.3 Radiobiological aspects . . . 23
1.3.4 Clinical indications . . . 25
1.4 Distinct dose delivery methods . . . 27
1.4.1 Synchrotron spatially fractionated techniques . . . 29
1.4.2 Spatial fractionation in charged particle therapy . . . 34
1.5 Work outline . . . 39

2 Materials & Methods **41**
2.1 Experimental validation of pMBRT at ICPO . . . 41
2.1.1 Description of ICPO facility . . . 41
2.1.2 Basic principles of dosimetry . . . 44
2.1.3 Small field dosimetry . . . 52
2.1.4 Experimental dosimetry in pMBRT . . . 55
2.2 Monte Carlo simulations . . . 64
2.2.1 The Monte Carlo method . . . 64
2.2.2 MC simulations in medical physics . . . 65
2.2.3 The Geant4/GATE simulation toolkit . . . 66
2.2.4 Simulations geometry and details for this work . . . 68
2.2.5 Parallelisation of the calculations . . . 73
2.2.6 Assessment of uncertainties on the computed dose . . . 74

3 Proton minibeam radiation therapy **75**
3.1 Assessment of the composition of peaks and valleys . . . 76
3.2 Experimental dosimetry evaluation of pMBRT . . . 78
3.2.1 Depth dose distributions . . . 78
3.2.2 Evaluation of normalised total doses in valley . . . 82

3.2.3 Lateral dose profiles . . . 83
3.2.4 Determination of output factors . . . 88
3.2.5 Summary and discussion . . . 89
3.3 MC evaluation of pMBRT using a magnetic collimation . . . 92
3.3.1 Comparison of mechanical and magnetic collimations . . . 94
3.3.2 Influence of several irradiation parameters . . . 96
3.3.3 Summary and discussion . . . 108

4 A potential renewed use of very heavy ions for therapy 111
4.1 Evaluation of physical dose distributions . . . 112
4.1.1 Depth dose distributions . . . 112
4.1.2 Estimation of the $NTD_{2.0}$ . . . 116
4.1.3 Lateral dose profiles . . . 118
4.2 Evaluation of secondary particles distributions . . . 122
4.2.1 Spatial distribution of secondary species . . . 123
4.2.2 Type of nuclear fragments and their yield . . . 129
4.3 Summary and discussion . . . 133

5 Final Discussion & Conclusions 137

6 Scientific Production 145

7 Résumé du travail de thèse en français 147
7.1 Contexte du projet de thèse . . . 147
7.2 Principaux résultats . . . 151
7.2.1 Implémentation de la pMBRT dans un centre clinique . . . 151
7.2.2 Impact de divers paramètres d'irradiation en pMBRT . . . 155
7.2.3 Fractionnement spatial avec des ions plus lourds . . . 158
7.3 Discussion & Conclusions . . . 161

Bibliography 165

List of Abbreviations 187

List of Figures 201

List of Tables 204

Chapter 1

Introduction

Contents

1.1 Cancer incidence and management 1
1.2 Radiotherapy: fundamentals and techniques 2
1.2.1 Brachytherapy 4
1.2.2 Radiometabolic therapy 5
1.2.3 Intraoperative radiotherapy 5
1.2.4 External beam radiotherapy 6
1.3 Charged particle therapy 9
1.3.1 Physical aspects 11
1.3.2 Technical aspects 17
1.3.3 Radiobiological aspects 23
1.3.4 Clinical indications 25
1.4 Distinct dose delivery methods 27
1.4.1 Synchrotron spatially fractionated techniques 29
1.4.2 Spatial fractionation in charged particle therapy 34
1.5 Work outline 39

1.1 Cancer incidence and management

Cancer is a group of diseases involving abnormal growth with the potential to invade or spread to other parts of the body through blood circulation or lymph vessels [WHO 2015]. Both external factors (tobacco, infectious organisms, exposition to radiations and chemicals) and internal factors (inherited genetic mutations, hormones and immune conditions) may lead to carcinogenesis [ACS 2015].

Cancer is one of the main causes of morbidity and mortality in the world. In 2012, the number of new cases and deaths were estimated to 14 millions and 8.2 millions, respectively [WHO 2015]. The number of new cases is expected to rise by about 70% over the next two decades [WHO 2015]. Worldwide, in 2012, the most frequent cases were lung (13.0%), breast (11.9%), colorectal (9.7%) and prostate cancers (7.9%) [WCRF 2015]. Recent advances in treatments and earlier diagnosis of cancer resulted in a significant improvement of survival rate in the last decades. As an example, the five-year relative survival for all cancers diagnosed in the United States

of America (USA) increased from 49% in the 1975–1977 period, to 68% between 2004 and 2010 [ACS 2015]. However, some types of cancer such as high grade malignant gliomas (glioblastomas) still have a very poor prognosis. The median survival time is of only 15 months due to tumour resistance to current therapeutic approaches [Bleeker 2012].

Each type of cancer requires a specific treatment depending on the tumour type, location, stage of the disease and general state of the patient. The most common treatment methods are surgery, chemotherapy and radiotherapy (RT). Many patients receive a combination of some of these three main modalities during their treatment.

Surgery is the oldest type of cancer therapy and remains the preferable option if the tumour is operable. Its goal is to remove all the cancerous tissue, or in some cases the entire organ affected by the disease. Surgery can be also used for diagnosis: after tumour resection, anatomo-pathological analyses lead to a precise determination of type and stage of the cancer, and allow choosing the most adequate treatment modalities.

Chemotherapy uses drugs to slow or stop the growth of rapidly-growing cells such as cancer cells. It is a non-targeted systemic treatment that also affects normal rapidly-growing cells such as marrow, digestive and reproductive cells, and hair follicles. Chemotherapy is thus an aggressive treatment for patients, causing important side effects such as nausea, blood disorders, alopecia and tiredness.

Radiotherapy is a localised treatment using ionising radiations to deposit a high quantity of energy within the tumour, in order to injure or destroy cancer cells. RT plays an important role in cancer management as, in industrialised countries, about 70% of cancer patients will receive RT for at least part of their treatment [IAEA-TRS-461 2008]. In addition, about half of the patients who are cured from cancer benefited from RT [IAEA-TRS-461 2008]. The number of patients effectively treated with RT is rapidly increasing due to the spread of high-precision treatments and imaging techniques. Therefore, the improvement of this expanding modality can have significant impact on the global outcome of cancer treatment.

1.2 Radiotherapy: fundamentals and techniques

As it was previously mentioned, RT is the medical use of ionising radiations to treat malignant tumours, or some benign lesions such as arteriovenous malformations. It is used both with curative or palliative intents.

Ionising radiations are able to damage cells either by directly breaking DNA strands, or indirectly, through the creation of free radicals by water radiolysis. The latter process is the dominant one in any type of RT in usual conditions. The basis of RT lies in the fact that abnormal cells have a reduced capability to repair DNA, in contrast to normal cells [Joiner 2009].

The benefit of a RT treatment has to be estimated by balancing the tumour control probability against the possible deleterious effects induced to normal tis-

sues. The tumour control probability (TCP) increases as a function of radiation dose until a plateau is reached, following a sigmoid curve. The same trend is observed for normal tissue complication probability (NTCP), as shown in figure 1.1. The therapeutic index is defined as the ratio of the maximum dose tolerated by normal tissue to the minimum dose required to control the tumour. The "therapeutic window" corresponds to the range of doses for which the TCP is much higher than the NTCP. It represents the difference in terms of dose-response between tumoural and normal tissue.

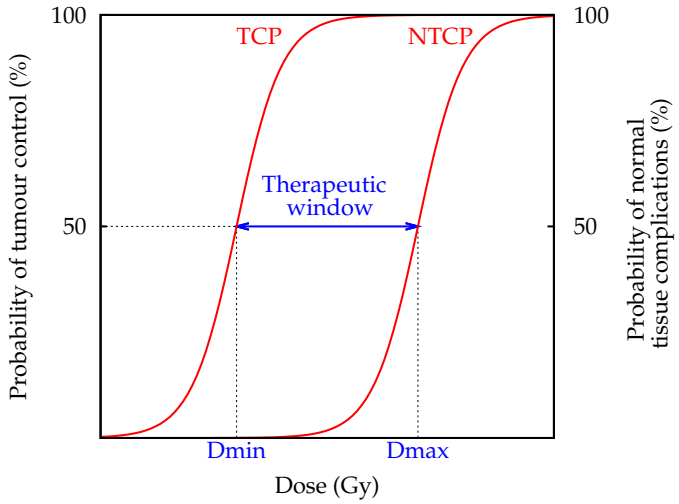

Figure 1.1: *Illustration of the concept of therapeutic window. A tumour can be effectively treated with RT if the range of doses D_{min}–D_{max}, or therapeutic window, is wide enough.*

If the therapeutic window is large enough, it is possible to effectively treat cancer using RT. However, for some types of cancers such as gliomas, the two curves lie in close vicinity, making the therapeutic window very narrow. In these cases, the risk of important damages to normal tissues prevents the possibility of reaching curative doses in the tumour. In order to widen the therapeutic window, either the radiation effect on tumour has to be enhanced (for example, by achieving a higher steepness in the TCP curve), or the normal tissue tolerance needs to be increased (shifting the NTCP curve towards higher doses), or both [Joiner 2009].

The first RT treatments were performed soon after the discovery of x-rays by W. Roentgen in 1895. E. Grubbe (Chicago, USA) irradiated a female patient suffering from a breast cancer recurrence in 1895 [Vujosevic 2010]. One year later, V. Despeignes (Lyon, France) observed tumour volume regression after using x-rays for the treatment of advanced stage stomach cancer [Despeignes 1896]. The same year, L. Freund (Vienna, Austria) successfully treated a five-year-old patient of a cutaneous tumour [Vujosevic 2010]. Soon after the discovery of radium by M. Curie in 1898, H.A. Danlos (Paris, France) used such a radioactive source to treat skin cancers in 1901 [Vujosevic 2010, Degiovanni 2014].

During the following 50 years, RT slowly spread, constrained to the development of x-rays tubes, Van de Graaff generators and betatrons machines, which generate superficial and orthovoltage x-rays (50–500 keV). The advent of ^{60}Co units in the early 1950's led to significant boost in the development of RT, making it possible to use higher photon energies ($>$ 1 MeV) for the treatment of deep-seated tumours [Podgorsak 2005]. But soon, the arrival of compact medical linear accelerators (linacs) to the hospitals open the door to more precise treatments thanks to their reliability, flexibility and their possibility to reach higher energies, becoming the most widely used equipments in modern RT.

Currently, RT may be classified in four categories: brachytherapy, radiometabolic therapy (RMT), intraoperative RT (IORT) and external beam RT (EBRT), being this latter the most common one. Details on these techniques will be given in the following sections.

1.2.1 Brachytherapy

Brachytherapy consists in applying permanent or temporary radioactive sources, encapsulated in metallic seeds, plaques or wires, close to the tumour (intracavitary or intraluminal therapy) or into the tumour (interstitial therapy). Typical sources employed are low energy gamma-emitting elements such as ^{192}Ir, ^{137}Cs and ^{125}I, or β^- emitting sources like ^{106}Ru. This technique delivers highly conformal dose distributions, thus minimising side effects in surrounding normal tissues. It is used with the aim of curing cancer in cases of small or locally advanced tumours.

Four types of brachytherapy treatments can be considered depending on the dose rate of the radioactive source employed [ICRU-38 1985]:

- Low-dose rate (LDR) techniques ($<$ 2 Gy/h), using a permanent implantation of sources, are mainly employed for treatment of head and neck, skin and prostate cancers.
- High-dose rate (HDR) techniques ($>$ 12 Gy/h) are commonly used for prostatic, bronchial, oesophageal, gynaecological and breast cancers, and involve temporary implantation of sources.
- Pulsed-dose rate (PDR) techniques are based on the delivery of short pulses of radiations (typically once an hour) to simulate the overall rate and effectiveness of LDR treatments. It is at present limited to gynaecological and head and neck cancers.
- Medium-dose rate (MDR) brachytherapy (between 2 and 12 Gy/h) also exists although is rarely used.

Born as a very basic and "manually-delivered" technique, brachytherapy has become a sophisticated treatment thanks to the advent of "remote afterloaders", *i.e.* devices allowing to automatically load and drive the radioactive source inside the patient body using a guide wire [AAPM-41 1993]. These machines allow optimising

the dose distributions by planning the successive positions occupied by the source during its path in the treatment site, as well as the time of residency in each position.

In appropriately selected cases, brachytherapy for primary tumours represents an approach comparable to surgery (*e.g.* localised prostate and breast cancers), achieving the same probability of cure without the need of resection, and with similar side effects [Guedea 2009]. In that sense, it often offers an alternative to surgery in cases where organ resection can cause functional and/or cosmetic morbidity [Harrison 1997].

1.2.2 Radiometabolic therapy

In RMT, radiopharmaceuticals are injected intravenously into the patient. They are made of molecules containing radioisotopes emitting β^- radiations (*e.g.* ^{131}I or ^{153}Sm) attached to a vector-medication which has high affinity for cancer tissues (*e.g.* peptide or monoclonal antibody). These electrons are only emitted locally in the tumour vicinity over a certain time, while avoiding surrounding normal tissues.

One of the major application of RMT is the use of ^{131}I in thyroid cancer treatments after surgical resection, in order to ablate any tumoural tissue remaining in the thyroid area or that have spread elsewhere in the body. In general, this technique is of particular interest to treat small and disseminated tumours, such as metastases. In particular, it constitutes an alternative to non-targeted systemic treatments such as chemotherapy, which can cause high toxicity in the patient body [Vuillez 2005].

1.2.3 Intraoperative radiotherapy

IORT is an intensive radiation treatment administrated at the time of surgery, directly at the tumour contact, or in the tumour bed after its resection. It is used to treat cancers that are difficult to remove during surgery and in cases where there is concern that microscopic amount of cancer will remain. IORT is administrated in one single treatment fraction, and can be used as a boost or as an exclusive treatment. Modern IORT is performed either with electron or low-energy photon beams by means of dedicated linacs equipped with sterile end-pieces or applicators of different shapes (see figure 1.2). As examples, the IntraOp Mobetron© system is a mobile linac that delivers electrons with discrete energies ranging from 6 to 12 MeV, while the Zeiss Intrabeam© system uses low-energy x-rays (50 kV).

At present, the most frequently treated tumour locations with IORT are breast cancer, head and neck tumours, prostate carcinoma, intra-thoracic malignancies and brain tumours [Krengli 2004]. In particular, the growing interest in partial breast irradiation (approximately 85% of relapses are confined to the same quadrant of the breast as the primary tumour [Krengli 2004]) in the last few years has boosted the use of IORT for breast cancer.

Finally, irradiation with IORT is, with brachytherapy, one of the sole radiotherapeutic options for local recurrences if repeated external RT is no longer possible [Kraus-Tiefenbacher 2007].

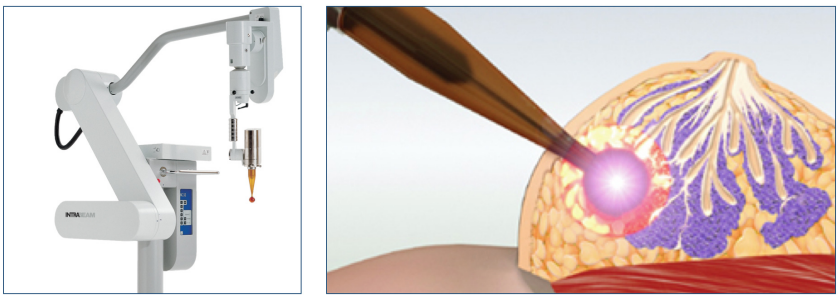

Figure 1.2: *Left: Intrabeam© system with applicator dedicated to breast treatment. Right: example of applicator insertion during a breast cancer IORT treatment. Taken from the Zeiss Website [Zeiss 2016].*

1.2.4 External beam radiotherapy

EBRT is the most commonly employed technique in RT, as 90% of RT treatments uses EBRT nowadays [Gerber 2008]. The radiation is external to the patient, mainly generated by linacs. They generate both high energy x-rays and electrons, which are the most widely used radiations in RT. In a typical linac, electrons (produced by an electron gun) are accelerated following straight trajectories inside vacuum tube structures (accelerating wave guides), thanks to high radio-frequency electromagnetic waves [Podgorsak 2005]. Electrons can be accelerated with discrete energies in the range from 4 to 25 MeV [Podgorsak 2005]. Megavoltage x-ray beams are produced by deceleration of the electron beam in high-Z (atomic number) metallic targets (Bremsstrahlung x-rays). As shown in figure 1.3, the beam interacts with several modifiers before reaching the patient. In particular, in electron irradiation mode, a scattering foil allows to diffuse the electron pencil beam to cover the field size required for treatment. In x-rays irradiation mode, in addition to the high-Z target, a flattening filter (low-Z material) is interposed in the beam. It is specially shaped to flatten the dose profile at the patient entrance level. Several collimators are used to conform the beam to the tumour shape, and monitor ion chambers allow to control the beam rate during the treatment.

Thanks to their sharp dose fall-off gradient in the first millimetres, electron beams can be employed directly to treat superficial tumours (less than 5 cm deep) [Podgorsak 2005] while the more penetrating megavoltage photon beams are favoured for deeper lesions (see figure 1.4). Although becoming less and less common, superficial and orthovoltage x-ray units (50–500 keV range) are still employed as an alternative to electron beams for treatment of superficial lesions such as skin cancers [Washington 2015].

During the last decades, the precision of EBRT has greatly improved thanks to important technical developments of several imaging modalities and irradiation devices. The advent of three-dimensional imaging such as computed tomography (CT), magnetic resonance imaging (MRI) and positron emission tomography

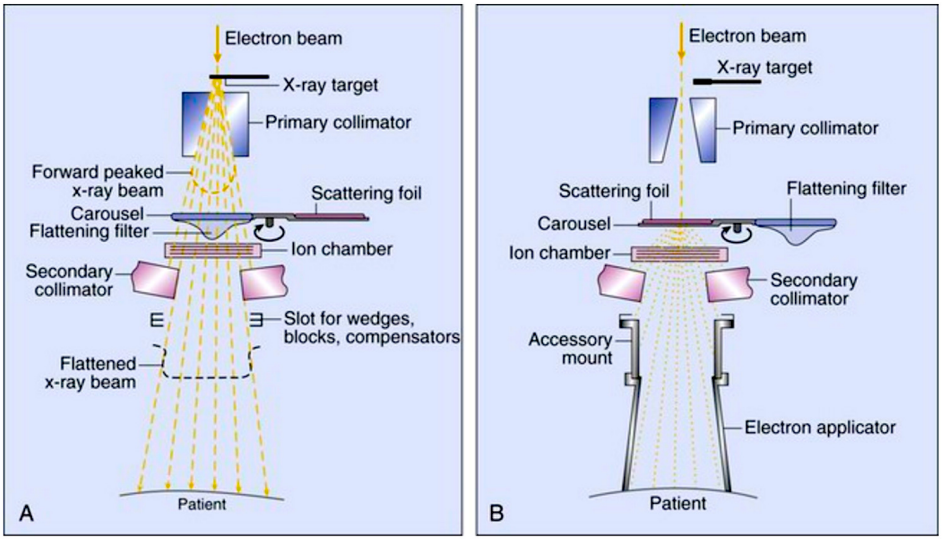

Figure 1.3: *Schematic view of the head of a modern linac operating in x-ray (left) or electron (right) irradiation modes. The beam traverses several modifiers before reaching the patient in order to conform the radiation field to the tumour, such as collimators, flattening filters (x-ray mode) or scattering foils (electron mode). Taken from the work of Zeman et al. [Zeman 2015].*

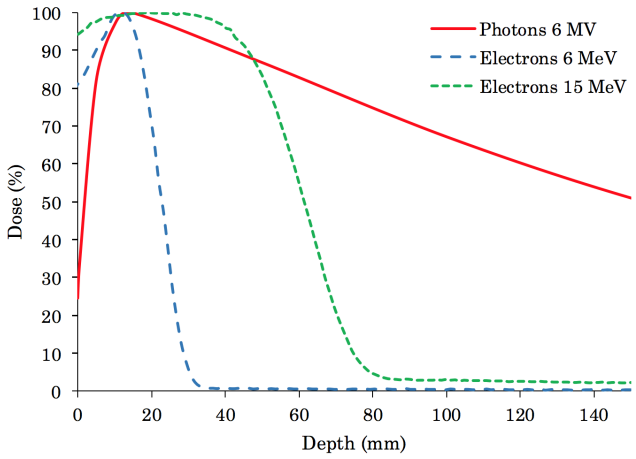

Figure 1.4: *Percentage depth dose distribution of a 6 MV-photon beam (solid line), compared to the sharp fall-off distribution at the end of the range for two electron beams of different energies (6 MeV and 15 MeV).*

(PET) have enabled direct visualisation of patient anatomy and metabolic processes [Vujosevic 2010] along with accurate definition of the RT target volumes and organs at risk. Modern RT has thus evolved from 2D non-site-specific techniques using bony anatomy landmarks towards three-dimensional conformational RT (3D-CRT) that uses three-dimensional reconstructions of images and computer optimisation

algorithms [Bucci 2005]. The most recent advancements include Intensity Modulated Radiotherapy (IMRT), Image Guided Radiotherapy (IGRT) and even four dimensional conformal RT (4D-CRT).

Intensity Modulated Radiotherapy (IMRT) is an advanced form of 3D-RT able to conform the dose to complex tumour shapes by varying the beam intensity (fluence) during treatment [IMRT-Group 2001]. One single irradiation field is constituted of a series of *beamlets* with different relative intensities. In that way, non-uniform and complex (*e.g.* concave) dose distributions can be achieved. An evolution is **Intensity Modulated Arc Therapy** (IMAT) in which the modulation is achieved by varying dynamically the dose-rate, the gantry angulation, and the relative position of the multi-leaf collimator's leaves during the beam delivery [Yu 2011]. This leads to significant reduction of irradiation time, minimising possible intra-fraction deviations.

The remarkable improvements in dose conformation require accurate targeting of the tumour volume. Along this line, **Image Guided Radiotherapy** (IGRT) allows reducing the planning target volume (PTV), thus minimising the volume of normal tissue irradiated. Linac on-board imaging devices make it possible to perform frequent planar (kV or MV x-rays) or 3D (cone-beam CT) imaging of the patient directly under the treatment machine in order to monitor and correct patient's position along the treatment.

As RT treatments are split in several fractions over several weeks, anatomical changes in the patient such as tumour shrinkage, weight loss or internal motion, can occur. In some cases, these modifications might result in dose deficiency in the target or dose excess in normal tissues. In **Adaptive Radiotherapy** (ART), images of the patient are daily performed to monitor the treatment volume variations, and modify the treatment plan [Yan 1997]. An adaptation of the treatment plan may be done *offline* (between fractions), *online* (just prior or during a fraction), or in a hybrid way [Lafond 2015].

The treatment conformality could also be degraded by internal intra-fraction motions. In particular, this problem concerns thoracic and abdominal lesions which are subject to respiratory-cycle motions. **Respiration-gated radiotherapy** incorporates the time scale in the planning procedure (4D-CRT). Four main strategies to reduce respiratory motion effects are possible: motion encompassing, breath-hold, respiratory gating and real-time tumour tracking [AAPM-76 2006]. The motion encompassing strategy proposes to irradiate a volume including the entire range of tumour motion within a respiration cycle, namely the internal target volume (ITV). In breath-hold methods, the patient has to hold his respiration at some point in the breathing cycle, during which the dose delivery occurs. The gating strategy monitors tumour motions and triggers the beam delivery in one specific phase of the breathing cycle. Finally, tracking consists in following in real-time tumour motions with the beam, or adapting the irradiation fields to these motions.

Stereotactic Irradiation (SI) is a highly precise RT method that uses several non-coplanar narrow beams focused towards the target. SI requires immobilisation devices associated to a coordinate system fixed to the patient (*e.g.* stereotactic

frame) to accurately target the tumour. As long as the target volume is small, SI enables the delivery of a high radiation dose in hypo-fractionation schemes (less than 5 treatment fractions). Historically, indications for SI were mainly intracranial lesions (benign and malignant tumours, arteriovenous malformations) but they have rapidly extended other extra-cranial locations such as spine tumours, some lung, pelvis (prostate) and hepatic lesions [Timmerman 2005].

One can distinguish **Stereotactic Radiation Surgery** (SRS) treatments, that are given in one single fraction, from **Stereotactic Radiotherapy** (SRT) where several sessions take place [Podgorsak 2005]. Both techniques can be carried out with specialised systems such as Gamma Knife© (GK) (^{60}Co sources) and CyberKnife© (CK) (6 MV x-rays), and dedicated or adapted linacs such as Novalis Tx©. Beam penumbras (80–20 %-width) in radiosurgery are larger than 3 mm in the best cases.

All the aforementioned techniques mainly use photons, which show an exponential decrease of the absorbed dose in depth, with a substantial exit dose remaining at the end of path. Moreover, some tumour types are known to be poorly sensitive to x-rays radiations. Osteosarcomas, malignant melanomas and glioblastomas are some examples [Dutreix 1990]. These limitations have triggered an interest for alternative approaches that either enhance tumour sensitivity to radiations or increase normal tissues tolerance, or both. Along this line, charged particles (protons and ions) ally a more selective distribution in depth with a higher biological effectiveness. Further details will be given in the following section.

1.3 Charged particle therapy

The very first cyclotron, that allowed to accelerate 80 keV protons, was constructed by E. Lawrence and M. Livingston in 1929. Later, in 1946, R. Wilson pointed out the favourable dose distributions of protons and their potential for cancer therapy to treat deep-seated tumours [Degiovanni 2014]. The first treatments (pituitary gland) with proton beams were performed in 1954 by C. Tobias and J. Lawrence at the Lawrence Berkley Laboratory [Tobias 1958]. By the early 1990's, proton therapy was mainly based in research institutions. The first hospital-based facility was built and started operation at the Loma Linda University Medical Centre in California [Slater 1992].

In parallel, the idea to use heavier ions rapidly arose. Pioneering work in heavy ion RT was performed at the Lawrence Berkley Laboratory where 2054 patients were treated with helium ions between 1957 and 1992 [Castro 1994, Degiovanni 2014, Jermann 2015]. Between 1975 and 1992, 433 patients were also treated with heavier ions such as C, N, O, Ne, Si, and Ar [Castro 1995, Jermann 2015]. About one half of the patients received their full treatments with heavy ions, the other half received heavy ions as a boost after photon or light-ion treatments. However, the important side effects observed after Ne and Ar irradiations [Degiovanni 2014],

including fatal complications [Castro 1994], made that the use of these ions was rapidly stopped. Only the use of carbon ions, which were considered to provide a good compromise between treatment of radio-resistant tumours and preservation of normal tissues, was maintained. As today, only protons and carbon ions are used in clinical facilities for therapy, the most common ones being protons. According to the Particle Therapy Co-Operative Group (PTCOG), 86% of the patients ever treated with particle therapy until 2014 were irradiated with protons, 11% with carbon ions, and 3% with other particle types (including neutrons) [Jermann 2015].

Charged particles are more advantageous than x-rays due to three main features, two of which pertain to physics and one to radiobiology:

- Charged particles have a more favourable depth dose deposition with respect to photons. Their energy deposition increases with penetration depth, reaches a maximum just before coming at rest in the region called the *Bragg peak*, and exhibits a rapid dose fall-off beyond this point (see figure 1.5). In the Bragg peak, they produce most of the damages to the cells, while sparing both proximal and deeper located normal tissues.

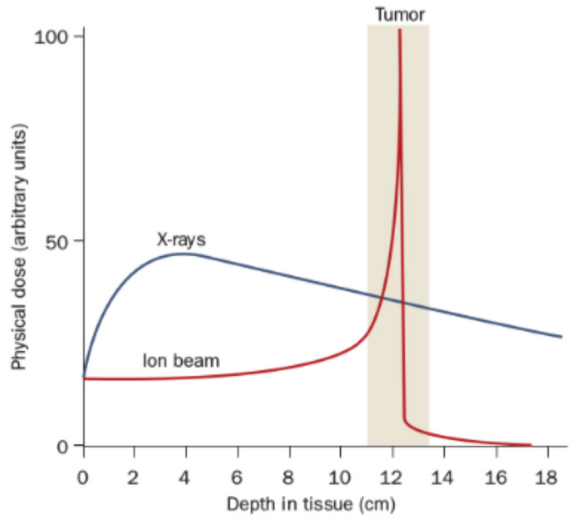

Figure 1.5: *Comparison of the depth-dose profiles of x-rays and mono-energetic ions. While x-rays exhibit an exponential decrease of the absorbed dose as a function of depth, charged particles deposit most of their energy at the end of their path, in the so-called Bragg peak, while sparing both proximal and distal located normal tissues. Taken from the work of Durante and Loeffler [Durante 2010].*

- Ions penetrate the patient with minimal diffusion, thus exhibiting reduced beam penumbras with respect to x-rays. Charged particle beams have thus the potential for higher dose conformality compared with photon beams, highly reducing the integral dose received outside of the target volume, as illustrated in figure 1.6. In that sense, charged particle therapy is of particular interest for

tumours located close to serially organised tissues where a small local overdose can cause significant complications [Paganetti 2012].

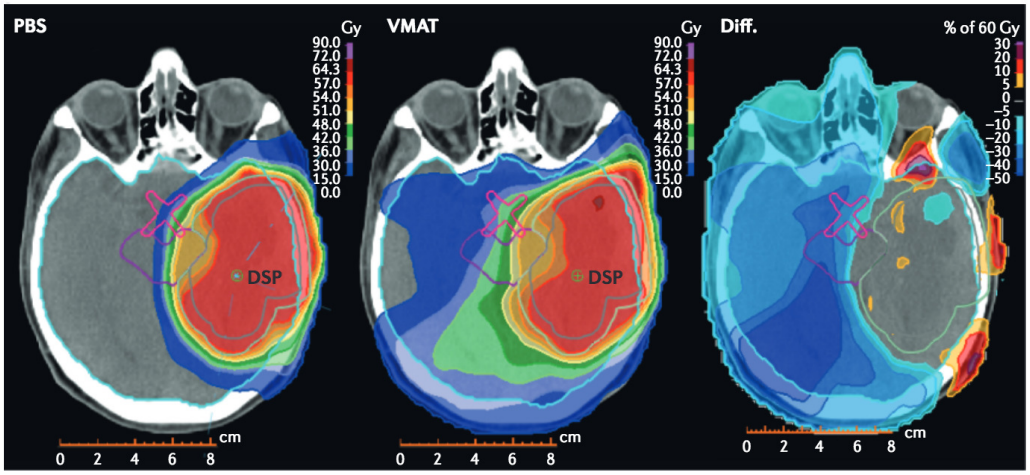

Figure 1.6: *Dose plans for a high-grade glioma in proton therapy using Pencil Beam Scanning delivery method (left) and in photon RT delivered with a IMAT (centre). On the right picture, the statistical variations of the dose distributions between the two techniques are shown. A significant dose bath (low doses) in IMAT technique with respect to proton therapy is observed. This can cause an increased risk of secondary cancers. Taken from the work of Baumann et al. [Baumann 2016].*

- Charged particles (especially heavy ions) exhibit a more condensed ionisation pattern in traversed cells than x-rays, thus creating more complex damages. This is reflected in an increase of the relative biological effectiveness (RBE), being the ratio of x-rays and ion dose producing the same biological effect. Concerning protons, recent studies suggest that they could induce different molecular and cellular responses with respect to photons, like capacity to induce complex DNA damages, and an enhanced ability to inhibit tumour invasion and angiogenesis [Girdhani 2013].

The following sections will describe in details the physics fundamentals, technical and radiobiological bases of charged particle therapy.

1.3.1 Physical aspects

As it was previously mentioned, the main physical advantage of charged particles over photons lies in their more selective dose deposition in depth. The typical Bragg peak curve is mainly due to three types of processes: **inelastic Coulomb scattering** (inelastic collisions with target electrons), **elastic Coulomb scattering** (elastic collisions with target nuclei), and **non-elastic nuclear reactions** (with production of secondary particles as a consequence). These three processes and their subsequent influence on the dose distribution will be detailed hereafter.

1.3.1.1 The depth dose profile curve

The depth dose profile of charged particles is mainly due to the dependence of energy loss on the energy of incident particles. In the entrance region, charged particles transfer most of their energy to the traversed medium through **inelastic collisions with the target electrons**. This can be characterised by the "electronic stopping power", defined as the average energy loss per unit path length. It is described by the Bethe and Bloch formula [Bethe 1930, Bloch 1933] for high velocity ions. The formulation of Fano [Fano 1963] is reported in equation 1.1:

$$\frac{\mathrm{d}E}{\mathrm{d}x} = \frac{4\pi e^4 Z_\mathrm{t} Z_\mathrm{p}^2}{m_\mathrm{e} v^2}\left[\ln\left(\frac{2m_\mathrm{e}v^2}{< I >}\right) - \ln(1-\beta^2) - \beta^2 - \frac{C}{Z_\mathrm{t}} - \frac{\delta}{2}\right] \tag{1.1}$$

where Z_t and Z_p are the target and projectile atomic numbers, respectively, e the electron charge, m_e the electron mass, v the projectile velocity, $\beta = v/c$ where c is the light velocity. C is a shell correction factor, δ is a density correction and $< I >$ refers to the mean ionisation energy.

The Bethe and Bloch equation expresses that the energy transfer through Coulombian interactions increases with the charge of the projectile, as described by the Z_p^2 quantity. The Z_t dependency denotes a more important energy loss in high-Z materials. Consequently, charged particles will have a shorter range in a high-Z medium (for example in lead) than in water. In addition, the stopping power of incident particles varies as the inverse square of their velocity ($1/v^2$), which explains why incident projectiles lose the main part of their kinetic energy at the end of their path, in the so-called Bragg peak.

At high velocities the atomic electrons are completely stripped off and the projectile charge is equal to the atomic charge Z_p. At lower velocities (for light ions below 10 MeV/u), the mean charge state decreases due to the interplay of ionisation and recombination (electron exchange) processes. To account for this phenomenon, Barkas proposed to replace Z_p by a projectile effective charge, Z_eff [Barkas 1963]. The dependence of Z_eff on the projectile velocity is described by the empirical formula equation hereafter:

$$Z_\mathrm{eff} = Z_\mathrm{p}\left[1 - \exp(-125\beta Z_\mathrm{p}^{-\frac{2}{3}})\right] \tag{1.2}$$

When the energy of the projectile goes below 10 keV/u, **elastic collisions with target nuclei** begin to contribute significantly to the energy loss and dominate the stopping power process at the very end of the charged particle path (last few μm). This second mechanism of energy loss is called "nuclear stopping power". The total stopping power is defined as the sum of the electronic and the nuclear stopping powers, and it is directly linked to the dose deposition.

Stopping power curves for protons and ^{12}C ions as a function of the kinetic energy of the projectile are shown in figure 1.7. For protons, inelastic collisions with atomic electrons are the dominant process for all energies. For ^{12}C ions, this process is also dominant except in the last few micrometres of path, where the nuclear stopping power becomes dominant.

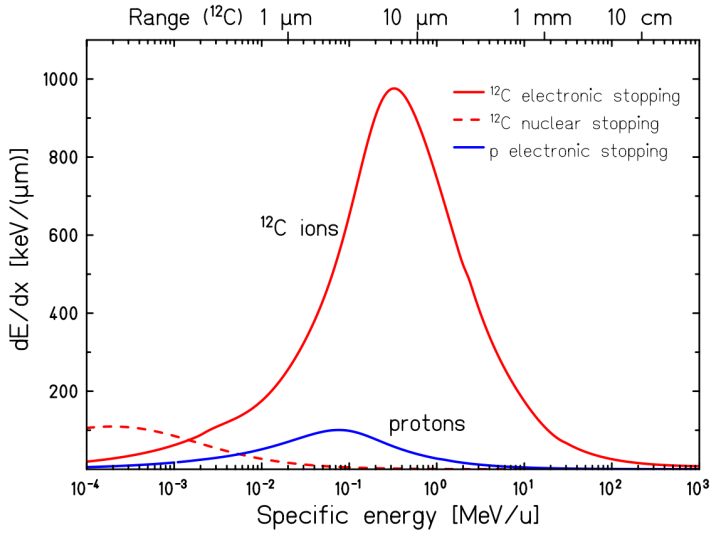

Figure 1.7: *Electronic and nuclear stopping power curves of ^{12}C ions and protons in water. Inelastic collisions with atomic electrons are the dominant process for all energies for proton interactions. The same situation is observed for ^{12}C ions where this process is also dominant except for the last few micrometres of path where the nuclear stopping power becomes dominant. The range of ^{12}C ions in water corresponding to their specific energy is indicated at the top. Taken from the work of Schardt et al. [Schardt 2010].*

1.3.1.2 Range straggling

As it can be seen in equation 1.1, the energy loss of a single ion as a function of depth would result in a very sharp peak near the stopping point. However, statistical fluctuations of the energy loss in the large number of collisions of the slowing-down process result in a broadening of the Bragg peak for a beam consisting of many particles [Paganetti 2012]. This leads to a Gaussian energy loss distribution, often referred to as energy or range straggling. The range straggling increases with the penetration depth in a given material [Schardt 2010].

Moreover, the range straggling varies approximately as the inverse of the square root of the particle mass. Consequently, the relative range straggling is smaller for heavier particles, as illustrated in figure 1.8. By comparing Bragg peaks of protons and carbon ions having the same mean range in water, it can be observed that the peak is much narrower for a carbon ion beam than for a proton one [Schardt 2010].

1.3.1.3 Lateral beam spread

Elastic collisions with target nuclei result in small deflections of the projectiles. The statistical repetition of these interactions is responsible for the creation of a multiple diffusion distribution, or "multiple Coulomb scattering". It results in a lateral spread of the charged particle beam (see figure 1.9). According to Highland [Highland 1975], this multiple diffusion can be well described by a Gaussian with a

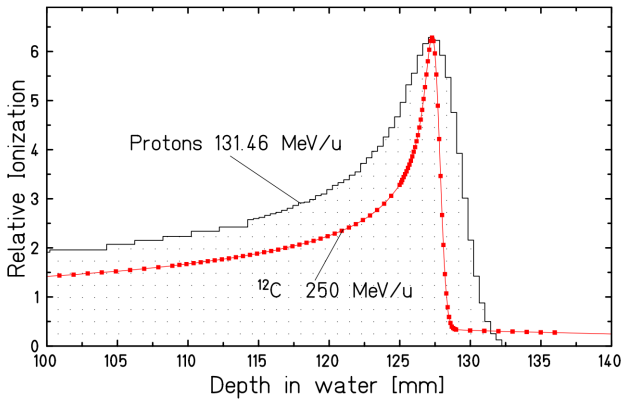

Figure 1.8: *Experimental depth dose curves of protons and carbon ions having the same mean range in water. Due to the higher relative range straggling with protons, the Bragg peak width is enlarged for this particle type with respect to the carbon ions distribution. Taken from the work of Schardt et al. [Schardt 2010].*

standard deviation σ_θ given by the following empirical formula:

$$\sigma_\theta = \frac{14.1\text{MeV}}{pv} Z_\text{p} \sqrt{\frac{L}{L_\text{R}} \left[1 + \frac{1}{9}\log_{10}\left(\frac{L}{L_\text{R}}\right)\right]} \text{ [rad]} \tag{1.3}$$

where p and v are the particle momentum and speed, Z_p the projectile charge number, L the target thickness and L_R the radiation length of the absorber material.

The $1/v$ dependency implies an increase of the angular spread as the particles slow down. Besides, multiple scattering effects for ion beams vary approximately inversely to the square-root of the mass of the particle [ICRU-1560 2007]. Comparing beams with a same range in water, the angular spread σ_θ of protons is three times larger than the one of carbon ions [Schardt 2010]. The use of heavy ions is thus of clinical relevance for treatments near organs at risk, allowing a safer approach to sensitive structures.

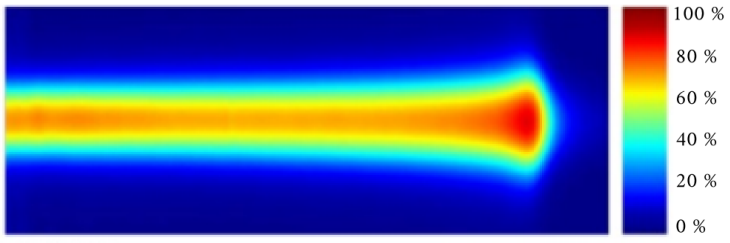

Figure 1.9: *Two-dimensional view of the depth dose distribution of a proton beam. The multiple Coulomb scattering process results in a lateral spread of the beam in depth, which increases with the slowing down of the particles. This results in a maximum enlargement of the beam at the Bragg peak.*

1.3.1.4 Nuclear interactions

High energy ions penetrating a thick absorber also undergo **nucleus-nucleus collisions**. According to ICRU 63 [ICRU-63 2000], nuclear reactions may be split in three categories:

- Elastic reactions in which the incident projectile scatters off the target nucleus, the total kinetic energy being conserved. The internal state of both target and projectile nuclei are unchanged by the reaction.
- Non-elastic reactions which refer to nuclear reactions where the kinetic energy is not conserved. For example, the target or projectile nucleus may undergo break-up, excitation to a higher quantum state, or a particle transfer reaction.
- Inelastic reactions which are a specific type of non-elastic reactions in which the final nucleus is the same as the bombarded one, but without kinetic energy conservation.

Non-elastic reactions are the most frequent nuclear reactions occurring in the energy range of charged particle therapy, resulting in fragmentation of the target and/or projectile nuclei. They result in a gradual depletion of primary ions from entrance to the end of range associated to a build-up of lower-Z fragments. The amount and multiplicity of secondary fragments rise with increasing depth (see figure 1.10), reaching a maximum at the Bragg peak, and decrease beyond it [Cussol 2011]. The most frequent fragments are the lightest ones (secondary protons, neutrons and alpha particles).

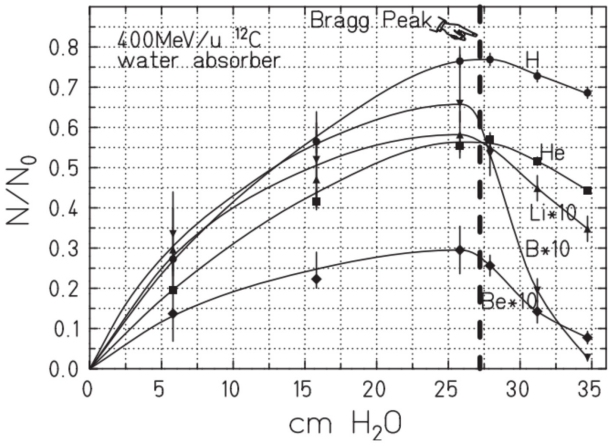

Figure 1.10: *Comparison of the production yields of several secondary fragments resulting from irradiation of a water phantom with a 400 MeV/u carbon ion beam. The contributions of Li, B and Be are magnified by a factor 10. The amount of fragments reaches a maximum at the Bragg peak, then diminishes. The most frequent fragments are H and He. Taken from the work of Haettner et al. [Haettner 2006].*

The loss of primaries is more pronounced at higher beam energies. For instance, for a carbon ions beam at 200 MeV/u about 30% of the primaries suffer from nuclear

reactions, whereas at 400 MeV/u 70% of carbon are absorbed by nuclear reactions [Haettner 2006]. As a consequence, the peak-to-entrance dose ratio get reduced with increasing projectile range. These two phenomena are clearly observed in figure 1.11.

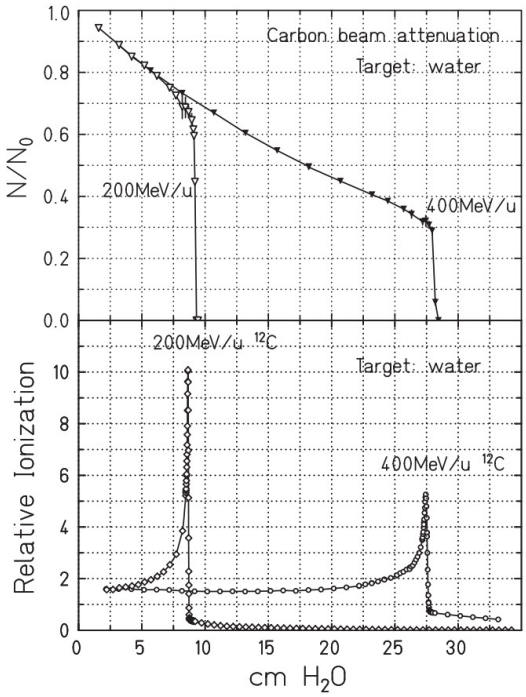

Figure 1.11: *Experimental attenuation of the primary beam in depth due to nuclear reactions for 200 and 400 MeV/u carbon beams (top), and related depth dose curves (bottom). The ratio of Bragg peak-to-entrance dose gets reduced as a function of the projectile's energy due to a greater beam attenuation. Taken from the work of Haettner et al. [Haettner 2006].*

While for proton beams only target fragmentation is possible, in the case of heavier ions, projectile fragmentation is the most important process leading to the build-up of secondary particles along the penetration depth. Because of reaction kinematics, target fragments travel with a low velocity and deposit their energy locally. However, projectile fragments are mainly forward directed and travel at almost the same velocity as the incident particle. Having a smaller mass than the projectiles, these light fragments consequently have a longer range (momentum conservation). Therefore, they are able to deposit their energy beyond the Bragg Peak, forming the so-called "fragmentation tail" as shown in figure 1.12. The amount of fragments produced, and therefore the fragmentation tail proportion, generally increases with the mass and charge of the primary particle. This feature is one of the drawbacks of the application of very heavy ions in therapy.

Furthermore, the angular distribution of fragments is much broader than the lateral spread of the primary ions caused by multiple Coulomb scattering, and can contribute to an additional lateral spread [Matsufuji 2005].

In consequence, nuclear fragmentation reactions deteriorate the ballistics of

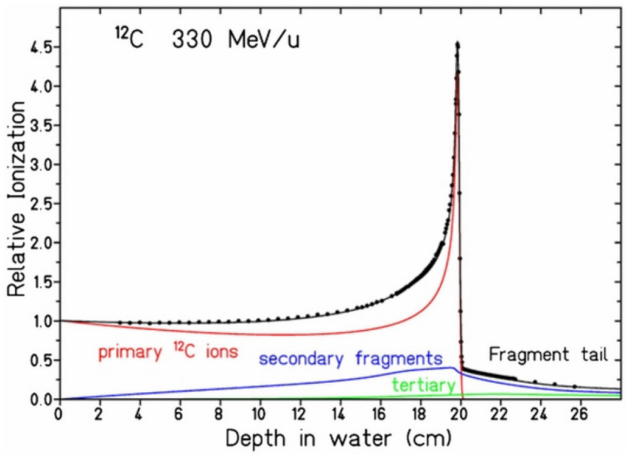

Figure 1.12: *Experimental depth dose curves of 330 MeV/u carbon ions in water, and calculated contributions of primary projectiles, secondary and tertiary fragments to the total dose. The dose tail extending beyond the Bragg peak is due to projectile fragments having a longer range than the projectiles in the medium. Taken from the work of Sihver et al. [Sihver 1998].*

charged particle beams in both longitudinal and transversal directions, especially in the Bragg peak region. Their contribution to the dose could reach 20 to 40% of the total dose for carbon ion beams [Böhlen 2010], having a significant impact on the dose distributions. It must be highlighted that the existing models describing these reactions suffer from important uncertainties. According to the literature, discrepancies between models and experimental data in terms of total nuclear non-elastic cross sections can reach 10% for proton and carbon ions [ICRU-63 2000, Böhlen 2010], due to a limited set of experimental fragmentation for model benchmarking. This results in non-negligible inaccuracies in dose calculations.

1.3.2 Technical aspects

1.3.2.1 Particle acceleration

Acceleration of protons and heavier ions requires more efficient systems than those needed for conventional RT. Despite new developments in acceleration systems (*i.e.* dielectric wall accelerators), the most common accelerators used in charged particle therapy are cyclotrons and synchrotrons. Both systems may be employed in proton therapy, while synchrotrons are required to accelerate heavier ions to clinically relevant energies. However, several cyclotron developments are ongoing for carbon therapy applications [Amaldi 2010].

Cyclotron sources

Cyclotrons deliver continuous proton beams with a fixed energy (*e.g.* around 230–250 MeV). An energy selection system, located at the cyclotron exit, may be em-

ployed to degrade the beam to lower energies. As schematic view of a cyclotron is depicted in figure 1.13. A cyclotron accelerates the proton beam using a high frequency (50–100 MHz) alternating voltage ranging from 30 to 100 kV [Paganetti 2012]. The voltage is applied between usually two or four hollow metal electrodes called "dees" (because of their "D"-shape in the first cyclotrons), located inside a vacuum chamber (see figure 1.13). The dees are placed face to face with a narrow gap between them. The protons are injected into the centre of this gap thanks to an ion source (plasma) located in the centre of the cyclotron. The dees are positioned between the poles of a large electromagnet which applies a static magnetic field perpendicular to the electrode plane. The magnetic field causes the ions trajectory to bend in a circular path due to the Lorentz force perpendicular to their direction of motion. Each time after the protons cross the gap to the other dee, the polarity of the radio-frequency (RF) voltage is reverted, thus, the electric field is in the correct direction to accelerate them. Due to the increasing speed of the particles, they move in a larger radius circle at each rotation, following a spiral path. When the desired energy is reached, the beam arrives at the rim of the dees. An extraction system then guides the accelerated protons out of the cyclotron into a beam transport system.

As accelerated particles approach the speed of light, their effective mass increases due to relativistic effects. To account for this change, either the RF has to be diminished, like in the case of synchrocyclotron (pulsed beams), or the magnetic field has to be increased with the radius of the particles' path, like in isochronous cyclotrons [Paganetti 2012].

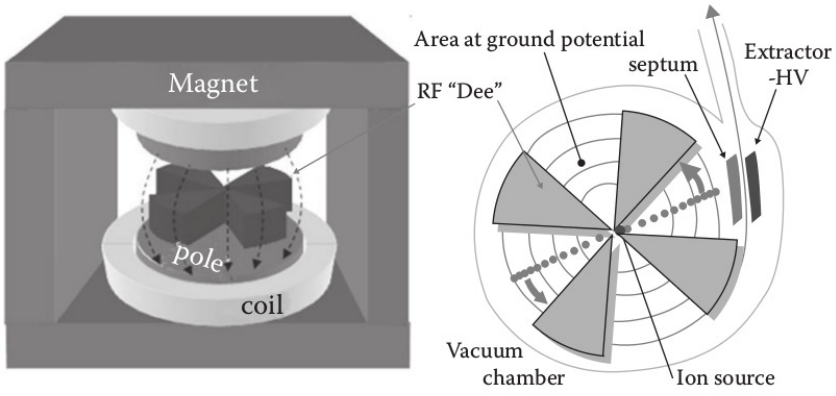

Figure 1.13: *Schematic drawing of a cyclotron. Charged particles are accelerated by means of an electric field applied between the dees. The particles keep moving in a spiral path thanks to a strong magnetic field applied by the magnets that curve their trajectories. Taken from the work of Paganetti [Paganetti 2012].*

Synchrotron sources

Synchrotrons produce pulsed beams of variable energy, in contrast to cyclotrons. A simplified drawing of a synchrotron is depicted in figure 1.14. Charged particles

are pre-accelerated thanks to a first acceleration system, like a linac or a microtron. The particles are then injected in the storage ring and cross RF cavities, where they are accelerated. Bending magnets (dipoles) allow to maintain the particles in a circular path, while focusing magnets (quadrupoles or sextupoles) focus the beam into the ring. The beam circulates around the ring repeatedly, gaining in energy at each round. Starting from an initial value determined by the injection energy, the magnetic field of the bending magnets is increased in conjunction with the beam energy to account for relativistic effects. When accelerated ions have reached the desired energy, the beam is extracted and guided towards the treatment rooms.

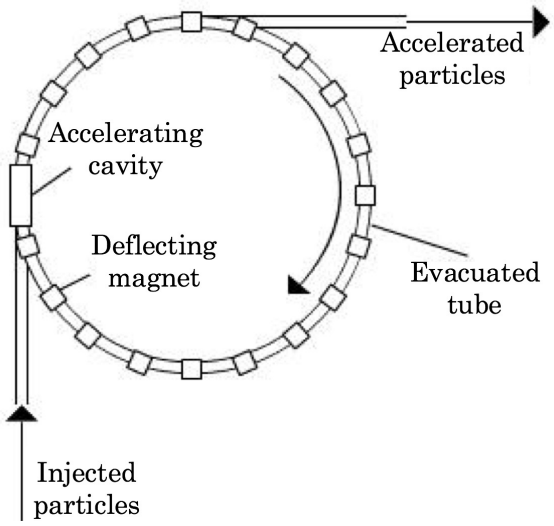

Figure 1.14: *Schematic drawing of a synchrotron. After being pre-accelerated, particles are injected in the storage ring where they are accelerated passing through RF cavities. Bending magnets deflect the particle trajectory around a circular path. Taken from the work of Ma and Lomax [Ma 2013].*

1.3.2.2 Beam delivery techniques in charged particle therapy

Once accelerated, the particles are guided into the treatment room through an optical transport system (typically, several sets of dipole and quadrupole magnets and collimators in a vacuum tube). The particles reaching the treatment room are quasi-mono-energetic (energy spread of several few percent) and have a lateral spread of only a few millimetres. For clinical applications, target coverage is needed and thus the beam needs to be spread out in lateral and longitudinal (depth) directions. In addition, in order to shape the beam to adequately treat the tumour, two systems of beam delivery are commonly used, namely passive scattering and active scanning [Paganetti 2005]. Nowadays, both delivery techniques are in use in proton and heavy ion facilities, although active methods are becoming more and more widespread.

Passive scattering

In passive scattering techniques, the proton beam is spread out by placing some scattering material into the path of the protons. Then, a combination of collimators and compensators conforms the dose to the target volume. The beam successively crosses the following items (see figure 1.15).

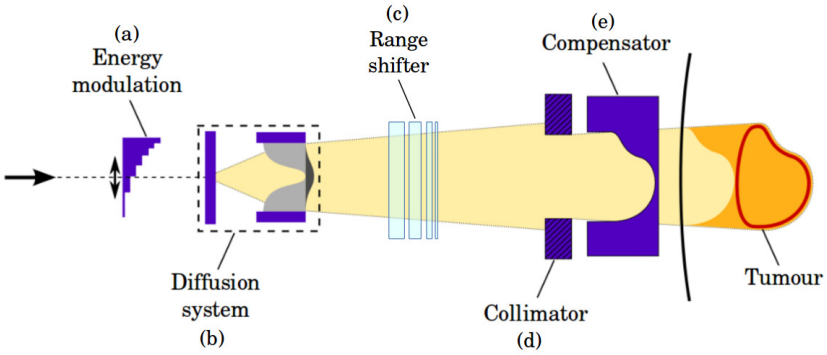

Figure 1.15: *Scheme of beam shaping method in a double scattering system consisting in a modulation wheel (a), a double diffusion system (b), a range shifter (c), an individualised collimator (d) and a range compensator (e). Taken and modified from the Ph.D. thesis of G. Bouillhol [Bouillhol 2013].*

- A *range modulator* (a) allows to spread out the Bragg peak to insure the in-depth coverage of the tumour. It is a wheel made of several blades of low-Z material (typically lexan or carbon) put in rotation during the beam delivery. The low-Z material causes slowing down of the beam with minimum increase of multiple scattering [Paganetti 2005]. Each blade of the wheel has a specific thickness and covers a given angle. This results in a superposition of several Bragg peaks of particles with different energies, creating the so-called spread-out Bragg peak (SOBP). See figure 1.16.

- A *diffusion system* (b) consisting in one or several scatter foils, is used to enlarge the narrow beam that reaches the beamline entrance. Such scatter foil consists in a thin high-Z material-slab that makes the charged particles scatter, thus laterally spreading the beam. For large fields, a double scattering is necessary. The double scattering technique (DS) is currently the most commonly used at proton therapy facilites worldwide.

- The *range shifter* (c) degrades the beam energy, therefore shifting the distal part of the SOBP to the desired depth. It consists typically of several slabs of variable thicknesses and materials (usually lead or lexan) inserted in the beamline. It allows conforming the beam to the distal part of the tumour.

- Individualised *collimator* (d) and *range compensator* (e) (see figure 1.17) are produced and used specifically for each patient in order to shape the beam

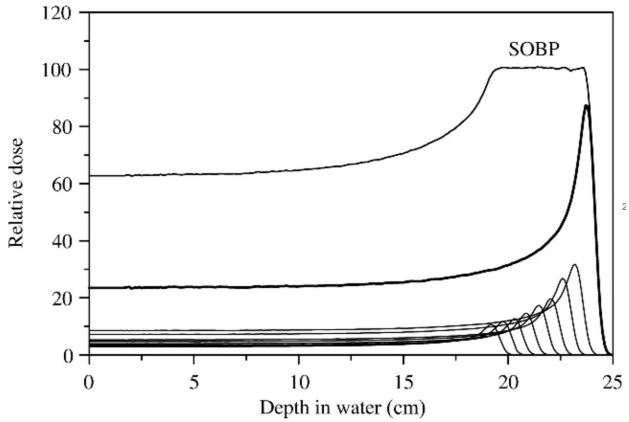

Figure 1.16: *A spread-out Bragg peak (SOBP) is created by superimposing the contribution of several Bragg peak curves of particles with different energies thus different ranges in the medium [ICRU-78 2007].*

to the target volume, both in lateral and depth directions. The collimator is often made of brass, with a sufficient thickness to stop the impinging particles. The compensator is made of low-Z material and is used to account for tissue homogeneities and the curvature of the patient surface.

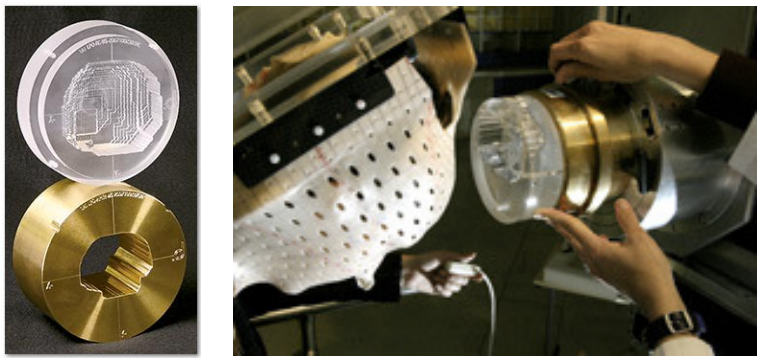

Figure 1.17: *Left: Individualised patient brass collimator (bottom) and lucite range compensator (top), taken from the Pennsylvania University website [Penn-Medicine 2016]. Right: The same elements are placed at the end of the beamline for patient treatment, taken from the Institut Curie website [Institut-Curie 2016].*

Active scanning

Profiting from the fact that charged particles can be deflected magnetically, narrow mono-energetic "pencil" beams can be scanned along the target volume in both horizontal and vertical directions by means of two magnetic dipoles (see figure 1.18). This technique is the so-called pencil beam scanning (PBS). In order to cover the

target volume in depth, the beam energy can be varied in the transport section of the facility, after the particles being extracted (see section 1.3.2.1). The target volume is typically scanned transversally in different iso-energy layers beginning with the deeper layer (maximum beam energy). One can distinguish two main scanning methods: spot and continuous scanning. Using the spot scanning technique, the beam is turned off between each spot delivery, while the beam is only stopped between two layers in continuous mode.

A hybrid delivery mode called uniform scanning (or wobbling) uses magnets to produce a broad beam which is then shaped using appropriate collimators. The target volume is scanned layer after layer by changing the beam energy using the modulator wheel in a static mode.

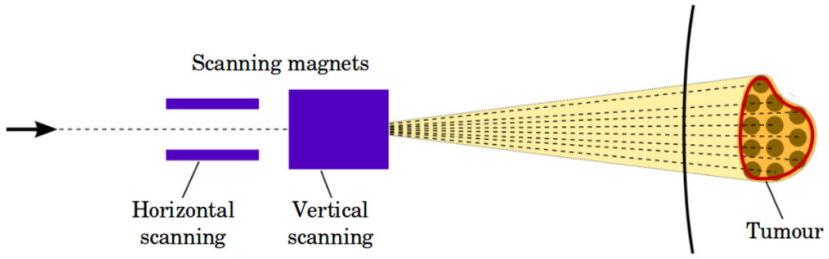

Figure 1.18: *Illustration of an active beam delivery method. Taken and modified from the Ph.D. thesis of G. Bouillhol [Bouillhol 2013]*

Active scanning methods greatly developed in the last years, as they present several advantages over the passive technique. First, active scanning techniques lead to less operating-costs than passive methods since they do not require any patient-specific hardware. Secondly, the material in the beam path is minimised, therefore reducing dose-rate loss and production of secondary particles such as neutrons. Finally, the spot intensity may be individually adjusted in order to compensate for dose variations due to heterogeneities in the beam path (before the target volume) [Schardt 2010]. However, such a method is demanding in terms of control and safety systems, and accelerator performances such as fast adjustability of the beam energy and intensity, and high stability and reproducibility of the beam position [Schardt 2010].

Radiation fields of scanned beams are inherently modulated in intensity and allow for a higher flexibility in tailoring the dose distribution than passive delivery methods. Active scanning have thus triggered the development of "intensity-modulated particle therapy" (IMPT), in analogy to the IMRT techniques used in photon RT [Lomax 1999]. IMPT has the potential to improve dose conformality and to better spare normal tissue over passive scattering techniques. Its implementation is currently pursued in clinical facilities, mainly with proton beams [Kooy 2015].

1.3.3 Radiobiological aspects

In contrast to x-rays and other neutral particles, charged particles increase their rate of energy deposition as they slow down with increasing penetration, finally releasing an intense burst of ionisation in the Bragg peak, as explained in the previous section [Joiner 2009]. This high rate of energy loss at the end of the particle range results in a dense ionisation column very effective in producing biological damages. The density of energy deposition in a particle track is known as the linear energy transfer (LET), being the amount of energy transferred by the radiations to the traversed medium per unit distance. High-LET radiations (>10 keV/μm) are thus able to induce multiple strand breaks in the DNA, leading to damages which are often non-repairable by the usual cellular mechanisms. Consequently, they have an enhanced cell-killing capacity with respect to low-LET radiations such as x-rays [IAEA-TRS-461 2008]. This is quantified by the **relative biological effectiveness** (RBE) which is defined as the ratio of x-rays and charged particle dose producing the same biological effect. Generally, the higher the LET, the higher is the RBE (see figure 1.19). However, there is an optimal LET for cell inactivation (around 100 keV/μm) where RBE reaches a maximum. For greater LET, irradiation produces more DNA double-strand breaks than are actually needed to kill the cell [Joiner 2009], resulting in a reduced effectiveness in inducing cell death per unit dose. This phenomenon is known as the "overkill effect" [Joiner 2009, Beyzadeoglu 2010] and is illustrated in figure 1.19.

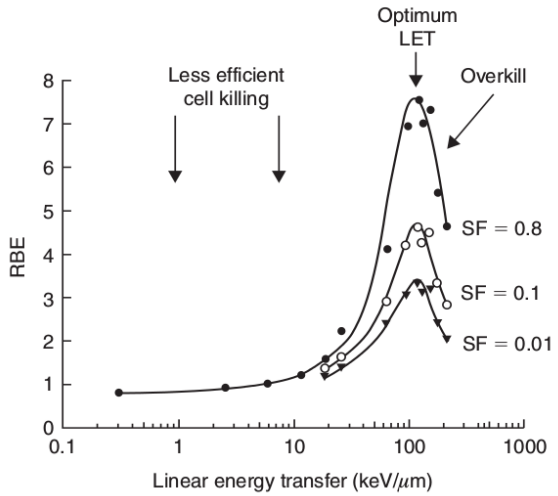

Figure 1.19: *Illustration of the dependence of RBE as a function of LET. RBE has been estimated at different dose levels (different cell survival fractions) of human kidney cells exposed in vitro to radiations. As one can see, there is an optimum LET for which RBE reaches a maximum. Greater LET radiations produce more damages than actually required for cell inactivation, resulting in a decrease of RBE values. This is known as the "overkill effect". Taken from the work of Joiner and van der Kogel [Joiner 2009].*

The RBE depends in a complex way on different parameters like particle type and energy, LET, dose and tissue type. Nevertheless, in clinical applications the RBE of protons is considered having a fixed value of 1.1 [Paganetti 2002, Paganetti 2012]. However, several *in vivo* and *in vitro* studies have pointed that RBE values in proton therapy show a linear dependence on LET [Paganetti 2002]. Giantsoudi *et al.* observed LET variations up to 30% in the Bragg peak, which could translate into RBE modifications. Moreover, there are emerging evidences that proton radiations might have distinct biological properties with respect to x-rays, such as complex DNA damage-inducing capacity, enhanced ability to inhibit tumour invasion and angiogenesis, and modulation of inflammation [Girdhani 2013]. This might also impact on the RBE values.

Nowadays, the use of variable RBE in proton therapy is hindered because of the lack of experimental data, which translates into considerable model uncertainties. Novel strategies for optimising proton therapy (and charged particle therapy in general) are currently emerging. One possibility could be the use of dose distribution optimisations based on physical quantities, that can be predicted with high accuracy. An example is LET-guided plan optimisation, in order to maximise dose-averaged LET in tumour while minimising dose-averaged LET in normal tissues since RBE values in proton therapy show a linear dependence on the LET [Giantsoudi 2013].

Charged particles heavier than protons exhibit an increased RBE in the Bragg peak as compared to the entrance region. For instance, carbon ions have a RBE of about 1 in the entrance channel, and as high as 3–4 in the Bragg peak region, thus exhibiting an advantageous differential biological effect between normal and tumoural tissues. This advantage is lost for very heavy ions (above O ions): the RBE is already high in the entrance region and does not increase much further in the Bragg peak (see figure 1.20). This is the reason why carbon ions were kept for clinical purposes: they provide a good compromise between the quality of the dose distributions and biological properties (see figure 1.21).

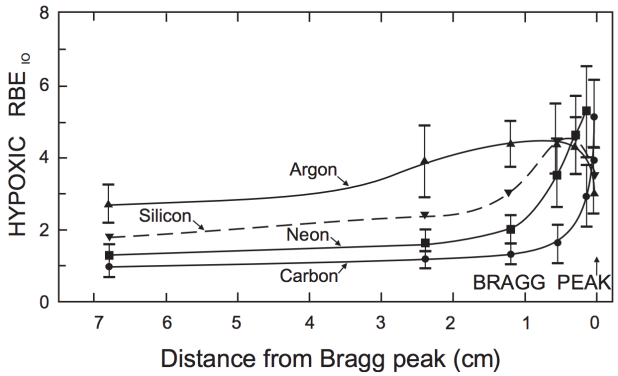

Figure 1.20: *RBE as a function of penetration depth for several ions. RBE values for carbon ions are kept close to 1 in the proximal normal tissues, while they significantly increase in the Bragg peak. In contrast, heavier ions such as argon exhibit high RBE values already in the proximal region. Taken from the work of Kraft et al. [Kraft 2009].*

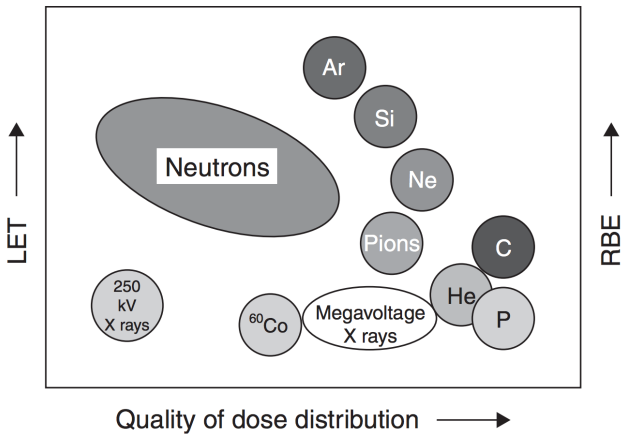

Figure 1.21: *Relative physical and radiobiological properties of different radiations and charged particles. Carbon ions and protons provide interesting dose distributions. Carbon ions have also higher LET and RBE in the Bragg peak which might confer an additional radiobiological advantage. With heavier ions like argon, silicon or neon, LET and RBE values are enhanced but the dose distributions are degraded due to the secondary fragments. Taken from the work of Joiner et al. [Joiner 2009].*

In addition, high-Z particles lead to a decrease of the **oxygen enhancement ratio** (OER) [IAEA-TRS-461 2008]. It is known that the presence of molecular oxygen increases indirect DNA damage through the production of free radicals with intracellular water. The OER represents the increase in radiation dose required to achieve the same biological effect in absence of oxygen than in the presence of normal levels of oxygen. High-LET radiations such as ion beams are less dependent on the oxygen effect (low OER) and represent a valuable tool for treatment of hypoxic tumours.

Nowadays, only proton and carbon ion beams are used in clinics. Though, the discussion about which ion species is the best biologically-suited for therapy is still open [Brahme 2001]. In particular, the interest for oxygen and helium beams is growing, especially at the Heidelberg Ion Therapy facility (HIT) in Germany, where some trials are planned to investigate the application of such ion beams [Haberer 2004].

1.3.4 Clinical indications

The favourable ballistics and radiobiological advantages make ion beams good candidates for the treatment of lesions located close to sensitive structures (where a small local overdose may lead to significant adverse effects), hypoxic and/or radio-resistant tumours, as well as some other indications for which other treatment modalities fail to provide satisfactory results [Combs 2012].

The lack of phase III clinical trials comparing photons and ions limits the confirmation of clinical advantages in charged particle therapy. The main reason for this

lack is the limited widespread of particle therapy facilities due to higher costs. However, proton therapy has been accepted by the medical community as a treatment of choice for some cancers, as evidenced by the American Society for Radiation Oncology (ASTRO) coverage policy [ASTRO 2014]. ASTRO recommends two coverage groups for proton therapy: (i) patients with specific diagnoses for which proton therapy is considered to be proven to be effective, and (ii) patients with cancer diagnoses where evidence of effectiveness of proton therapy is still emerging.

The first group concerns paediatric cancers (especially tumours of the brain such as low-grade gliomas, meningiomas, medulloblastomas, ependymomas). Those are cases in which the sparing of (still in development) normal tissues is of utmost importance to prevent from potential late complications [Habrand 2009]. Certain adult cancers such as ocular melanoma, where proton therapy is often an alternative to enucleation [Dendale 2006] are also concerned. For tumours of the skull base, especially chordomas and chondrosarcomas, proton therapy can be also considered as the treatment of choice to be applied when possible [Hug 2000, Combs 2012]. Some early works demonstrated that proton treatment led to higher local control rates compared to photon RT [Colli 2001]. In addition, the great evolution of photon RT with techniques like IMRT makes new comparisons necessary.

The second group includes other cancer sites, such as thoracic [Bush 2013], abdominal [Ling 2012] and pelvic malignancies [Ma 2013]. Head and neck cancers, for which proton studies have demonstrated safety and efficacy, especially for adenoid cystic carcinomas [Pommier 2006], are also concerned.

Carbon ion therapy is less widespread than proton therapy. However, there are clear indications that carbon therapy could have a key role where tumour radiation resistance is a limitation for proton therapy [Blakely 2004]. Several studies, mostly Japanese, revealed the high efficiency of carbon ion therapy [Kamada 2012] for inoperable bone and soft-tissue sarcomas [Kamada 2002], head and neck [Mizoe 2004], lung [Miyamoto 2007], liver [Kato 2004], prostate cancers [Tsuji 2005], and post-operative pelvic recurrence of rectal cancers [Yamada 2011]. In particular, excellent local tumour control rates were observed after carbon ion therapy for treatment of stage I non-small cell lung cancer (90% local control and 68% survival at 5 years [Miyamoto 2007]) and hepatocellular carcinoma (81% local control at 5 years [Kato 2004]).

As today, no randomised clinical trials have been performed to corroborate the benefit of carbon ions as compared to protons or advanced photon RT techniques. This is partly due to the limited availability of carbon ion centres. The first centres to offer several ion beams opened only recently (*e.g.* HIT in Germany and Centro Nazionale di Adroterapia Oncologica (CNAO) in Italy), and will permit a direct comparison of carbon ion therapy with proton or photon RT. In particular, clinical trials comparing protons and carbon ions have already been initiated at HIT for chordoma of the skull base [Nikoghosyan 2010].

The previous sections summarise the state of the art of RT. Despite the considerable advancements carried out during the last decades, RT treatments still remain

unsatisfactory in some cases. In particular, the treatment of radio-resistant tumours, lesions located in the vicinity of sensitive structures (e.g. spinal cord) or some paediatric cancers, is still challenging today. The main limitation of RT continues being the tolerance of normal tissues to radiations. Finding new treatment avenues is of utmost importance.

It is known that a variation of the physical parameters of irradiation may have a direct impact on the biological effects induced by radiations. In this sense, one strategy to improve the normal tissue tolerance is to take advantage of the use of distinct beam type (particle type and energy), fractionation schemes, dose-rate or spatial distributions. Along this line, new irradiation approaches using distinct dose deposition methods are being explored. Among them, spatially fractionated techniques have already prove their worth.

1.4 Distinct dose delivery methods: spatial fractionation of the dose

The concept of spatially fractionated radiotherapy (SFRT) was introduced at the beginning of the 20$^{\text{th}}$ century with the aim of minimising the skin radiation damage, a frequently occurring adverse effect with orthovoltage x-rays units. The use of a perforated screen, or "grid", proposed by A. Köhler (Germany) in 1909, helped reducing these adverse effects [Köhler 1909]. This technique creates similar conditions to a treatment with multiple small pencil beams.

Grids were used until the advent of megavoltage x-rays machines in the 1950's and their associated better skin sparing. Abandoned until the 1970's, the use of grids was re-introduced with megavoltage x-ray beams under the name of "grid therapy" [Mohiuddin 1990, Mohiuddin 1999]. Grid therapy is nowadays employed at few american hospitals for the shrinking of bulky malignancies (with palliative intent). The spatial fractionation of the dose is achieved by means of brass grid collimators (see figure 1.22) placed at the linac head exit.

However, grid therapy presents some limitations. Indeed, this technique uses large pencil beam sizes (around 1×1 cm^2) that are highly scattered in the tissues due to the use of megavoltage energies. A promising new strategy appeared with the birth of two spatially fractionated synchrotron techniques: microbeam radiotherapy (MRT) and minibeam radiotherapy (MBRT). These techniques use sub-millimetric beams of 25–100 μm and 500–700 μm, respectively, associated with low-energy (kilovoltage) x-rays, reducing scattering. The combination of extremely small field sizes, kilovoltage x-rays beams and spatial fractionation of the dose in MRT and MBRT has been shown to increase normal tissue resistance. The associated dose profiles consist of a pattern of *peaks* and *valleys*, with high doses along the beams path and low doses in the spaces between them. The minimum dose in the central region between two beams is named the valley dose and the dose at the centre of the beam is the peak dose. The ratio between these two magnitudes is called the peak-to-valley dose ratio (PVDR) and it is an important dosimetric parameter, since it

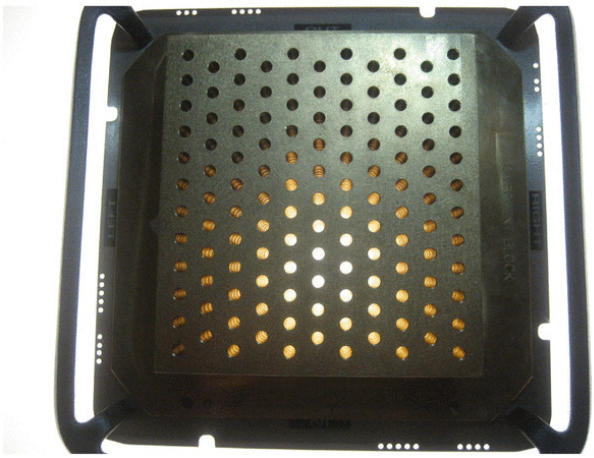

Figure 1.22: *Grid collimator used with megavoltage x-ray beams. Taken from the work of Buckey et al. [Buckey 2010].*

influences the biological response [Dilmanian 2002]. The PVDR depends on the incident beam energy and width, as well as on beam spacing, irradiation field size and tissue composition. High PVDR values and low valley doses are needed to ensure normal tissue sparing [Dilmanian 2002]. An example of a typical MBRT lateral dose profile is shown in figure 1.23. Such techniques thus combine a spatial fractionation of the dose with the use of very small beam sizes, exploiting the so-called "dose-volume effect": the smaller the beam size is, the higher the normal tissue tolerance [Hopewell 2000]. Further details on the two techniques will be given in the next section.

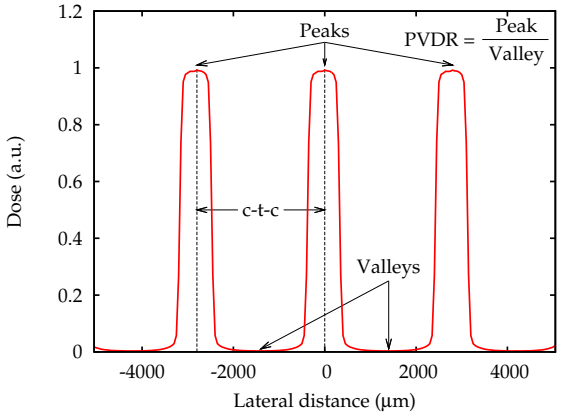

Figure 1.23: *Example of a MBRT dose profile pattern. Some relevant dosimetric parameters of spatially fractionated irradiations are depicted. The ratio of the peak dose over the valley dose is called the peak-to-valley dose ratio (PVDR). The distance separating two minibeams centers is known as the centre-to-centre distance (c-t-c).*

1.4.1 Synchrotron spatially fractionated techniques

Both MRT and MBRT use low-energy x-rays (energy spectrum ranging from 50–600 keV with a mean energy around 100 keV) produced by third-generation synchrotron sources. The main features of such synchrotron sources are an extremely high dose-rate (several thousands Gy within less than 1 s) and a very small beam divergence [Martínez-Rovira 2012]. Extremely high dose-rates are required to deliver high doses in short times while avoiding the spread of the sub-millimetric beams by cardio-synchronous motions, while the small beam divergence allows to achieve very steep dose gradients in the target volume.

In the following section, MRT technique will be described. Then, details will be given on MBRT.

1.4.1.1 Microbeam Radiotherapy (MRT)

MRT was born in 1992 at the National Synchrotron Light Source at Brookhaven National Laboratory [Slatkin 1992, Slatkin 1995], and was then developed in parallel at the European Synchrotron Radiation Facility (ESRF) in Grenoble (France). Nowadays, MRT is also explored in other synchrotrons around the world such as Spring 8 in Japan and the Australian Synchrotron.

MRT uses an array of microscopically thin (25 to 100 μm) and nearly parallel beams separated by centre-to-centre (c-t-c) distances ranging from 200 to 400 μm [Slatkin 1992]. Numerous experiments showed that MRT provides a remarkable tissue sparing effect in normal tissues and a preferential damaging effect in tumour, even with highly inhomogeneous dose distributions.

Concerning normal tissue sparing, the first MRT biological experiment carried out in NSLS in 1995 showed that doses as high as 625 Gy in one single fraction are well tolerated by normal tissues [Slatkin 1995]. Since, several pre-clinical experiments have confirmed the normal tissue sparing capability of MRT irradiations in different animal models such as weanling piglets cerebellum [Laissue 2001], suckling rat brains [Laissue 1999], adult rat brains [Slatkin 1995, Laissue 1998, Dilmanian 2002, Dilmanian 2005, Bouchet 2016], CNS of duck embryo *in ovo* [Dilmanian 2001], mouse and rat skin [Dilmanian 2003, Zhong 2003] and rat spinal cords [Laissue 2013].

Dilmanian *et al.* observed that the sparing effect of MRT is no longer maintained when the valley dose reaches the tissue tolerance limit for broad beam irradiations. Therefore, the damage threshold of MRT seems to be highly related to the valley dose [Dilmanian 2002].

The biological basis of normal tissue preservation after MRT irradiations, is not well understood yet. One participant is the so-called dose volume-effect: the smaller the field size is, the higher the tolerance of normal tissues [Curtis 1967, Hopewell 2000, Lawrence 2010]. This effect has been known since the 1960's when Zeman and collaborators investigated the possible hazards of heavy cosmic rays in astronauts brain [Zeman 1959, Zeman 1961, Curtis 1967]. They irradiated mice brains with 22.5 MeV deuteron beams of several widths and evaluated the threshold dose to produce necrotic lesions along the first half of the beam path (1.5 mm)

within 24 days. As shown in figure 1.24, the tolerance doses remain almost constant for fields larger than 0.1 mm, threshold under which the tolerance doses increased dramatically. Figure 1.25 shows histology images of mice brains irradiated with 22.5 MeV deuteron beams with a diameter of 1 mm (280 Gy entrance dose) and 25 μm (4000 Gy entrance dose). This figure clearly shows a tissue destruction when irradiated with the 1 mm-wide beam, while a much higher dose is necessary to achieve similar results with a 25 μm-wide beam.

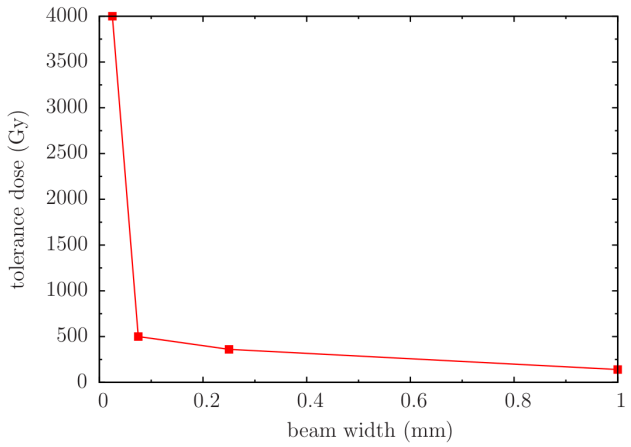

Figure 1.24: *Reconstruction of the results obtained by Zeman et al. showing the tolerance doses of mice brains to irradiation with 22.5 MeV deuteron beams of several widths [Zeman 1959]. There is an inverse relationship between radio-sensitivity and volume of tissue exposed for small volumes. This is known as the dose-volume effect.*

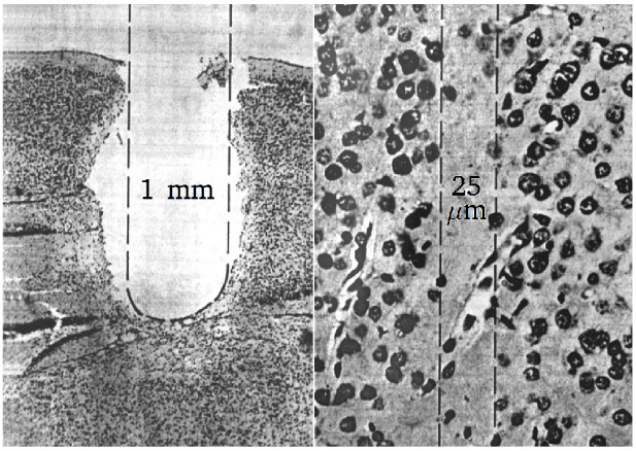

Figure 1.25: *Histology images of mice brains illustrating the dose-volume effect. On the left, complete tissue destruction is observed after irradiation with a 22.5 MeV deuteron beam of 1 mm diameter and an entrance dose of 280 Gy. On the right, an entrance dose of 4000 Gy is necessary to achieve similar results with a 25 μm-wide beam. Taken from the work of Zeman et al. [Zeman 1961].*

The dose-volume effect might be explained by the stem cell depletion hypothesis: for each organ, there is a critical volume that can be repopulated by a single survival stem cell that migrates from the nearby tissue to recover the tissue damaged by the radiation [Yaes 1988]. Thus, the combination of sub-millimetric field sizes and spatial fractionation of the dose provides a further gain in tissue sparing thanks to the biological repair of the microscopic lesions by the minimally irradiated contiguous cells.

There are indications that some other effects may be participating in tissue sparing. The role of the so-called non-targeted effects needs to be disentangled. Those include cell signalling effects like cohort effects (signal mediated effects between cells irradiated with high and low doses within an irradiated volume [Marín 2015]) and others, like abscopal effect [Siva 2015, Fernandez-Palomo 2015], a phenomenon where localised irradiation of a particular tumour site causes a response in an other distant site. Another possible player, likely associated to cell communication, was hypothesised to be hyperplasia, and migration of endothelium and glial cells of the valleys [Dilmanian 2002], being capable to repair and/or replace the damaged tissue of the peaks. The initiation of migration, proliferation and differentiation of the progenitor glial cells could be assisted by distant bystander effects from the dying cells [Dilmanian 2007, Kashino 2009]. Related to that is the potential contribution of the "microscopic prompt tissue-repair" effect, that describes the fast (within days or even hours) repair of capillary blood vessels via regeneration of angiogenic cells surviving in the undamaged areas of valleys [Serduc 2006, Bouchet 2015b].

In addition, there are strong indications that there is a differential response of tumour *versus* normal tissues in SFRT. Indeed, a remarkable preferential tumouricidal effect of MRT has been observed even with inhomogeneous distributions. Several studies reported tumour growth delay and in some cases, complete tumour ablation with a non-uniform tumour dose distribution [Laissue 1998, Dilmanian 2001, Dilmanian 2002, Laissue 2007, Regnard 2008, Bouchet 2010]. The preferential tumouricidal effect of MRT is thought to be partly due to deleterious damages in tumour vasculature. Indeed, while no major modification is observed in normal vasculature after MRT irradiation [Bouchet 2010], tumours show a denudation of vascular endothelium [Bouchet 2010, Bouchet 2015b], a decrease in the number of vessels [Bouchet 2010, Bouchet 2013] leading to a decrease in blood perfusion [Bouchet 2010, Bouchet 2015b] and to tumour hypoxia [Bouchet 2013].

At the cellular level, another possible explanation might be an increased capacity of normal tissue cells, in contrast to tumour cells, to mount an effective repair response to remove the damaged cells [Crosbie 2010]. Indeed, Crosbie *et al.* observed rapid intermixing of lethally irradiated cells (peaks) with minimally irradiated cells (valleys) 24 h after MRT irradiation in inoculated EMT-6.5 mice tumours, while, in normal mice skin, peak-dose irradiated-cells showed minimal evidence of migration up to 3.5 days post-irradiation. The rapid intermixing of lethally irradiated cells with undamaged cells within the tumour may accentuate cell-mediated communication. This extensive cells migration in tumour, as well as DNA double-strand breaks formation in non-irradiated cells, could be induced by bystander effects [Kashino 2009].

In addition, Bouchet *et al.* highlighted different aspects of the response of tumour to MRT at the molecular level. In particular, they recorded a cytostatic effect and an activation of adaptive immunity, that might partly explain MRT effectiveness [Bouchet 2015a].

The aforementioned phenomena challenge many of the current paradigms in conventional RT, since they seem to implicate different biological mechanisms from those involved when direct damage by ionising radiation takes place.

1.4.1.2 Minibeam Radiotherapy (MBRT)

Despite the high clinical potential of MRT, its widespread clinical implementation is today limited due to the requirement of extremely high dose-rates. Only synchrotron facilities enable fast enough irradiation speeds to prevent from artifacts caused by cardio-synchronous pulsations. Moreover, only low-energy x-rays (< 200 keV) with low scattering allow to ensure very high PVDR values.

To overcome these limitations, MBRT has been proposed by Dilmanian *et al.* [Dilmanian 2006]. MBRT uses 500–700 μm-wide beams, separated (c-t-c) by 1200 μm or larger spaces. Thanks to these thicker beams, the lateral dose profiles are less subject to beam smearing caused by cardiac pulsations and thus a high dose-rate is not required. In addition, the use of higher beam energies is compatible with such thicker beams, which results in lower entrance dose to deposit the same integral dose in tumour [Prezado 2009a, Prezado 2009b]. Nevertheless, the distinct beam widths and spacings of MBRT with respect to MRT may lead to different biological effects.

The first hint of the upkeep of the sparing effect with thicker beams (270 μm-wide and 11 mm-high) was observed after irradiations of rat brains with a single microplanar beam at an entrance dose of 750 Gy [Dilmanian 2005]. While one week after irradiation immuno-histochemicals studies showed a loss of oligodendrocytes and astrocytes within the beam path, at two months they observed a restoration of these cell populations. Even thicker beams were evaluated: the same group partially irradiated normal rat brains with unidirectional irradiation geometry: 680 μm wide minibeams spaced by 1360 μm [Dilmanian 2006]. After irradiations, the rats were followed for 7 months and showed no paralysis or behavioural changes at any time for doses up to 170 Gy.

Deman *et al.* realised partial brain irradiations (4×4 mm^2 covered area) of normal rats using four unidirectional minibeams: 620 μm-wide spaced with 600 μm non-irradiated gaps between each minibeam [Deman 2012]. They used 120 Gy peak radiation dose delivered in one single fraction by monochromatic beams (80 keV x-rays). After a one-year follow-up (MRI and histological studies), they observed no clinical alteration.

The first systematic and long-term study of dose escalation (peak doses from 50 to 400 Gy) in MBRT was carried out by Prezado *et al.* [Prezado 2015]. They performed whole brain irradiations with 600 μm-wide minibeams spaced by 1200 μm. The animals were followed-up one year after irradiations by At the same time, this study established an upper threshold (100 Gy peak dose) for whole rat normal brain

tolerance to MBRT.

In addition, several studies have also confirmed the therapeutic effectiveness of MBRT. Prezado *et al.* performed a dose escalation study by irradiating 9L gliosarcoma bearing-rats over a 8 mm × 8 mm area with white beam MBRT, using 640 μm-wide beams and 1120 μm c-t-c distance [Prezado 2012b]. They observed a gain factor of three in the mean survival time of the rats irradiated with 100 Gy peak dose with respect to the controls (un-irradiated). In another work, glioma bearing-rats were irradiated with monochromatic interleaved minibeams (620 μm-width and 5 mm-high) to achieve a homogeneous dose of 54 Gy in the tumour [Deman 2012]. They observed a significant increased lifespan of glioma bearing-rats with respect to untreated animals (200%).

Thanks to lower requirements in terms of dose-rate delivery with respect to MRT, MBRT has the potential of application outside synchrotron sources. This strategy could enhance the widespread of MBRT, mostly by diminishing the costs and easing access to this technique (implementation at hospitals). The transfer of MBRT into a conventional equipment using kilovoltage x-ray beams has already been accomplished by our research team. This was realised within the framework of the *TransMBRT* project (*expanding the use of MiniBeam Radiation Therapy by means of cost-effective equipment*), funded by the "Institut thématique multi-organismes cancer" within the framework of the french "Plan Cancer 2009–2013". Further details cannot be given due to patent protection.

1.4.1.3 Potential advantages of MRT and MBRT

The potential advantages of MRT and MBRT over the existing clinical RT and radio-surgery techniques might include the following:

- A superior normal tissue tolerance to radiations, allowing the use of higher and potentially curative doses in the tumour.
- Narrower beam penumbras (10–40 μm) with respect to radio-surgery beams (several millimetres), making them a good candidate for the treatment of tumours close to sensitive structures such as spinal cord, or for the treatment of illnesses such as epilepsy and Parkinson disease with negligible secondary effects [Serduc 2010, Romanelli 2013].
- A potentially more effective combination with radio-sensitisers (high-Z elements loaded in tumour) due to the larger photoelectric cross section in the energy range of MRT and MBRT.
- A potential temporary disruption of the blood-brain barrier [Serduc 2006] (brain capillaries protecting the central nervous system by regulating the entrance of molecules from blood flow into the extracellular fluid) that might allow a selective delivery of a chemotherapy drugs to small areas in the brain (improving the therapeutic index).

A further improvement in this kind of novel RT approaches is the combination of the benefits of charged particle therapy and spatial fractionation, in order to further reduce the side effects of radiations. The aim of this Ph.D. work was to explore this new strategy, as explained in the next sections.

1.4.2 Spatial fractionation in charged particle therapy

As explained in previous sections, charged particles have several advantages over x-rays radiations, both in terms of physics and radiobiology. The combination of these advantages with those of SFRT could help enhancing the therapeutic index for some cancers with poor prognosis. As today, the exploration of such an innovative strategy is one of the main concerns of the research team NARA (New Approaches in RAdiotherapy) of the laboratory "Imagerie et Modélisation en Neurobiologie et Cancérologie" (IMNC) where I did my *Ph.D* thesis. Along this line, NARA has been exploring several strategies:

- The concept of **proton MBRT** has been recently proposed by our team [Prezado 2013]. Thanks to the widespread of clinical proton facilities, experimental implementation and evaluation of this technique are achievable. As today, the assessment of both therapeutic effectiveness and potential gain in normal tissue sparing of this technique are one of the main objectives of our team.

- The use of **carbon and oxygen MBRT** could bring into play the enhanced biological effectiveness of such ions, offering an additional advantage. Despite the fact of being less accessible than protons, carbon and oxygen beams are today available at several clinical and research facilities, offering the possibility of an experimental evaluation.

- Another avenue, explored for the first time in this thesis, is the concept of **very heavy ions MBRT**, using neon and heavier ions. The idea is to take advantage the reduced OER of such heavy ions to help curing radio-resistant hypoxic tumours. Although, the availability of such very heavy ion beams is limited, the establishment of a first theoretical proof of concept is one of the objective of the research team.

The rationale for these three innovative techniques, as well as the state of the art, will be presented in the following sections.

1.4.2.1 Proton minibeam radiotherapy (pMBRT)

Proton minibeam radiotherapy (pMBRT) was first proposed by Prezado and Fois in 2013 [Prezado 2013]. This Monte Carlo (MC) study, showed that an array of 700 μm-wide clinical proton minibeams (105 MeV) would allow treating a tumour located in the centre of the brain with a homogeneous (high) dose distribution, while normal tissues in the beam path would benefit from a spatial fractionation of the

dose (see figure 1.26). Several configurations (beam energies, c-t-c and collimation methods) were evaluated. In this proof of concept, the PVDR values observed in normal tissues were similar or higher than the ones obtained in x-rays MBRT [Prezado 2011], for which biological efficiency has already been proven.

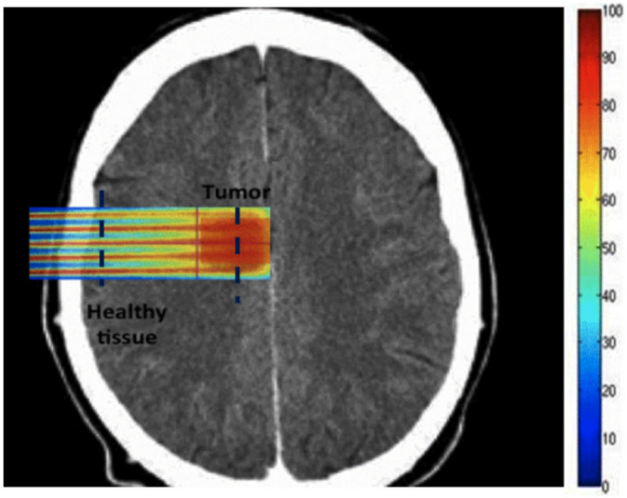

Figure 1.26: *Illustration of a dose distribution following a pMBRT irradiation of the brain. While normal tissues in the beam path benefit from a spatial fractionation of the dose, the tumour receives a quasi-homogeneous dose distribution. Taken from the work of Martínez-Rovira et al. [Martínez-Rovira 2015].*

The main possible advantages of pMBRT with respect to x-rays MBRT are the following:

- A negligible dose is deposited in the normal tissues after the Bragg peak, further reducing the secondary effects with respect to x-rays MBRT.
- Thanks to the lateral scattering of protons, a homogeneous dose distribution can be achieved in the tumour with one single minibeams array. In contrast, in x-ray MBRT the use of several arrays is needed, leading to complex and error-prone irradiation geometries.
- Tissue response in pMBRT might significantly differ from that of x-ray MBRT, probably showing more advantageous properties. Indeed, as previously mentioned, recent studies pointed out distinct biological properties of protons with respect to x-rays, such as complex DNA damages and modulation of inflammation [Girdhani 2013].

The aforementioned advantages triggered the implementation of this technique as a part of my *Ph.D.* work. In particular, I performed the experimental proof of concept and the first dosimetric evaluation of pMBRT at a clinical centre, as well

as the evaluation of the influence of setup parameters and magnetic collimation for pMBRT (see *Chapter 3*).

Another proof of the physical feasibility of pMBRT with proton beams of therapeutic energies (100 and 109 MeV pristine Bragg peaks) at a clinical facility was given in the work of Dilmanian *et al.* [Dilmanian 2015]. In order to assess the minibeam's broadening in depth (full-width at half-maximum), they used a 300 μm pinhole collimator to irradiate radiochromic films interspersed with plastic slabs. A tungsten multislit collimator was employed to produce an array of 300 μm-width planar minibeams Although this work confirms the technical feasibility of pMBRT, Dilmanian and collaborators did not assess the resultant dose distributions or PVDR values. However, their results suggest a spatial fractionation at the entrance and a homogenisation at the Bragg peak location, in agreement with our work [Peucelle 2015a].

A first biological indication of the advantages of this approach was provided by the irradiation with 20 MeV-protons of artificial skin models with 10 or 50 μm-wide irradiation channels (c-t-c distance of 500 μm) on a quadratic raster [Zlobinskaya 2013]. Comparing with other samples irradiated homogeneously at the same average dose (2 Gy), they found an enhanced normal tissue viability as well as lower levels of inflammatory parameters (Interleukin-6, TGF-Beta, and Pro-MMP1) and reduced genetic damages after microchannel irradiation compared to homogeneous irradiation. Using the same proton energy, the same team compared homogeneous field and minibeam (180 μm$\times$180 μm) irradiations of *in vivo* mouse ear model (same average dose of 60 Gy, corresponding to peak doses of 6000 Gy in minibeam configuration) [Girst 2015]. While severe ear swelling, desquamation and erythema developed a few week after broad beam irradiations, the use of minibeams reduced the adverse effects as no ear swelling or other skin reactions were observed at any time after minibeam irradiations. Despite the fact that the beam energy is not clinically relevant and that the geometry and parameters of irradiation differ from pMBRT, these works provided the first hints of potential gain in normal tissue sparing when spatial fractionation of the dose is used in combination with protons.

Besides, a recent MC study explored a spatial fractionation of the dose in proton therapy using scanned pencil beams in a square lattice irradiation pattern [Klodowska 2015]. Using 100 μm-wide beams, they used several proton energies (from 60 to 120 MeV) and c-t-c (from 1 to 6 mm), and found PVDR values similar than those of x-rays MRT.

All these works published soon after the proof of concept [Prezado 2013] show that the interest in such spatially fractionated techniques in proton therapy is rapidly growing.

1.4.2.2 Carbon and oxygen minibeam radiotherapy

Another approach is to profit from the enhanced biological effectiveness of carbon and oxygen ions, in particular at the end of their penetration depth (*i.e.* in the tumour), and from their ballistic advantages, while minimising the beams impact

on normal tissue thanks to MBRT.

A first MC study aiming to evaluate the possible advantages of carbon and oxygen minibeams was performed during the *Ph.D.* of G. Fois [Fois 2013]. This work pointed out that arrays of 700 μm-minibeams spaced with c-t-c ranging from 1400 to 3500 μm leads to much higher PVDR values with respect to proton MBRT, with the highest PVDR observed for oxygen beams. In addition, G. Fois showed that carbon and oxygen minibeams provide considerable narrower penumbras than pMBRT and GK, with values ranging from 100 to 500 μm [Fois 2013], thanks to the reduced multiple scattering and range straggling with the greater mass of such charged particles.

In parallel, a first biological experiment at a research facility suggested some advantages of the combination of carbon beams with MBRT. One sole rabbit brain was irradiated with arrays from four 90° angles, aiming to produce a solid irradiation field (40.2 Gy) at the target [Dilmanian 2012]. Indeed, in contrast to what happens in pMBRT, with carbon ions, and for the chosen configuration (300 μm-wide beams, 1050 μm c-t-c), the lateral scattering of the minibeams is too small to allow a dose homogenisation at the Bragg peak position. After 6-months observation, the rabbit behaved normally and MRI images showed significant damages in the target, associated with little damage in the surrounding brain.

More recently, the first experimental dosimetric study of carbon and oxygen MBRT has been performed at a clinical ion beam facility (HIT, Germany) by our team [Martínez-Rovira 2016]. Two detectors (radiochromic films and diamond detector) were used to evaluate and cross-check the dose distributions obtained with clinically relevant ion beam energies. A good agreement was found between the two data-sets. This work confirms the upkeep of spatial fractionation of the dose with such ions, as illustrated in figure 1.27 showing a radiochromic film exposed to an array of oxygen minibeams. The results obtained so far encourage to continue with the exploration of these new avenues. In particular, it is feasible to implement this technique at a clinical facility, and to perform reliable studies to guide preclinical trials.

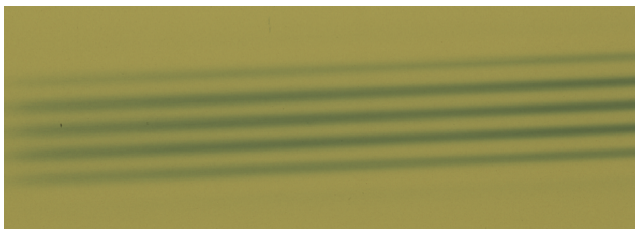

Figure 1.27: *Gafchromic© film irradiated in the longitudinal direction with oxygen minibeams. The minibeams are coming from the right. Taken from the work of Martínez-Rovira et al. [Martínez-Rovira 2016].*

1.4.2.3 Very heavy ion minibeam radiotherapy

The treatment of radio-resistant tumours, in particular hypoxic tumours, remains one of the major challenges in RT. Tumour hypoxia leads to resistance to RT and anticancer chemotherapy, as well as predisposing for increased tumour metastasis [Brown 2007]. Compared to conventional RT, heavy ion therapy is less dependent on the oxygen effect (low OER). In addition, the produced ionisation column is dense enough to be able to induce multiple strand breaks in the DNA, thus leading to damages that are often non-repairable by the usual cellular mechanisms. Unfortunately the biologically efficient region (high RBE) of such very heavy ions also extends into the normal tissues in front of the tumour (see figure 1.28 left), causing heavy late damage.

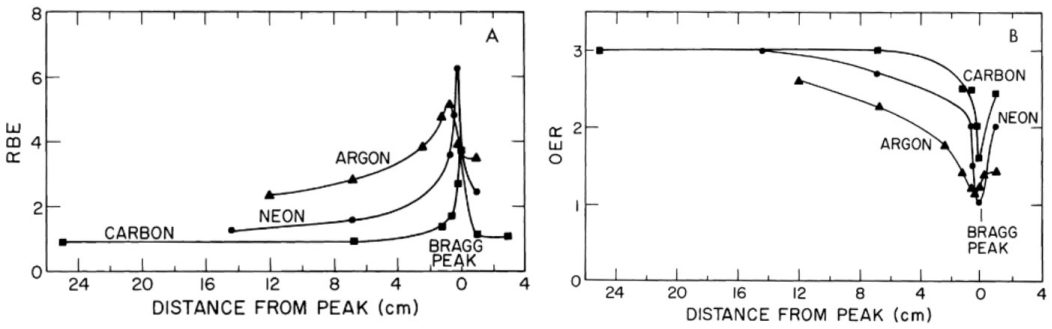

Figure 1.28: *RBE (A) and OER (B) in cultured human cells calculated at the 10% survival level, plotted as a function of distance in water from the Bragg peak position. While RBE values for carbon ions are kept close to 1 in the proximal normal tissues and then dramatically increase in the Bragg peak vicinity, with heavier ions they are already high in the proximal region and do not increase much at the end of the range. Concerning OER, the values are very low (close or equal to 1) with very heavy ions in the Bragg peak, in contrast with carbon ions where an oxygen effect is maintained. Adapted from the work of Tobias et al. [Tobias 1977].*

Indeed, in early stages of charged particle therapy, radiobiological experiments showed that radio-resistant hypoxic tumours could be ablated with very heavy ions such as argon. Such charged particles started to be used in 1977 at the BEVALAC facility (Berkeley, USA). A majority of patients received neon ion treatments, although some of them were also treated with carbon, silicon and argon beams [Castro 1978, Castro 1994]. The results in terms of local control of hypoxic tumours were encouraging, in particular in the case of macroscopic salivary gland carcinomas, paranasal sinus tumours, soft tissue sarcomas, macroscopic sarcomas of bone, locally advanced prostate carcinomas and biliary tract carcinomas [Linstadt 1991]. However, due to large side-effects in normal tissue, irradiations were stopped after few patients [Castro 1994].

The remarkable tissue sparing observed in x-rays MBRT might allow profiting from the high tumouricidal capability of those very heavy ions, while reducing at

maximum their side-effects. It would open the door to the renewed used of very heavy ions (neon or heavier).

Since the radiobiological features of MBRT are expected to greatly differ from those of conventional charged ion therapy (broad beam irradiations), established RBE values are very likely not to be valid. Along this line, whether a possible overkill effect for the heavier ions in the distal part of the Bragg peak would be totally maintained or compensated by other phenomena appearing in SFRT, it is yet to be explored.

These are the reasons why I probed the physical aspects of this new avenue by means of MC simulations in *Chapter 4*.

1.5 Work outline

The work performed during this *Ph.D.* thesis aimed at exploring the spatial fractionation of the dose using both proton and very heavy ion beams, by means of experimental studies and MC simulations. In *Chapter 2* of this manuscript, materials and methods employed will be detailed. My personal contributions on both pMBRT and very heavy ion MBRT projects are presented in two separate parts (*Chapters 3 and 4*).

The physical bases of pMBRT were already established thanks to previous works as aforedescribed. Within this framework, the objectives of my *Ph.D.* work were (i) to carry out the first technical implementation and experimental evaluation of pMBRT at a clinical facility (Institut Curie - Proton Therapy centre in Orsay) by means of a mechanical collimation, and (ii) to evaluate the potential of a magnetic collimation for pMBRT by means of MC simulations, as well as assess the impact of different irradiation parameters on the dose distributions. The results concerning this work will be reported in *Chapter 3*.

In *Chapter 4*, a MC study exploring a potential renewed use of neon and heavier ions (Si, Ar and Fe) for RT, using spatial fractionation of the dose, will be presented. In particular, this study aimed at performing an advanced physical (dosimetric) study in order to determine if an advantage might be expected from such a novel approach where radiobiological magnitudes might notably depart from the standard ones.

General conclusions and reflections about the work performed during this *Ph.D.* thesis will be developed in *Chapter 5*. Finally, *Chapter 6* compiles the scientific production.

Chapter 2

Materials & Methods

Contents

2.1 Experimental validation of pMBRT at ICPO 41
2.1.1 Description of ICPO facility 41
2.1.2 Basic principles of dosimetry 44
2.1.3 Small field dosimetry 52
2.1.4 Experimental dosimetry in pMBRT 55
2.2 Monte Carlo simulations 64
2.2.1 The Monte Carlo method 64
2.2.2 MC simulations in medical physics 65
2.2.3 The Geant4/GATE simulation toolkit 66
2.2.4 Simulations geometry and details for this work 68
2.2.5 Parallelisation of the calculations 73
2.2.6 Assessment of uncertainties on the computed dose 74

This chapter is devoted to the description of the materials and methods employed in this work. The first part will describe the experimental dosimetry studies performed for pMBRT. The Institut Curie - Proton Therapy Centre in Orsay (ICPO) will be presented, then, details about the dosimetry protocol as well as the detectors employed during this work will be given.

MC dosimetry was also performed in this work. The MC method, as well as the simulations details will be presented in the last section of this chapter.

2.1 Experimental validation of pMBRT at ICPO

As previously mentioned, one of the main task carried out during this *Ph.D.* work was the technical implementation of pMBRT and its dosimetric evaluation at a clinical centre, in particular ICPO, that will be described hereafter.

2.1.1 Description of ICPO facility

At ICPO, a C230 isochronous cyclotron from Ion Beam Applications company (IBA) delivers 230 MeV protons at the accelerator exit and supply three treatment rooms (see figure 2.1). Two treatment rooms have horizontal fixed beamlines and employ a DS delivery system. The proton maximum energies in these rooms are 201 MeV

in the so-called "Y1" room, and 76 MeV in "Y2", corresponding to a proton range in water of approximately 26 and 4 cm, respectively. At present, the Y1 room is devoted to intracranial treatments, while only ocular treatments are performed in the Y2 room. The third room is equipped with a rotating gantry from IBA. The final part of the gantry, namely the nozzle, allows both passive and active beam delivery methods to be used. At the moment, only DS and US modes are available. The commissioning of the PBS system is ongoing. The maximum energy in this room is 230 MeV. The gantry is able of doing a 220°-rotation, allowing to reach treatment locations previously inaccessible with a horizontal beamline. This room serves primarily for paediatric cancer patients.

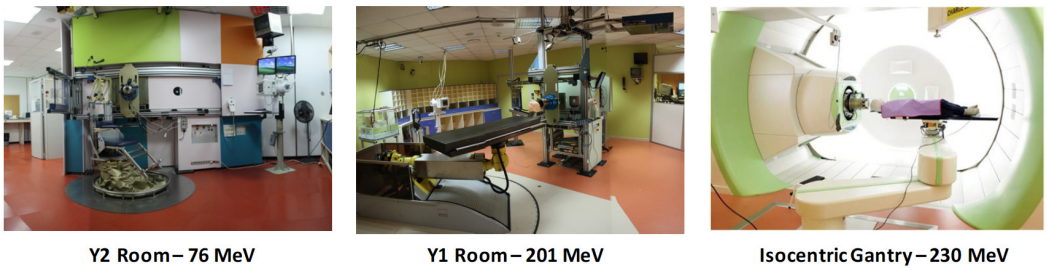

Figure 2.1: *Pictures of the three treatment rooms of ICPO. Y1 and Y2 rooms have horizontal fixed beamlines that use DS delivery method. In the third room, the isocentric gantry allows the beam to be rotated around the patient. The gantry nozzle permits both passive and active beam delivery.*

In Y2 (ocular treatments), patients receive their treatment in a sitting position. In the gantry room, they are lying down on a treatment couch. In Y1, both positions are possible thanks to a robotised device able to control either a treatment couch (see figure 2.2 left) or a chair (see figure 2.2 right). This allows to increase the possible beam angulations during treatment.

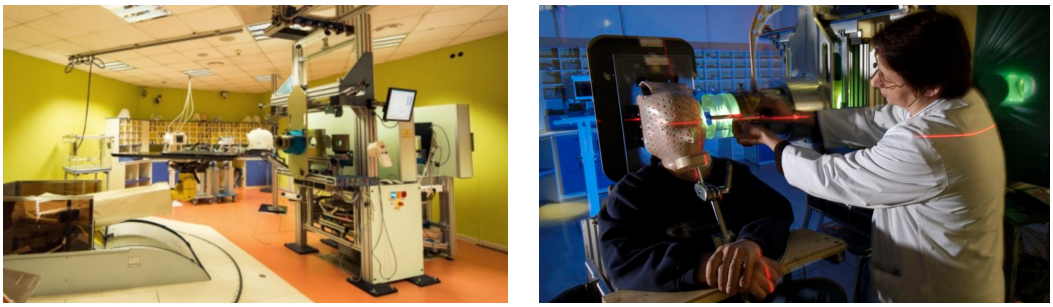

Figure 2.2: *Left: ICPO horizontal Y1 proton therapy treatment room. At the of the beamline is positioned the treatment couch. Right: The patient is positioned on the chair treatment.*

pMBRT uses a spatial fractionation of the dose. As explained in the proof of concept [Prezado 2013], this can be achieved by two methods:

- A mechanical collimation, using a multislit collimator.
- A magnetic collimation, *i.e.* using several sets of quadrupole magnets to focus the beam. Along this line, the existing PBS system could be modified for pMBRT purposes.

For the experimental validation of pMBRT, a first prototype of collimator was used. The beam was segmented into one (single slit) or several (multislit) minibeams by means of brass collimators specifically designed for the pMBRT technique, as shown in figure 2.3. A thickness of 5 cm was chosen since it is the one used for proton therapy treatments at this range of energies. These collimators were manufactured at ICPO by means of electrical discharge machining. Four collimator-prototypes with different beam widths and minibeam c-t-c distances were investigated. Their specifications are reported in table 2.1. An additional brass squared-shape collimator was added after pMBRT collimators to limit the irradiation area to 2×2 cm^2. This corresponds to the dimension of a rat brain, that is the animal model chosen to perform the pre-clinical studies of the technique.

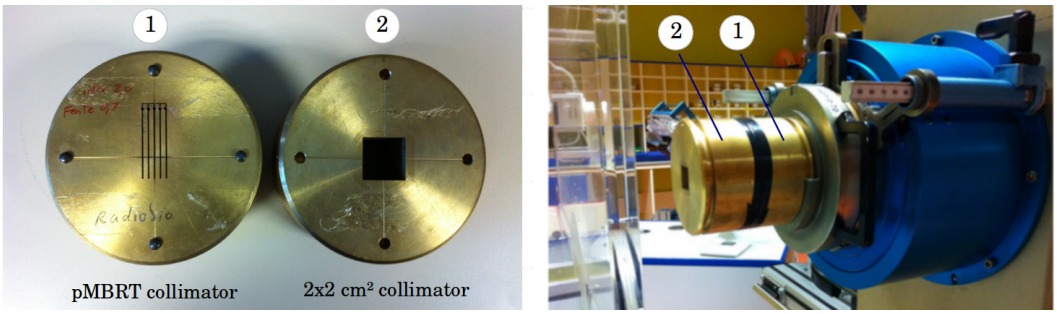

Figure 2.3: *pMBRT multislit and 2×2 cm^2 collimators (left). The machining process created 3.5 cm-long slits. To achieve the desired irradiation area (2 × 2 cm^2), an additional square collimator was added after the pMBRT collimator on the beamline nozzle (right).*

Collimators features			
Collimator	Slits width	Number of slits	c-t-c
Multi1	700 μm	5	3500 μm
Multi2	700 μm	5	2700 μm
Multi3	400 μm	5	3200 μm
Single	700 μm	1	N.A.

Table 2.1: *Specifications of the four pMBRT collimator prototypes investigated in this work.*

The characteristics of the Y1 beamline were the most interesting for an accurate definition of the minibeams (thin beam, narrow penumbras) using a mechanical collimation. This is the reason why all experiments were conducted in the Y1

treatment room. The beam characteristics at the room entrance (680 cm away from the isocentre) are reported in table 2.2. In addition, a schematic view of the Y1 beamline with all the beam modifiers is presented in figure 2.4. In particular, the effective source (*i.e.* effective origin of scattering [Gottschalk 2004]) in Y1 is located far away from the isocentre (540 cm), which permits to use parallel slits, thus offering very narrow penumbras at the patient level. In addition, Y1 presents the smallest beam divergence (around 5 mrad) among the three treatment rooms at ICPO.

E	ΔE	Beam angular divergence
201 MeV	1.0 MeV	4.3 mrad (H) / 5.4 mrad (V)

Table 2.2: *Beam characteristics at the Y1 room entrance (680 cm away from the isocentre).*

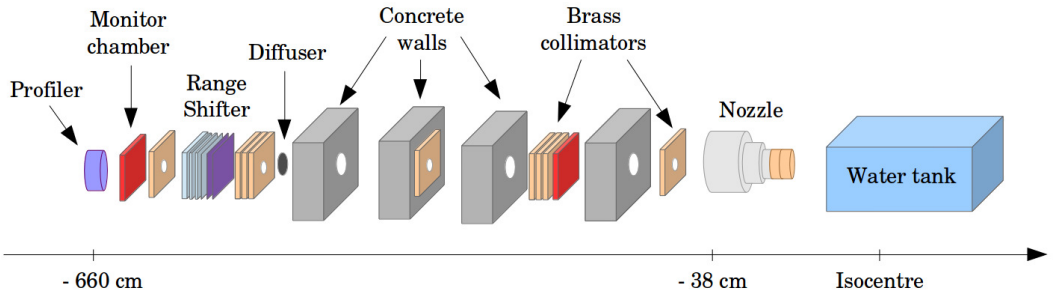

Figure 2.4: *Schematic view of the Y1 beamline (not to scale).*

The main targets of pMBRT will likely be neurological cases, *i.e.* tumours of the brain that might be stabilised against cardiac and pulmonary cycles. In order to consider the worst treatment case (the centre of a human brain), 100 MeV Bragg peaks, corresponding to a proton range of 7.7 cm in water, were used for pMBRT implementation at ICPO. The energy degradation in the treatment room was performed by means of the range shifter, using 148.5 mm of lexan. In this work, only simple Bragg peaks were considered in order to reproduce the same conditions as those of the MC proof of concept. In addition, the first biological experiments in pMBRT will concern rat brains, in which a tumour will not exceed a diameter of 3–5 mm. The width of the Bragg peaks considered in this work allowed to cover 3 and 5 mm with 90 and 96% of the prescription (Bragg peak) dose, respectively. A SOBP was thus not needed for this first phase.

In order to establish the technical feasibility of pMBRT at a clinical centre, an in-depth dosimetric evaluation campaign was carried out at ICPO. Further details about the methodology and materials employed are presented in the next section.

2.1.2 Basic principles of dosimetry

Prior to any treatment, the main task of the medical physicist is to precisely calibrate the radiation beams, thus requiring an accurate dosimetry. As stated in the

international code of practice for dosimetry, there are strong evidences that eradication of a primary tumour requires an accuracy of ±5% in the delivery of an absorbed dose to the target volume. In this section, the basic principles of dosimetry will be presented. In addition, the main challenges of small field dosimetry will be addressed.

2.1.2.1 Dosimetric quantities

Dosimetry is the measurement of the absorbed dose deposited by ionising radiations in a material (*i.e.* human body). Water, being the main component of the human body, is the reference medium in RT. Thus, absorbed dose to water D is the mainly used quantity of interest in RT, since it relates closely to the biological effects of radiations [IAEA-TRS-398 2001]. D is expressed in grays (Gy) [J/kg] and is defined as the mean energy deposited by ionising particles $\mathrm{d}\varepsilon$ in a mass element $\mathrm{d}m$, as expressed in equation 2.1:

$$D = \frac{\mathrm{d}\varepsilon}{\mathrm{d}m} \text{ [Gy]} \tag{2.1}$$

The energy imparted ε is the sum of all the energy entering the volume of interest minus all the energy leaving the volume, taking into account any mass-energy conversion (particle creation or annihilation processes, within the volume.

The transfer of energy from IR to the medium involves a series of steps. First, uncharged particles must transfer their energy to charged particles (secondary electrons) which can then travel along the medium while depositing their energy by means of ionisations in a continuous way. Kerma ("Kinetic Energy Released per unit MAss") is a measure of energy transferred $\mathrm{d}E_{\mathrm{tr}}$, *i.e.* the sum of the initial kinetic energies of charged particles set in motions) in a mass element $\mathrm{d}m$, as denoted in equation 2.9:

$$K = \frac{\mathrm{d}E_{\mathrm{tr}}}{\mathrm{d}m} \text{ [Gy]} \tag{2.2}$$

The secondary electrons may then transfer their energy either by collisions or radiative interactions (Bremsstrahlung). Kerma is therefore usually divided into two components: the collision kerma K_{col} and the radiative kerma K_{rad} [Podgorsak 2005]. K_{col} can be expressed as:

$$K_{\mathrm{col}} = K - K_{\mathrm{rad}} = K(1-g) \tag{2.3}$$

where g is the fraction of kinetic energy dissipated by radiative emission. According to ICRU [IAEA-TRS-398 2001], kerma relates to the primary particle fluence ϕ as expressed in equation 2.5:

$$K = (\frac{\mu_{\mathrm{tr}}}{\rho})E\phi \tag{2.4}$$

$$K_{\mathrm{col}} = (\frac{\mu_{\mathrm{en}}}{\rho})E\phi \tag{2.5}$$

where μ_{tr} and μ_{en} refer to the mass energy transfer and absorption coefficients, respectively. Equation 2.5 considers a mono-energetic beam with particles having

an energy E. To consider poly-energetic beams, $\phi_E = \mathrm{d}\phi/\mathrm{d}E$ has to be introduced, as follows:

$$K = \int_0^{E_{\max}} E\phi_E \left(\frac{\mu_{\mathrm{tr}}(E)}{\rho}\right) \mathrm{d}E \tag{2.6}$$

The secondary electrons path may be larger than the dimension of the mass element, and, in that case, only a part of the energy transferred by the incident particle will be actually deposited in the medium. In that sense, the absorbed dose D concerns the energy *imparted* to an elementary volume, whereas kerma concerns energy *transferred*, as the charged particles can leave the elementary volume, taking a fraction of the initial kinetic energy with them. However, if any charged particle kinetic energy leaving the elementary volume is replaced by an exactly equal amount entering the volume, the absorbed dose equals the collision kerma [Mayles 2007]. In that case, a so-called "charged particle equilibrium" (CPE) exists, and the relation between absorbed dose and kerma for a poly-energetic beam is given by:

$$D = K_{\mathrm{col}} = \int_0^{E_{\max}} E\phi_E \left(\frac{\mu_{\mathrm{en}}(E)}{\rho}\right) \mathrm{d}E \tag{2.7}$$

An analogous quantity to kerma for charged particles (primary beam) is cema C ("Converted Energy per unit MAss"), which quantifies the energy transferred by charged particles in electronic collisions $\mathrm{d}E_{\mathrm{c}}$, disregarding energy dissipation by secondary electrons (*i.e.* δ-rays), in a mass $\mathrm{d}m$ of a medium:

$$C = \frac{\mathrm{d}E_{\mathrm{c}}}{\mathrm{d}m} \tag{2.8}$$

Equivalent relationships can thus be derived for directly ionising radiations (charged incident particles such as electrons, protons or heavy ions). For charged particles the relevant physical quantity is the stopping power S. As it was the case for kerma, S can also be divided in collision S_{col} and radiative S_{rad} components. Considering a mass element, the energy lost in the form of Bremsstrahlung is likely to escape the considered medium. It is thus appropriate to employ the collision stopping power S_{col} rather than the total stopping power S [Mayles 2007]. Cema can be expressed as the fluence of primary charged particles times their stopping power:

$$\frac{\mathrm{d}E_{\mathrm{c}}}{\mathrm{d}m} = \frac{S_{\mathrm{col}}}{\rho}\phi \tag{2.9}$$

In analogy to the relation between kerma and absorbed dose, cema is not necessarily equal to absorbed dose, as some of the δ-rays can leave the mass element. To introduce absorbed dose, it must be assumed that an electronic equilibrium (δ-rays) exists in the medium [Mayles 2007]. In that case, D relates to C and S_{col} through equation 2.10:

$$D = C = \frac{S_{\mathrm{col}}}{\rho}\phi \tag{2.10}$$

Finally, considering a poly-energetic radiation, the absorbed dose is denoted as:

$$D = \int_0^{E_{\max}} \phi_E \left(\frac{S_{\mathrm{col}}(E)}{\rho}\right) \mathrm{d}E \tag{2.11}$$

2.1.2.2 How to correlate the dosimeter readout to absorbed dose ?

In order to measure absorbed dose to water, it is necessary to introduce a radiation sensitive device (dosimeter) into the medium. The readout from a dosimeter will generally be proportional to the energy absorbed in its sensitive material and thus to the absorbed dose in this material [Mayles 2007]. The sensitive volume of the dosimeter may contain a gaseous, liquid or solid medium [Podgorsak 2005]. Generally, the sensitive medium of the dosimeter is not of the same material as the medium in which it is embedded. In that case, it is necessary to apply a conversion factor to correlate the dose absorbed in the sensitive material D_{det} to the absorbed dose in the medium D_{med}, as illustrated in figure 2.5. The detector can be thought of as a cavity introduced into the uniform medium of interest. The so-called "cavity theory" proposes to evaluate f_{Q} thanks to equation 2.12 [Mayles 2007]:

$$f_{\text{Q}} = \frac{D_{\text{med}}}{D_{\text{det}}} \tag{2.12}$$

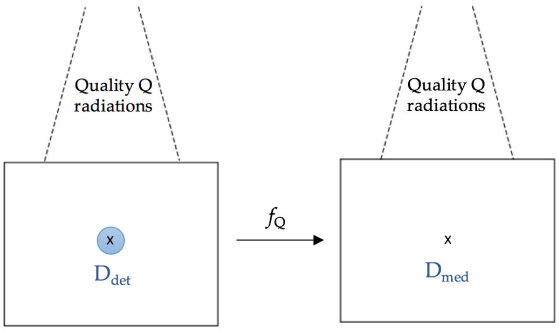

Figure 2.5: *Scheme illustrating the general situation of a measurement by means of a detector introduced into a medium (left). For a given exposure to radiations of quality Q, it leads to the D_{det} quantity. To convert it into the dose D_{med} in the medium in the absence of the detector (right), one has to multiply by f_Q.*

Several situations can be considered for the determination of f_{Q} depending on the size of the sensitive detector. Figure 2.6 shows a schematic of tracks taken by secondary electrons produced in a cavity irradiated by a megavoltage photon beam [Horowitz 2006]. A cavity is considered as "small" if the range of secondary electrons impinging the cavity is much larger than the cavity's dimensions (figure 2.6 A). In that case, all energy deposited in the cavity is contributed by electrons generated by interactions outside of the cavity. In the case of an "intermediate" cavity, a non-negligible proportion of the energy deposited in the cavity comes from electrons generated by interactions with the cavity material (figure 2.6 B). A "large" cavity has much higher dimensions than the range of secondary electrons, and most of the energy deposited in the cavity is due to electrons generated by the interactions within the cavity (figure 2.6 C).

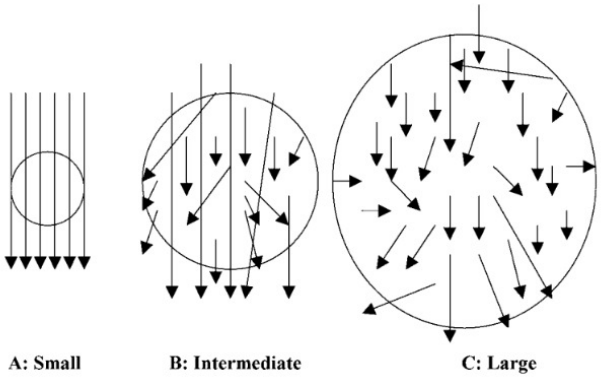

Figure 2.6: *Illustration of secondary electron tracks in (A) a small cavity, (B) an intermediate cavity, and (C) a large cavity. Taken from the work of Horowitz et al. [Horowitz 2006].*

Corresponding to these three scenarios, three distinct cavity theories apply:

- **Cavity theory for small detectors**, also known as the **Bragg-Gray theory**. The conditions for application of the Bragg-Gray theory are the following [Podgorsak 2005]: (i) the cavity must be small when compared with the range of charged particles incident on it, so that its presence does not perturb the fluence of charged particles in the medium, and (ii) the absorbed dose in the cavity is deposited solely by charged particles crossing it (*i.e.* photon interactions in the cavity are assumed negligible and thus ignored). Under these two conditions, the dose to the medium D_{med} is related to the dose in the cavity D_{cav} as follows, by combining equations 2.11 and 2.12:

$$f_{\text{Q}} = \frac{\int_0^{E_{\max}} \phi_E \left(\frac{S_{\text{col}}(E)}{\rho}\right)_{\text{med}} \text{d}E}{\int_0^{E_{\max}} \phi_E \left(\frac{S_{\text{col}}(E)}{\rho}\right)_{\text{det}} \text{d}E} \tag{2.13}$$

  The Bragg-Gray theory assumes that all collision energy losses result in energy deposition within the cavity, *i.e.* that charged particles lose energy by continuous slowing down, in a large number of extremely small energy-loss events. However, in practice, some δ-rays released in the cavity would have sufficient energy to escape from the cavity, carrying some of their energy with them. Spencer and Attix proposed an extension of the Bragg-Gray theory that takes into account these δ-ray. In the **Spencer-Attix theory**, the secondary electron fluence is divided into two components based on a user defined energy threshold Δ. All secondary electrons that lose an amount of energy in the cavity below Δ are assumed to be local to the cavity, while all electrons that lose energy above Δ are assumed to escape entirely. According to Spencer and Attix, the conversion factor f_{Q} can be determined with the following expression:

$$f_{\text{Q}} = \frac{\int_\Delta^{E_{\max}} \phi_E \left(\frac{L_\Delta(E)}{\rho}\right)_{\text{med}} \text{d}E + \phi(\Delta) \left(\frac{S_{\text{col}}}{\rho}\right)_{\text{med}} \Delta}{\int_\Delta^{E_{\max}} \phi_E \left(\frac{L_\Delta(E)}{\rho}\right)_{\text{det}} \text{d}E + \phi(\Delta) \left(\frac{S_{\text{col}}}{\rho}\right)_{\text{det}} \Delta} \tag{2.14}$$

The value of Δ is related to the size of the cavity, and Spencer and Attix suggested that Δ be set equal to the energy of electrons with a range (in the cavity material) just sufficient to cross the cavity [Mayles 2007].

- **Cavity theory for large detectors**: it considers detectors whose dimensions are greater than the maximum range of secondary electrons generated in the cavity material. In that case, the primary beam produces secondary electrons that have not a sufficient energy to cross the cavity. A "Transient Charged Particle Equilibrium" (TCPE) is observed in the cavity. Considering this particular equilibrium state, the conversion factor estimated by this theory is given by:

$$f_{\mathrm{Q}} = \frac{\int_0^{E_{\max}} E\phi_{\mathrm{E}} \left(\frac{\mu_{\mathrm{en}}(E)}{\rho}\right)_{\mathrm{med}} \mathrm{d}E}{\int_0^{E_{\max}} E\phi_{\mathrm{E}} \left(\frac{\mu_{\mathrm{en}}(E)}{\rho}\right)_{\mathrm{det}} \mathrm{d}E} \tag{2.15}$$

- **Cavity theory for intermediate detectors**. The two previous cases are not easily applicable to clinical beams that have a continuous energy spectrum and do not meet neither the Bragg-Gray conditions nor the large cavity requirements. Burlin extended the Bragg-Gray and Spencer-Attix theories to cavities of intermediate dimensions by introducing a large cavity limit to the Spencer-Attix equation using a weighting parameter between the mass energy-transfer coefficient $(\mu_{\mathrm{en}}/\rho)^{det}_{med}$ and the stopping power ratio $(S_{\mathrm{col}}/\rho)^{det}_{med}$. The **Burlin cavity theory** can be written as follows:

$$f_{\mathrm{Q}} = d\left(\frac{S_{\mathrm{col}}}{\rho}\right)^{med}_{det} + (1-d)\left(\frac{\mu_{\mathrm{en}}}{\rho}\right)^{med}_{det} \tag{2.16}$$

where d is a weighting factor that varies between unity for small (Bragg-Gray) cavities and zero for large cavities. Burlin provided a formalism to estimate the d parameter [Burlin 1966].

The aforedescribed cavity theories have been specifically developed for photon beam irradiations. In particular, the cavity sizes are defined with respect to the range of electrons produced by photon interactions. For most applications in charged particle beams like electrons, protons and heavy ions, all cavities are considered to be small, so the Bragg-Gray theory applies [Horowitz 2006].

In the previous sections, basic quantities and theoretical concepts of dosimetry have been introduced. In practice, accurate dosimetry has to be carried out in order to characterise any clinical beam prior treatments. To be able to determine the dose in any point within the patient, physicists need to implement a model of the clinical beam into the TPS. To provide basic data for this beam model, measurements must be performed on the treatment machine. It is convenient to divide these measurements in two categories: absolute and relative dosimetries. Both concepts will be detailed in the next sections.

2.1.2.3 Absolute dosimetry

Absolute dosimetry at a reference point is the determination of absorbed dose. It is required to calibrate a clinical beam before any RT treatment is performed. The ionisation chamber (IC) is the recommended dosimeter to be used for absolute dose determination in all international codes of practice like the International Atomic Energy Agency (IAEA) Technical Reports Series (TRS) 398 [IAEA-TRS-398 2001] and American Association of Physicists in Medicine (AAPM) [AAPM-TG-51 1999]. IC comes in various shapes and sizes, however it is basically a cavity filled with gas (air most of the time) with two electrodes. A voltage potential is applied between the electrodes to create an electric field in the filled gas. During irradiation, the gas of the cavity is ionised, ion-pairs are created and the resultant positive ions and electrons move to the electrodes of the opposite polarity under the influence of the electric field. This generates an ionisation current which is measured by an electrometer circuit. Each ion pair created deposits or removes a small electric charge to or from an electrode, such that the accumulated charge is proportional to the number of ion pairs created, and hence to the radiation dose. The codes of practice, like TRS 398, provide recommendations in order to relate to raw reading (*i.e.* collected charges) of the IC to the absorbed dose in water. The TRS 398 describes reference conditions such as field size, dosimeter type and measurement depth in water, for each radiation type and energy (*i.e.* beam quality). In reference conditions, the absorbed dose to water is determined following the formalism described in equation 2.17:

$$D_{\mathrm{Q,w}} = M_{\mathrm{Q}} \times N_{w,Q_0} \times k_{Q,Q_0}[Gy] \tag{2.17}$$

where M_{Q} is the reading of the dosimeter (with the reference point of the chamber positioned in the reference position), corrected for the influence of temperature and pressure ($k_{\mathrm{TP}} = [P_0 \times (T + 273.2)]/[P \times (T_0 + 273.2)]$ with T_0=20.0°C and P_0=101.3 kPa), electrometer calibration (k_{elec}), polarity effect (k_{pol}) and ion recombination (k_s). N_{w,Q_0} is the calibration factor in terms of absorbed dose to water for the dosimeter at the reference quality Q_0. k_{Q,Q_0} is a chamber specific factor that corrects for differences between the reference beam quality and the actual quality being used Q. Further details about these correction factors can be found in the codes of practice [IAEA-TRS-398 2001, AAPM-TG-51 1999].

Depending on the beam quality, the TRS 398 recommends the use of either cylindrical or parallel plane chambers, or both (see figure 2.7). While in photon RT only cylindrical IC are recommended for absolute dosimetry, in proton beams both types may be used. However cylindrical chambers are preferred due to lower uncertainties in the determination of $D_{\mathrm{Q,w}}$ with this type of dosimeter. In all cases, IC used for absolute dose determination have to be calibrated in a reference laboratory that will provide the N_{w,Q_0} calibration factor to be applied.

The reference conditions vary from a radiation type to another. For instance, with high energy photon beams, clinical dosimetry calculations are often referenced to the depth of dose maximum z_{max} [IAEA-TRS-398 2001]. For proton beams, the recommended measurement depth is located in the middle of the SOBP for a

modulated beam, or in the plateau region (3 g/cm^2) for mono-energetic beams.

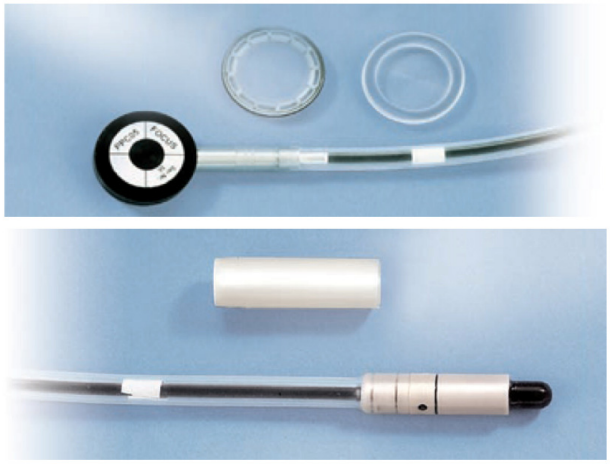

Figure 2.7: *Top: parallel plane chamber (PPC05 from IBA). Bottom: cylindrical chamber (CC13 from IBA). Taken from the IBA website [IBA 2016].*

2.1.2.4 Relative dosimetry

In practice, the actual treatment situation is different from the reference conditions used for beam calibration. It is thus crucial to measure the dose for a wide range of conditions representative of the clinical use. These measurements are then related to the absolute dose in reference conditions. The main ones are the following:

- **Off-axis profiles**, also known as lateral dose profiles, measure the variation of the dose with distance from the central beam axis at a given depth.
- **Depth dose profiles** report the variation of the dose with depth along the beam central axis. It is also called percentage depth dose (PDD).
- **Scatter factors**, or output factors (OF), determine the variation of the absorbed dose at a reference point as a function of beam size.

Relative dosimetry can be performed using a wide range of dosimeters, which differ in terms of shape, size and materials. IC of a smaller size than those used in absolute dosimetry (*e.g.* Pinpoint (0.016 cc), or CC13 (0.125 cc)) are mostly employed. Among the other types of dosimeters commonly used are radiographic or radiochromic films, thermoluminescent dosimeters (TLD), semi-conductors such as silicon diodes or metal oxide semiconductor field effect transistors (MOSFET,) gel dosimeters and diamond dosimeters. Further details will be given on some of these detectors in the following sections. Additional informations about these detectors can be found in the work of Podgorsak [Podgorsak 2005].

In relative dosimetry, there is a higher flexibility in the choice of the phantom to be employed, as measurements are always relative to some reference situation. The main choices are remotely controlled water phantoms (also known as water tanks) and solid plastic phantoms [Mayles 2007]. Water tanks are ideal for measuring dose distributions over several directions. However, such a hardware is cumbersome and requires large setup time. This is the main reason why, in many cases, the use of a solid slabs phantom is preferable for faster and easier measurements, provided the relationship between dosimeter readings in plastic and water has been established for the clinical beam at the time of calibration [IAEA-TRS-398 2001]. The composition of plastic material of solid phantoms differs from one phantom type to another. In general terms, materials with effective atomic number and electron density reasonably close to water such as polymethylmethacrylate (PMMA) and polystyrene are mainly used [Mayles 2007]. It is necessary to quantify water equivalence of each of these materials in terms of dose before any utilisation in clinics.

2.1.3 Small field dosimetry

Conventional RT (3D-CRT) traditionally uses beam apertures of dimension ranging from 4×4 cm^2 to 40×40 cm^2. However, recent developments in RT have substantially increased the use of smaller fields. For instance, radiosurgery employs field dimensions that may reach only several millimetres (*e.g.* GK [Elekta 2016]). In IMRT, non-uniform large fields are composed of several small fields called segments. Minimum segment sizes used in clinics are often limited to 2×2 cm^2 due to the difficulty to perform accurate measurements below that dimension, as it will be explained hereafter. The development of such advanced RT techniques have rose the need for accurate dosimetry methods using smaller fields.

A treatment field is generally considered as "small" when its dimensions are lower than the lateral range of the charged particles that contribute to the dose deposited in a point along the central axis of the beam [Das 2008]. In high energy photon RT, this criterion applies to field sizes below approximately 3×3 cm^2. Below that limit, the approximations of classical RT physics start to be valid to a lesser extent due to the following reasons:

- A **loss of lateral charged particles equilibrium** (CPE) is observed when the beam cross-section is smaller than the maximal range of secondary electrons depositing the dose. This means that charged particles can exit the field but are not compensated for by charged particles entering from an adjacent area, as would happen in a larger field. This phenomenon has an impact on both the absorbed dose at the centre of the beam and on the FWHM of the beam.

- When the source, having a finite dimension, becomes relatively large compared to the field size, a **partial occlusion of the source** occurs (see figure 2.8). This leads to an overlapping of the beam penumbras. As a consequence, a

large percentage of small fields are made up by penumbra, making volume averaging within the detector a problematic issue.

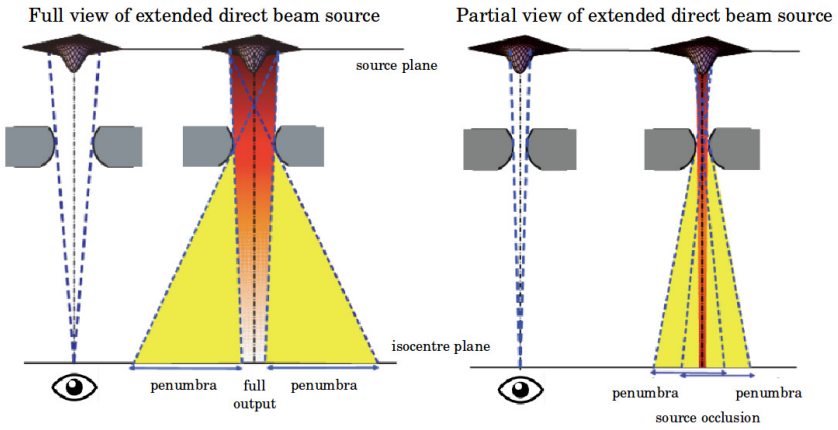

Figure 2.8: *Illustration of the detector field of view of the source. On the left, the field size is large enough to allow a full view of the beam source from the detector's point of view, while on the right the small field size leads to a partial occlusion of the source, resulting in penumbras overlap and drop in output. The eyes represent the detector's point of view. Modified from the work of Aspradakis et al. [Aspradakis 2010].*

- While inserting a measuring device into a large radiation field has a relatively small effect that can be adequately corrected for, in small fields, **the currently available detectors cause large perturbations**.

For the aforementioned reasons, measuring the dose delivered by small fields is much more challenging than in standard fields and is more error-prone. Incorrect measurement of lateral dose profiles or OF may result in incorrect data being entered into the TPS, which could result in mistreatment of patients.

An additional difficulty is that not many available detectors provide high spatial resolution with enough sensitivity, reduced energy dependence, reproducibility, *etc.* Among the suitable types of commercialised dosimeters are:

- **Micro-IC**, based on the same principle than conventional IC, have a smaller detection volume ranging from 0.007 for the Exradin A16 Micropoint to 0.015 cm^3 in the case of the PTW Pinpoint [ISFPM-Task-group 2008]. However, the reduction of the IC cavity size may lead to a decrease in the signal/noise ratio.

- **Diodes** (semi-conductor p-n junctions) provide a good alternative for relative dosimetry because of their very small collecting volume ($< 0.1\ mm^3$). However, at very small field sizes, diodes are limited by perturbation correction factors changes due to the relatively dense collecting medium (silicon) with respect to water [Scott 2012].

- **Diamond detectors** work as solid IC with electrodes placed in both sides of a diamond piece. This type of detector is nearly water-equivalent as the Z of carbon (Z=6) is close to that of water ($Z\simeq$7.4). They are known to be LET-independent, however their response may show variations as a function temperature [Vatnitsky 1993] and dose-rate [De Angelis 2002]. Until recently, only natural diamonds were employed as radiation devices. Synthetic diamonds, that can be made more reproducible than detectors based on natural diamond, with better dose-rate independency properties, start to be developed as in the work of Marsolat *et al.* [Marsolat 2013].

- **Radiographic and radiochromic films** can provide 2D dose distributions. Radiochromic films are more advantageous than the radiographic ones as they do not require chemical processing after irradiation [Niroomand-Rad 1998] and are more water equivalent [Palmer 2015]. In radiochromic films, the active part is made of a monomer crystal which is sensitive to radiations. Films irradiation leads to a polymerisation reaction which results in a colour change in the film. These types of films allow an excellent spatial resolution, however their handling is delicate and their use require post-processing (not online detector).

- **TLD** are made of thermolusminescent crystals such as LiF:Mg,Ti and LiF:Mg,Cu,P [Hranitzky 2006]. They come in different shapes like powders, cubes or cylinders. When irradiated with ionising radiations, the crystal suffer from excitation or ionisation phenomena that create charge carriers. After irradiation, one has to measure the intensity of visible light emitted from a crystal in the detector when heated. The intensity of light emitted is dependent upon the radiation exposure. Such dosimeters are advantageous for small field dosimetry thanks to their small size. However their handling is very delicate and time-consuming.

In a recent study, Bassinet *et al.* have determined small fields OF using different types of active detectors and passive dosimeters for several types of facility allowing stereotactic RT and radiosurgery [Bassinet 2013]. Figure 2.9 shows the OF measured in a Novalis© system. The measurements with the different detectors were comparable for field sizes higher than 12 mm, while their behaviour differs significantly for field sizes lower than 10 mm [Bassinet 2013]. This work thus highlights a need for metrology standards in small fields. In particular, introduction of correction factors for active dosimeters is required.

An international working group on reference dosimetry of small and non-standard fields has been established by the IAEA in cooperation with the AAPM Therapy Physics Committee in order to develop standardised recommendations for dosimetry procedures and detectors. They have proposed a new formalism for the dosimetry of small and composite fields that extends recommendations given in conventional codes of practice for clinical reference dosimetry [Alfonso 2008]. In particular, they recommend the use of a small intermediate calibration field (f_{clin}) closer to the

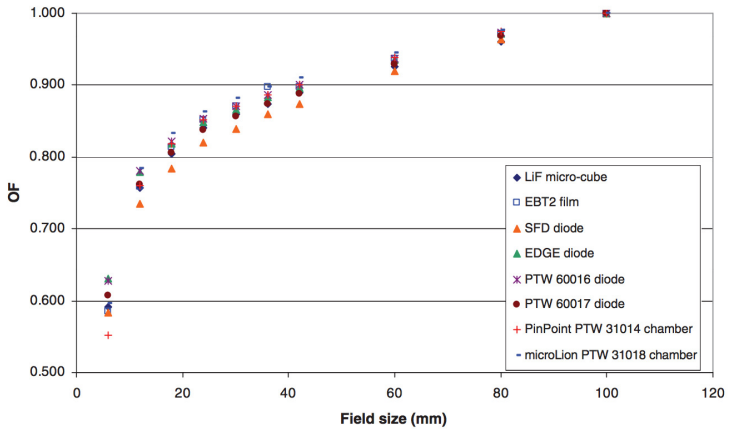

Figure 2.9: *OF measured with different active and passive dosimeters for a Novalis© system equipped with microMLC. Taken from the work of Bassinet et al. [Bassinet 2013].*

patient-specific clinical fields. In the paper, a distinction is made between static and composite fields that will not be explained here. They introduced a new correction factor ($k^{f_{\text{clin}},f_{\text{ref}}}_{Q_{\text{clin}},Q_{\text{ref}}}$) which accounts for differences between the conditions of field size, geometry, phantom material, and beam quality of the conventional reference field f_{ref} and the new intermediate clinical reference field f_{clin}. Adapted from the TRS 398 (see equation 2.17), the absorbed dose to water $D^{f_{\text{clin}}}_{w,Q_{\text{clin}}}$ at the reference depth in water, in a beam of quality Q_{msr} and reference field f_{msr} and in the absence of the chamber is given by:

$$D^{f_{\text{clin}}}_{w,Q_{\text{clin}}} = M^{f_{\text{clin}}}_{Q_{\text{clin}}} N_{w,Q_0} k_{Q,Q_0} k^{f_{\text{clin}},f_{\text{ref}}}_{Q_{\text{clin}},Q_{\text{ref}}} \tag{2.18}$$

where Q_{ref} is the beam quality of the conventional reference field f_{ref}, and Q_{clin} the beam quality of the intermediate reference field f_{clin}. Despite the fact that this work presents a harmonised formalism for small field dosimetry, no international code of practice or recommendations exist at present for its practical implementation, and a substantial research effort is still required [Alfonso 2008].

Although significant research and developments are being performed in terms of detection devices and dose determination formalisms, further improvements are still needed in the domain of small field dosimetry. Further difficulties exist in emerging spatially fractionated techniques like pMBRT, where smaller field sizes (one order of magnitude smaller than those used in radiosurgery) are employed. The following section will be devoted to the presentation of the challenging experimental techniques implemented for pMBRT evaluation.

2.1.4 Experimental dosimetry in pMBRT

pMBRT uses even smaller beams ($<$ 5 mm). Dosimetry in such fields requires an extremely high spatial resolution (in the order of micrometres). In addition, possible

variations in LET with such small beam sizes need to be taken into account. Very few commercially available detectors meet such exigent requirements and new dosimetric strategies have to be explored.

In previous experimental works in x-rays MRT and MBRT, several detectors were investigated. Brauer-Krisch *et al.* provided a review of the systems tested in x-rays MRT [Bräuer-Krisch 2010]. The detectors investigated include IC, alanine dosimeters, MOSFET detectors, Gafchromic© films, radiochromic polymers, TLDs, polymer gels, fluorescent nuclear track detectors, optically stimulated luminescence (OSL) detectors and silicon strip detectors. Some of them do not provide good enough resolution like alanine or IC, and many have a strong energy dependence like MOSFET or silicon detectors. In MBRT, the experimental dose assessment in white beam [Dilmanian 2008] and monochromatic MBRT [Deman 2011] was tried using 3D polymer gel dosimetry. This technique does not allow to perform accurate dose measurements, although it could be useful to check the irradiation geometry for example to confirm that an interlaced geometry could be maintained in a human head with the presence of bone [Dilmanian 2008]. Gafchromic© films were shown to allow performing satisfactory absolute and relative dose measurements, providing the best reproducibility and accuracy [Prezado 2011, Prezado 2012a]. Prezado *et al.* developed the first dosimetric protocol to guide the preclinical MBRT trials at ESRF [Prezado 2011]. It was a "two steps" protocol based on Gafchromic© films dosimetry. It consists in: (i) the determination of absorbed dose under reference conditions following the recommendations of the TRS 398, and then (ii) the determination of absorbed dose in non-reference conditions (MBRT) through the assessment of the scatter factors. Gafchromic© films were also used both to measure scatter factors in MBRT [Prezado 2012a] and to perform relative dosimetry: evaluation of dose distributions in the phantom [Prezado 2011].

More recently, Livingstone *et al.* performed the characterisation of a single crystal diamond detector (SCDD) PTW microDiamond© (60019) in x-rays MRT and MBRT [Livingstone 2016]. In particular, they showed a good agreement in PVDR assessment between SCDD and Gafchromic© EBT3 films. This might be a good alternative for an online dosimetry.

In this work, dosimetry in pMBRT was inspired by the "two-steps" protocol [Prezado 2011]. Details of both reference and non-reference conditions parts will be presented in the following sections. Then, the materials and setups used for relative dosimetry will be described. In particular, two types of dosimeters were compared: Gafchromic© EBT3 films and a PTW microDiamond© detector.

2.1.4.1 Absolute dosimetry for pMBRT

Determination of absorbed dose under reference conditions

The absolute dosimetry was performed by following as closely as possible the recommendations for proton therapy applications compiled in the IAEA TRS 398 [IAEA-TRS-398 2001]. In the case of the 100 MeV mono-energetic proton beams used in this work, the TRS 398 recommends a reference depth z_{ref}=3 g/cm^2, in

the "plateau" region as the reference condition. In our case, the reference point of the chamber (on the central axis at the centre of the cavity volume) was placed at a reference depth of 22.6 mm water-equivalent thickness (WET) (corresponding to the minimal depth reachable in the water tank, due to the presence of the entrance window of the water tank) in order to be closer from the depth corresponding to the middle of a rat brain. A cylindrical IC CC13 from IBA was carefully positioned in a water tank (BluePhantom^2 IBA) [IBA 2016]. The distance between the collimator exit and the phantom was chosen to be 7 cm, being a clinically relevant distance. A reference field size (broad-beam conditions) of 5×5 cm^2 instead of 10×10 cm^2 was selected since it is closer to the field sizes employed in MBRT, as recommended by Alfonso *et al.* [Alfonso 2008]. The absorbed dose to water under reference conditions was then obtained following the IAEA formalism as described in section 2.1.2.1 [IAEA-TRS-398 2001].

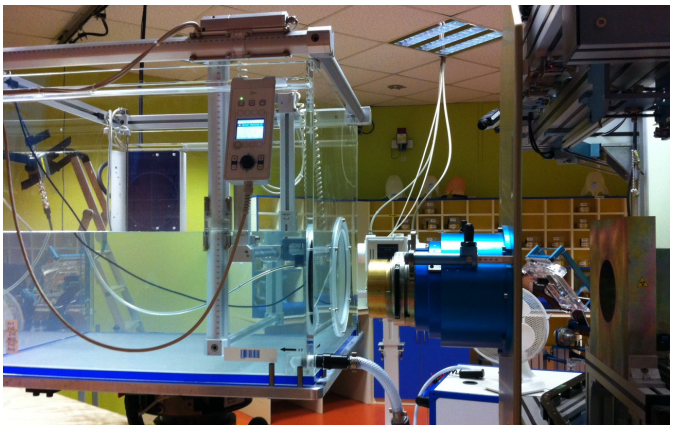

Figure 2.10: *Experimental setup for absolute dose determination in reference conditions (broad beam). The water tank is located after the nozzle with a 5×5 cm^2 collimator.*

Determination of absorbed dose under non-reference conditions (MBRT)

To translate the absolute dose measured in the broad beam configuration (reference conditions) to the dose deposited with one or several minibeams, the scatter factors (or OF) were used, as it was done in x-rays MBRT [Prezado 2011]. In this work, the OF were assessed by means of Gafchromic© films (EBT3) irradiated at several depths either in a IBA SP34 (RW3) solid phantom [IBA 2016] and in water in two configurations: (i) broad beam (5×5 cm^2 reference field size), and (ii) pMBRT arrays.

OF were then determined as the ratio of the dose being deposited in the central point of the irradiated field by the minibeam and the reference field, at several depths. They were assessed for both single and several multislits collimators. Hence, the peak dose at a given depth z in water can be assessed as:

$$D_{\text{peak}}(z) = D_{\text{ref}}(z) \times \text{OF}(z) \tag{2.19}$$

The use of solid water phantoms (RW3) allowed acquiring dose information in the first centimetres, as it was not possible in water due to the presence of the water tank entrance wall. Composition of the SP34 slabs used in this work are reported in table 2.3. Absolute dose in the films was related to absorbed dose to water by means of a film calibration. Further details will be given in section 2.1.4.2.

IBA SP34 slabs properties	
Composition	Density
RW3 (98% polystyrene + 2% TiO_2)	1.045 (g/cm^3)

Table 2.3: *Composition and density of SP34 IBA solid plate phantom [IBA 2016].*

2.1.4.2 Relative dosimetry

Relative dosimetry was performed to evaluate the dose distributions in pMBRT. Considering the demanding requirements for spatially fractionated RT dosimetry, two alternative detectors were selected for this relative dosimetric study:

- Gafchromic© films EBT3 [Gafchromic© 2016]
- PTW microDiamond© 60019 detector [PTW 2016]

Lateral dose profiles were measured with both detectors, and PVDR values comparisons were carried out. Additional relevant parameters such as minibeams width and penumbra (80%–20%-width) were also evaluated. In contrast, depth dose profiles were acquired using EBT3 films only. The geometry of the PTW diamond detector did not allow to acquire PDD curves without inducing an averaging effect in the measurements (see figure 2.17 hereafter).

Gafchromic© EBT3 films

In this work, Gafchromic© films were used since they provide the high spatial resolution needed to perform accurate measurements in the sub-millimetric field sizes used [Prezado 2011, Martínez-Rovira 2012, Martínez-Rovira 2014], associated to a wide dose range sensitivity from 0.1 to 40 Gy [Gafchromic© 2016]. The EBT3 films come in sheets composed by an active layer of 0.028 mm positioned in the middle of two matte polyester substrate layers of 0.12 mm. They provide a uniformity better than ± 3% in dose, and their symmetrical geometry allows to irradiate and scan them on the two sides. Another advantage is that EBT3 films are water resistant, thus permitting their use in water phantoms.

Radiochromic films, as passive dosimeters, do not provide direct readouts, and time-consuming post-irradiation operations are needed to obtain the dose. In general, films handling was carried out taking into account the recommendations provided by Task Group 55 of the AAPM [Niroomand-Rad 1998]. In this study, a flat bed red-green-blue (RGB) scanner (Epson Perfection V750-M Pro Scanner) served

for films readout, at 1200 dpi resolution, following the methodology described in the work of Devic *et al.* [Devic 2005]. Until recently, radiochromic film dosimetry has relied on the use of information from a single colour channel of a RGB scanner (the red channel, which is more sensitive). However, new methods to evaluate radiochromic film dosimetry data scanned in multiple colour channels are emerging today. The rationale for these methods is that they allow for the separation and removal of the non dose-dependent portions of a film image leaving a residual image that is dependent only on absorbed dose [Micke 2011]. In particular, Micke *et al.* proposed a triple channel protocol. In this study, both triple channel and single red channel methods were tested. Similar results were obtained, with less noisy results using the red channel method. This last technique was thus selected for this study. The transmission scanner readings of the films (I) were obtained by extracting the red channel from the triple image. The optical density (OD) at each pixel was then calculated thanks to the following expression:

$$\mathrm{OD} = -\log_{10}\left(\frac{I}{I_0}\right) \tag{2.20}$$

where I and I_0 are the readings for exposed and unexposed film pieces, respectively. The absorbed dose (D) at any point in the film was computed by using a calibration curve (evolution of D as a function of OD) determined prior to experiments in reference conditions (z_{ref} = 22.6 mm, 5×5 cm^2 field size). Several dose points (from 0 to 20 Gy) were considered to construct the calibration curve (see figure 2.11). Expression 2.20 and calibration curves were implemented in a home-made C++ program in order to convert the scanner readings into doses.

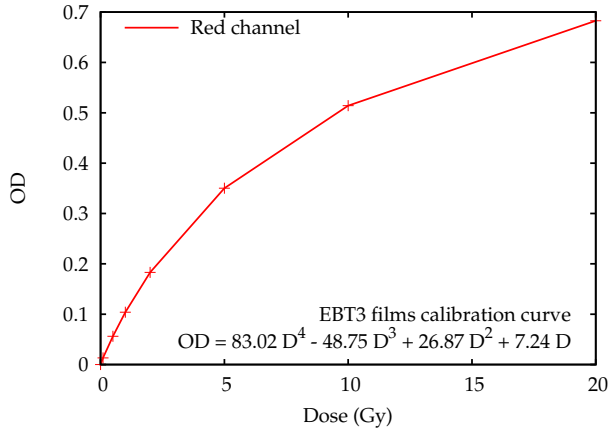

Figure 2.11: *Red channel dose calibration curve for EBT3 films.*

For dose distribution assessments, irradiations of the films were performed in three configurations, as depicted in figure 2.12:

- **Configuration (i)**: The films were irradiated along the beam direction in a 40×40 cm^2 water tank (IBA BluePhantom^2) using a home-made dedicated support (see figure 2.13).

- **Configuration (ii)**: The films were placed along the beam direction in a 10 cm-thick solid water phantom.
- **Configuration (iii)**: The films were irradiated perpendicular to the beam direction interspersed among 1 cm (entrance) and 0.5 cm-thick (Bragg peak region) solid water slabs.

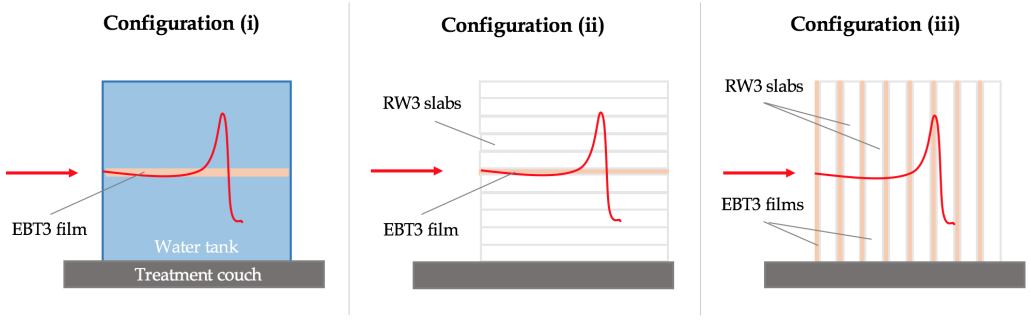

Figure 2.12: *Experimental setups for Gafchromic© films irradiations for relative dosimetry. The red arrows show the direction of the proton minibeams.*

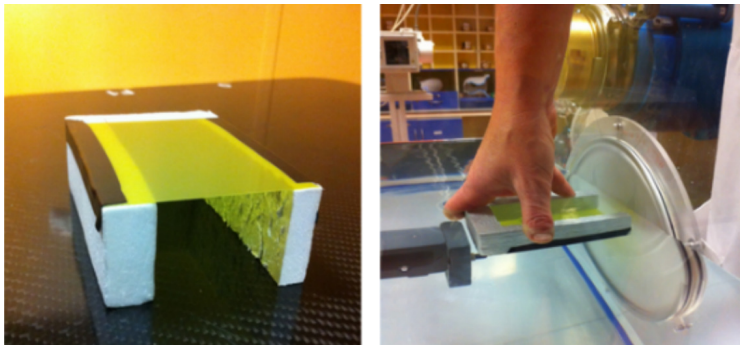

Figure 2.13: *Home-made support dedicated to irradiation of EBT3 films in the longitudinal direction in water, i.e. configuration (ii) (left). The support was maintained in a fixed position using the remote-controlled part of the water tank (right).*

The first and second configurations were used to measure the depth dose curves, while the third one served to measure transversal dose profiles. The distance between the phantom and the pMBRT collimators exit was 7 cm. Figure 2.14 shows films irradiated in the transversal direction (left) and in the longitudinal direction (right).

Configuration (ii) was chosen as a complement of configuration (i) in order to obtain information about the dose deposition in the first centimetres, impossible in water due to the presence of the water tank's entrance window. In order to cope the potential artifacts in the dose distributions created by residual air gaps between the film and the slabs phantom, as reported in the work of Zhao *et al.* [Zhao 2010],

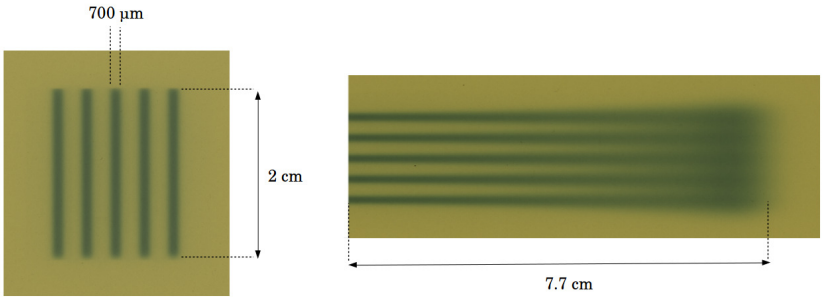

Figure 2.14: *Pieces of Gafchromic© films irradiated in the transversal (left) and longitudinal directions (right) with a multislits collimator (not to scale).*

the common practice of tilting the film plane a few degrees away from the beam central axis was followed [Vatnitsky 1997]. In our measurement, a tilt of 4° was thus applied to the phantom position for configuration (ii) measurements. The depths of the films in the solid phantoms (z_w) were corrected by a depth scaling factor (C_m), being the ratio between the phantom material and the water mass stopping powers, [IAEA-TRS-398 2001], as shown in equation 2.21:

$$z_w = z_m \times C_m \times \frac{\rho_m}{\rho_w} \tag{2.21}$$

with z_m being the physical thickness of the solid phantom, and ρ_w and ρ_m the water and solid phantom densities, respectively. Table 2.4 shows values of densities and mass stopping powers S used for water-equivalent depths calculations. The mass stopping power of EBT3 was calculated following NIST recommendations [NIST-PSTAR 2016].

Materials properties			
Material	$\rho(g/cm^3)$	$S(MeV.cm^2/g)$	C
Polystyrene	1.045	7.140	0.980
EBT3	1.2	7.000	0.961
Liquid water	1.0	7.287	1

Table 2.4: *Densities, mass stopping powers (S) and depth scaling factors for 100 MeV protons for water-equivalent depth calculation.*

The decrease of radiochromic films sensitivity with high LET leads to the so-called "quenching effect" [Kirby 2009, Martišíková 2010]. This phenomenon increases with depth, as the mean LET of charged particle beams depends on the penetration depth. In proton beams, decrease in the darkening efficiency up to 20% with respect to photons was previously observed in other works in the Bragg peak [Zhao 2010]. The quenching correction factors (QCF) to be applied were calculated as the ratio of the dose deposited by a 5×5 cm^2 fied size in water at a given depth

measured with a parallel plane IC (D_{IC}(z)), and with Gafchromic© films (D_{film}(z)), as expressed in:

$$\mathrm{QCF}(z) = \frac{D_{\mathrm{IC}}(z)}{D_{\mathrm{film}}(z)} \tag{2.22}$$

Figure 2.15 shows the two PDD curves obtained with both IC and films, and the calculated QCF to be applied. An under-response in the Bragg peak region of around 30% was found. QCF for depths shallower than 2 cm were extrapolated to 1, since direct measurements were not possible due to the thickness of the water tank wall (1.7 cm water equivalent). The calculated QCF were applied in both peak and valley regions. Indeed, Morgane Dos Santos, a post-doctoral researcher in the NARA team, determined in a MC study (using Geant4-DNA) that no differences in LET were found between the two regions with pMBRT irradiations. These results were confirmed later by confronting experimental measurements of films with those of the microDiamond© detector (see *Chapter 3*). All relative measurements presented in this manuscript are corrected for the aforementioned factors.

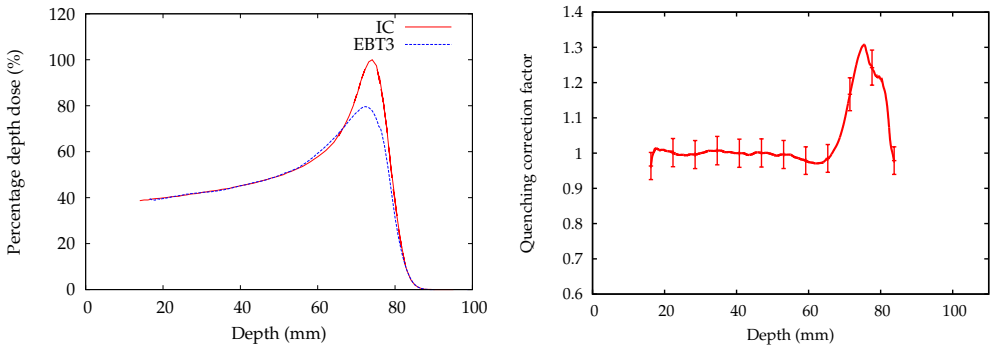

Figure 2.15: *Left: Depth dose curves measured with the IC and Gafchromic© films in the water tank. An under-estimation of the dose is observed in the film at the Bragg peak. Right: Quenching correction factors to be applied to the films measurements. Values of QCF for depths inferior to 2 cm were extrapolated to 1, as direct measurements were not possible due to the thickness of the water tank wall.*

Uncertainties in films dose measurements were evaluated following the method described in the work of Sorriaux *et al.* [Sorriaux 2013]. The main contributions to the overall uncertainty come from the absolute dose determination with the IC (2%), the measurement of the films OD (0.5%), films calibration (1.5%) and mean standard deviation in the average dose in the peak and valley regions (2%). The overall uncertainty amounted to 3.2%. To incorporate other possible sources of uncertainty (*e.g.* misplacing or misalignment of the films in the phantom, inaccuracies in the phantom positioning), a conservative value of 4% was considered.

PTW microDiamond© 60019 detector

The PTW microDiamond© 60019 detector consists of a single crystal (synthetic) diamond embedded in a PMMA waterproof cylindrical housing. The sensitive volume (diamond) is a cylinder of 0.004 mm^3 with 1.1 mm radius and thickness 1 μm^2 [PTW 2016]. The diamond surface is located 1.5 mm below the top surface of the housing [Ciancaglioni 2012]. Several works have demonstrated the suitability of the microDiamond© detector for relative dosimetry in clinical proton beams [Mandapaka 2013, Marinelli 2014]. In addition, it is nearly water equivalent for all beam energies and it has been proven to be LET independent [Mandapaka 2013, Rossomme 2016]. This last specification is of particular interest in proton therapy beams where LET are expected to vary with depth. This could also cope for potential LET variations that might occur between peaks and valleys in pMBRT. This point, along with the high spatial resolution when the detector is oriented perpendicular to the beam (1 μm) make the microDiamond© adequate for measurements in very small proton beams like those used in pMBRT, as depicted in figure 2.16.

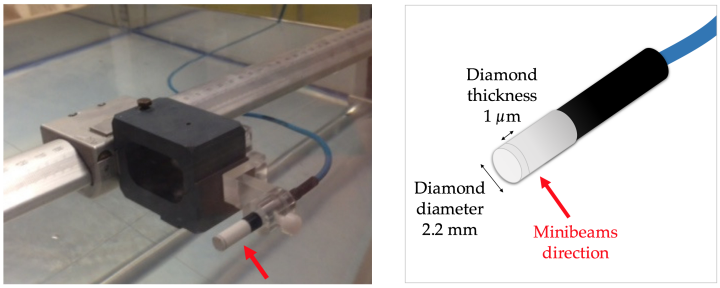

Figure 2.16: *The microDiamond© detector was positioned inside the BluePhantom² scanning system (left). In order to take advantage from the 1 μm dimension of the active volume, the detector was oriented perpendicular to the beam direction (right).*

When the detector was positioned as in figure 2.16, the signal was integrated over 2.2 mm in depth. This configuration allowed the precise characterisation of lateral dose profiles (resolution of 1 μm in the lateral direction), but not of PDD curves as in the Bragg peak area (steep dose gradient) an averaging effect would have appeared. If the detector had been positioned in the other direction (see figure 2.17), the averaging effect would have occurred in the fractionation direction. This is the reason why only lateral profiles were assessed with this detector.

Contrary to film dosimetry, diamond detectors are active dosimeters, providing a direct display of the collected charge (therefore of the dose) thanks to a dedicated electrometer. Before lateral profile characterisations, the reproducibility of the detector response was verified. The microDiamond© was plugged into the IBA electrometer (CCU) and positioned inside the BluePhantom² scanning system to perform lateral profiles measurements (see figure 2.16 left). The scanning step of IBA system was set to its minimum value, *i.e.* 100 μm.

Uncertainties in relative dose measurement with SCDD mainly come from the

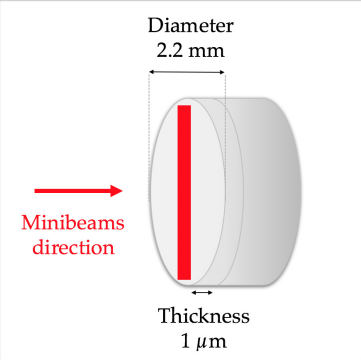

Figure 2.17: *If the diamond detector had been positioned in parallel direction for PDD acquisition, an averaging effect would have occurred in the fractionation direction.*

electrometer reproducibility (1%), the scanning system accuracy (±0.1 mm) and the mean standard deviation in the average dose in the peak and valley regions (2%). To be conservative, an overall uncertainty of 3% was considered.

2.2 Monte Carlo simulations for spatially fractionated charged particle therapy

Combining a spatial fractionation of the dose with the use of sub-millimetric charged particle beams is a novel strategy to further improve the therapeutic index of RT. In such innovative techniques, radiobiological magnitudes like RBE are expected to greatly differ from those of standard broad beam irradiations. In this context, the first needed step was to establish the physical basis of the technique, by evaluating the dose distributions and secondary production, in order to correlate with biological observations in a second time. Within this framework, an important part of this *Ph.D.* work was devoted to MC dosimetric studies of both proton and very heavy ion minibeams.

In this section, the MC method and the code used in this work, namely GATE/Geant4, will be presented. Then, the simulations details will be described.

2.2.1 The Monte Carlo method

MC methods are a class of numerical methods based on the use of random numbers [Metropolis 1949]. Nowadays, MC methods are widely used to solve complex physical and mathematical problems, particularly those involving multiple independent variables. In that case, the considered problem has to be reformulated in terms of probability and random variables describing stochastic processes. MC methods apply in numerous fields like, for instance, finance, environmental sciences or physics.

The first MC methods emerged in the 1940's. Their rise was related to the research within the framework of the "Manhattan project", concerning the development of thermonuclear weapons. Originally, the methods consisted in computerised

simulations of neutron diffusion (stochastic process) in fissionable materials, and are thus closely linked to computer developments. While the first applications of MC methods were mostly military, their use has significantly spread towards medical and radioprotection fields over the last past decades for the simulation of particles transportation through the matter.

Applied to particle transport, the MC principle is the following: when a primary particle undergoes several interactions with the traversed medium and, as a consequence, loses part of its energy, this energy is deposited at the location of the interaction, and in some cases this can lead to the creation of secondary particles. Using MC methods, the primary particle will be followed until it has deposited the totality of its energy, resulting in either its disappearance or rest. Then, the tracking of the secondary particles created will start, proceding in a same manner. Each set of primary plus secondary particles constitutes a stochastic *history*. The history of one single primary particle is thus a succession of random draws that will determine its energy, trajectory or interaction mode with the traversed medium.

The MC methods yield to same information as the result of the Boltzmann equation, with the same interaction model, but are much easier to implement. In MC methods, the practical implementations of the particle transport equation can be classified as (i) *detailed* (microscopic) simulations, (ii) *condensed* simulations (iii) and *mixed* simulation algorithms. Detailed simulations will provide the exact solution of the transport equation, but are time consuming if the energy is higher than 100 keV [Salvat 2011]. This is the reason why they are used for low energy particles only. Condensed algorithms simulate the global effects of the collisions during a step, by having recourse of multiple-scattering theories. In mixed algorithms, hard collisions, with energy loss larger than a specified cut-off value, are simulated one by one, while only global effects are simulated for the soft collisions (with scattering angle or energy loss less than the corresponding cut-offs).

2.2.2 MC simulations in medical physics

MC calculations in medical physics started in the 1970's. One of the first applications was linked to radiation dosimetry, with the calculation of water to air stopping-power ratios (essential for the conversion of IC readings into dose absorbed to water) for use in electron beam dosimetry [Berger 1975, Nahum 1978]. MC techniques have also played an important role in other aspects of radiation dosimetry with IC. For instance, simulations of the response of an IC in a ^{60}Co beam have been performed by Nath and Schulz [Nath 1981] in order to calculate the correction factor which accounts for attenuation and scatter in an IC's walls (K_{wall}).

MC simulations have then gathered more importance in medical physics since the 1980's, with growing applications in nuclear medicine imaging [Zaidi 1999], modelling of external radiotherapy using photon [Verhaegen 2003] and electron beams [Ma 1999]. Interests in applications of MC techniques to clinical treatment planning have also grown, although the use of MC in clinics is still not widespread nowadays, mainly related to the high demand in terms of calculation resources and

time. The AAPM released a Task Group report concerning issues associated with clinical implementation of MC-based TPS [Chetty 2007].

With the increase of MC use, several MC codes allowing medical applications have been consequently developed. Among the most frequently used codes are EGSnrc [Kawrakow 2000], Geant4 [Agostinelli 2003], MCNPX [McKinney 2012], PENELOPE [Salvat 2011] and FLUKA [Böhlen 2014]. Three simulation platforms based on Geant4 and devoted to medical physics applications, GATE [Strulab 2003], GAMOS [Arce 2008] and TOPAS [Perl 2012], have also been developed. They are largely used in the medical physics community at present. Further details about the GATE simulation platform and the Geant4 code will be given in the next section.

2.2.3 The Geant4/GATE simulation toolkit

2.2.3.1 An overview

In this work, GATE (Geant4 Application for Emission Tomography) was employed. It is an open source MC simulation platform developed by the international OpenGATE collaboration and devoted to numerical simulations in medical physics [Open-Gate 2016]. GATE is based on the Geant4 code and encapsulates its libraries. Geant4 (GEometry ANd Tracking 4) is a C++-based MC application toolkit developed at CERN [Agostinelli 2003]. It was devoted to high energy applications up to 10 TeV but now allows simulations for low energies applications (down to a few eV) and all kind of particles. A large number of processes, models, cross-sections and simulation parameters are available. The simulation of particle transport is performed using condensed algorithms (see section 2.2.1) in Geant4 [Agostinelli 2003]. Various validation studies were carried out for medical applications, especially concerning conventional (photon) RT [Carrier 2004, Faddegon 2008] and charged particle therapy [Cirrone 2005, Jarlskog 2008, Böhlen 2010].

GATE was first developed for nuclear medicine applications, such as the modelling of planar scintigraphy, single photon emission computed tomography (SPECT) and PET acquisitions [Strulab 2003]. Then, its application scope has been extended to x-rays CT and RT studies [Jan 2011], and, more recently, further developments have been carried out for proton and carbon therapy simulations [Grevillot 2010, Grevillot 2011, Grevillot 2015]. GATE uses predefined classes allowing configuring simple or highly sophisticated experimental settings. The input files describe the physics specifications (in the so-called physics lists), geometries, source of primary particles and management of outputs in various formats. For dosimetry and RT applications, GATE allows the user to record dose distributions in a voxelised frame.

In this work, the study for very heavy ions was performed first, in 2014. At that time, the last GATE version was the 6.2 one but we encountered some problems using this version: the emission of fluorescence and Auger electrons seemed to not be correctly considered. It was then confirmed by some members of the GATE collaboration and we continued working with the previous 6.1 version. Later, from 2015, the 7.0 version of GATE was employed for simulations with proton beams.

2.2.3.2 The physics

In Geant4/GATE, physics interactions between a particle and a material occur through *processes*. Each *process* may be implemented directly, *via* the use of *cross-sections*, or in terms of a model class linked to the *process*. Geant4 provides several *models* for a given process. Each model has an associated energy range, and for each process, the whole energy range has to be covered by models.

There are seven main categories of physics processes in Geant4 [Geant4-Collaboration 2012], two of which apply for the simulations developed along this work: electromagnetic (EM) and hadronic physics models. The EM category includes standard and low energy EM processes. In this work, the electromagnetic processes have been simulated by using the standard model, which has been widely validated and covers the range energy of interest for charged particle therapy applications. The hadronic category deals with neutron interactions, nucleus-nucleus scattering, photo-nuclear and electro-nuclear interactions and other high-energy processes (up to GeV). The hadronic models available in Geant4 are depicted in figure 2.18.

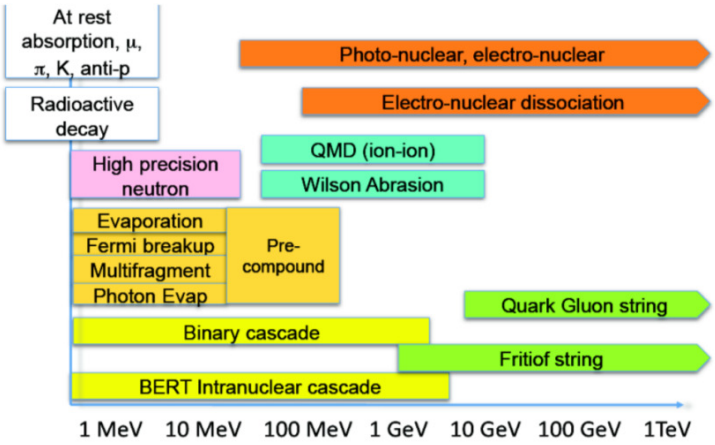

Figure 2.18: *Available hadronic models in Geant4. Taken from the Geant4 tutorial presentations [Geant4-Tutorial 2014].*

As mentioned in *Chapter 1*, as charged particles penetrate tissue, they undergo inelastic nuclear reactions and lead to significant yields of secondary products. With heavy ions, nuclear fragments of different LET may be produced, strongly impacting the resulting biological dose distribution. An accurate prediction of the secondary products fluence is thus necessary to precisely simulate the spatial dose distributions. Within this context, a particular care has to be given to the selection of hadronic models in Geant4 for charged particle therapy applications. Two nuclear models are currently recommended by the Geant4 developers to perform simulations in charged particle therapy [Geant4-Physics-Manual 2007]: G4BinaryLightIonReaction (proton therapy applications) and G4QMDReaction (carbon therapy applications). The

first one is a binary intra-nuclear cascade (BIC) and derives from the Binary Cascade model for light ion reactions [Folger 2004]. This is a hybrid model between a classical cascade code and a quantum molecular dynamics (QMD) description because the participating particles (*i.e.* either primary particles or particles generated or scattered during the cascade process) are described by means of Gaussian wave functions [Geant4-Physics-Manual 2007]. Each nucleus is modelled as a set of discrete nucleons, positioned at sample locations. Only binary interactions are modelled, between a primary or secondary particle and an individual nucleon of the target nucleus. In this model, scattering between participants is not taken into account. The second model that may be employed for charged particle therapy applications is a QMD-like model [Koi 2010]. As for the BIC model, the basic assumption of a QMD model is that each nucleon is described by a gaussian wave function which is propagated inside the nuclear medium. In contrast to the BIC model, all nucleons of the target and of the projectile are taken into account with the QMD. Each nucleon is thus considered as a participant. The QMD model thus simulates nucleus-nucleus scattering for targets and projectiles of all A, therefore being more suitable for heavy ion interactions simulations.

Recent studies attempted to benchmark the nuclear models implemented in Geant4 for proton therapy [Chen 2009, Pinto 2016] and carbon therapy applications [Böhlen 2010, Braunn 2013, Dudouet 2014] by assessing their ability to reproduce experimental data. Although very few works investigated the validity of these models for simulations of heavier ions, one can cite the work of Jalota *et al.* that investigated Geant4 models for simulations of ^{56}Fe ion beams in various media [Jalota 2012]. Globally, all these studies demonstrated significant discrepancies between experimental nuclear interactions cross-sections and Geant4 models. However, the further improvement of these models is limited by the lack of experimental data, especially fragmentation data with substantial uncertainties in the case of heavy ions.

In this work, the recommended BIC model, which has been validated for proton applications, has been chosen for proton interactions, while the QMD model has been selected for heavier ions. Although the QMD model can lead to inaccuracies, the simulations performed within this study were proofs of concept and did not imply direct clinical applications. The exact values of PVDR might differ, but not the general conclusions of this work. The possible discrepancies due to models inaccuracies were thus not critical in our case. Additional information about the physics lists used in this work will be addressed in sections 2.2.4.2 and 2.2.4.3.

2.2.4 Simulations geometry and details for this work

In this work, MC simulations were performed considering a magnetic collimation of the minibeams. The water phantom and the collimation method employed are similar for both pMBRT and very heavy ion simulations. They will be described first, then simulation details will be given for the two techniques separately. Finally, the method used to evaluate uncertainties on the calculated dose will be presented.

2.2.4.1 Simulation geometry

As previously stated, the main targets of spatially fractionated RT using proton and very heavy ions are neurological cases, which can be stabilised against cardiac and breath cycles. In this study, a cylindrical phantom with dimensions mimicking a human head (16 cm high and 16 cm diameter) was thus considered. This type of phantom was used in previous dosimetric works [Siegbahn 2006, Spiga 2007, Prezado 2013]. The beam direction corresponded to the longitudinal axis of the cylinder. The spatial fractionation was considered in the transversal direction. The dose map was collected in a parallelepiped scoring region with dimensions 4 cm × 5 mm × 16 cm located at the centre of the water phantom, using the so-called "DoseActor" of GATE. A schematic view of the geometry is shown in figure 2.19. The scoring region was split in voxels of different dimensions depending on the primary ion considered, as it will be detailed in the next sections.

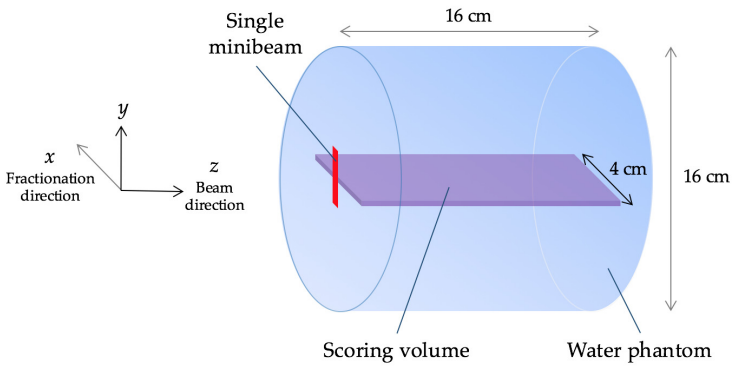

Figure 2.19: *Illustration of the simulated geometry. The parallelepiped scoring region is placed inside the cylindrical water phantom whose dimensions mimic a human head.*

To simulate a magnetic collimation of the beam, quadrupole magnets have been assumed to provide minibeams with the desired dimensions (for example 700 μm × 2 cm) impinging in the cylindrical water phantom aforedescribed. Rectangular minibeams were thus created using the General Particle Source (GPS) of Geant4. The *beam2d* angular distribution was selected. Realistic beam divergences were considered and a Gaussian shape was assumed for the beam angular spread (from 1 to 7 mrad, depending on the simulation). As in previous works [Prezado 2013, Fois 2013], only one single minibeam was simulated to save calculation time. For each spatial location, the total dose was evaluated as the sum of the contributions of each individual minibeam to cover the desired area (for instance 2×2 cm^2).

2.2.4.2 MC simulations in pMBRT

Following the recent recommendations on the OpenGate collaboration, the physics-builder mechanism, using predefined Geant4 physics-lists, was employed for the

physics lists creation [Open-Gate 2016]. The recommended physics list for medical applications QGSP_BIC_HP_EMY was selected [Cirrone 2011]. The electromagnetic option (EMY) corresponds to the standard model with option 3, suitable for low-energy electromagnetic processes.

Only pristine Bragg peaks were considered for pMBRT simulations as explained in section 2.1.1. The scoring region described in section 2.2.4.1 was split in voxels of 50 μm $\times$ 5 mm $\times$ 500 μm. The range production cuts were set to 50 μm for all secondary particle types. The number of simulated primary showers was $3{\times}10^8$, leading to an average uncertainty of 0.3%.

The aim of this work was to evaluate the potential of a magnetic collimation method for pMBRT as a first step to assess the use of a modified PBS system. First, a comparison of magnetic and mechanical collimations was performed, based on the experimental data described in section 2.1.4. The composition of peaks and valleys in terms of primary and secondary particles was also assessed. Then, the impact of several irradiation parameters on the dose distributions was assessed. In particular, the following parameters were investigated:

- Width of minibeams
- Air gap (AG) between the minibeams collimation exit and the phantom surface
- Beam angular divergence (σ)
- Beam energy (E) and energy spread (ΔE)
- Irradiation field size (covered area)

Those parameters were varied departing from standard conditions defined as 100 MeV protons (ΔE = 2.5 MeV) with an angular divergence of 3 mrad. The minibeams were assumed to be collimated at the phantom surface (AG = 0 cm). As figures of merit, depth dose curves, lateral dose profiles and PVDR values were assessed. In addition, the contribution to the dose of secondary products were evaluated in both peaks and valleys.

2.2.4.3 MC simulations for very heavy ion MBRT

As no recommendations exist for very heavy ion beam applications, the physics lists recommended for carbon beam therapy within the 6.1 GATE version were employed in this work for both electromagnetic and hadronic models. Hadronic processes and models employed are reported in table 2.5. The $\mathrm{d}E/\mathrm{d}x$ (restricted stopping power) and lambda (mean free path) tables were pre-calculated using 220 bins between 100 eV and 100 TeV. The limits on the step size ("step function") were chosen to be 0.05 mm for protons and 0.02 mm for other ions, as recommended.

Four heavy ions have been selected in the scope of this work: ^{20}Ne, ^{28}Si and ^{40}Ar, that have been investigated in the past in the BEVALAC facility and then abandoned due to large side effects, and ^{56}Fe, which has never been explored in a

Hadronic processes					
Hadronic processes	Particles	Geant4 processes	Geant4 models	Geant4 data sets	Energy range
Elastic scattering	GenericIon	G4HadronElasticProcess	G4LElastic	G4HadronElasticDataSet	-
	All other particles	G4UHadronElasticProcess	G4HadronElastic	G4HadronElasticDataSet	-
Inelastic process	Protons	G4ProtonInelasticProcess	G4BinaryCascade	G4ProtonInelasticCrossSection	0-20 GeV
	GenericIon	G4IonInelasticProcess	G4QMDReaction	G4IonShenCrossSection	0-20 GeV
	Deuteron	G4DeuteronInelasticProcess	G4QMDReaction	G4IonShenCrossSection	0-20 GeV
	Triton	G4TritonInelasticProcess	G4QMDReaction	G4IonShenCrossSection	0-20 GeV
	Alpha	G4AlphaInelasticProcess	G4QMDReaction	G4IonShenCrossSection	0-20 GeV
Inelastic scattering	Neutron	G4NeutronInelasticProcess	G4NeutronHPInelastic	G4NeutronHPInelasticData	0-20 MeV
			G4BinaryCascade	G4NeutronInelasticCrossSection	14 MeV -20 GeV

Table 2.5: *Geant4 hadronic processes and associated models used in this study.*

clinical way. As explained in section 2.2.4.1, a magnetic collimation was assumed. Rectangular minibeams (700 μm $\times$ 2 cm) of the four heavy ions were simulated. The minibeams impinged the cylindrical water phantom described in section 2.2.4.1, in which a virtual centrally-located tumour was assumed. The irradiations were performed with a 2 cm-long SOBP centered at 7 cm-depth, as illustrated in figure 2.20.

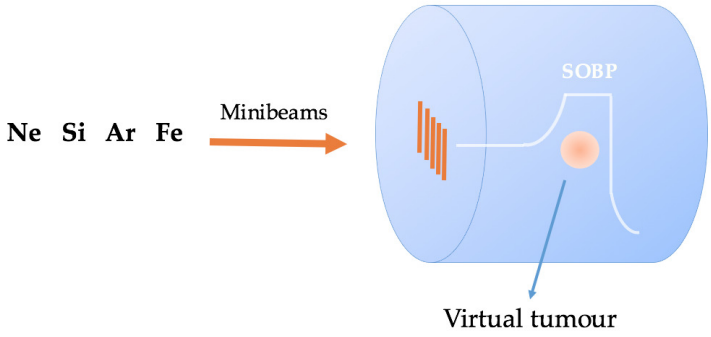

Figure 2.20: *Schematic view of the simulation setup with very heavy ions. A SOBP extends from 6 to 8 cm in the longitudinal direction in order to cover a virtual tumour located at the centre of the water phantom.*

To simulate the SOBP, the contribution of several pristine Bragg peaks (with a Gaussian energy spread of ΔE/E=0.1) was weighted and summed. The weight formula of Jette and Chen, developed for proton beams SOBP creation, was used as a starting point to calculate each beam weight [Jette 2011]. According to their method, the SOBP's width is divided into n equal intervals, and mono-energetic beams of range equal to the depth of the ends of these intervals are used, with weights given by w_{k} for k = 0, 1, ...,n. The weight to be applied for the beam k is determined using equation 2.23:

$$w_{\mathrm{k}} = \begin{cases} 1 - \left(1 - \frac{1}{2n}\right)^{1-1/p} & \text{for} \quad k = 0 \\ \left[1 - \frac{1}{n}\left(k - \frac{1}{2}\right)\right]^{1-1/p} - \left[1 - \frac{1}{n}\left(k + \frac{1}{2}\right)\right]^{1-1/p} & \text{for} \quad k = 1...n-1 \\ \left(\frac{1}{2n}\right)^{1-1/p} & \text{for} \quad k = n \end{cases} \tag{2.23}$$

with p being a coefficient for which Jette and Chen propose optimal values for va-

rious widths of the SOBP. Since this formula is related to classic clinical proton beams, it was not directly applicable to our specific configuration, namely the use of very heavy ions with very small field sizes. The weights were thus empirically adjusted to obtain a flat SOBP (±2.5%) in terms of physical dose. Due to the extreme sharpness of mono-energetic Bragg peaks obtained (see hereafter figure 2.21), a large number of mono-energetic Bragg peaks were superimposed to produce a flat SOBP: 41 mono-chromatic beams for neon and silicon, and 51 for argon and iron. Minimum and maximum energies employed to generate the SOBP for each ion are reported in table 2.6.

Heavy ions minibeams energy (MeV/u)				
	Ne	Si	Ar	Fe
Minimum energy	221	270	296	374
Maximum energy	261	319	351	447

Table 2.6: *Minimum and maximum energies employed in the simulations to create the 2 cm-long SOBP for each type of charged particle for 8 cm maximum depth.*

As previously, the dose map was recorded in the aforedescribed scoring region (see figure 2.19). A special attention was given to the choice of the voxel's size. Indeed, due to reduced range straggling with heavy ions, the Bragg peak obtained with a mono-energetic beam is very narrow. As a consequence, the choice of the voxel size in the beam direction (depth) was a critical point in this study in order to avoid any averaging effect. As shown in figure 2.21, for a silicon beam, voxel sizes below 200 μm led to an averaging effect in the Bragg peak. Using a dimension of 1 mm in depth, the peak intensity was under-estimated by 20%. Finally, the voxel sizes were chosen to be 50 μm × 5 mm × 200 μm for Ne and Si, and 50 μm × 5 mm × 100 μm for Ar and Fe. A range cut value of 50 μm was used for all particles. The number of simulated primary showers was 10^7, leading to an average uncertainty of 0.6%.

In this work, the following c-t-c distances were evaluated: 1400, 2100, 2800 and 3500 μm. All of them are multiple of the minibeam width (700 μm). The number of minibeams needed to cover the desired area (2×2 cm^2) for each c-t-c is displayed in table 2.7.

Number of beams in an array	
c-t-c distance (μm)	Number of beams
1400	15
2100	10
2800	8
3500	6

Table 2.7: *Number of minibeams needed to cover a 2×2 cm^2 field size as function of the c-t-c distance.*

The lateral dose profiles, depth dose curves in both peak and valley, PVDR

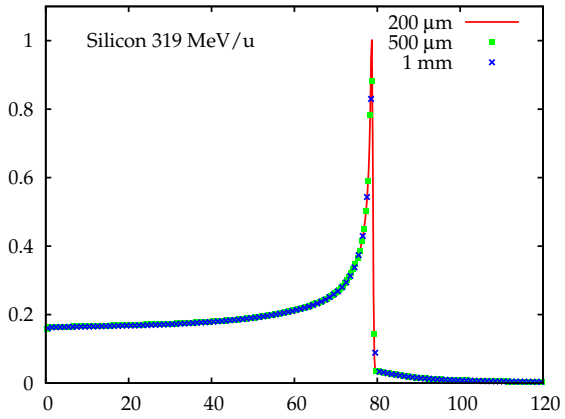

Figure 2.21: *Depth dose distribution for one single mono-energetic silicon minibeam (319 MeV/u) in the water phantom obtained with several voxel dimension(200 µm, 500 µm and 1 mm) in the beam direction. An averaging effect was observed when voxel dimensions below 200 µm were employed (for Si), leading to an under-estimation of the Bragg peak intensity.*

values, minibeam's width and penumbra (80–20% width) were evaluated as figures of merit. PVDR values were assessed on the central peak of each array of minibeams considered. Beam's width and penumbra were evaluated considering only one single minibeam. In addition, the contribution to the dose of secondary products were evaluated in both peaks and valleys. In particular, the hadronic products created by fragmentation of projectiles and target nuclei at depths shallower than the Bragg peak were studied. Since they may significantly contribute to the dose deposition (high RBE), a special attention was given to their specific contribution in valleys and in dose tails.

In addition, the number and type of secondary nuclear fragments arriving or being created in the peaks and valleys was assessed. For that purpose, parallelepiped scoring regions (700 μm $\times$ 2 cm $\times$ 2 mm) at different depths in both peak and valley regions were employed. A Phase Space File (PSF) was generated in each parallelepiped scoring region, using the GATE "PhaseSpaceActor". A PSF records the state variables of particles entering or being produced in the considered scoring region. They were then used to extract information about the type of the particles reaching of being created in this volume.

2.2.5 Parallelisation of the calculations

Since MC simulation is a stochastic method, a large number of particle histories are simulated to achieve a desired statistical accuracy. One way to spare time is to perform the computation in a parallel fashion by taking advantage of advanced parallel computer architectures [Seco 2013]. By distributing the total computation load to several computing units, a significant speedup factor can be achieved. Two

types of parallelism can be considered: (i) *task parallelism*, which is the simultaneous execution on multiple cores of many different functions across the same or different datasets, and (ii) *data parallelism*, being the simultaneous execution on multiple cores of the same function across the elements of a dataset.

Most of the MC packages, including GATE, have successfully developed parallel computing platforms to allow running simulations in a cluster of computers. The MC dose calculations carried out during this *Ph.D.* thesis have been parallelised under three main multicore Central Processing Unit (CPU) clusters (task parallelism):

- IMNC/ARIANE cluster: 39 dual Intel© Xeon processors, which each processor containing 8 to 32 cores (728 cores in total).
- IN2P3 cluster: 737 quad and hexa Intel© Xeon processors (2.53–2.66 GHz), which each processor containing 4 to 8 cores (16496 cores in total).
- TGCC Curie cluster: 1440 Intel© Nehalem-EX X7560 processors (2.26 GHz), which each processor containing 8 cores (11520 cores in total).

Under such platforms, the total number of particle histories is distributed to different computing units, which then perform simulations simultaneously and independently of each other. Before this distribution, the Gate Job Splitter (gjs) tool was employed to split the main macro in several ones. It allows to affect one unique calculation seed to each macro, permitting to generate independent sequences of pseudo-random numbers.

At the end of the calculation, the dose from all the units was accumulated using a home-made C program. This kind of method is inherent to MC simulations, as the simulation of each primary is performed sequentially.

2.2.6 Assessment of uncertainties on the computed dose

For all simulations computed within this work, the dose uncertainty in one single voxel was computed using equation 2.24, as recommended by Chetty *et al.* [Chetty 2006]:

$$s_{\bar{d}_k} = \sqrt{\frac{1}{(N-1)}\left(\frac{\sum_{i=1}^{N} {d_{k,i}}^2}{N} - \left(\frac{\sum_{i=1}^{N} d_{k,i}}{N}\right)^2\right)} \tag{2.24}$$

where $s_{\bar{d}_k}$ is an estimate of the standard error of the mean dose in the voxel k, $d_{k,i}$ is the dose deposited in voxel k by independent history i, and N is the total number of primary histories.

The global uncertainty on dose distributions was computed as the root mean square of the uncertainties of the bins with doses above half the maximum score. As previously mentioned, the overall uncertainty amounted to 0.3% and 0.6% (two standard deviations), for protons and very heavy ions simulations, respectively.

Chapter 3

Proton minibeam radiation therapy

Contents

3.1 Assessment of the composition of peaks and valleys 76

3.2 Experimental dosimetry evaluation of pMBRT 78

3.2.1 Depth dose distributions 78

3.2.2 Evaluation of normalised total doses in valley 82

3.2.3 Lateral dose profiles 83

3.2.4 Determination of output factors 88

3.2.5 Summary and discussion 89

3.3 MC evaluation of pMBRT using a magnetic collimation . . 92

3.3.1 Comparison of mechanical and magnetic collimations 94

3.3.2 Influence of several irradiation parameters 96

3.3.3 Summary and discussion 108

Proton Minibeam Radiation Therapy is a novel RT approach combining the ballistic advantages of protons with the well-established normal tissue sparing of MBRT. As stated in section 1.4.2.1, the main advantages of pMBRT over x-rays MBRT are (i) the deposition of a negligible dose in the normal tissues after the Bragg peak, (ii) the possible achievement of a homogeneous dose distribution in the tumour using one single array of minibeams, and (iii) probable distinct biological properties such as complex DNA damages and modulation of inflammation. These interesting features have triggered the implementation of pMBRT as a part of my *Ph.D.* work. As mentioned in *Chapter 2*, there are two possible ways to generate proton minibeams: mechanical and magnetic collimations. The mechanical collimation has been chosen to implement pMBRT for the first time at a clinical facility.

The first section of this chapter will be devoted to a preliminary assessment of the composition of peaks and valleys in terms of particle type, by means of a MC study. Then, the experimental dosimetric study of pMBRT at the Institut Curie - Proton Therapy Centre in Orsay will be presented. This has been accomplished by means of multislit collimators. A magnetic collimation has also been explored in the last part of this chapter. The first theoretical evaluation (MC simulations) of pMBRT using this method will be presented.

3.1 Assessment of the composition of peaks and valleys

Although the dosimetric advantages of the pMBRT technique were already emphasised in the proof of concept [Prezado 2013], the composition of peaks and valleys in terms of particle type was not evaluated. This point is of particular importance, especially in valleys which are known to be responsible for tissue sparing. In order to give a better analysis of the dose distributions, a first assessment of the contribution of primaries and secondaries to the dose distributions was performed hereafter in a MC study. A simple rectangular minibeam (700 μm$\times$ 2 cm) was simulated 7 cm away from the water phantom surface. The beam energy distribution followed a Gaussian shape, centred at 100 MeV with a standard deviation of 2.5 MeV. The angular distribution was defined as a Gaussian with 5 mrad standard deviation. An array of 5 minibeams spaced by a c-t-c distance of 3500 μm was considered.

Figure 3.1 presents the respective contributions of primary and secondary particles to the total dose PDD curves for an array of 700 μm-beams (c-t-c of 3500 μm). Although the distributions may vary with irradiation configuration, only one case is presented here as a first approach. In the peak, the primary protons are the main responsible for dose deposition. Only 10% of the total dose is due to the secondary particles at the phantom surface, then a smooth decrease of their contribution is observed. At the Bragg peak (74 mm), a dramatical fall off of secondaries occurs, directly linked to the total stop of the primary protons.

In contrast, the secondaries are the main responsible of the valley dose until 30 mm-depth. From that depth, they are overstepped by the contribution of primary protons. Indeed, due to Coulomb scattering, more and more primaries are able to reach the centre of the valley region with increasing depth, the contribution reaching a maximum at the Bragg peak.

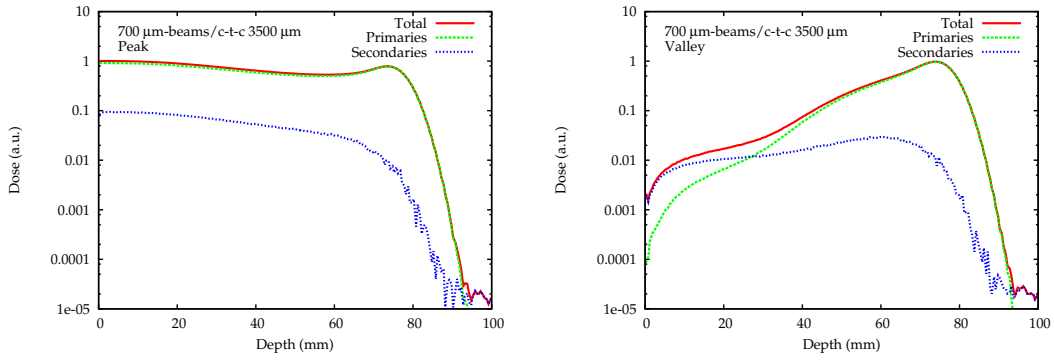

Figure 3.1: *Contribution to the peak and valley dose distributions of primary projectiles and secondary products for an array of proton minibeams in a water phantom. The distributions are normalised to the maximum normal dose in peak (left) and in valley (right).*

In addition, figure 3.2 decomposes the secondaries species' contributions to the peak (left) and valley (right) depth dose distributions. The maximum of the total sum of secondary products (gammas, δ-rays and other fragments coming from target

fragmentation) was taken as a normalisation point. In both peak and valley regions, the contribution of gammas is several orders of magnitude lower than other products. In the peak, the contributions of δ-rays is the dominant one until the Bragg peak. In the vicinity of the Bragg peak, the contributions of δ-rays falls rapidly, while a build up in the fragmentation products contribution is observed, due to the increase of nucleus-nucleus collisions. In the distal part, the nuclear fragments fall off in turn due to the total stop of incident protons. In the valley, the contribution of target fragmentation products is dominant at all depths. Interactions of fragments with the medium produce in turn δ-electrons, which follow an increasing trend with a build up in the Bragg peak. Among the fragmentation products, secondary protons are in majority in both peak and valley regions, as illustrated in figure 3.3.

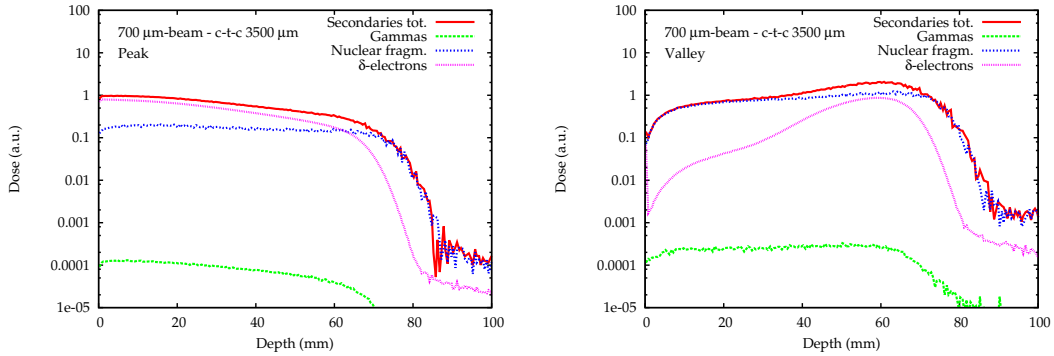

Figure 3.2: *Contribution of the different species of secondary particles to the peak (left) and valley (right) depth dose curves. The dose was normalised to the maximum of the total sum of secondary products. "Secondaries tot." and "nuclear fragm." refer to "secondaries total" and "nuclear fragments", respectively.*

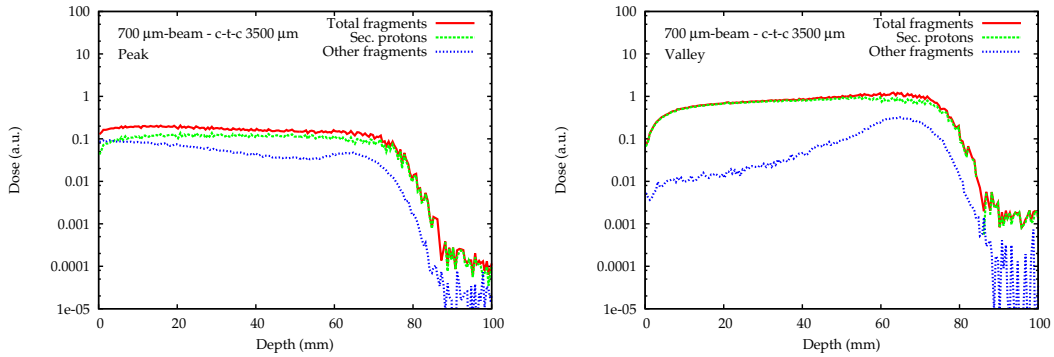

Figure 3.3: *Contribution of the different species of secondary particles to the peak (left) and valley (right) depth dose curves. The dose was normalised to the maximum of the total sum of secondary products."Sec. protons" refer to "secondary protons".*

These preliminary results thus show that secondaries' contribution to valley dose is of particular importance in the first centimetres as it is the dominant one. Then,

the primary protons are the main contributors to the valleys, like in the peaks. In that sense, the mean RBE values are not expected to significantly vary between peaks and valleys. This will have to be confirmed by biological experiments.

Interestingly, it was found that the valley dose was mainly due to secondary protons (shallow depths) and primary protons (further depths). This constitutes an advantage over x-rays MBRT, where valleys are mainly due to electrons and gammas that contribute further to the dose.

However, this example explored a simplified simulation geometry that does not include any shaping element. It must be highlighted that with the presence of such shaping element, for example in the case of a mechanical collimation, the contribution of secondaries could be highly increased due to interactions with the elements of the beamline. This might further increase the secondaries' contribution to valleys at shallow depths, thus increasing the total valley dose. This point will have to be investigated in further studies.

3.2 Experimental dosimetry evaluation of pMBRT

This dosimetry work allowed the experimental validation of pMBRT. The technical implementation of the technique was carried out by means of a mechanical collimation at a clinical facility (ICPO). This was the first time that measurements in such small proton field sizes were successfully performed. Very few commercially available detectors meet the requirements needed for pMBRT dosimetry, in particular a micrometric spatial resolution and a low LET dependency. In this work, two detectors were selected: Gafchromic© films EBT3 and the PTW microDiamond© 60019 detector. While diamond detectors are known to have a negligible dependence on LET, this is not the case of EBT3 films, for which correction factors have been applied (see *Chapter 2*).

First, the dose distributions (PDD and lateral dose profiles) obtained with the different pMBRT collimators will be reported. PVDR values, minibeam's penumbra and width, and OF, needed for absolute dose determination in pMBRT (see *Chapter 2*), will be presented.

3.2.1 Depth dose distributions

As previously explained, the depth dose distributions have been assessed by means of Gafchromic© films. With the microDiamond© which was oriented perpendicular to the beam (to obtain a 1 μm resolution in the fractionation direction), it was not possible to acquire PDD curves without inducing an averaging effect in 2.2 mm (diameter of the detector) in depth. See section 2.1.4.2. Figure 3.4 shows a couple of EBT3 films irradiated along the beam direction.

The figure on the top corresponds to the irradiation with the single slit collimator. The increase of beam width as a function of depth due to multiple Coulomb scattering is clearly visible. The bottom film shows the dose deposition for an irradiation with one array. One can see that the spatial fractionation of the dose is

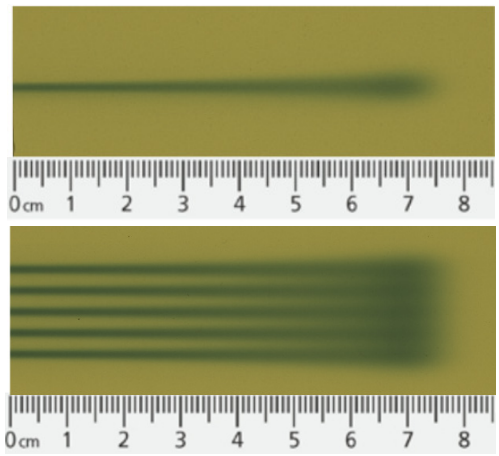

Figure 3.4: *Gafchromic© films irradiated longitudinally in the RW3 phantom with one minibeam (top) and with an array of 5 minibeams with the 700 µm-slits/c-t-c 3500 µm collimator (bottom).*

maintained until 6.7 cm-depth, from where a homogenisation of the dose is achieved in the target (Bragg peak position), as predicted in previous theoretical studies [Prezado 2013].

The increase of minibeam width with depth has been quantified by the assessment of FWHM in solid water, as shown in figure 3.5. Considering one single slit (left figure), the FWHM at the phantom entrance (1380 ± 80 μm) is already much wider than the slit width (700 μm). This is due to the "long" distance between the slit collimator and the phantom entrance (7 cm) chosen for the first implementation, which causes beam enlargement due to the angular divergence (around 5 mrad in the Y1 beamline) and protons scattering in air. Since these first tests, an optimisation of this parameter has been performed. Details will be given later on. In depth, the multiple Coulomb scattering broadens the beam until 3700 ± 200 μm at the Bragg peak location.

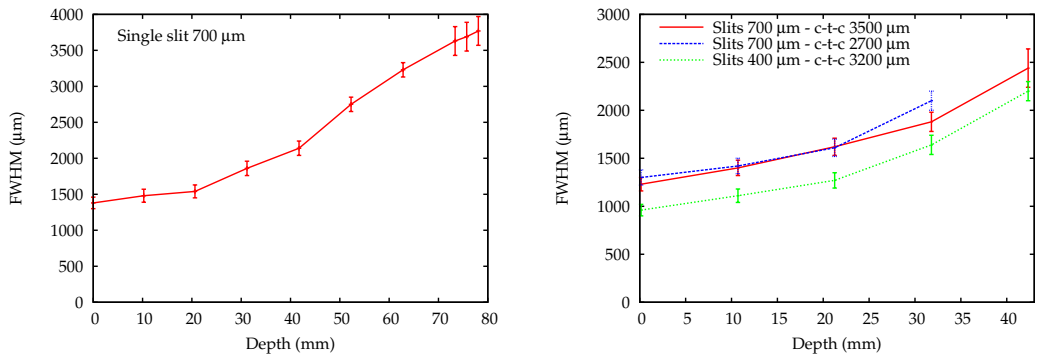

Figure 3.5: *Evolution of the full-width at half maximum (FWHM) as a function of depth for the single slit (left) and multislit collimators (right) in the solid water phantom. Beyond 30 mm (700 µm/c-t-c 2700 µm) and 40 mm (other collimators), FWHM values were not measurable in the central peak due to the increase of the valley dose.*

Considering the multislit collimators (see figure 3.5 right), individual beam FWHM was not measurable beyond 40 mm in depth (even beyond 30 mm with the Multi2 collimator) due to the increase of valleys, as illustrated in figure 3.6 (the characterisation of the lateral dose profiles will be addressed in section 3.2.3). With the 700 μm-multislit collimators, FWHM values are similar to the single slit case (left figure) at the phantom entrance. However, from 40 mm-depth, they start to be larger with multislit collimators due to the contribution of peripheral minibeams. For instance, the FWHM for the 3500 μm c-t-c-multislit collimator is 2400 $\pm$ 200 μm at 40 mm-depth, while being 2100 $\pm$ 100 μm with the single slit. Using the 400 μm-multislit collimator, FWHM values are overall reduced, ranging from 960 $\pm$ 60 μm at the phantom entrance to 2200 $\pm$ 100 μm at 40 mm-depth. In that sense, the use of smaller slits could enhance the dose-volume effect. To diminish the distance between the collimator exit and the phantom would also lead to a reduction of FWHM at the phantom entrance, as it will be discussed later.

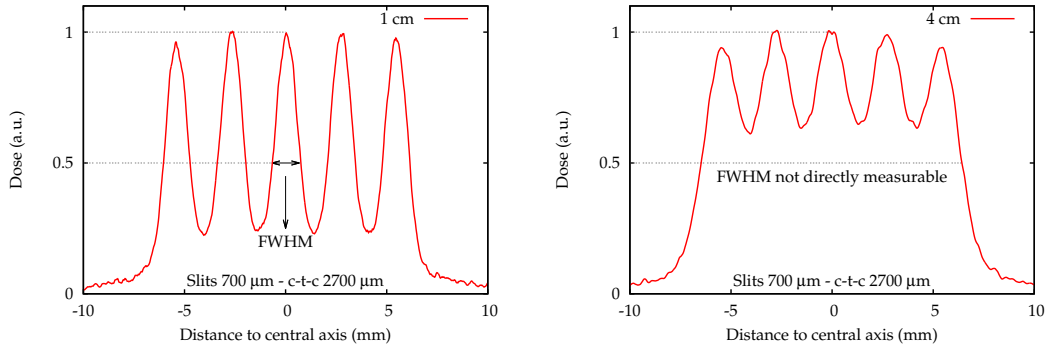

Figure 3.6: *The FWHM is directly measurable at shallow depths in the phantom using the 700 μm-slits/2700 μm collimator (left). From 40 mm in depth (right) the valley dose is so high that the determination of FWHM is no longer possible.*

As explained in section 2.1.1, only simple Bragg peaks (no SOBP) were used in this study. Figure 3.7 shows the depth dose curves for the central peak of arrays of minibeams obtained in water (left) and in the solid water phantom (right). In water, the depth dose cannot be drawn for depths shallower than 20 mm due to the presence of the water tank entrance window. In contrast, measurements performed in solid water provided the whole PDD curves.

The two data sets (water and solid water) were in agreement within the uncertainty bars ($\pm$7%, not shown here) considered for these delicate measurements with several correction factors taken into account (QCF, depth scaling factors). However, in both cases, the shape differs from the standard proton depth dose curve. In particular, the intensity of the Bragg peak (at 7.4 cm) is reduced in comparison with a broad beam configuration. This is explained by a loss of lateral equilibrium near the central region of the beam as the field size shrinks [Newhauser 2015]. As a consequence, the ratio of the scattered protons with respect to the primary beam di-

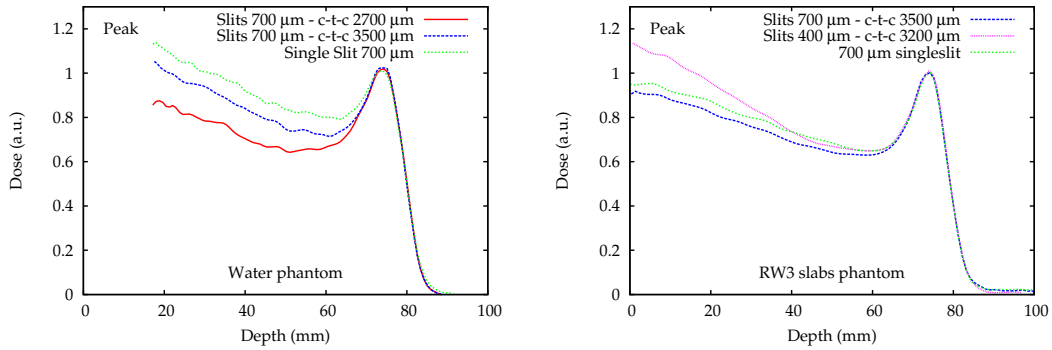

Figure 3.7: *Depth dose curves in the central peak of minibeams arrays obtained in water (left) and solid water (right). Each curve is normalised with respect to the Bragg peak dose. Each colour corresponds to one collimator.*

mension is high, which induces a dose reduction along the beam axis. This effect gets more pronounced for narrower slits (400 μm), as shown in figure 3.7 right. It points out the fact that there is a lower limit in the beam size suitable for pMBRT, as theoretically shown by Martínez-Rovira *et al.* for grid therapy [Martínez-Rovira 2015]. Besides, when a multislit collimator is employed, the Bragg peak is less reduced than with a single slit due to the contribution of the peripheral minibeams to the central peak dose, as seen in figure 3.7 left.

Concerning the valleys, the dose increases as a function of depth reaching a maximum in the Bragg peak (see figure 3.8), as a consequence of Coulomb scattering of protons. For a given slit-width, the use of smaller c-t-c increases the valley dose (see figure 3.8 left) due to a higher contribution of the adjacent minibeam tails.

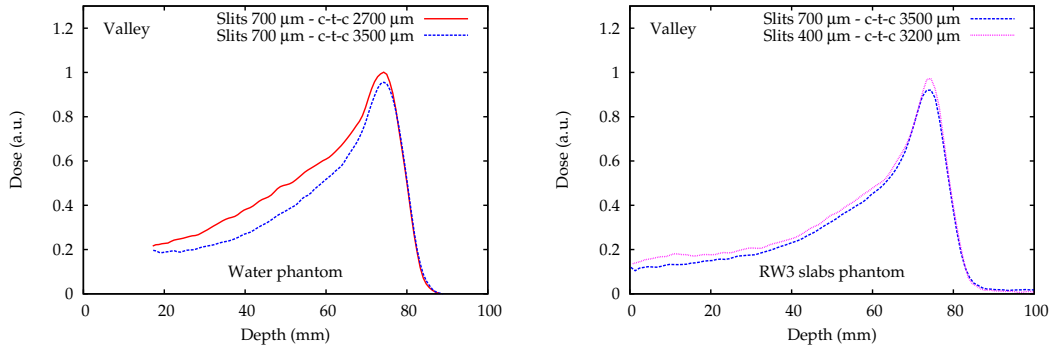

Figure 3.8: *Depth dose curves in valley obtained in water (left) and solid water (right). Each curve is normalised with respect to the Bragg peak dose in the peak. Each colour corresponds to one collimator.*

As previously mentioned, in spatially fractionated RT techniques, the valley dose is considered responsible for normal tissue sparing, and must be kept under

the tolerance doses for seamless irradiations [Dilmanian 2002]. Within this context, an assessment of the valley and average doses at different depths in normal tissues (considering a pMBRT irradiation of the brain) has been performed as a percentage of the Bragg peak dose. The results are reported in table 3.1.

Estimation of valley and average doses as a function of Bragg peak dose				
	700 μm-slits/c-t-c 3500 μm		400 μm-slits/c-t-c 3200 μm	
Depth	Valley dose (%)	Average dose (%)	Valley dose (%)	Average dose (%)
0 cm	11.0 ± 0.8	34 ± 1	13.0 ± 0.9	33 ± 2
3.5 cm	20 ± 1	36 ± 1	22 ± 1	48 ± 3

Table 3.1: *Estimation of valley and average doses received at different points in the normal tissues considering pMBRT irradiations with the Multi1 (700 μm-slits/c-t-c 3500 μm) and Multi3 (400 μm-slits/c-t-c 3200 μm) collimators in solid water. The data are expressed as a percentage of the Bragg peak dose.*

At the phantom entrance, assimilated to the skin, the valley doses are only 11% and 13 % of the Bragg peak dose with the 700 μm-slits/c-t-c 3500 μm (Multi1) and 400 μm-slits/c-t-c 3200 μm (Multi3) collimators, respectively. At the middle point of the irradiated brain hemisphere (3.5 cm in depth), the valleys amount to 20% of the Bragg peak dose with the Multi1 and 22% with the Multi3 collimator. Concerning average doses (see table 3.1), the values observed are in the order of those observed in conventional proton therapy [Paganetti 2012]. Indeed, in the case of a non-modulated (mono-energetic) Bragg peak, the entrance dose is already around 30-40% of the Bragg peak dose (it may amount 80% of the SOBP with a modulated beam), and increases with depth.

3.2.2 Evaluation of normalised total doses in valley

A pMBRT treatment will be likely given in one single fraction. In order to establish the equivalence of the valley doses with the standard fractionation scheme of 2 Gy/fraction, the normalised total dose ($NTD_{2.0}$) was assessed, as it was done in a previous work for MRT [Martínez-Rovira 2010]. The $NTD_{2.0}$ is expressed as follows:

$$NTD_{2.0} = nd\frac{\left(1+\frac{d}{\alpha/\beta}\right)}{\left(1+\frac{2.0}{\alpha/\beta}\right)} \tag{3.1}$$

where d is the dose per fraction and n the number of treatment fraction (n=1 for pMBRT). The α/β ratio is linked to the biological response of the tissue under consideration and depends on its renewal capability.

Equation 3.1 derives from the linear-quadratic (LQ) model for the biological response to IR [Flickinger 1990]. This model is often employed in clinics to compare different fractionation schemes in conventional RT because it fits satisfactorily the experimental cell survival curves in most cases. Although this model is only based on direct damages induced by IR (evaluated from clonogenic assays) and does not

take into account the non-targeted effects that are likely to play a role in pMBRT, it has been used as a first rough approximation in this study, mainly because it is the only suitable model at the moment. In addition, RBE has not been taken into account here, as the biological consequences of pMBRT irradiation might greatly differ from those of conventional proton therapy, making the established RBE values not applicable. The LQ model has been experimentally and theoretically validated up to about 10 Gy/fraction, and is widely used to quantify the effects of RT at low and medium doses. Above 10 Gy, the model might overestimate radiation-mediated cell killing, thus would become progressively less accurate [Brenner 2008]. However, based on animal data, it has been found to be still acceptable for the design of clinical trials based on doses per fraction of 15 to 18 Gy [Brenner 2008]. A maximum valley dose of 11 Gy in one fraction has been considered in this work, thus being in the acceptable dose range for application of the model.

For $NTD_{2.0}$ calculations, the α/β ratios for the skin and the middle brain were taken as 8.8 Gy and 2 Gy, respectively [Turesson 1989]. A prescription dose of 50 Gy (Bragg peak location) was considered, being a much higher dose than that usually given in radiosurgery (maximum 15 to 20 Gy in one fraction). The valley doses for this prescription (from table 3.1) and their associated $NTD_{2.0}$ are reported in table 3.2.

Estimation of $NTD_{2.0}$ in the valley for a prescription dose of 50 Gy				
	700 μm-slits/c-t-c 3500 μm		400 μm-slits/c-t-c 3200 μm	
Depth	Valley dose (Gy)	$NTD_{2.0}$ (Gy)	Valley dose (Gy)	$NTD_{2.0}$ (Gy)
0 cm	5.5 ± 0.4	7.3 ± 0.5	6.5 ± 0.3	9.2 ± 0.6
3.5 cm	10.0 ± 0.7	30 ± 2	11.0 ± 0.9	36 ± 3

Table 3.2: *Estimation of $NTD_{2.0}$ in the valley considering a prescription dose of 50 Gy at the Bragg peak for irradiations with the Multi1 (700 μm-slits/c-t-c 3500 μm) and Multi3 (400 μm-slits/c-t-c 3200 μm) collimators in solid water.*

Considering this prescription, the $NTD_{2.0}$ in the skin reached 7.3 Gy and 9.2 Gy with the 700 and 400 μm collimators, respectively. These values are well below the dose of 50 Gy for which risks of severe skin toxicity have been reported [Ginot 2010]. In the case of the brain, the $NTD_{2.0}$ amounted to 30 Gy and 36 Gy in the middle brain for the two aforementioned collimators. Once again, these doses are under the tolerance dose for the brain (72 Gy), for which a 5% risk of symptomatic radiation necrosis has been predicted with the standard fractionation scheme [Lawrence 2010]. This means that doses as high as 50 Gy in one fraction might be delivered with pMBRT while keeping the valley dose at acceptable levels, below the tolerance doses to broad beam irradiation.

3.2.3 Lateral dose profiles

As explained in *Chapter 2*, the lateral dose profiles were assessed using both EBT3 films and the microDiamond© detector. Figure 3.9 presents several films irradiated

with the 700 μm-slits/c-t-c 3500 μm collimator at different depths in the RW3 phantom and the corresponding lateral dose profiles. In agreement with the theoretical predictions [Prezado 2013], a pattern of peaks and valleys is observed in the first centimetres in contrast to the (quasi) homogeneous dose distribution at the Bragg peak.

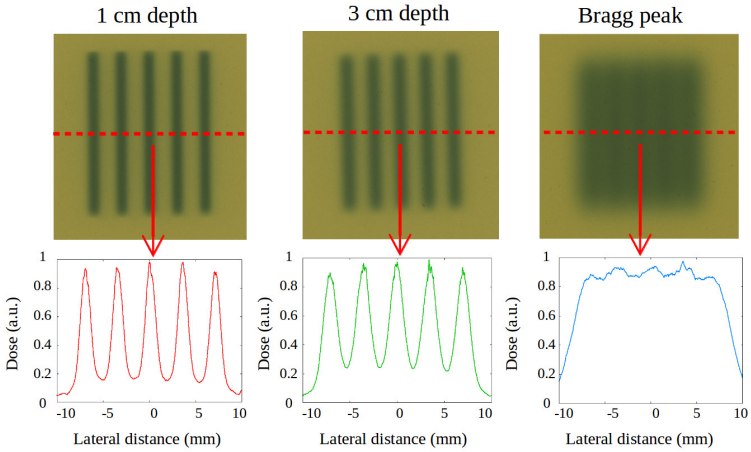

Figure 3.9: *This series of films irradiated at different depths in the solid water phantom (700 μm-slits/c-t-c 3500 μm collimator) shows how the spatial fractionation is maintained in the normal tissues while a (quasi) homogeneous dose distribution is reached in the target.*

Figure 3.10 shows examples of lateral dose profiles determined by EBT3 films in solid water for the single slit (left) and the 400 μm-slits/c-t-c 3200 μm collimator (right). With this collimator, a homogenisation is also achieved at the Bragg peak. Considering the profiles obtained with single slit, a slight asymmetry is visible, especially at shallow depths. This phenomenon was found in several data sets. The most probable explanation is a default of machinery of the single slit collimator prototype.

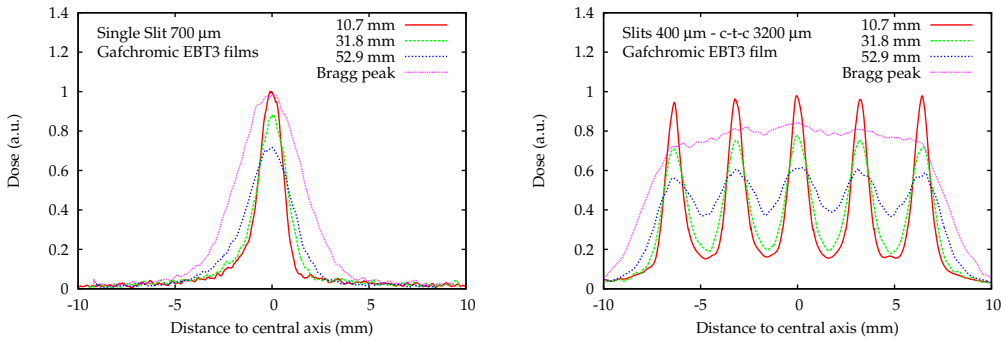

Figure 3.10: *Lateral dose profiles at several water-equivalent depths in the slabs phantom obtained with EBT3 films with the single slit (left) and the Multi3 (400 μm/c-t-c 3200 μm) collimators.*

Additional lateral dose profiles were acquired with the microDiamond© for both Multi1 (700 μm-slits/c-t-c 3500 μm) and Multi3 (400 μm-slits/c-t-c 3200 μm) collimators, as depicted in figure 3.11. Profiles at depths shallower than 30 mm were not acquired due to the presence of the water tank entrance window and the thickness of the detector itself. As shown in these two figures, the pattern of minibeams appears well-resolved with both detectors.

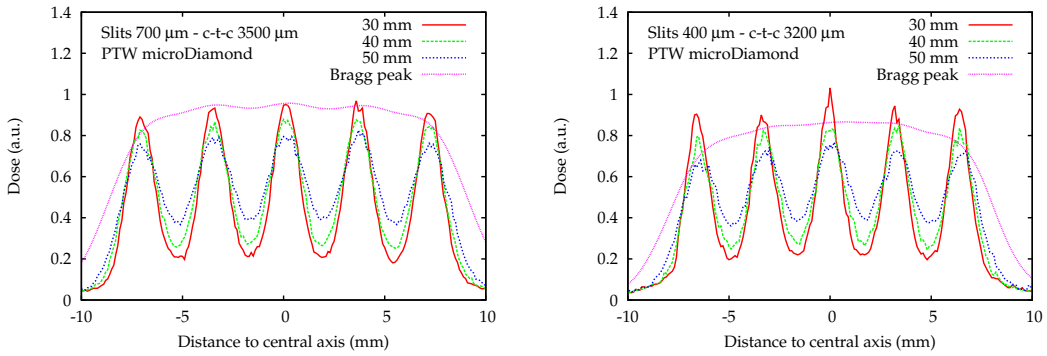

Figure 3.11: *Lateral dose profiles at several depths in water obtained with the PTW microDiamond© detector. Both 700 µm-slits/c-t-c 3500 µm (left) and 400 µm-slits/c-t-c 3200 µm (right) collimators were tested.*

For quantification, PVDR values and beam penumbras were assessed with both detectors. First of all, figure 3.12 shows the comparison of PVDR values determined with EBT3 films in both water and solid water. In water, PVDR values were assessed on the films irradiated longitudinally to the beam direction in the water tank. For the aforementioned reason, PVDR at depths shallower than 17 mm (water equivalent thickness of the tank window) were not measurable. Uncertainties were larger for these measurements ($\pm$5%) due to the difficulty to assess the exact depth on the scanned film. The results are in agreement in the two materials within uncertainty bars, indicating the equivalence of the two materials.

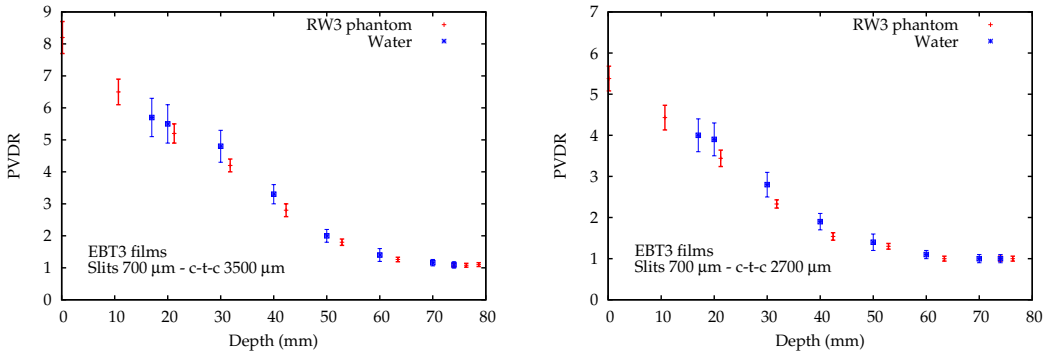

Figure 3.12: *Comparison of PVDR values obtained for 700 µm-slits/c-t-c 3500 µm (left) and 700 µm-slits/c-t-c 2700 µm (right) collimators with EBT3 films in water and solid water phantom. The two data sets are in agreement within the uncertainty bars.*

Figure 3.13 compares PVDR obtained with films irradiated in solid water for all multislit collimators. As expected, the multiple Coulomb scattering causes a continuous decrease of PVDR in depth. At a given depth and with a fixed slit width, the highest PVDR values are obtained with the largest c-t-c distance. Despite a better homogenisation in the target with the 700 μm/c-t-c 2700 μm collimator, lower PVDR values were reached in normal tissues (maximum of 5.4 $\pm$ 0.3 at the phantom entrance). The dose homogenisation already occurred from 50 mm, which could limit the potential normal tissue sparing, making this collimator not suitable for pMBRT. The Multi2 collimator was thus discarded for further studies. Using the other two collimators, a quasi-homogenisation (PVDR = 1.08 $\pm$ 0.06) was reached from 7 cm-depth while allowing much higher PVDR values, with a maximum of 8.2 $\pm$ 0.5 at the phantom entrance with the 700 μm-slits, and 7.9 $\pm$ 0.5 with the 400 μm-slits. The PVDR followed a similar trend, despite the smaller slits width of the Multi3 collimator. This was due to the higher ratio of lateral scattering with respect to the dose deposited by the primary beam with the 400 μm-slits collimator. This could be also partly explained by the minibeam penumbra, as it will be detailed hereafter.

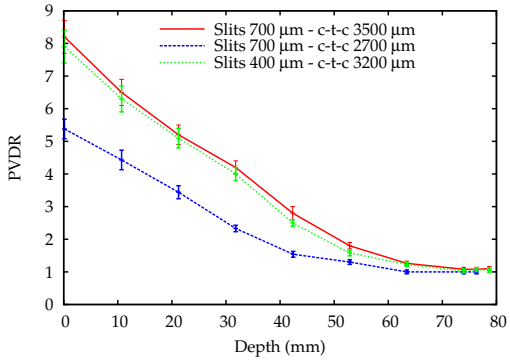

Figure 3.13: *PVDR values as a function of depth measured with EBT3 films in solid water for the three multislit collimators.*

Similar results were obtained with the microDiamond© detector (within uncertainty bars) as shown in figure 3.14 right. Contrary to the diamond detector, Gafchromic© films are known to be LET dependent. There was a possibility that the mean LET of protons differs between peak and valley regions. As mentioned in *Chapter 2*, MC tests were performed by a post-doctoral researcher of the team to investigate this point. The tests showed no differences in LET between the two regions. The agreement observed here between the films (LET dependent) and the diamond (LET independent) data confirms that the mean LET of protons does not significantly vary between peaks and valleys, thus facilitating film dosimetry in pMBRT.

Figure 3.15 compares the minibeam penumbras (80%-20%-width) for all collimators measured with EBT3 films in solid water. Penumbras increase as a function of depth because of multiple Coulomb scattering. Their values range from 500 μm

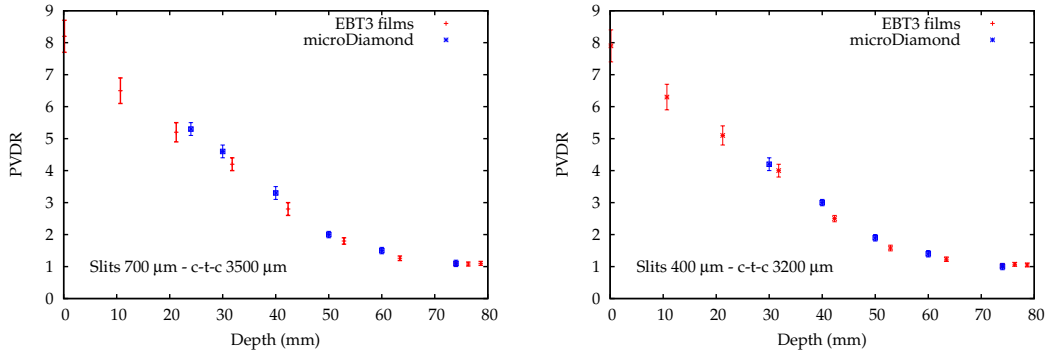

Figure 3.14: *Comparison of PVDR values obtained for 700 µm-slits/c-t-c 3500 µm (left) and 400 µm-slits/c-t-c 3200 µm (right) collimators with EBT3 films and the PTW microDiamond© detector. The two data sets are in agreement within the uncertainty bars.*

at the phantom entrance to a maximum of 2300 μm at the Bragg peak. These are particularly low values, especially in the normal tissues. Even at large depths, penumbras are narrower than in conventional radiosurgery, where they are larger than 2.5 mm in the best cases [Guerrero 2003, García-Garduño 2008]. These very low penumbras are thus a valuable advantage for pMBRT, allowing extremely high dose gradients in the field edges, and thus a high conformation.

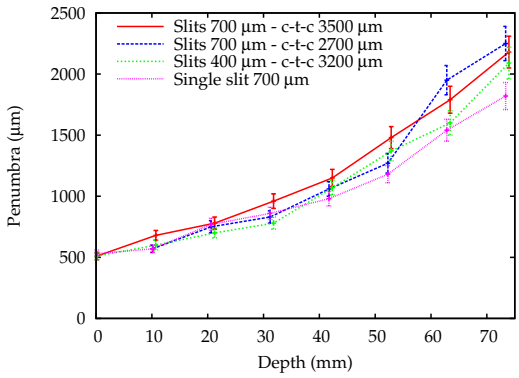

Figure 3.15: *Penumbras as a function of depth measured with EBT3 films in solid water for the different pMBRT collimators.*

For a fixed slit width, penumbra values were identical in the first centimetres in single and multislit configurations. The contribution to the dose of the tails of nearby minibeams make them widen for the mutlislits. This phenomenon was more pronounced with the Multi2 collimator having the smallest c-t-c distance. A very low reduction of penumbra is observed when smaller slits (400 μm) are used. With this collimator, the penumbras remain large with respect to the beam width. This phenomenon unfortunately favours the increase of valleys. This is the reason why the reduction of slit-width was not efficient enough to obtain lower PVDR than those with the Multi1 collimator (700 μm/c-t-c 3500 μm).

The results were confronted to those obtained with the microDiamond© detector for the Multi1 and Multi3 collimators (see figure 3.16). The two data sets were in agreement within the uncertainty bars, confirming that these two types of detectors are suitable for pMBRT, and proves the reliability of the measurements.

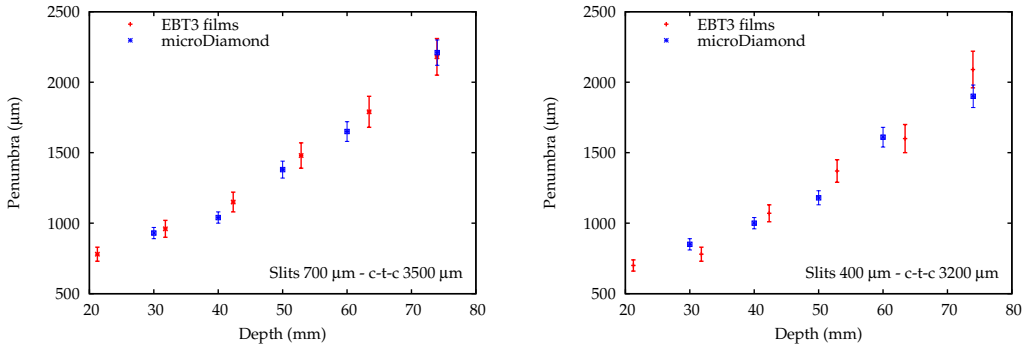

Figure 3.16: *Comparison of penumbras obtained for the 700 µm/c-t-c 3500 µm (left) and 400 µm/c-t-c 3200 µm (right) collimators with EBT3 films and the PTW microDiamond©.*

3.2.4 Determination of output factors

The knowledge of OF allows to determine peak and valley doses in pMBRT conditions, directly from one single measurement of absolute dose performed with the ionisation chamber in the broad beam reference conditions described in section 2.1.4.1, thanks to the following expressions:

$$D_{\text{peak}}(z) = D_{\text{ref}}(z) \times \text{OF}(z) \tag{3.2}$$

$$D_{\text{valley}}(z) = \frac{D_{\text{peak}}(z)}{PVDR(z)} \tag{3.3}$$

OF were assessed for all collimators except for the Multi2, which was found to be not suitable for pMBRT (see section 3.2.3). Due to the very small field sizes employed, very low OF, ranging from 0.1 to 0.5, were obtained (see figure 3.17). Those values are significantly lower than those found in x-rays MBRT (0.80 ±0.04) [Prezado 2011] due to a more important lateral scattering suffered by protons.

With 400 μm-slits, a 33% reduction was observed with respect to the 700 μm-multislit collimator. A similar dose reduction occurred when a single slit was used with respect to the 700 μm/c-t-c 3500 μm collimator. This was due to the additional contribution of the peripheral minibeams' tails to the central peak dose when several minibeams are generated. Such lower OF will consequently increase irradiation time to deliver a same prescribed dose in the target with smaller slits. In addition, it could induce a higher production of secondary products, including neutrons, by interaction of protons with the collimator. However, it has been shown, in a recent MC study carried out in our team, that the contribution of neutrons to the dose in pMBRT will be lower than 1% of the prescribed dose [Guardiola 2016].

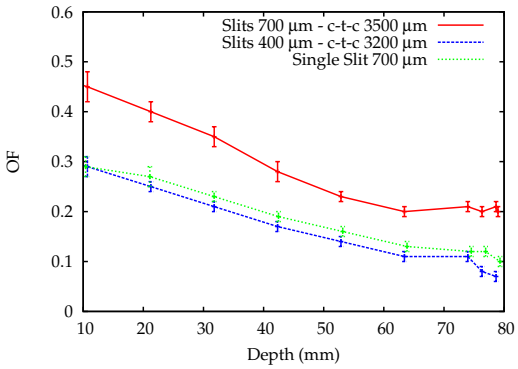

Figure 3.17: *OF as a function of depth determined with EBT3 films in solid water.*

3.2.5 Summary and discussion

This experimental proof of concept was carried out thanks to the first technical implementation of pMBRT at a clinical facility (ICPO). This work confirmed that the dose distributions of an array of 100 MeV (clinical relevant energy) proton minibeams might be favourable to treat a tumour in the centre of the brain (7.5 cm depth, the worst scenario) with a homogeneous dose distribution, while the normal tissues in the beam path might benefit from the spatial fractionation of the dose. This study thus experimentally validated the concept of minibeam generation by means of a mechanical collimation. Despite the dosimetric challenges imposed by this technique (small field sizes, variations of the mean LET of the beam as a function of depth), successful measurements were carried out with two types of detectors: Gafchromic© films (EBT3) and PTW microDiamond© detector. This was the first time that measurements were performed in such small (sub-millimetric) proton field sizes. Both detectors showed suitable characteristics for pMBRT dosimetry and led to a good agreement, within the uncertainty bars. The main results of this work have been compiled in an article published in the *Medical Physics* journal [Peucelle 2015a]. See *Chapter 6*.

Among the three multislit collimators investigated, the Multi2 (700 μm/ c-t-c 2700 μm) presented the lowest PVDR (maximum of 5.4 at the phantom entrance), and did not allow to maintain a spatial fractionation until the Bragg peak depth, due to a too small c-t-c distance. It was thus found to be not suitable for pMBRT applications. Both Multi1 (700 μm/c-t-c 3500 μm) and Multi3 (400 μm/c-t-c 3200 μm) collimators provided higher PVDR values in the normal tissues (maximum values around 8 at the phantom entrance), while allowing a dose homogenisation at the Bragg peak. These values are below those obtained with x-rays MBRT, where they are around 20 in the normal tissues [Prezado 2009b]. Even so, a gain in tissue sparing might already be obtained with such PVDR, as it was already confirmed in a first biological experiment described hereafter. In addition, further optimisations of the technique might lead to higher PVDR values. This point will be discussed hereafter.

Although lower OF values were obtained, thinner FWHM were observed with Multi3 collimator thanks to smaller slits (400 μm). In that sense, this collimator could enhance the dose volume effect in the normal tissues. The Multi3 collimator has thus to be favoured among the three prototypes presented in this study. Nevertheless, this work showed that 400 μm constitutes the lower limit in terms of slit width, due to a significant reduction of the Bragg peak intensity. This dimension also meets the technical limitation in terms of collimator machining.

For the aforementioned reasons, the 400 μm-slits collimator was kept for the first pre-clinical studies with rats, that have already started in autumn 2015. This dosimetric work provided the elements needed for the dosimetry protocol to be used in this first biological study. The whole brain of normal rats was irradiated using both conventional proton therapy (broad beam) and pMBRT with a same average dose of 25 Gy in one single fraction. This corresponded to a peak dose of 58 Gy with pMBRT. The follow-up of the animals lasted 7 months, including MRI imaging and histological studies. Important cerebral and skin damages were observed in rats irradiated in broad beam conditions. In the pMBRT group, only a reversible epilation following the minibeams paths occurred, while no brain damages were found.

The potential of pMBRT, could be enhanced by either optimising the irradiation setup or exploiting a magnetic collimation for minibeam generation. This second avenue will be explored in section 3.3. Concerning mechanical collimation, the best suitable collimator for pMBRT is the one that offers the best compromise between high PVDR, low valley doses, narrow FWHM and low neutron yield, while allowing a homogenisation at the Bragg peak. In this context, I took part in a MC optimisation study of the collimator design and irradiation configuration that has been carried out by a post-doctoral researcher of our team [Guardiola 2016]. Based on the experimental observations presented in this chapter, 400 μm-slits were kept for the optimisation. Several collimator materials (brass, nickel, iron, tungsten), thicknesses, shapes and c-t-c distances were investigated, as well as different phantom-to-collimator distances (PCD). A specific concern has been the neutron yield and dose deposited in the phantom using such multislit collimators. Although higher PVDR values were found with a tungsten multislit collimator, a brass collimator would be more advantageous in terms of neutron contamination, manufacturing cost and micro-etching. Concerning collimator's thickness, a gain in PVDR was observed when going from 5 to 10 cm. However, the OF would be reduced by 25%, meaning that the number of neutron produced in the collimator will increase by 25% to deposit the same peak dose [Guardiola 2016]. The best compromise between spatial fractionation of the dose in the normal tissues and homogenisation in the target was found with a c-t-c of 3200 μm. In addition, it was found that other arrangements of the slits (*e.g.* divergent collimator with a slits inclination following the beam divergence) do not offer any advantage over the use of a parallel arrangement. Finally, the study showed that, considering a target located at 7 cm-depth, a parallel-slit tungsten or brass collimator of 5 cm thickness and a c-t-c of 3200 μm placed at between 2 and 5 cm (PCD) should be privileged [Guardiola 2016].

Considering these results, the main parameter that has to be optimised with respect to the existing experimental setup is the PCD. In this first experimental study, the use of two successive 5 cm-thick collimators (multislit + additional square cap) constrained us to use a PCD equal or superior to 7 cm. Figure 3.18, taken from the work of Guardiola *et al.*, shows that a decrease of the PCD from 7 to 2 cm could, on one hand, diminishes the FWHM at the phantom entrance by a factor 1.5 (left), therefore enhancing the dose volume effect, and on the other hand improves the PVDR values by a factor 10 at the phantom entrance, while maintaining a homogenisation from 7 cm-depth (right).

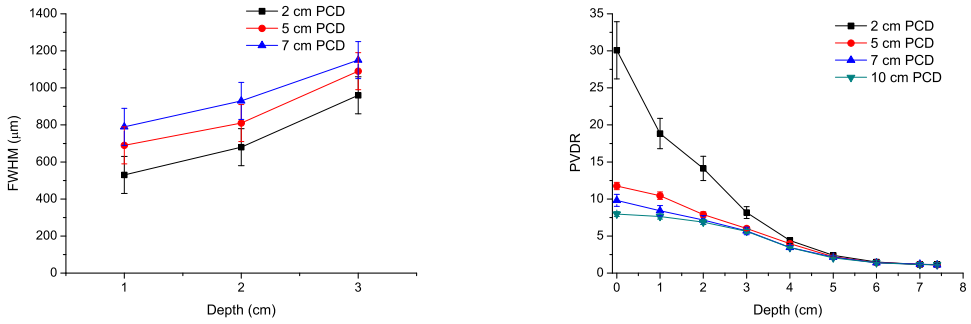

Figure 3.18: *Simulated FWHM (left) and PVDR values (right) as a function of depth using a brass collimator for several PCD. A decrease of the PCD from 7 to 2 cm reduces the FWHM by a factor 1.5, and increases the PVDR values by a factor 10. Taken from the work of Guardiola et al. [Guardiola 2016].*

These promising results might mean that the conception of a new collimator (that does not require an additional cap) allowing a shorter PCD, should optimise the minibeam generation, in order to take full advantage of both enhanced dose volume effect and higher PVDR values in the normal tissues. Another simple solution would be the inversion of the two existing collimators, placing the square cap before the multislit collimator. This would reduce the PCD to 2 cm.

In this study, a target located around 7 cm-depth was considered. As previously stated, one of the major interest of pMBRT is the possibility to use only one single array to treat an intracranial tumour. Considering that point, the main drawback of such a mechanical collimation is that the collimator has to be optimised for each target depth/beam energy. In order to improve the technique and to allow an easy clinical implementation at hospitals, another strategy would be the use of a magnetic collimation. This would avoid the need for optimisation and machining of one collimator per patient, which is a common practice nowadays, and could also reduce the neutron yield. This strategy has been explored in the following section, by means of MC simulations.

3.3 Monte Carlo evaluation of pMBRT using a magnetic collimation

This section aims to assess the pMBRT technique assuming another way to generate the minibeams: a magnetic collimation. In the manner of active beam delivery systems developments over passive beamlines, a magnetic collimation for pMBRT might offer several advantages over a mechanical collimation. In particular, as shown in section 3.2, the use of a multislit collimator considerably reduces the dose-rate, leading to very low OF. This goes with an increase of secondary neutron yields. Using a magnetic collimation method for pMBRT would thus allow to increase the dose-rate (200 Gy/min achievable with a PBS system) as well as reducing the neutron production. In addition, this would make the technique more flexible in terms of realisation of minibeam patterns/geometry.

As aforementioned, a magnetic collimation for pMBRT could be made by modifying the sets of quadrupole magnets of an existing PBS system. The PBS systems in use today in proton beamlines allow to scan a narrow pencil beam (7 mm–1 cm) over the treatment field by magnetically deflecting it by means of dipole magnets (see section 1.3.2.2). Before scanning, a pair of quadrupoles allows to adjust the width of the beam spot at isocentre. Figure 3.19 gives an example of this type of equipment for PBS purposes. Modifying either the magnetic field of the quadrupoles, their number, the distance between the magnets, or by including other elements such as sextupoles, might allow a magnetic collimation of the sub-millimetric beams needed for pMBRT.

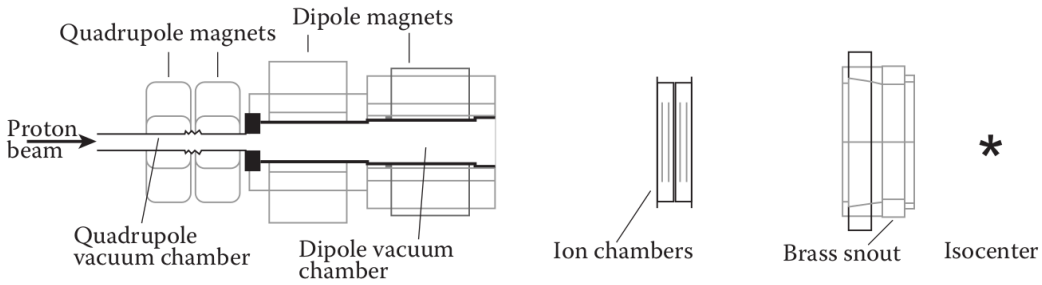

Figure 3.19: *Schematic view of an equipment used to deflect the beam in PBS mode. Taken from the work of Paganetti [Paganetti 2012].*

The operating of a quadrupole magnet is presented in figure 3.20. The left picture shows an example of quadrupole magnet made of four bar-magnets arranged in a manner to produce four poles. In practice, the quadrupoles used for the transport of beams are made of electromagnets (electromagnetic coils). On the right, the figure also shows the field lines produced by this quadrupole. The red arrows show the direction of the magnetic field while the blue arrows indicate the direction of the Lorentz force on a positive particle (proton) going into the page plane. The field lines all cancel each other out at the centre of the quadrupole. It means that

a particle beam would feel no force passing through the centre of the quadrupole. The further from the centre of the quadrupole, the stronger the field gets. Particle beams which are further off axis will thus get focused more strongly.

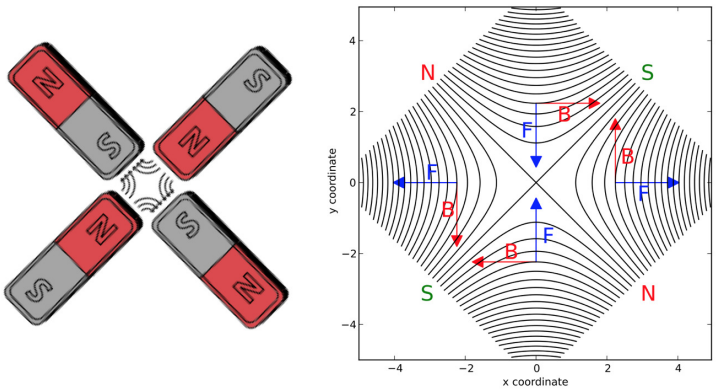

Figure 3.20: *Left: four bar-magnets arranged to form a quadrupole magnet. Right: magnetic field lines of an idealised quadrupole field in the plane transverse to the nominal beam direction.*

It can be seen that, while the particle beam is being focused in the vertical direction (forces directed towards the quadrupole's centre), it is simultaneously being defocused in the horizontal direction (forces directed towards outside of the quadrupole). Indeed, quadrupoles focus in one plane while defocusing in the other. The combination of two types of quadrupoles, one as shown in figure 3.20, and the other one rotated through 90 degrees, in order to focus the beam in the horizontal plane and defocus it in the vertical one, can lead to a focalisation in both planes. To do so, the two quadrupoles have to be correctly arranged, in terms of distance between them, and intensity of the magnetic field (B).

In this section, a MC dosimetric study was carried out in a water phantom to explore the potential dosimetric advantages of a magnetic collimation. A rectangular minibeam of the desired dimension was assumed to be created at the focusing point of a set a quadrupole magnets, as aforedescribed. The simplified source employed in those calculations (see section 2.2.4.1) does not take into account the interactions of the beam with all the shaping elements of the beamline, that could create some scattered radiations, contaminating the dose distributions. However, this study constitutes a first exploration that triggered an in-depth evaluation on how to modify an existing PBS system to allow the generation of sub-millimetric beams. This study was performed in collaboration with ICPO by Tim Schneider and is under patent protection.

In the first section, simulations of magnetically generated minibeams have been performed and the results will be compared to those of the experimental study. In a second section, the influence of several irradiation parameters on the dose distributions will be studied and PVDR values will be assessed for several configurations. Finally, recommendations for a further implementation of pMBRT using a magnetic generation of the minibeams will be discussed in the last section of this chapter.

3.3.1 Comparison of mechanical and magnetic collimations

In order to do a first comparison, arrays of minibeams have been simulated considering the same configuration as the experimental evaluation of pMBRT *i.e.* an air gap (AG) of 7 cm between the minibeams creation and the phantom surface was considered. The beam energy distribution was chosen to be as close as possible from the Y1 characteristics for pMBRT implementation. It followed a Gaussian shape, centred at 100 MeV with a standard deviation of 2.5 MeV. The angular distribution was defined as a Gaussian with 5 mrad standard deviation.

Figure 3.21 shows the depth dose distributions obtained in water in both peak and valley regions with a magnetic collimation (MC) and with a mechanical collimation (experimental data). In general, the peak curves follow similar trends than the experimental curves in water. However, the Bragg peak reduction with 400 μm-beams with respect to 700 μm-ones is less pronounced than with the mechanical method. Concerning the valleys, the dose is significantly higher with the mechanical collimation. This could be explained by a higher contamination of valleys by secondary products created by interactions with the collimator material, as it was already mentioned in section 3.1.

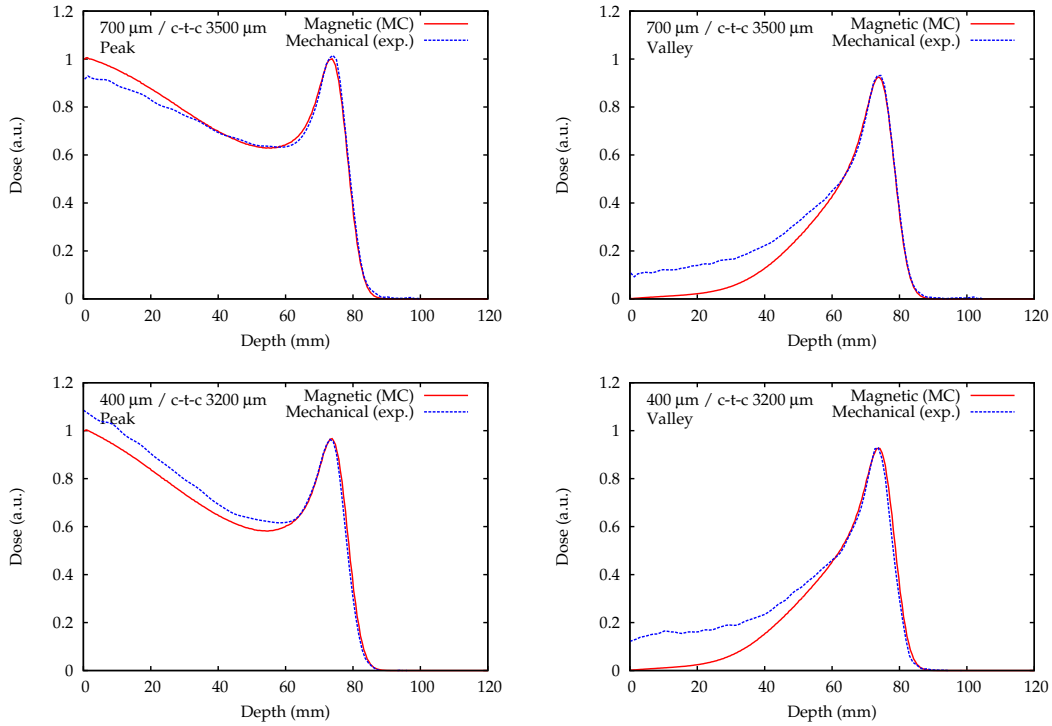

Figure 3.21: *PDD curves in the peak (left) and valley (right) with a 700 µm/c-t-c 3500 µm (top) and 400 µm/c-t-c 3200 µm (bottom) configuration, for both magnetic (MC) and mechanical (experimental) collimations.*

Figure 3.22 depicts FWHM values as a function of depth, calculated considering one single minibeam. For the MC data, the uncertainty bars were smaller than the symbols. It can be seen that FWHM are much larger with the mechanical collimation, especially for the array of 700 μm-minibeams. For instance, with a mechanical collimation, the FWHM amounted to 960 $\pm$ 60 μm and 1230 $\pm$ 70 μm at the phantom surface for the 400 μm and 700 μm arrays, respectively, while they only reached 865 $\pm$ 6 μm and 966 $\pm$ 7 μm with a magnetic collimation. In figure 3.23, the penumbras are presented as a function of depth. In a same way, they are in the same order in both data sets, although being slightly superior with the mechanical data. The smaller FWHM and penumbra with a magnetic collimation could be linked to the reduction of scattered radiations when avoiding the use of a "solid" collimator, but as well to the simplicity of the source employed in the calculations, which does not account for the contamination of scattered radiations along the beamline (before any end-collimator). In addition, the mechanical machinery of the slits has been performed with a precision of about $\pm$ 10% ($\pm$ 70 μm and $\pm$ 40 μm uncertainties on the slit width in for the 700 μm and 400 μm-slits collimators, respectively). This could explain the fact that differences are more important with 700 μm-beams.

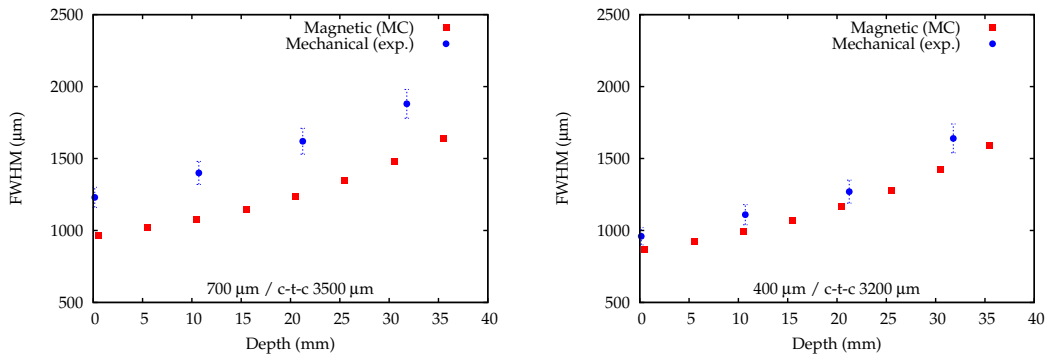

Figure 3.22: *FWHM values as a function of depth for the 700 μm/c-t-c 3500 μm (left) and 400 μm/c-t-c 3200 μm (right) c-t-c configurations. The uncertainty bars for the MC data were smaller than the symbols.*

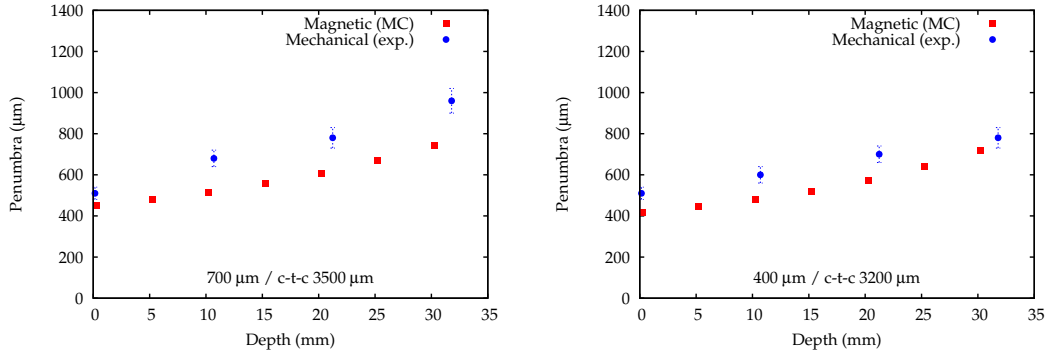

Figure 3.23: *Penumbra values as a function of depth for the 700 μm/c-t-c 3500 μm (left) and 400 μm/c-t-c 3200 μm (right) c-t-c configurations. The uncertainty bars for the MC data were smaller than the symbols.*

Figure 3.24 presents the PVDR values obtained in water. As a consequence of the increased valley doses with a mechanical collimation observed in figure 3.21, PVDR values are much higher in the first centimetres with a magnetic collimation. The values decrease from 1000 at the phantom entrance, to 10 at 4 cm-depth. As previously mentioned, with a mechanical collimation, the beam crosses and interacts with the collimator, therefore increasing the amount of scattered radiations and secondary production. These productions contribute to the off-field areas in the first centimetres of medium, *i.e.* valleys, thus leading to reduced PVDR values. Avoiding the use of any beam shaper for the minibeam generation thus highly improves the PVDR values. With a magnetic collimation, a dose homogenisation is also achieved at the Bragg peak position (74 mm). This collimation method thus has the potential for a better normal tissue sparing thanks considerably lower valley doses in the normal tissues, leading to higher PVDR values. However, as mentioned previously, the efficiency of the pMBRT technique could be enhanced by optimising the irradiation setup. In the next section, the influence of several irradiation parameters on the dose distributions has been assessed.

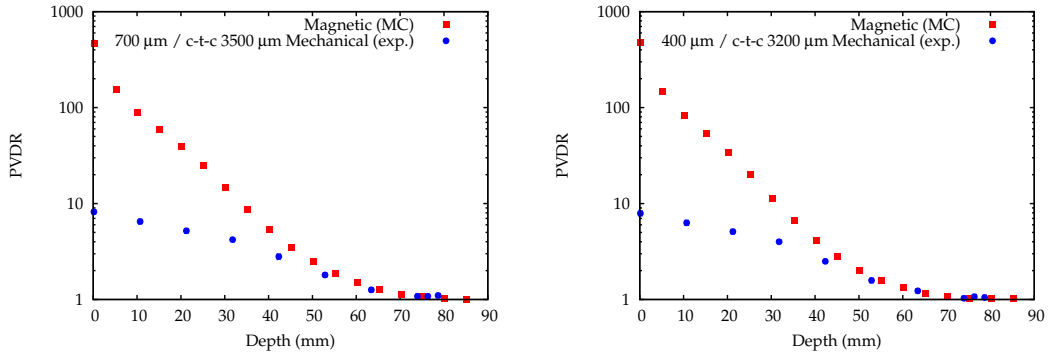

Figure 3.24: *PVDR values as a function of depth for the 700 µm/c-t-c 3500 µm and 400 µm/c-t-c 3200 µm configurations. The uncertainty bars for the MC data were smaller than the symbols.*

3.3.2 Influence of several irradiation parameters on the dose distributions

In order to take full advantage of pMBRT, all irradiation parameters that may have an influence on the dose distributions should be optimised. Considering a magnetic collimation based on a modified PBS system, some characteristics of the beam might not be tuned, as in active beam delivery systems avaible today some parameters are imposed by the accelerator and beam transport system (*e.g.* energy spread, beam divergence). However, the determination of optimised parameters for pMBRT could guide the further conception of novel facilities or hardwares that would be especially designed for pMBRT irradiations. In this section, the influence of several irradiation parameters on the dose distributions has been evaluated. As in the experimental proof of concept (see section 3.2), only simple Bragg peaks (no

SOBP) were considered in this first approach. As reference conditions, the protons' energy was set to 100 MeV (ΔE = 2.5 MeV), the beam divergence was 3 mrad. The minibeams were assumed to be collimated at the phantom surface. The parameters that will be varied along the study will be defined in the related sections.

3.3.2.1 Influence of the beam width

In order to profit from the dose-volume effects, beam sizes as small as possible should be preferred. As discussed in section 3.2, the small beam widths used in pMBRT (sub-millimetric) lead to a significant reduction of the Bragg peak intensity. One consequence is the existence of a lower limit in the minibeam's width suitable for pMBRT. With a mechanical collimation, this limit was reached using the 400 μm/ c-t-c 3200 μm collimator, for which the Bragg peak-to-entrance ratio started to be inferior to 1. In that case, the setup used (PCD of 7 cm) led to a FWHM at the phantom entrance of 960 μm. This limit was explored with a magnetic collimation in this MC study, considering a minibeam collimated at the phantom surface (*i.e.* AG = 0 cm). As shown in figure 3.25 left, all sub-millimetric beam widths result in a significant decrease of the Bragg peak with respect to the entrance dose. However, higher peak-to-entrance ratios are recovered with supra-millimetric beam widths, and a conventional proton PDD curve is even retrieved from 3 mm-wide beams (see figure 3.25 right).

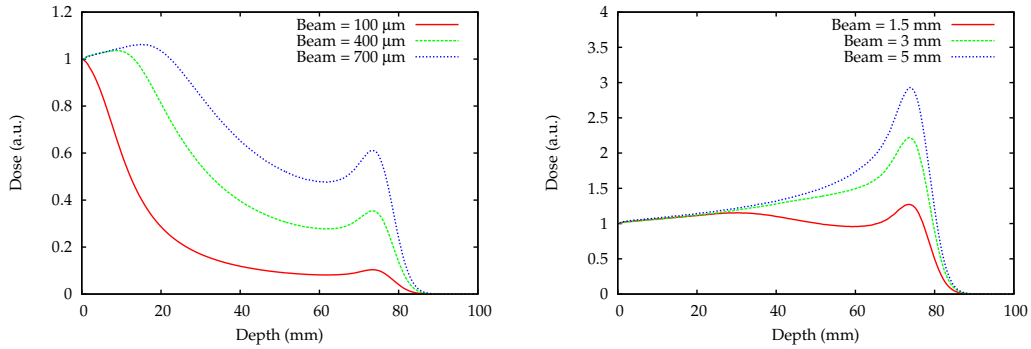

Figure 3.25: *PDD curves related to different sub-millimetric (left) and supra-millimetric beam widths (right). Data are normalised to the entrance dose of each PDD curve.*

As previously mentioned, the Bragg peak reduction is due to the high ratio of scattered protons that "escape" outside of the primary beam due to multiple Coulomb scattering. This behaviour is well illustrated in figure 3.26. With a 700 μm minibeam (left), the multiple Coulomb scattering causes a dramatic lateral spread with respect to the beam dimension (demarcated thanks to the dashed lines). In contrast, with a larger beam of 5 mm-width (right), the ratio of scattered protons at the Bragg peak is low with respect to the beam dimension, and a standard proton PDD curve is maintained (see figure 3.25).

To maintain a higher dose deposition at the end of the proton range (Bragg peak)

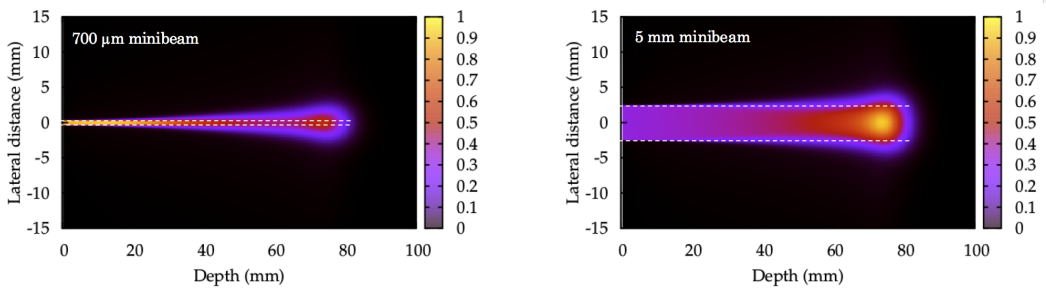

Figure 3.26: *2D distributions in the water phantom obtained by the irradiation with of one single 700 µm (left) and 5 mm-wide minibeam (right). The white lines demarcate the minibeam dimension. For the smallest beam, at the Bragg peak, the ratio of scattered protons due to multiple Coulomb scattering is high with respect to the beam dimension.*

would offer an additional advantage to the pMBRT technique. Therefore, it could be interesting to consider the use of arrays of larger beams for pMBRT. Despite the fact that the dose-volume effect should be less important with supra-millimetric beams, a gain in tissue sparing might be preserved anyway with respect to broad beam irradiations. This is yet to be explored. Exploiting this idea, figure 3.27 compares the 2D dose distributions in water achieved by using arrays of both 700 μm (c-t-c of 3500 μm) and 3 mm beams (c-t-c of 4.2 mm) covering a 2×2 cm^2 target area. A c-t-c of 4.2 mm was selected after few tests in order to obtain a same homogenisation level at the Bragg peak than with the 700 μm-beams pattern. For the 3 mm-beams array, the maximum dose is deposited at the Bragg peak, in contrast to the 700 μm-array for which it occurs at the phantom entrance. In both cases, a spatial fractionation is observed in the proximal normal tissues and at the same time a homogenisation takes place at the Bragg peak (see figure 3.28).

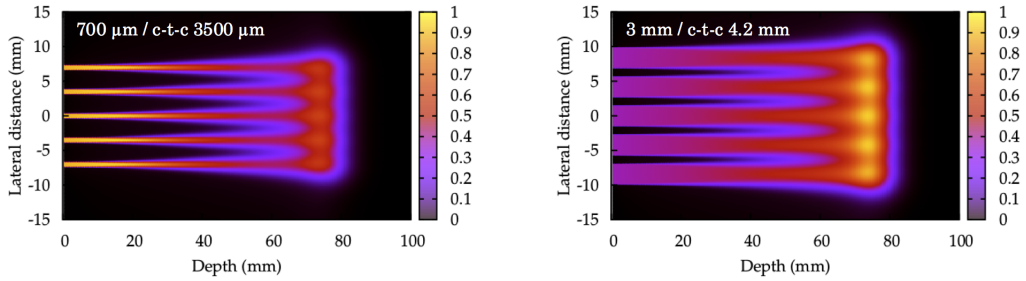

Figure 3.27: *2D distributions in the water phantom obtained by the irradiation with an array of 700 µm (c-t-c 3500 µm) (left) and 3 mm (c-t-c 4.2 mm) minibeams (right). In both cases, an homogenisation is reached at the Bragg peak. However, the maximum dose is delivered at the Bragg peak with the 3 mm-minibeams array.*

Figure 3.29 left presents the PVDR values as a function of depth for both arrays. Same values are obtained in the Bragg peak, but PVDR are much lower in the normal tissues for the 3 mm-array. Especially, PVDR are considerably reduced from 3 cm-depth (around 5), being this reduction a factor 10 with respect to the 700 μm array.

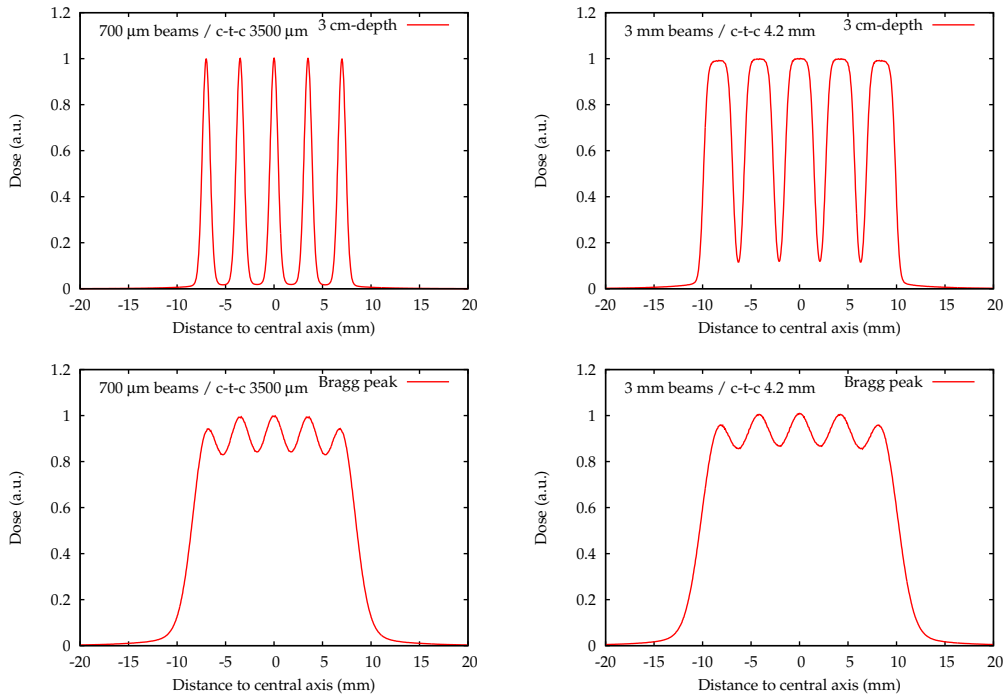

Figure 3.28: *Lateral dose profiles in the water phantom at 3 cm-depth (top) and at the Bragg peak (bottom) obtained with irradiation with arrays of 700 µm/c-t-c 3500 µm (left) and 3 mm/c-t-c 4.2 mm (right).*

An alternative would be to use larger c-t-c distances and several arrays, as it was already performed in x-rays MBRT. For instance, a c-t-c of 9 mm led to PVDR values comparable to the 700 μm array in the first centimetres, and even higher values from 30 mm (see figure 3.29 right). In order to create a homogeneous dose distribution at the target, three interlacing arrays should be used.

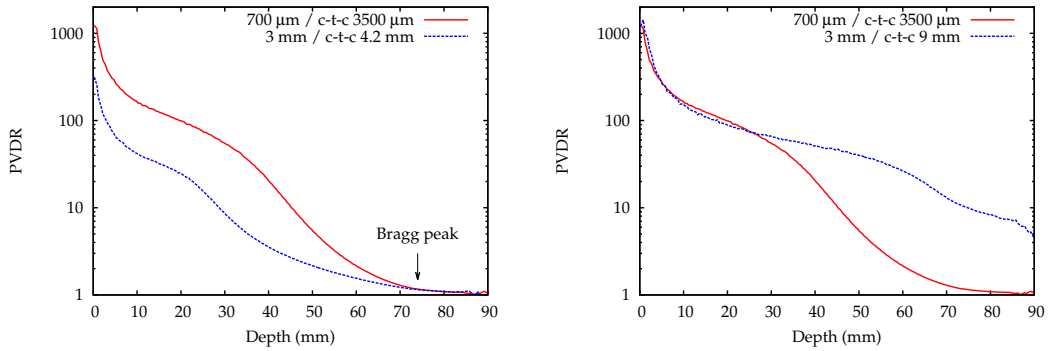

Figure 3.29: *PVDR values as a function of depth for several configurations. Left: to achieve a same homogenisation at the Bragg peak, low PVDR values are found with the 3 mm-beams array. Right: with a larger c-t-c, comparable PVDR values are observed in the proximal normal tissues, while the homogenisation is lost at the Bragg peak.*

Biological studies have to be performed to assess if a dose-volume effect would be maintained with such larger beams before further exploration of this strategy. A first hint was already observed during the rats experiments described in section 3.2.5. Indeed, the experimental setup with the 400 μm-slits/c-t-c 3200 μm collimator provided beams widths comprised between 1 and 1.2 mm within the rats' head. Even with these wider beams, a significant gain in tissue sparing was observed with respect to broad beam irradiations, as explained in section 3.2.5.

3.3.2.2 Influence of the air gap

In this case, one single minibeam (700 μm $\times$ 2 cm) with a 3 mrad angular divergence was simulated at several distances from the phantom surface. Figure 3.30 left depicts the corresponding lateral dose profiles at the phantom surface. When the AG was enlarged, the FWHM was increased due to scattering in air and beam divergence (see table 3.3). As a consequence, a lower Bragg peak reduction was observed as shown in figure 3.30 right. The conventional proton PDD curve starts to be recovered from a FWHM of about 1.5 mm at the phantom entrance, as it was previously observed in section 3.3.2.1. Changes in the PDD curve shape are not significant for the small distances usually employed in therapy (from 2 to 5 cm).

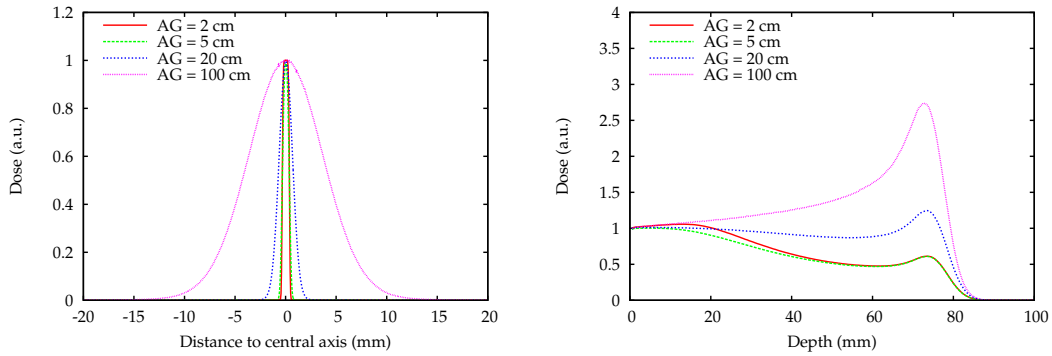

Figure 3.30: *Lateral dose profiles (left) and PDD curves (right) obtained with one single minibeam (700 μm $\times$ 2 cm) related to different AG. Data are normalised to the entrance dose of each curve.*

AG	FWHM at phantom entrance (μm)
2 cm	710 $\pm$ 5
5 cm	710 $\pm$ 5
20 cm	1550 $\pm$ 11
100 cm	8700 $\pm$ 60

Table 3.3: *FWHM at the phantom entrance obtained with a 700 μm $\times$ 2 cm minibeam collimated at different distances from the phantom.*

The AG between the minibeam birth and the phantom/patient surface thus has to be minimised to maintain low FWHM and benefit at maximum from the dose-

volume effect. In addition, this study also emphasises possible changes in the PDD shape when the distance varies. A precise control of this parameter will thus be needed in a future implementation of a magnetic collimation for pMBRT.

3.3.2.3 Influence of the beam divergence

Realistic beam divergences, from 1 to 7 mrad, were considered here, with no AG between the minibeams and the phantom entrance. As depicted in figure 3.31, in all cases, a build up in the dose deposition was observed in the first two centimetres, then a fall off of the dose occurred until the Bragg peak. The build up, that was not observed in the experimental study (see figure 3.7), is due to the high ratio of primary protons remaining concentrated in the peak in the first centimetres. Those primary protons create secondary electrons that are forward directed and deposit their energy straight in the minibeam path. This phenomenon is observed even for large beam divergences thanks to the proximity of the source, that overcomes the impact of the angular spread at this point.

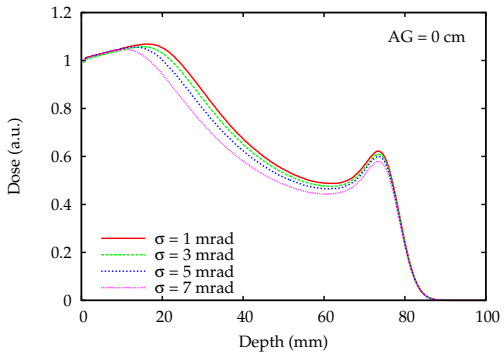

Figure 3.31: *PDD curves obtained with one single minibeam (700 µm × 2 cm) with several angular divergences considering no AG. Data are normalised to the entrance dose of each curve.*

When the divergence increases, the decreasing of dose starts at shallower points. For instance, the fall off occurs at 11 mm for a divergence of 7 mrad, and at 17 mm with 1 mrad. This is explained by the higher proportion of forward directed protons with the smallest divergence, which thus stay in the minibeam path at deeper points. In addition, the Bragg peak-to-entrance dose ratio slightly decreased when the divergence was enlarged. A variation lower than 1% was observed between 1 and 7 mrad. Figure 3.32 shows no great differences in lateral spread at the Bragg peak between 1 and 7 mrad.

In addition, figure 3.33 depicts the lateral dose profiles at the phantom surface (left) and at 3 cm in depth considering different divergences. The entrance dose in the central peak was taken as a normalisation point in all cases. At the surface, only small differences appear. At 3 cm-depth, the higher the divergence is, the larger the dose profile, as expected, but the influence of the divergence remains low. Indeed,

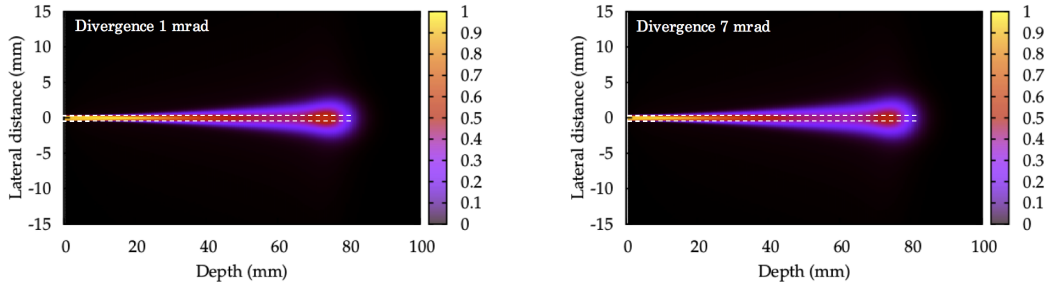

Figure 3.32: *2D distributions in the water phantom obtained by the irradiation with of one single 700 μm-beam with an angular divergence of 1 mrad (left) and 7 mrad (right). The source was located at the phantom entrance. The white lines demarcate the minibeam dimension.*

in that case where the AG was minimised, the small divergences considered here are negligible with respect to the multiple Coulomb scattering and do not highly impact the dose distribution. In consequence, considering an array of minibeams (700 μm/c-t-c 3500 μm) to cover a 2×2 cm^2 area, PVDR values were quite similar in both entrance and Bragg peak regions when the divergence was increased (see figure 3.34). Between 30 and 60 mm depth, a very small reduction in PVDR values was observed when the divergence increases.

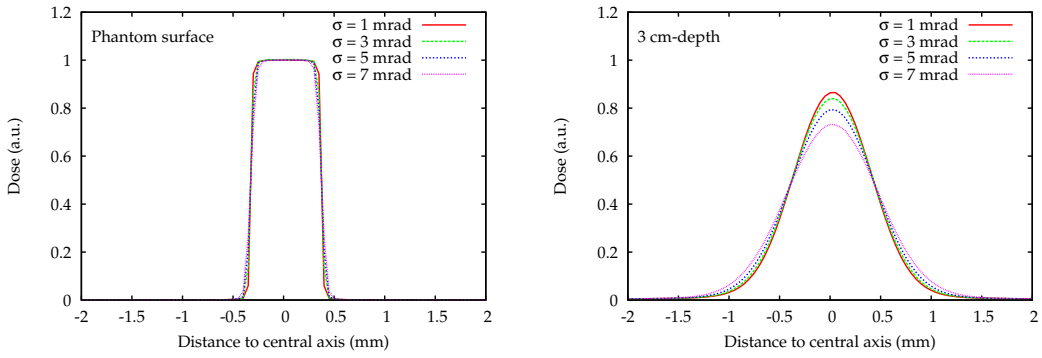

Figure 3.33: *Lateral dose profiles at the phantom surface (left) and at a depth in water of 3 cm (right) considering several beam divergences with the minibeams collimated at the phantom surface. The data are normalised with respect to the entrance dose.*

However, the collimation system will likely impose a nozzle-to-phantom distance (*i.e.* an AG) of several centimetres. Considering now an AG of 7 cm, the dose profiles are very different depending on the divergence, as shown in figure 3.35. Indeed, as the beam travels several centimetres in air before reaching the phantom surface, the divergence has more impact here, and the beam arrives at the phantom entrance with a larger dimension when a large divergence is considered. As a consequence, at 3 cm in depth (right figure), the profiles are also more largely widened.

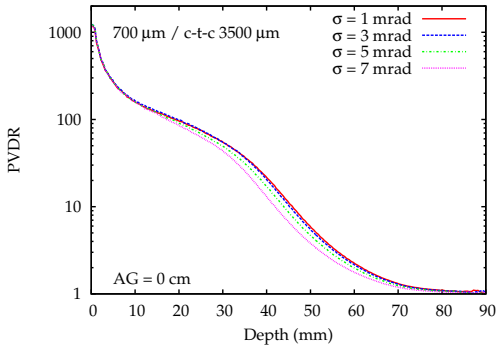

Figure 3.34: *PVDR values as a function of depth for an array of minibeams (700 µm / c-t-c 3500 µm) generated at the phantom surface, and several beam divergences.*

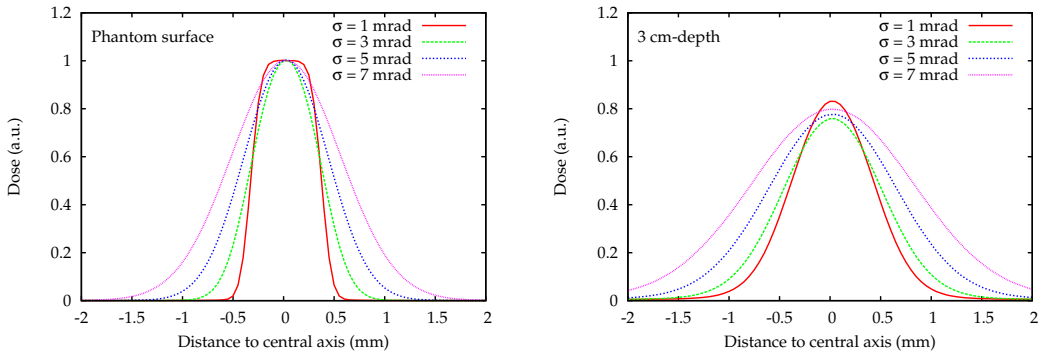

Figure 3.35: *Lateral dose profiles at the phantom surface (left) and at a depth in water of 3 cm (right) for 700 µm beams considering several beam divergences. An AG of 7 cm was assumed. The data are normalised with respect to the entrance dose.*

The corresponding PDD curves are shown in figure 3.36. The curves highly differ from one another due to the impact of the divergence. Apart from the 1 mrad case, the dose build up in the first centimetres vanished for larger beam divergences. In accordance with what was observed in the previous sections, the Bragg peak-to-entrance ratio is increased when the divergence increases.

Figure 3.37 shows high differences in PVDR values. The higher the divergence, the lower the PVDR, especially at shallow depths. Indeed, larger divergences lead to higher ratio of protons being scattered "outside" of the primary beam, feeding the valleys. In conclusion, if the AG between the minibeams and the phantom entrance is minimised, the impact of the divergence of the dose distribution will be low. However, if technical properties impose the presence of an important AG, low beam divergences have to be favoured.

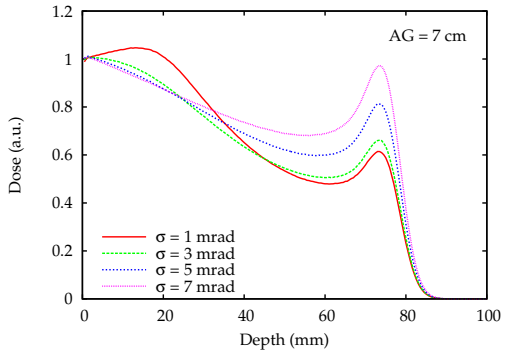

Figure 3.36: *PDD curves obtained with one single minibeam (700 µm × 2 cm) with several angular divergences at 7 cm from the phantom surface. Data are normalised to the entrance dose of each curve.*

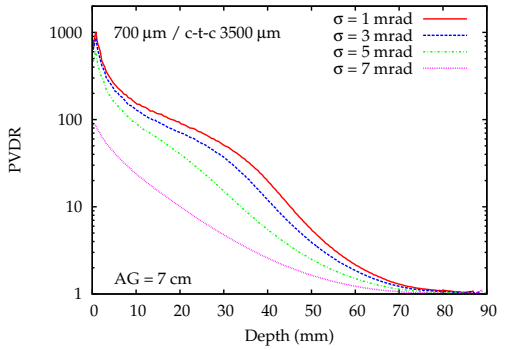

Figure 3.37: *PVDR values as a function of depth for an array of minibeams (700 µm / c-t-c 3500 µm) and several beam divergences. An AG of 7 cm was considered.*

3.3.2.4 Influence of the energy distribution

The influence of the energy distribution has been studied in this section. First, the mean proton energy was varied considering a fixed energy spread of 2.5 MeV in each case. As shown in figure 3.38, as the beam energy decreases, the width of the Bragg peak diminishes because straggling is nearly a constant fraction of the range [Paganetti 2012], and the peak-to-entrance ratio is lowered. This phenomenon is well known in conventional proton therapy, however it is more pronounced with sub-millimetric field sizes, and results here in dramatical changes in the PDD curves. The energy considered for the experimental proof of concept (100 MeV) was chosen to correspond to a Bragg peak position at the centre of the human brain. As shown here, higher energies led to an increased reduction of the Bragg peak intensity due to fluence reduction.

In addition, minibeams of lower mean energy suffer from a more rapid widening, as shown in figure 3.39. However, the FWHM is relatively lower at the Bragg peak (indicated by black arrows on the figure) for the lowest beam energy. This will have

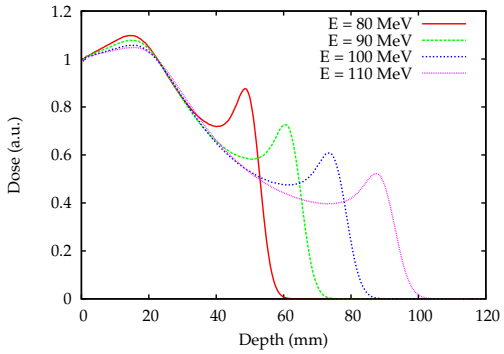

Figure 3.38: *PDD curves obtained with one single minibeam (700 μm $\times$ 2 cm) with several mean proton energy, considering fixed energy spread of 2.5 MeV.*

an impact on the dose distribution when an array of minibeams is used, as shown hereafter. Figure 3.40 depicts the 2D distribution of arrays of 700 μm minibeams with a c-t-c of 3500 μm for both 80 MeV (left) and 110 MeV protons (right). While a quasi-homogeneous dose is delivered at the Bragg peak with 110 MeV protons (90 mm-depth), separation between the minibeams is still visible at the Bragg peak of the 80 MeV-array (50 mm-depth). The lateral dose profiles obtained at the Bragg peak are also shown in figure 3.41.

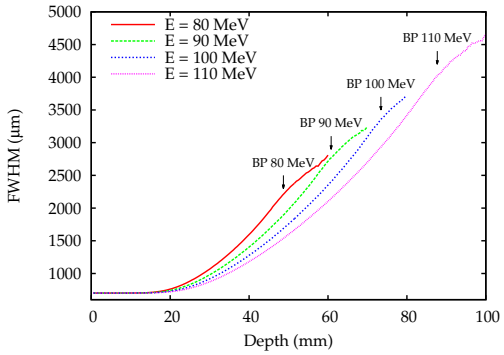

Figure 3.39: *FWHM values obtained one single 700 μm-wide minibeam of different mean energies. The black arrows indicate the Bragg peak (BP) for each energy considered.*

In addition, the PVDR values for the four energies tested are reported in figure 3.42 left. The values are similar at the phantom entrance for all energies, than a steeper fall off is observed with lower beam energies. However, the PVDR at the Bragg peak remain higher for low energies, resulting from a lesser homogenisation. In that case, the use of smaller c-t-c should be considered. For example, smaller c-t-c distances have been explored for the 80 MeV-array (see figure 3.42 right). PVDR of 1.092 $\pm$ 0.004 and 1.519 $\pm$ 0.006 were found at the Bragg peak location with a c-t-c of 2100 and 2800 μm, respectively, in contrast to 2.52 $\pm$ 0.01 with 3500 μm.

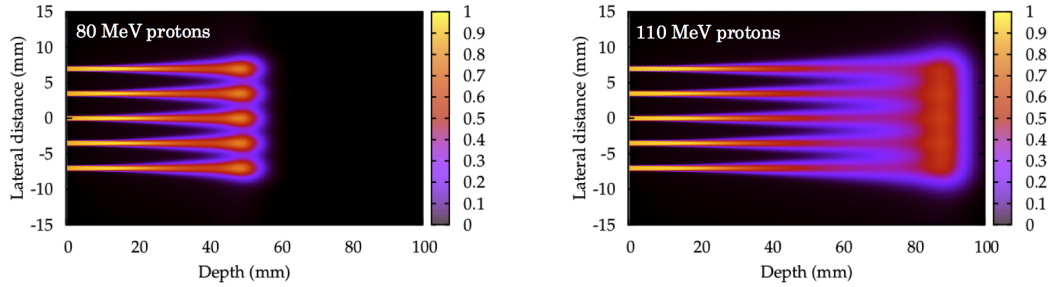

Figure 3.40: *2D distributions in the water phantom obtained by the irradiation with an array of 700 µm minibeams (c-t-c 3500 µm) with a mean proton energy of 80 MeV (left) and 110 MeV (right).*

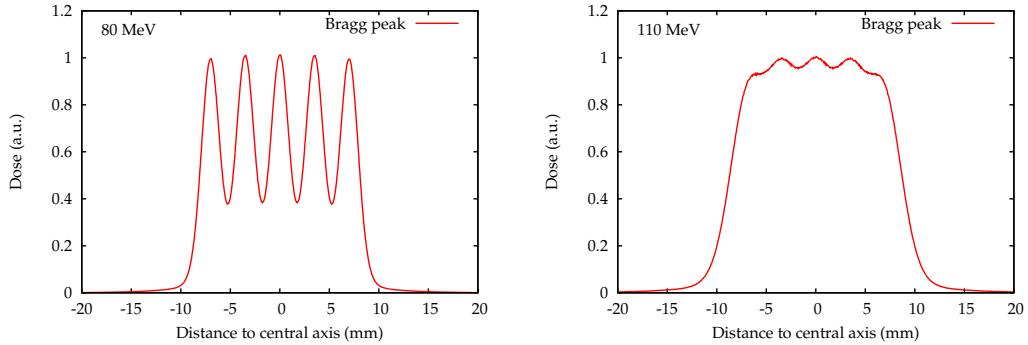

Figure 3.41: *Lateral dose profiles at the Bragg peak location obtained with the 80 MeV (left) and 110 MeV-proton (right) arrays of 700 µm minibeams (c-t-c 3500 µm).*

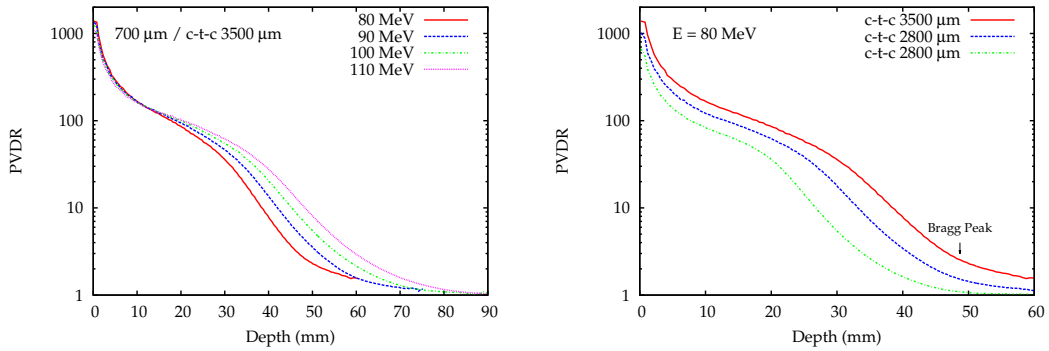

Figure 3.42: *Left: PVDR values as a function of depth for the 700 µm/c-t-c 3500 µm configuration with several mean proton energies. Right: PVDR values as a function of depth for 80 MeV proton minibeams with several c-t-c distances.*

The energy spread parameter (ΔE) also impacts the Bragg peak width as well as the Bragg peak-to-surface ratio, as shown in figure 3.43 left. The higher ΔE is, the larger the Bragg peak width, and the lower the Bragg peak-to-surface ratio. However, despite significant changes in the PDD curve, PVDR values are similar with all energy spread values tested, as shown in figure 3.43 right. As far as possible,

low energy spread have to be favoured in order to preserve a high Bragg peak.

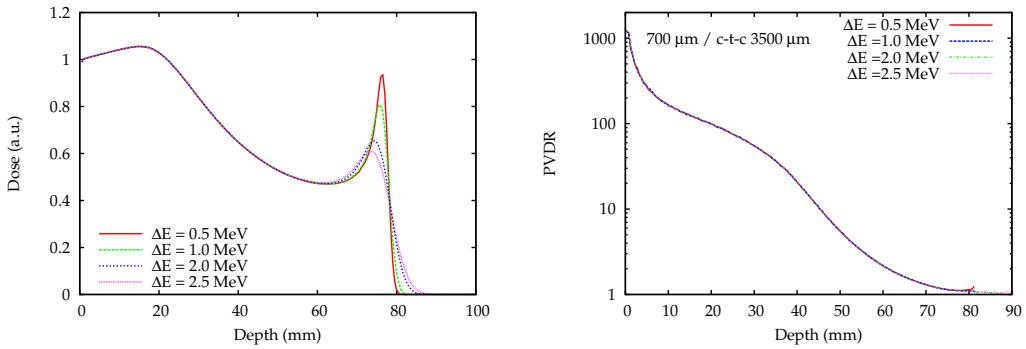

Figure 3.43: *Left: PDD curves obtained with one single minibeam (700 µm × 2 cm) with several energy spread with a fixed mean proton energy of 100 MeV. Right: PVDR values as a function of depth considering an array of 700 µm-minibeams with a c-t-c of 3500 µm.*

3.3.2.5 Influence of the irradiation field size (covered area)

In this section, the influence of the irradiation field size (number of minibeams) will be adressed. Two field sizes, 2×2 cm^2 and 5×5 cm^2 are compared, using beams of 700 µm and 3 mm. In this case, the dose scoring was performed in a 10 cm-wide box (instead of 4 cm for 2×2 cm^2) in order to take into account the contribution of the lateral tails until the most peripheral minibeams when the superposition is made (see section 2.2.4.1).

Figure 3.44 compares the PVDR values obtained with a 2×2 cm^2 and a 5×5 cm^2 irradiation field is covered by a same pattern of minibeams (same beam width and c-t-c distance). Interestingly, PVDR values are similar for the two irradiation field sizes. This differs from what is observed in x-rays MBRT, where a reduction of PVDR values was reported when the field size (number of beams) increased [Prezado 2009b]. The main difference comes from the composition of valleys. As shown in section 3.1, in pMBRT the valleys are mainly composed of secondary protons (shallow depths) and primary protons (further depths, therefore reduced speed). In contrast, in x-rays MBRT electrons and gammas are the dominant contributions. These latter have larger ranges and contribute further to the dose in the lateral direction (lateral tails). With proton minibeams, the lateral tails of one single minibeam are restricted to a very close area.

Indeed, as illustrated in figure 3.45 where an array created by the superposition of several individual minibeams is represented in grey, one individual minibeam only contributes to the dose of its closest neighbour. The peak indicated with the black arrow is mainly fed by the red minibeam, and also by the lateral tails of the green and blue minibeams, while the purple one does not significantly contribute to the designed peak. This is thus why same PVDR values are obtained with both field sizes. A larger area could be covered with a pMBRT array with the same efficiency, being an important advantage with respect to x-rays MBRT.

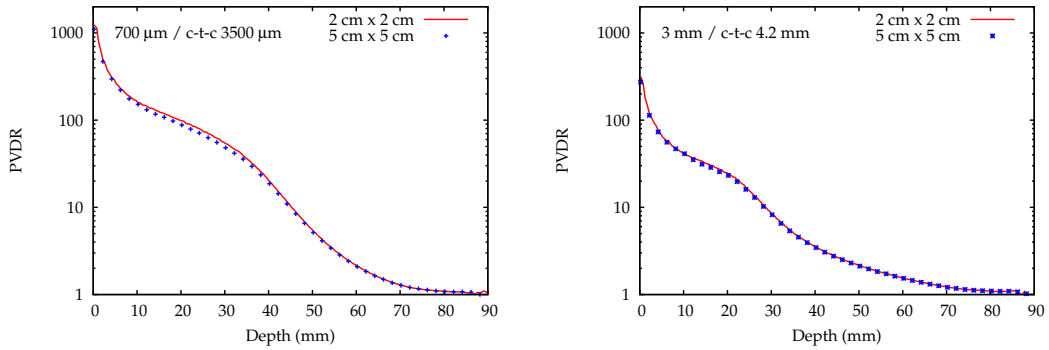

Figure 3.44: *Comparison of PVDR values in water as a function of depth considering an array of 700 µm-minibeams with a c-t-c of 3500 µm (left) and 3 mm-minibeams with a 4.2 mm c-t-c necessary to cover 2×2 cm² and 5×5 cm² areas.*

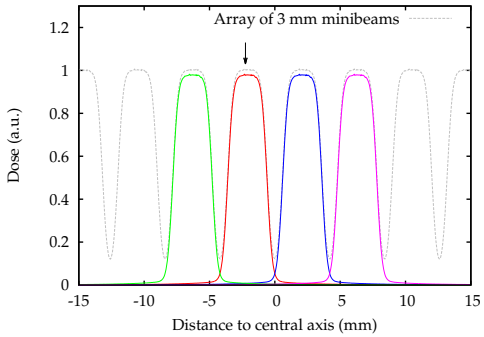

Figure 3.45: *An array of minibeams (grey) is made from the superposition of several individual minibeams. The peak indicated with the black arrow is mainly fed by the red minibeam, and also by the lateral tails of the green and blue minibeams. The purple one does not significantly contribute to the designed peak.*

3.3.3 Summary and discussion

The first experimental evaluation of pMBRT has been recently performed using a mechanical collimation. Although this study has demonstrated promising results, the potential of the pMBRT technique could be enhanced by shaping the beams using a magnetic collimation. The possible advantages of this method over the mechanical collimation include (i) an increase of the dose-rate, (ii) a lower neutron yields thanks to elimination of the metallic collimator, (iii) a reduction of the scattered radiations feeding the valleys (allowing higher PVDR values to be reached), (iv) a more flexible application of pMBRT, without the need for producing and optimising patient individualised collimators.

By comparing arrays of minibeams magnetically simulated in the same configuration as the experimental evaluation of pMBRT (*i.e.* same distance between the minibeams birth and the phantom entrance), this study emphasised the high valley

contamination by scattered radiations when a mechanical collimation was used, resulting in a significant decrease in PVDR values in the first centimetres of water. The use of a magnetic collimation has thus the potential to offer higher PVDR values in the normal tissues. This has to be confirmed by experimental measurements when such a collimation method will be available.

In addition, the impact of different irradiation parameters on the dose distributions were investigated in order to guide the forthcoming setup optimisations for pMBRT. The results obtained in this study are summarised in table 3.4.

Influence of several irradiation parameters				
	FWHM	Bragg peak-to-entrance ratio	PVDR in NT	Hom. at the target
↗ beam width	↗	↗	↘ for same hom. in target	↘ for same PVDR in NT
↗ AG	↗	↗	↘	↗
↗ mean energy	↘ in depth	↘	↗	↗
↗ energy spread	≃	↘ dramatically	≃	≃
↗ angular divergence	↗	↗	↘	≃
↗ irradiation field	≃	≃	≃	≃

Table 3.4: *Summary of the influence of irradiation parameters on the dose distributions. "NT" and "hom." respectively stand for "normal tissues" and "homogenisation".*

The best irradiation configuration for pMBRT would be the one offering the narrowest FWHM in normal tissues (favouring the dose-volume effect), the highest peak-to-entrance ratio, the highest PVDR values in normal tissues and the highest degree of homogenisation at the target. This study showed that the reduction of the AG, low beam divergence and low energy spread favoured small beam FWHM at the phantom entrance. However, to maintain a higher dose deposition at the end of the proton range (Bragg peak) larger beams would offer an additional advantage to the pMBRT technique. The use of larger beams (3 mm) to create a pMBRT array has been investigated in this theoretical study since they are more advantageous in terms of Bragg peak-to-entrance ratio. Although the dose-volume effect would be less important with such beams than with sub-millimetric beams, a gain in tissue sparing might be preserved anyway. The results obtained in this work showed that it should be possible to maintain a spatial fractionation of the dose in the normal tissues. Although, only biological studies could demonstrate the preservation of a sparing effect with larger beams.

In summary, the best compromise would be the use of minibeams collimated as close as possible from the patient, with a dimension, energy spread and beam divergence allowing a reasonable Bragg peak-to-entrance dose ratio (factor around 1) to ensure a high energy deposition at the target.

As previously mentioned, a magnetic collimation for pMBRT could be based on a modification of an existing PBS system [Schneider 2016]. A first evaluation performed at ICPO by Tim Schneider and Annalisa Patriarca (in collaboration with our team) showed that the beamline in the present PBS configuration does not allow to provide sub-millimetric beams. To get sub-millimetric fields some modifications of the nozzle need to be done. For patent protection, no further details can be provided.

Chapter 4

A potential renewed use of very heavy ions for therapy

Contents

4.1 Evaluation of physical dose distributions 112
4.1.1 Depth dose distributions 112
4.1.2 Estimation of the $NTD_{2.0}$ 116
4.1.3 Lateral dose profiles 118
4.2 Evaluation of secondary particles distributions 122
4.2.1 Spatial distribution of secondary species 123
4.2.2 Type of nuclear fragments and their yield 129
4.3 Summary and discussion 133

As explained in *Chapter 1*, despite major improvements in RT in the last decades, the treatment of hypoxic tumours still remains one of the major challenges in RT. In this context, the use of very heavy ions for therapy (*e.g.* Ne, Si, Ar), which are less dependent on the oxygen effect than x-rays, was explored in the past (BEVALAC facility, USA). Between 1975 and 1992, 433 patients were treated with C, N, O, Ne, Si and Ar ions [Castro 1995, Jermann 2015] for various malignancies. Very heavy ions showed encouraging results in terms of local control of hypoxic tumours, in particular for the treatment of macroscopic salivary gland carcinomas, paranasal sinus tumours, soft tissue sarcomas, macroscopic sarcomas of bone, locally advanced prostate carcinomas and biliary tract carcinomas [Linstadt 1991]. Unfortunately, their RBE is also very high in the normal tissue in front of the tumour causing serious late damage, including fatal complications [Castro 1994]. For that reason, the use of such particles for therapy was rapidly stopped, a few years after their first use. The work presented in this chapter aims to explore a new RT approach that might trigger a renewed use of such very heavy ions in therapy, by profiting from the well-established normal tissue sparing of MBRT. Four ions have been selected: Ne, Si, Ar and Fe. Table 4.1 presents the beam facilities in which these types of heavy ions were or are available.

Since the biological response to such kind of irradiation is expected to highly differ from the one of conventional (broad beam) charged particle therapy, the established RBE values are likely not to be valid. As a first stage, the main goal of this work was to establish the proof of concept of this new avenue with unknown

Overview of heavy ion beam facilities producing very heavy ions				
Type of heavy ion	Z	Facilities	Use	Operating period
Ne	10	BEVALAC, Berkeley, USA	Clinical	1975 - 1992
		HIMAC, Chiba, Japan	Research	Since 2008
Si	14	BEVALAC, Berkeley, USA	Clinical	1975 - 1992
		HIMAC, Chiba, Japan	Research	Since 2008
Ar	18	BEVALAC, Berkeley, USA	Clinical	1975 - 1992
		HIMAC, Chiba, Japan	Research	Since 2008
Fe	26	HIMAC, Chiba, Japan	Research	Since 2008

Table 4.1: *Overview of the heavy ion beam facilities that produce or have produced the ions investigated in this study.*

radiobiological consequences from a physics point of view. A good understanding of the dosimetric properties in such irradiations would allow evaluating the interest of a further exploration. In addition, this dosimetric knowledge is needed in order to guide the biological experiments and observations. Within this context, an in-depth dosimetric MC study was performed.

In the first part of this chapter, the computed dose distributions will be presented. Secondly, an in-depth assessment of the role of secondary particles contamination of the valley doses, which is one of the most critical aspects in MBRT, will be reported. Finally, a summary of the main dosimetric properties highlighted in this work will then be addressed in a third section, and the results discussed.

4.1 Evaluation of physical dose distributions

In this section, dose distributions (PDD and lateral dose profiles) for the different considered ions and c-t-c explored will be presented. In addition, relevant dosimetric parameters such as beam width, beam penumbra and PVDR values will be reported.

4.1.1 Depth dose distributions

Despite the use of sub-millimetric field sizes, the reduced Coulomb scattering for heavy ions permits to maintain a standard Bragg peak shape since a large proportion of the primary beam is kept in the peak region, in contrast to pMBRT [Prezado 2013]. One example is given in figure 4.1 left for one single mono-energetic argon minibeam (700 μm $\times$ 2 cm) impinging in a water phantom. In this study, a 2 cm-long SOBP centered at 7 cm, was considered for each ion. Figure 4.1 right shows the SOBP curve (between 60 and 80 mm) obtained with one single minibeam of argon, observing a flatness criterion of $\pm$2.5%. As already explained, this study has been restricted to physics, and the SOBP have been generated in terms of physical dose. The curves for the other ions follow a similar trend.

As an example, figure 4.2 shows the 2D spatial distribution in the water phantom for one single minibeam with both neon and iron ions. For both ions, the beam progressively widens as a function of depth, and a more important lateral spread is observed at the end of their range. This is due to elastic collisions with atomic

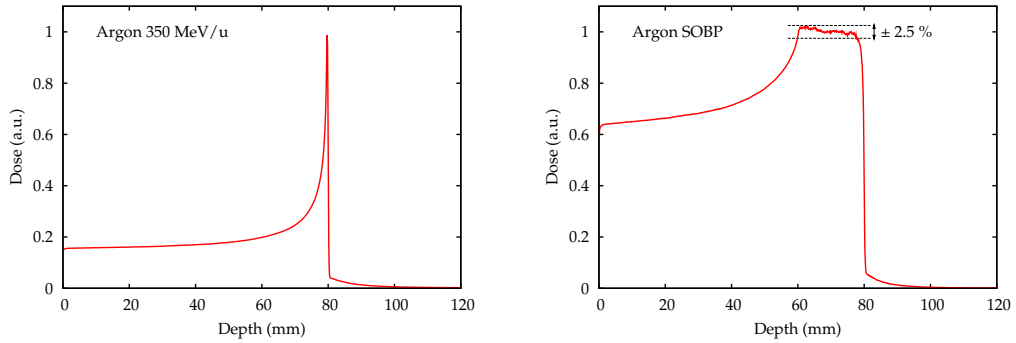

Figure 4.1: *PDD of one single mono-energetic (351 MeV/u) (left) and SOBP (right) argon minibeam in the water phantom. The SOBP flatness meets the ±2.5% criterion.*

nuclei, as explained in *Chapter 1*. This phenomenon is more pronounced with a neon beam due to the $1/\sqrt{Z}$ dependency of the lateral spread. However, the beam enlargement observed with such very heavy ion beams is very low compared to those with lighter ions like protons (see *Chapter 3*).

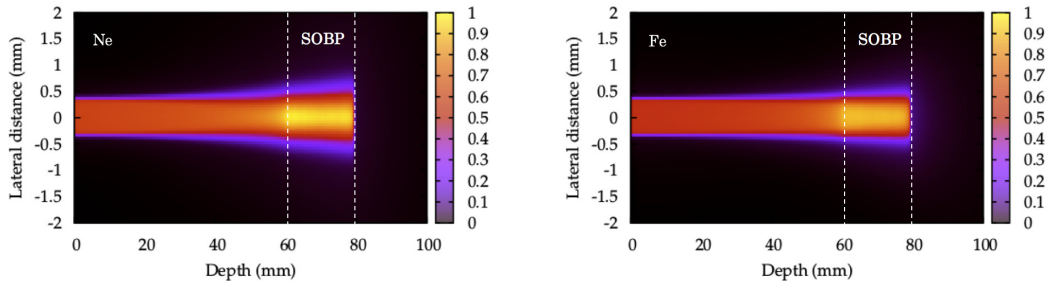

Figure 4.2: *2D distributions in the water phantom obtained after irradiation with one single minibeam of neon Z=10 (left) and iron Z=26 (right). The lateral spread due to elastic Coulomb scattering in the SOBP is much more reduced with a higher Z-particle.*

Figure 4.3 shows the 2D dose distribution obtained with an array of neon minibeams spaced with c-t-c distances of 1400 μm (left) and 3500 μm (right) in the water phantom. One part of the dose contribute to the valley regions, the contribution being higher for smaller c-t-c distances.

Figure 4.4 depicts the depth dose curves obtained in both peak and valley regions for all ions. Only the two extreme c-t-c are shown. The peak depth dose distribution does not significantly vary with c-t-c and ion type. In contrast, the valley's PDD highly differ. The valley dose behaviour as a function of depth for the different ions considered is reported in figure 4.5. It is expressed as a percentage of the SOBP maximum dose. Exact values are reported in table 4.2. The valley dose increases as a function of depth until the distal part of the SOBP. This is because the valleys are

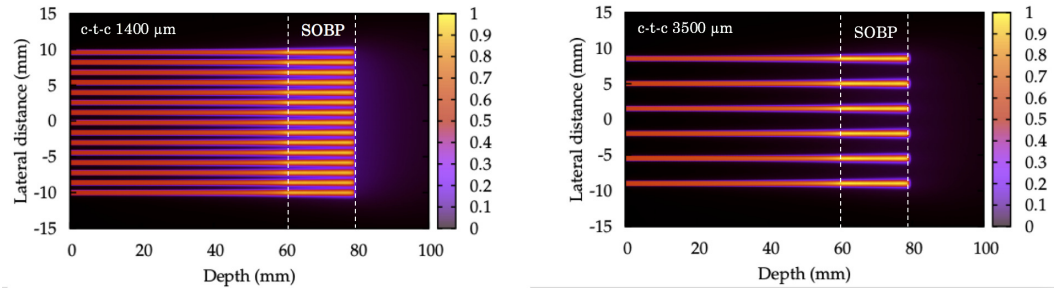

Figure 4.3: *2D dose distribution obtained with an array of neon minibeams (700 µm) spaced with a 1400 µm (left) and 3500 µm c-t-c distance (right). Due to the lateral spread of the minibeams, one part of the dose feeds the spaces between the minibeams, i.e. the valleys.*

mostly the result of the dose deposited by scattered secondary products. Indeed, as the primary beam traverses the medium, more and more energy is deposited through collisions with atomic electrons, part of which (δ-electrons) will be able to travel to the valleys. In addition, the contribution of fragmentation processes after nucleus-nucleus collisions become more and more important with increasing penetration depth. The produced fragments are mainly forward directed, but their distribution is broader than the lateral spread of the primary ions caused by multiple Coulomb scattering, and, in consequence, they also contribute to valleys. This specific aspect will be more detailed in section 4.2.1.

The valley dose decreases when the c-t-c is enlarged, since a lower proportion of secondary species will have an energy and an angular aperture large enough to reach the centre of the valley region, especially in the case of heavier ion fragments. In addition, in general terms, the heavier the ion is, the lower the valley dose. Also related to secondary products, this is explained by a higher production of forward directed heavy fragments with high-Z projectiles, contributing less to the valleys. The exact shape of these curves can be explained by the participation of secondary products. A detailed explanation will be given in section 4.2.1.

As already mentioned, valley doses are a crucial parameter in spatially fractionated techniques since they are believed to be the main responsible for tissue sparing [Dilmanian 2002]. From a quantitative point of view, the valley dose in this work is maintained to a very low level in normal tissues with respect to the peak (SOBP) dose. In the proximal normal tissues (60 mm-depth), the maximum valley doses are obtained with an array of neon minibeams for a c-t-c distance of 1400 μm, being 12.7% of the prescribed dose (SOBP). The valley dose then drops to 1.6% for a c-t-c of 3500 μm for neon. At the same depth (60 mm), minimum valley doses are obtained with the heaviest ion (iron), being 6.8% and 0.3% of the prescribed dose for a c-t-c of 1400 μm and 3500 μm, respectively.

The nuclear interactions are also the responsible for the fragmentation tail, that extends beyond the SOBP (see figure 4.6). As explained in *Chapter 1*, the light fragments emitted by the fragmenting projectiles travel with a velocity close to the

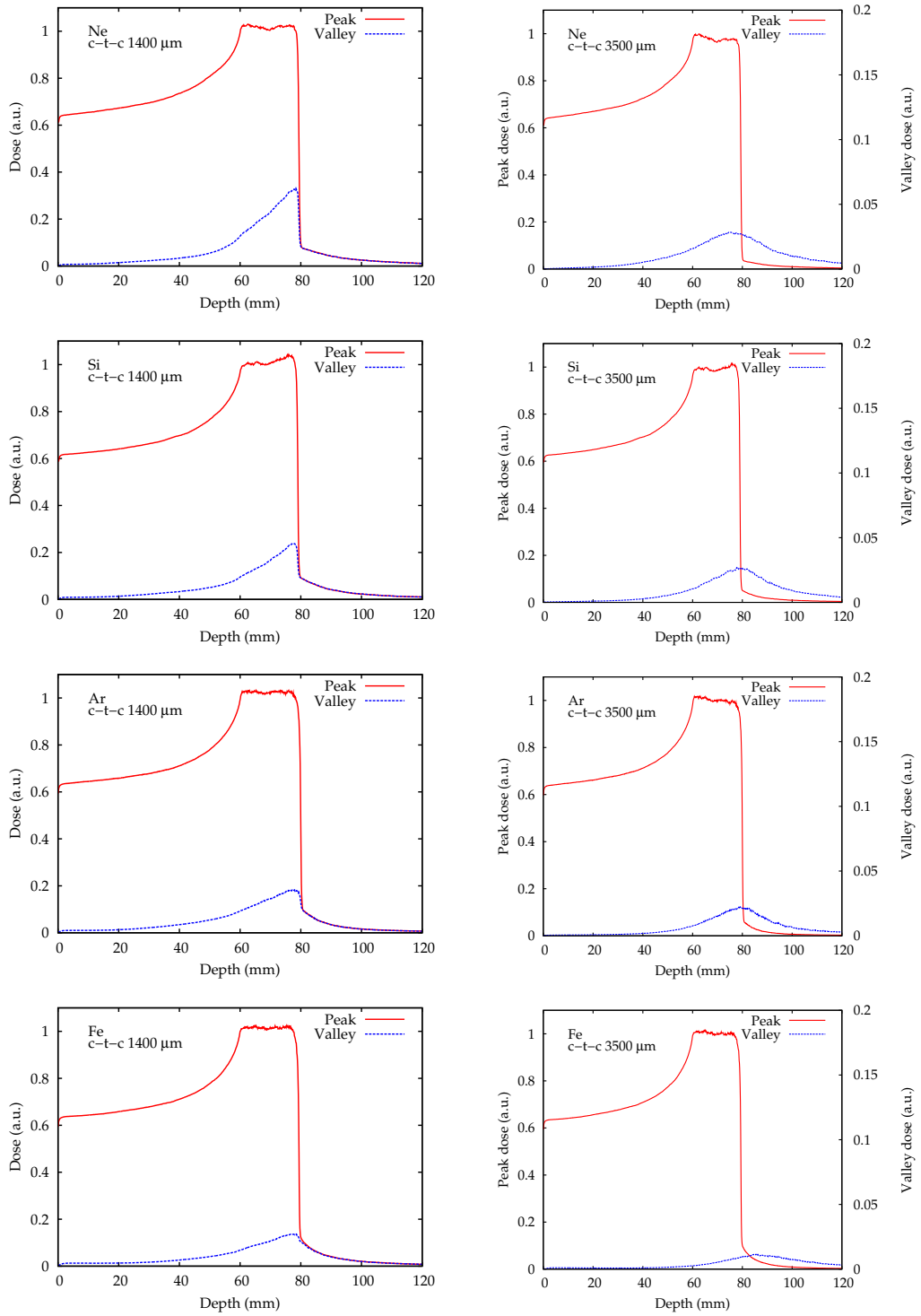

Figure 4.4: *Depth dose distributions obtained in both peak and valley region with an array of neon minibeams for c-t-c distances of 1400 µm (left) and 3500 µm (right), normalised with respect to the SOBP maximum dose for each considered ion. The larger the c-t-c distance, the lower the valley dose, due to a lower proportion of secondary species reaching the centre of the valley region. Also, in general terms, the heavier the ion is, the lower the valley dose. This is related to a higher production of forward directed heavy fragments with high-Z projectiles, contributing less to the valley region.*

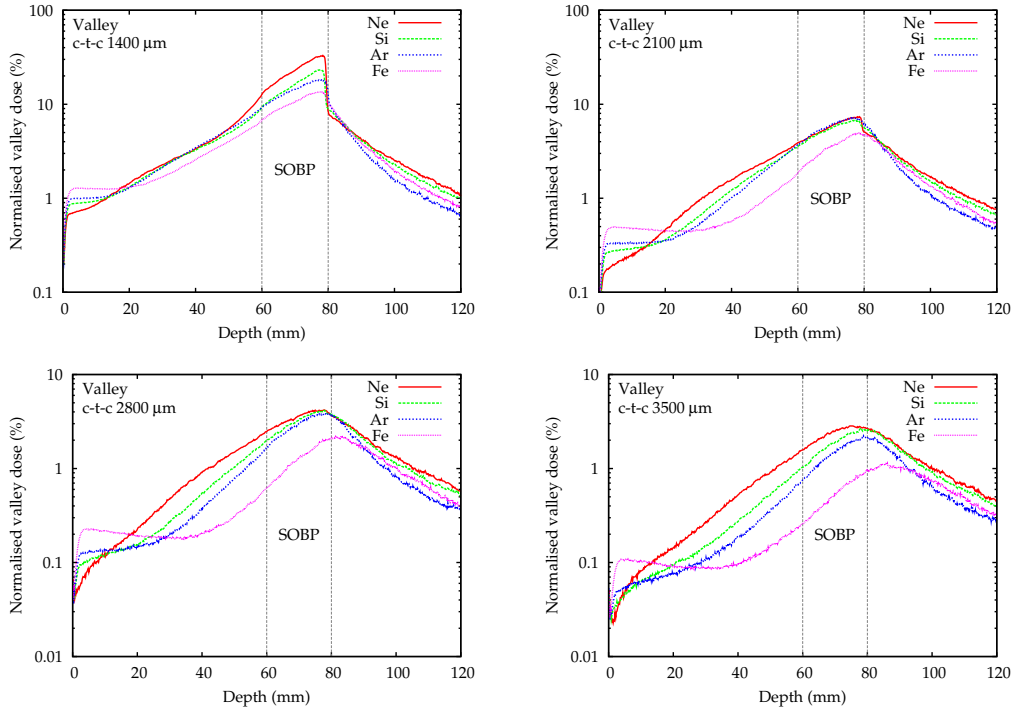

Figure 4.5: *Valley doses as a function of depth normalised with respect to the SOBP maximum dose for each considered ion, for all the c-t-c distances investigated.*

projectiles' one. They consequently have a longer range, being able to deposit their energy beyond the Bragg peak. Figure 4.6 depicts the fragmentation tails in both peak and valley regions for an array of argon minibeams with several c-t-c. In the peak, the dose ratio between SOBP and fragmentation tail decreases with larger c-t-c in both peaks and valleys, due to the less important contribution of peripheral minibeams of the array when the space between two minibeams is enlarged.

In order to preserve distal normal tissues (beyond the SOBP), fragmentation tails have to be kept as low as possible, especially in the valleys, which have to be sufficiently low to ensure tissue sparing. As shown in figure 4.7, the valley doses in the tail are lower than 8% of the prescription dose for any ion and they are noticeably reduced for a c-t-c of 3500 μm, where they are all below 2.5%. In general terms, valley tail doses are lower with the heaviest ions due to the higher production of forward directed (heavy) fragments that contribute mainly to the peak. The minimum was found for iron, with only 1% of the prescription dose.

4.1.2 Estimation of the $NTD_{2.0}$

As in the case of pMBRT (see *Chapter 3*), an estimation of the $NTD_{2.0}$, based on the linear quadratic model [Flickinger 1990], was performed for valley doses. A prescription of 50 Gy in one fraction was assumed, being a very high dose not

Valley doses as a percentage of the SOBP maximum dose in normal tissues (%)				
Depth (mm)	Ne	Si	Ar	Fe
	c-t-c 1400 μm			
10	0.859 ± 0.006	0.936 ± 0.002	1.020 ± 0.003	1.260 ± 0.003
20	1.44 ± 0.01	1.31 ± 0.01	1.290 ± 0.008	1.311 ± 0.003
40	3.36 ± 0.03	3.22 ± 0.02	3.44 ± 0.03	2.58 ± 0.02
60	12.7 ± 0.1	9.26 ± 0.07	9.19 ± 0.07	6.76 ± 0.06
	c-t-c 2100 μm			
10	0.246 ± 0.001	0.290 ± 0.002	0.333 ± 0.002	0.472 ± 0.002
20	0.462 ± 0.006	0.362 ± 0.004	0.351 ± 0.003	0.448 ± 0.002
40	1.57 ± 0.02	0.897 ± 0.01	1.01 ± 0.01	0.566 ± 0.006
60	3.9 ± 0.4	3.55 ± 0.04	3.67 ± 0.04	1.86 ± 0.02
	c-t-c 2800 μm			
10	0.125 ± 0.003	0.118 ± 0.001	0.134 ± 0.002	0.214 ± 0.001
20	0.222 ± 0.004	0.151 ± 0.002	0.143 ± 0.002	0.195 ± 0.001
40	0.89 ± 0.01	0.539 ± 0.008	0.382 ± 0.007	0.201 ± 0.003
60	2.43 ± 0.03	1.95 ± 0.03	1.67 ± 0.03	0.62 ± 0.01
	c-t-c 3500 μm			
10	0.081 ± 0.001	0.062 ± 0.001	0.060 ± 0.001	0.102 ± 0.001
20	0.143 ± 0.003	0.095 ± 0.001	0.076 ± 0.002	0.091 ± 0.001
40	0.534 ± 0.008	0.272 ± 0.005	0.187 ± 0.004	0.099 ± 0.002
60	1.58 ± 0.02	1.03 ± 0.02	0.75 ± 0.02	0.262 ± 0.005

Table 4.2: *Valley doses expressed as a percentage of the maximum SOBP dose as a function of depth in the normal proximal tissues.*

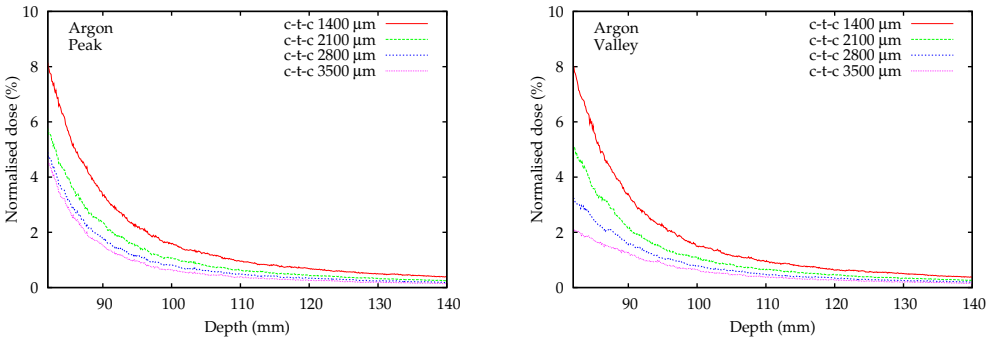

Figure 4.6: *Influence of the c-t-c: Dose tails in peak (left) and valley (right) regions for arrays of argon minibeams. Data are normalised with respect to the SOBP maximum dose.*

usually employed in RT, as in radiosurgery the doses are in order of 15–20 Gy maximum in one fraction. Considering the aforementioned prescription, the valley would receive a maximum dose of 6.4 Gy in the normal tissues at 60 mm-depth. In order to estimate the $NTD_{2.0}$ at that point, an α/β ratio of 2 Gy, corresponding to the brain [Turesson 1989], was selected. The corresponding $NTD_{2.0}$ reaches 13.4 Gy, well below the normal tissue tolerance in the brain, where a 5% risk of

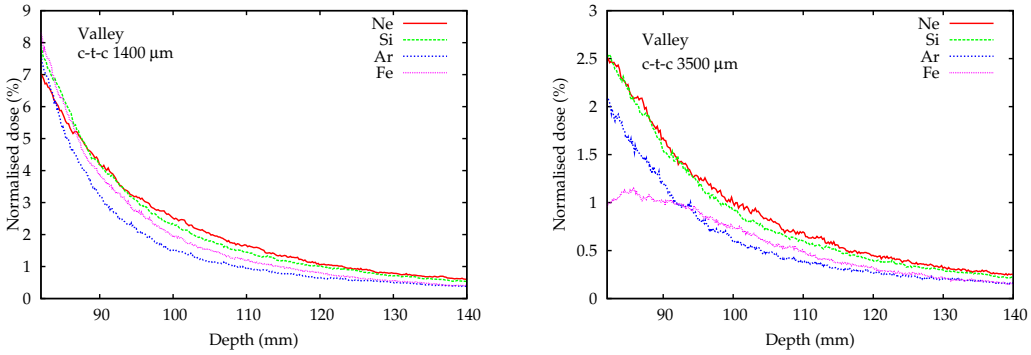

Figure 4.7: *Influence of the ion type: Dose tails in the valley region with a c-t-c distance of 1400 µm (left) and 3500 µm (right). The dose is normalised with respect to the SOBP maximum dose of each considered ion.*

radiation necrosis with the standard fractionation scheme is predicted to occur at 72 Gy [Lawrence 2010]. This means that very high doses as high as 50 Gy in one fraction might be delivered to the SOBP while insuring low valley doses, below the normal tissue tolerance. Although the $NTD_{2.0}$ remains an approximation, in this case it gives a hint that a sparing effect might be expected. In addition, recent studies have reported a significantly longer overall survival in glioma-bearing patients treated with doses as high as 80–90 Gy in several fractions in conventional RT [Tanaka 2005], and with hyperfractionated concomitant boost proton radiotherapy, in particular 96.6 Gy equivalent photon in 56 fractions [Mizumoto 2010]. Spatially fractionated techniques such as very heavy ion MBRT might allow the delivery of even higher potentially curative doses for radio-resistant tumours (50 Gy in one fraction), therefore offering a higher probability of tumour control.

4.1.3 Lateral dose profiles

As explained in *Chapter 1*, profiles consist in a pattern of peaks and valleys. Their exact shapes result from the behaviour of individual minibeams in depth. Therefore, width and penumbra (80–20% width) of one single minibeam have been assessed. As shown in figure 4.8, both parameters increase as a function of depth mainly because of multiple Coulomb scattering and the contribution of fragmentation products. Concerning FWHM, its value ranges from 700 μm at the phantom entrance to 900 μm in the distal part of the SOBP (for the lightest ion), with a moderate increase until the vicinity of SOBP. In the first centimetres, penumbra values are very small (< 50 μm at the entrance) with respect to the beam width (700 μm). For this reason, the rapid rise of penumbra values is not accompanied by an appreciable increase of beam width until penumbras are larger than 100 μm. Penumbra values (50–300 μm) are one order of magnitude narrower than in conventional radiosurgery, which are larger than 2.5 mm in the best cases [Guerrero 2003, García-Garduño 2008]. In

addition, they are also more reduced than in pMBRT for which values range from 500 to 1700 μm with a magnetic collimation [Prezado 2013]. This point constitutes a significant advantage for tissue sparing due to the steep dose fall-off between the target volume and nearby critical structures. The heavier the ion is, the narrower the penumbra, due to the reduced multiple Coulomb scattering. A decrease of around 50% in penumbra values is observed when going from the lightest (Ne) to the heaviest ion considered (Fe).

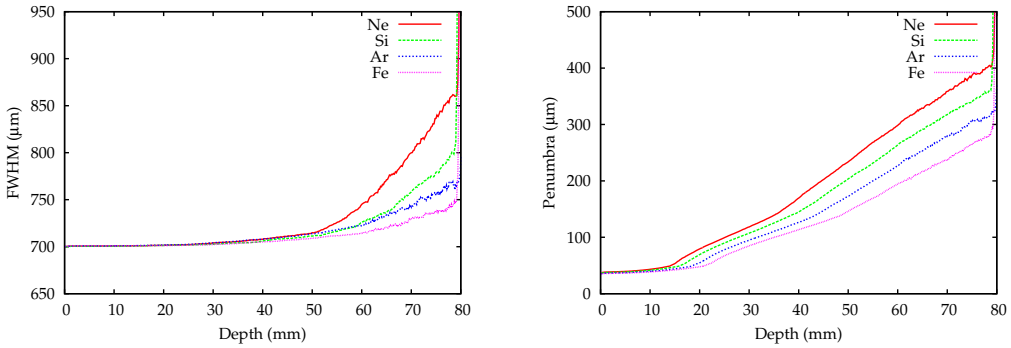

Figure 4.8: *Full width at half maximum (left) and 80-20% penumbra width (right) as a function of depth assessed on one single minibeam. Both FWHM and penumbras increase as a function of depth because of multiple Coulomb scattering. FWHM values show a moderate increase until the SOBP and then a rapid widening from the target position, still being one order of magnitude narrower than in conventional radiosurgery.*

Such reduced penumbras and FWHM allow to maintain a spatial fractionation of the dose (pattern of peaks and valleys) in depth, for all c-t-c distances and heavy ions explored. Figure 4.9 shows some examples of lateral dose profiles computed at shallow depths (normal tissue). Valley doses are increased when the c-t-c is reduced, as explained in section 4.1.1.

As already mentioned, in spatially fractionated techniques the ratio between peak and valley doses (PVDR) is a relevant dosimetric parameter. High PVDR values (along with low valley doses), are needed to ensure normal tissue sparing [Dilmanian 2002]. As it has been explained in section 4.1.1, the higher the c-t-c distance is, the lower the valley doses, and therefore the higher the PVDR. This behaviour is illustrated in figure 4.10 showing PVDR values obtained with an array of silicon and argon minibeams and several c-t-c. For instance, with an array of argon minibeams, the PVDR values at 4 cm-depth are 20.5 $\pm$ 0.3 with a 1400 μm c-t-c, increasing up to 370 $\pm$ 16 with 3500 μm. In general terms, the heavier the ion is, the higher the PVDR (see figure 4.11), thanks to a lesser contribution of heavier fragments to the valleys (see section 4.1.1).

For all ions, maximum PVDR are obtained at the phantom entrance, where the values exceed 1000 for a c-t-c of 3500 μm while being around 100 for a c-t-c of 1400 μm. PVDR curves then exhibit a smooth decrease with depth, directly

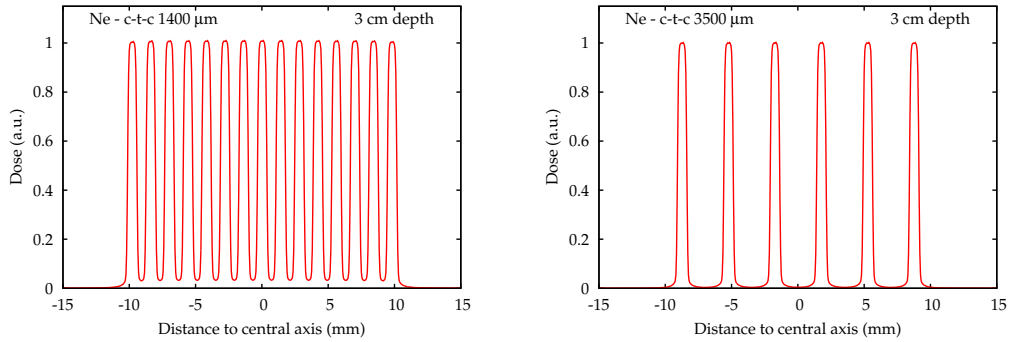

Figure 4.9: *Lateral dose profiles at 3 cm resulting from a neon MBRT irradiation. The left figure corresponds to a c-t-c distance of 1400 µm, while a c-t-c of 3500 µm was used in the right one.*

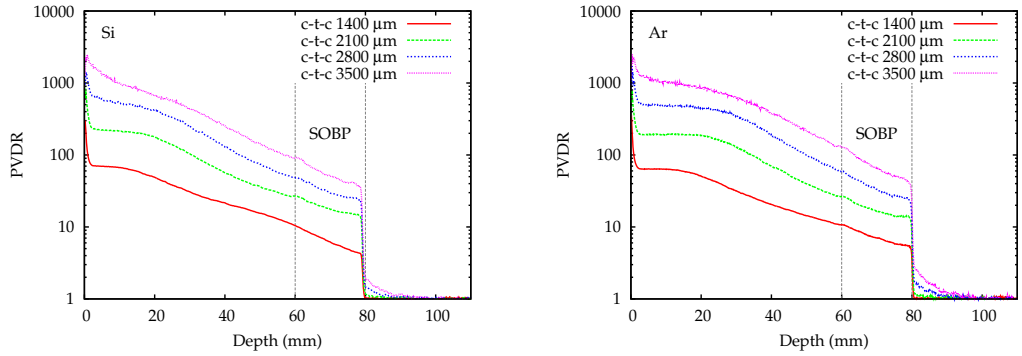

Figure 4.10: *Influence of the c-t-c distance: PVDR values as a function of depth obtained with an array of silicon (left) and argon minibeams (right). The higher the c-t-c distance is, the lower the valley doses, and therefore the higher the PVDR values.*

related to the increase of valleys, as previously shown in figure 4.5. In the SOBP, PVDR superior to 1 are observed, meaning that the spatial fractionation is also retained at that depth. As explained in *Chapter 1*, local tumour control has been observed in several x-rays MBRT with inhomogeneous dose distributions, which suggest a potential preferential tumouricidal effect of MBRT. However, if needed, a homogeneous dose distribution might be achieved in the tumour by using interlaced geometries. Precise interlacing has already been accomplished in previous MRT and MBRT studies [Serduc 2010, Prezado 2012b]. In contrast, PVDR close to one are reached in the tails. However since the doses in this region are maintained to a very low level with respect to the SOBP dose, as previously mentioned (see section 4.1.1), no side effects are expected.

As a global tendency, PVDR values vary inversely to the valley dose behaviour. With an array of iron minibeams, for instance, the valley dose strongly increases

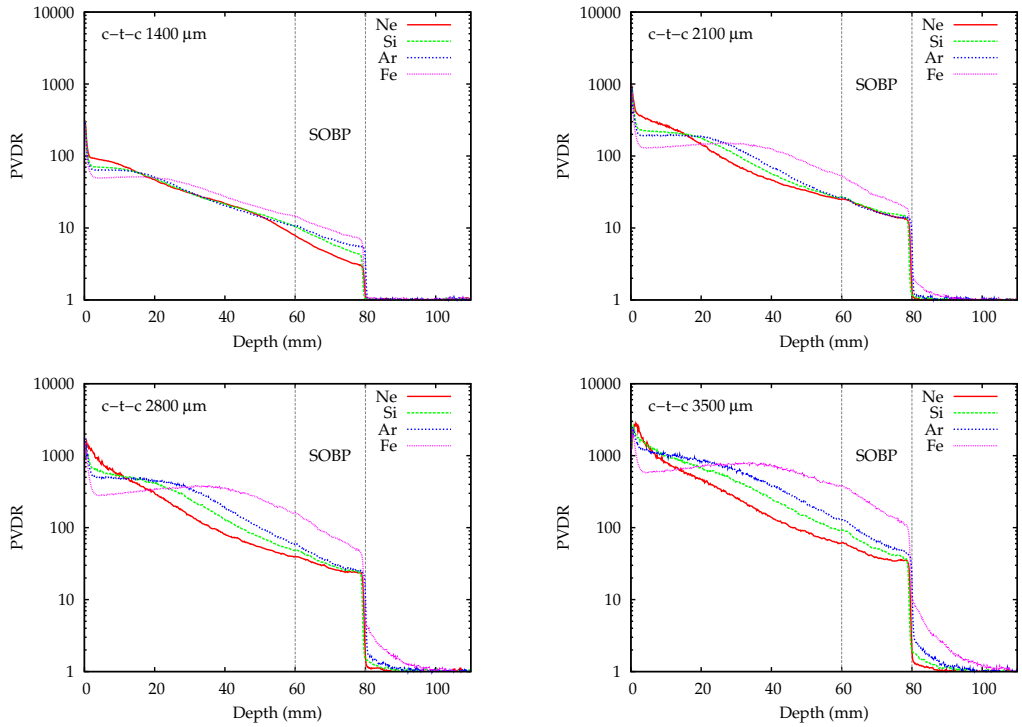

Figure 4.11: *Influence of the Z: PVDR values as a function of depth for all the considered c-t-c distances. In general terms, the heavier the ion is, the higher the PVDR values are, due to a higher production of forward directed heavier fragments with high-Z projectiles, thus less contributing to the valley dose.*

when entering the phantom (see figure 4.5 in section 4.1.1), directly affecting PVDR, whose values decrease. The opposite trend is observed at around 4 cm-depth where a maximum value in PVDR results from a local minimum in the valley dose. Further details will be given in section 4.2.1.

Numerical PVDR values for every c-t-c distance and ions are reported in table 4.3. Regarding all ions, extremely high PVDR are obtained, much superior than in x-rays MBRT [Prezado 2009b] for which normal tissue sparing has already been proven [Prezado 2015]. This might lead to a net gain in tissue sparing. In addition, PVDR values surpass those obtained in the same configuration with arrays of proton minibeams (700 μm $\times$ 2 cm). At all depths, PVDR for heavy ions are much greater than with protons, for which they range from 1.00 $\pm$ 0.05 to 2.0 $\pm$ 0.1 for a 1400 μm, and from 11.0 $\pm$ 0.6 to 162 $\pm$8 with 3500 μm [Prezado 2013] (see also section 3.2.3). Even with the largest c-t-c (3500 μm), PVDR values for protons are almost one order of magnitude lower than with very heavy ions. This is mainly due to important Coulomb scattering with protons, making the primaries contributing to a greater extent to the valley dose, consequently diminishing the PVDR values.

PVDR values as a function of depth for very heavy ion minibeam arrays				
Depth (mm)	Ne	Si	Ar	Fe
	c-t-c 1400 μm			
5	87.5 ± 0.5	69.6 ± 0.3	64.1 ± 0.2	49.5 ± 0.2
10	75.7 ± 0.5	66.9 ± 0.3	63.1 ± 0.3	50.6 ± 0.2
20	46.8 ± 0.8	48.9 ± 0.7	50.8 ± 0.7	49.1 ± 0.4
40	21.8 ± 0.4	21.6 ± 0.4	20.5 ± 0.3	24.7 ± 0.4
60	7.83 ± 0.1	10.4 ± 0.2	10.7 ± 0.2	14.9 ± 0.3
SOBP	4.39 ± 0.07	6.2 ± 0.1	7.0 ± 0.1	9.8 ± 0.2
Tail	1.00 ± 0.04	1.01 ± 0.04	1.03 ± 0.05	1.04 ± 0.04
	c-t-c 2100 μm			
5	322 ± 5	222 ± 2	191 ± 1	128 ± 0.5
10	256 ± 4	215 ± 2	192 ± 2	135 ± 0.5
20	146 ± 2	177 ± 2	186 ± 2	146 ± 0.8
40	46.6 ± 0.5	56.7 ± 0.7	70.0 ± 0.9	124 ± 1
60	25.2 ± 0.3	26.8 ± 0.3	26.5 ± 0.3	53.1 ± 0.7
SOBP	16.8 ± 0.2	17.5 ± 0.2	16.7 ± 0.2	28.4 ± 0.4
Tail	1.04 ± 0.02	1.09 ± 0.02	1.12 ± 0.05	1.63 ± 0.03
	c-t-c 2800 μm			
5	763 ± 23	610 ± 9	496 ± 6	284 ± 13
10	531 ± 12.0	528 ± 8	476 ± 7	297 ± 13
20	299 ± 5	424 ± 6	455 ± 7	333 ± 2
40	81.0 ± 1	129 ± 2	187 ± 4	350 ± 5
60	39.7 ± 0.6	48.6 ± 0.7	58.1 ± 1	160 ± 3
SOBP	27.4 ± 0.4	29.6 ± 0.4	33.2 ± 0.5	77.0 ± 1
Tail	1.05 ± 0.03	1.29 ± 0.03	1.52 ± 0.05	3.14 ± 0.08
	c-t-c 3500 μm			
5	1297 ± 50	1290 ± 36	1150 ± 30	58.6 ± 5
10	829 ± 24	999 ± 27	1049 ± 26	624 ± 5
20	468 ± 20	676 ± 28	843 ± 38	718 ± 17
40	137 ± 5	254 ± 9	370 ± 16	714 ± 23
60	61.2 ± 1.8	91.8 ± 3	129 ± 5	376 ± 15
SOBP	38.9 ± 1.3	51.0 ± 1.8	66.2 ± 2.8	182 ± 9.2
Tail	1.23 ± 0.07	1.56 ± 0.08	2.3 ± 0.1	7.0 ± 0.4

Table 4.3: *PVDR values obtained at several depths with the four c-t-c distances and ions.*

4.2 Evaluation of secondary particles distributions

The contribution of secondary particles (gammas, δ-rays (electrons) and nuclear fragments) strongly affects the dose distributions, especially in valleys. The study of their contribution to the dose is thus of particular importance. Along this line, first, the spatial distribution of secondaries in peaks and valleys will be reported, with a special attention given to valleys. In addition, the type and amount of nuclear fragments created during a very heavy ion MBRT irradiation will be assessed.

4.2.1 Spatial distribution of secondary species

Figure 4.12 shows the proportion of primaries and secondaries contributing to the total dose in both peak and valley regions. In the peak, the dose is mainly due to primaries, while the contribution of secondaries ranges from only 10% of the total dose in the entrance to 20% in the SOBP, for all ions. In contrast, the valleys are primarily fed by the secondary particles directed with large angular aperture. The primaries contribute to valleys to a lesser extent, mainly in the SOBP region, and even at shallower depth with low-Z ions, due to a more important lateral scattering. In addition, the lower the Z of the primary beam is, the higher the contribution of the primaries in the valley. With neon, they are even the main contribution to the valley dose in the SOBP (70% of the total dose).

The contribution of each type of secondaries will be presented separately hereafter, in both peak and valley regions.

4.2.1.1 Contribution of secondaries to the peak dose

Figure 4.13 shows the contribution of secondary products to the peak depth dose distributions for the four considered ions. The maximum of the total sum of secondary products (gammas, δ-rays and other products) was taken as a normalisation point. As aforementioned, the maximum contribution of secondaries only amounts to 20% of the total dose in the SOBP (see figure 4.12). Since no differences were found between the different c-t-c considered in this study, only one case (3500 μm) is shown. The resultant depth dose distribution of secondary products is mainly affected by δ-rays in the proximal normal tissues, then by nuclear fragments which become the dominant contribution in the SOBP region. Overall, gammas participation is several orders of magnitude smaller than the others, as is was already the case with arrays of proton minibeams (see section 3.1).

After the small build-up region in the entrance, δ-electrons provide a quasi-constant dose deposition in depth until reaching the SOBP, where, related to the slowing down of primaries, the contribution of secondary electrons starts to decrease. In contrast, since the nucleus-nucleus collisions cross sections increase as a function of depth, it results in an increasing trend of the nuclear products dose distribution in the peaks, overcoming the decrease of δ-rays contribution in the SOBP. The heavier the ion is, the larger the nucleus-nucleus collision cross-sections, and therefore, the steeper the increase of secondary nuclear product contribution. As a consequence, the depth at which the dose deposition by secondary nuclear fragments becomes dominant over electrons is shallower for the heavier ions.

In the distal part of the SOBP, the rapid fall-off of nuclear products contribution corresponds to the complete stop of the primary beam. The contribution of nuclear products having a longer range than primaries after the SOBP forms the fragmentation tail. These nuclear products interact with the medium, producing themselves secondary electrons, which explains the δ-rays tracks in this region.

Nuclear fragments are expected to have greater LET than gammas and electrons, and are thus likely to cause more biological damages in the tissues. In the peak

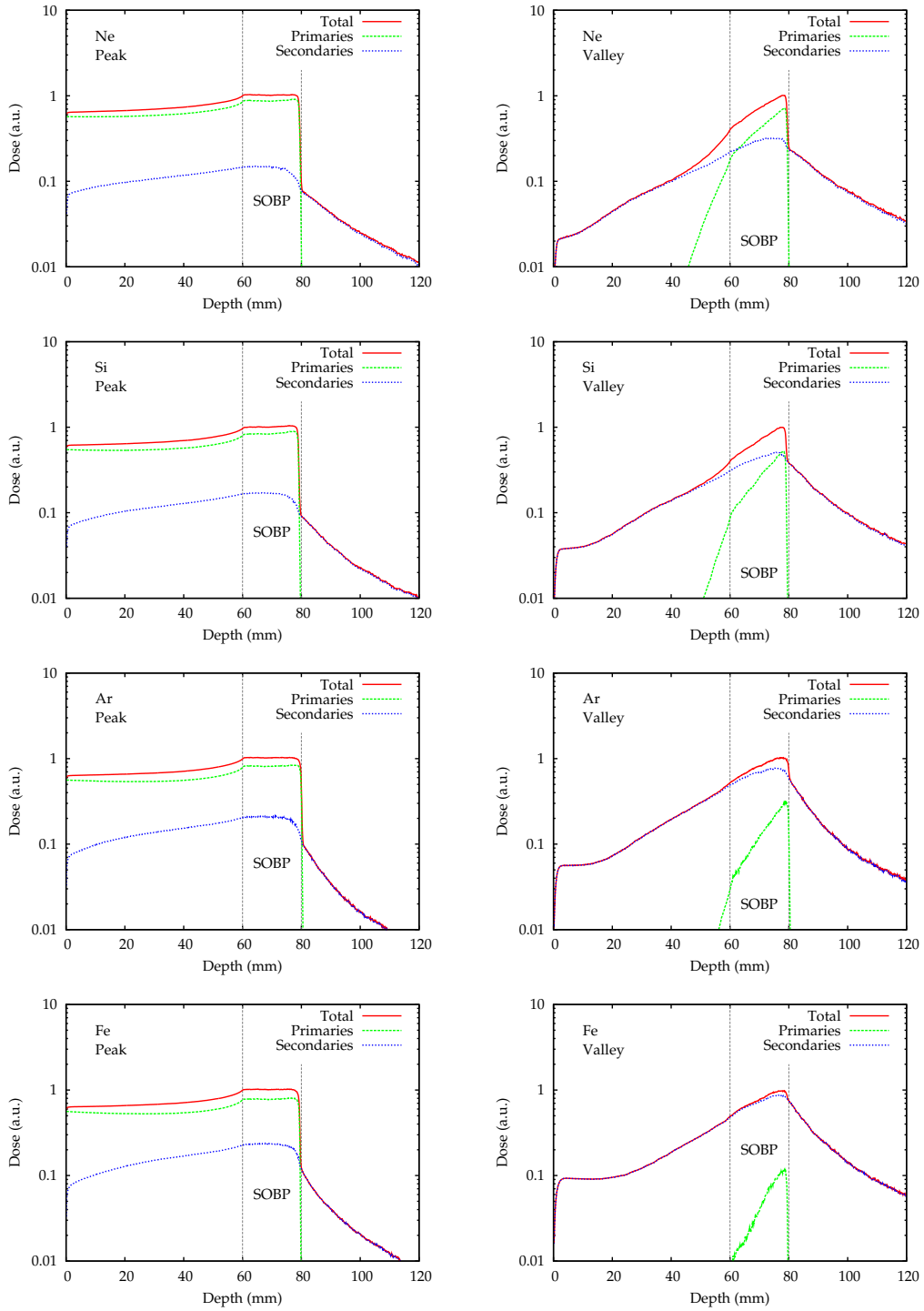

Figure 4.12: *Contribution to the peak and valley dose distributions of primary projectiles and secondary products for arrays of several ions (c-t-c of 1400 µm). The distributions are normalised to the maximum normal dose in peak (left) and in valley (right). In valleys, the contribution of primaries only appears in the vicinity of the SOBP, and is higher for low Z ions.*

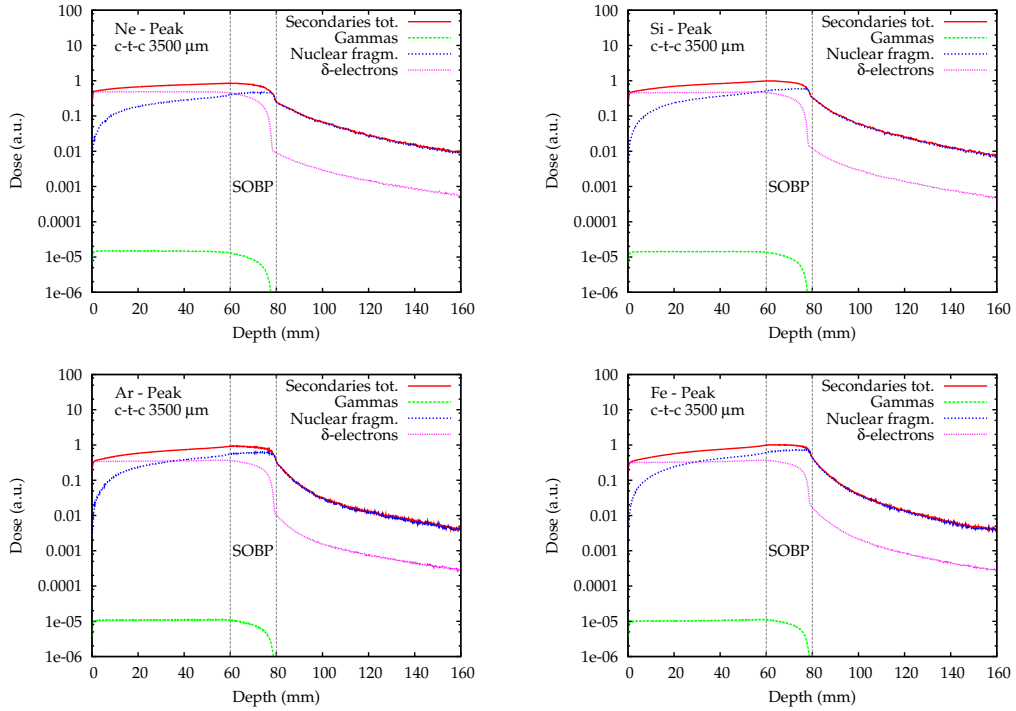

Figure 4.13: *Contribution of the different species of secondary particles to the peak depth dose curve as a function of primary ion. The dose was normalised to the maximum of the total sum of secondary products. A c-t-c distance of 3500 µm was considered. "Secondaries tot." and "nuclear fragm." refer to "secondaries total" and "nuclear fragments", respectively.*

region, the contribution of these higher LET species in the normal tissues is not critical as the tissue sparing would be insured by the low valley doses. It could even be an asset in the SOBP in order to induce more damages in the tumour.

4.2.1.2 Contribution of secondaries to the valley dose

As explained in section 4.2.1, the main contribution to the valley dose is due to secondaries. Indeed, they are the only contributors to the valley dose at the phantom entrance. They are also the main contribution to valleys in the SOBP, except in the case of neon with a c-t-c of 1400 μm where they only represent 30% of the total dose. Figures 4.14 to 4.17 show the participation of the different secondary species to the valley doses for the four ions and c-t-c distances investigated in this study. Concerning secondary nuclear fragments, the trend is the opposite than in peaks: the heavier the incident ion is, the deeper the point where the dose deposited by nuclear fragments is the dominant one. Indeed, in the peak, high-Z projectiles create forward directed (small angular spread) heavy fragments that reach the valley at a deeper point. In addition, the contribution of nuclear fragments becomes dominant (over δ-electrons) at shallower depths for larger c-t-c distances. For instance, with argon, it occurs at 30 mm for a c-t-c of 1400 μm (see figure 4.14) and at only 5 mm

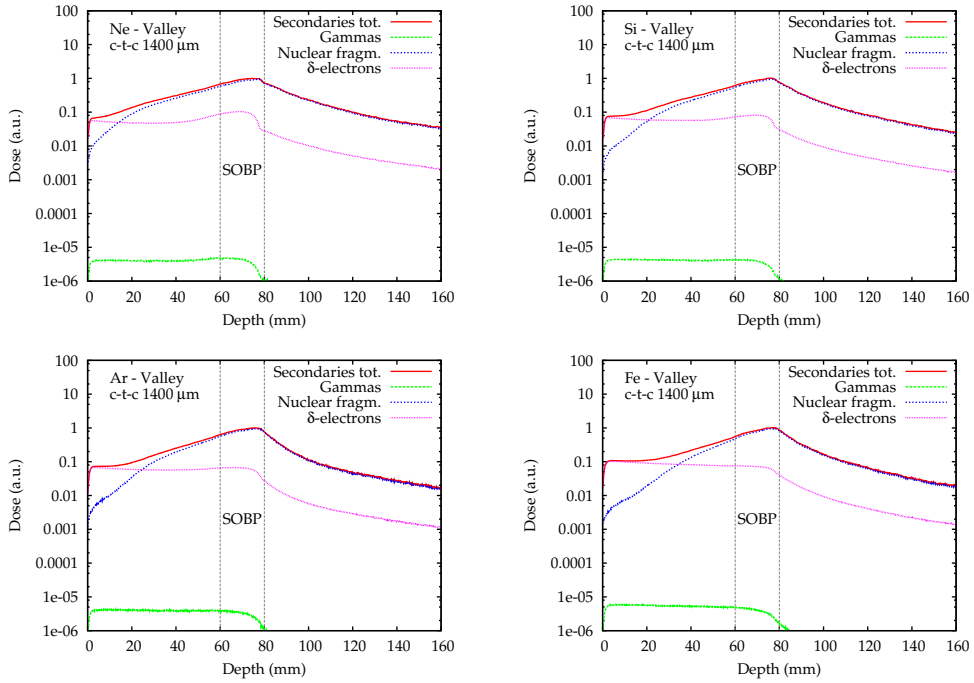

Figure 4.14: *Contribution of the different species of secondary particles to the valley depth dose curves as a function of primary ion, with a c-t-c distance of 1400 µm.*

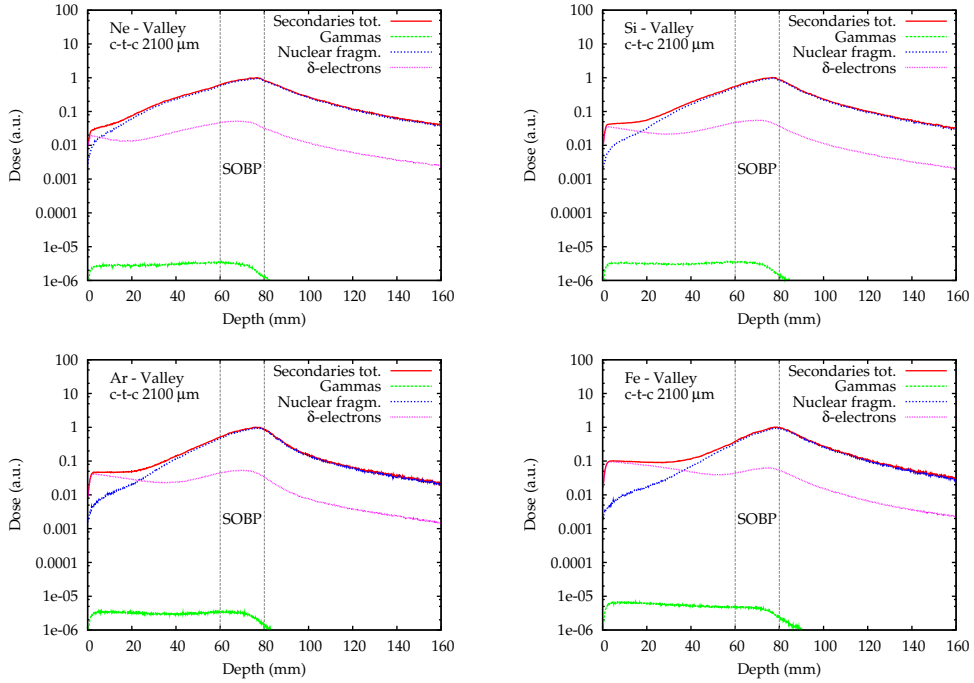

Figure 4.15: *Contribution of the different species of secondary particles to the valley depth dose curves as a function of primary ion, with a c-t-c distance of 2100 µm.*

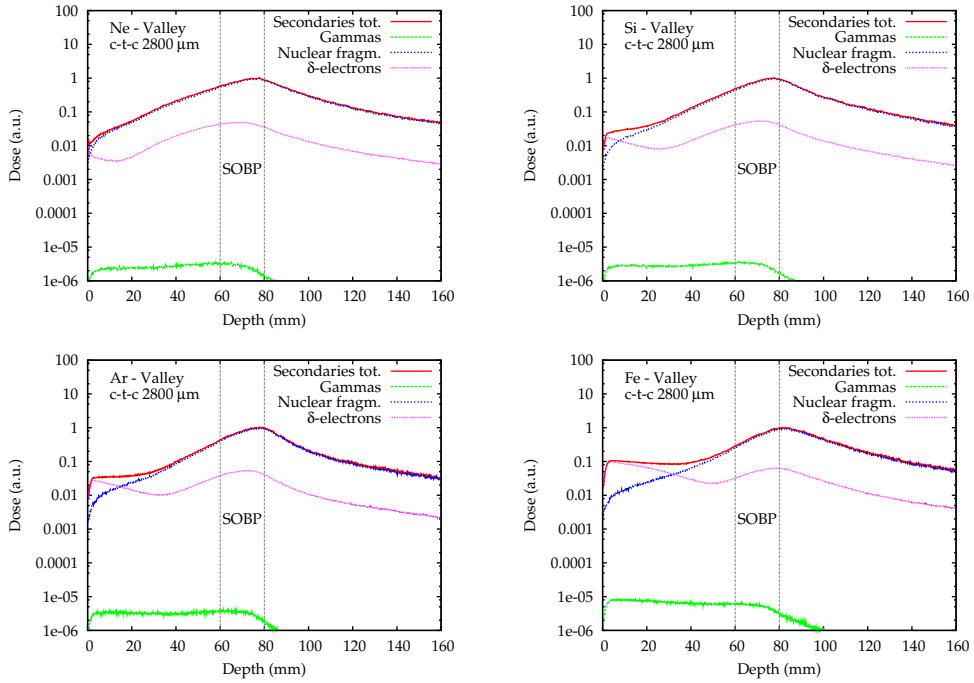

Figure 4.16: *Contribution of the different species of secondary particles to the valley depth dose curves as a function of primary ion with a c-t-c distance of 2800 µm.*

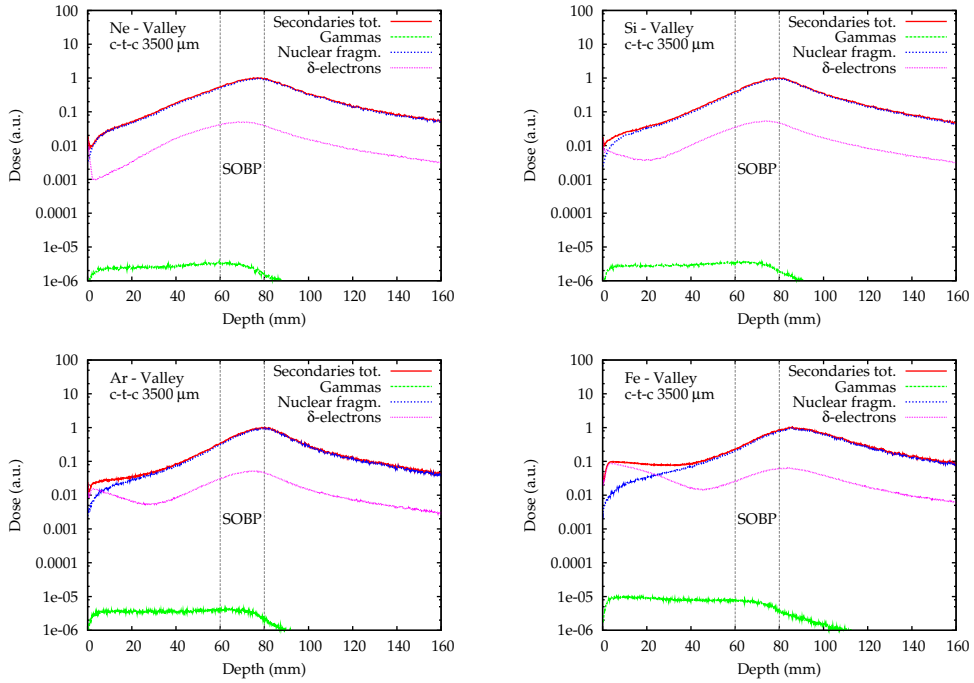

Figure 4.17: *Contribution of the different species of secondary particles to the valley depth dose curves as a function of primary ion, with a c-t-c distance of 3500 µm.*

for a c-t-c of 3500 μm (see figure 4.17). This is due to the fact that the range of one part of secondary electrons is shorter than half of the c-t-c distance and therefore, they are not able to reach the centre of the valleys.

However, as secondary electrons are in average more energetic at the same depth for heavier ions (see table 4.4), they consequently remain the dominant participants until deeper points when higher-Z projectiles are employed. For example, for a c-t-c of 2100 μm, δ-rays dominate the distribution until 5 mm for neon, while they are dominant until 40 mm with iron (see figure 4.15).

Electron maximum energy and range at 4 cm-depth in the peak		
Ion	Maximum energy (MeV)	Maximum range (μm)
Ne	0.41 ± 0.02	1335 ± 160
Si	0.46 ± 0.02	1820 ± 160
Ar	0.56 ± 0.04	2070 ± 290
Fe	0.66 ± 0.04	2580 ± 290

Table 4.4: *Electrons maximum energies and ranges in liquid water at 4 cm-depth in the peak region. The electron ranges were estimated thanks to the NIST database [NIST-ESTAR 2016].*

In addition, two examples of electrons spectra for an irradiation with neon ions are presented in both peak and valley regions in figure 4.18. For the sake of simplicity, only one single minibeam was considered. The spectra in the valley were assessed 1750 μm away from the minibeam's centre, which would correspond to the centre of the valley if an array with a c-t-c of 3500 μm had been considered. The most probable energy do not significantly vary with the penetration depth in both peak and valley regions. However, the maximum energy of electrons decreases with increasing depth. In addition, in the valley, the number of electrons significantly rise with depth, reaching a maximum in the SOBP.

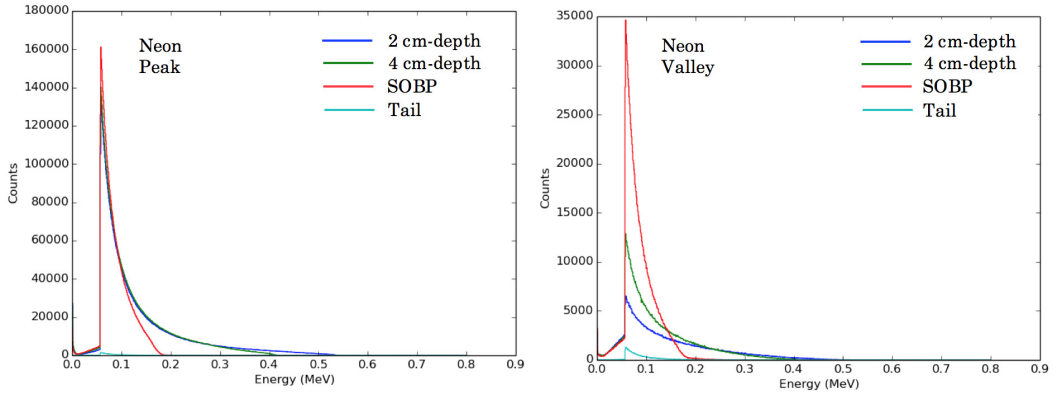

Figure 4.18: *Electron spectra in peak (left) and valley region (right) at several depths for an irradiation with one single neon minibeam. The spectra in valley were assessed 1750 μm away from the minibeam's centre.*

The dose distribution of δ-electrons is almost constant until the SOBP with a c-t-c of 1400 μm, as it was the case in the peak. When the c-t-c is enlarged (see figures 4.15 to 4.17), the shape of the δ-rays distribution becomes more complex: after a small build-up, a decrease of dose deposition is observed. The reason is the reduction of the primary beam velocity and the subsequent decrease of secondary electrons energy and range. Then, the production of electrons by nuclear fragments interactions with the medium results in an increasing trend of the dose deposited by δ-rays, reaching a maximum in the SOBP. After that point, a smooth descent is observed. This behaviour is all the more pronounced with increasing c-t-c distances and heavier ions. In particular, the δ-rays distribution of iron minibeams with a c-t-c distance larger than 1400 μm strongly influences the total valley dose distribution (see figure 4.5) which follows a remarkably distinct trend with respect to the other ions. This also consequently impacts the PVDR curve (see figure 4.11). As an example, the case of iron for a c-t-c of 3500 μm will be detailed hereafter.

As shown in figure 4.17, δ-rays are the main participants to the valley dose of iron up to 25 mm depth, from which the nuclear fragmentation processes take the upper hand. The nuclear fragments also produce themselves δ-rays, which explains the inflection point at 40 mm-depth from which the contribution of δ-rays rises again. Consequently, this results in an increase of the valley dose from this point, as it was depicted in figure 4.5. A similar trend is observed with argon with a c-t-c of 3500 μm. However, the build-up region is much shorter in comparison with iron. Also, the inflection point (where δ-rays created by nuclear fragments become more important) appears at shallower depths (30 mm) and is less pronounced. In contrast, with lighter ions such as neon, secondary electrons are created further in the lateral direction due to a higher lateral spreading of light incident particles. This allows to compensate the fall-off in the contribution of electrons (see figure 4.17).

To ensure normal tissue sparing, the contribution of nuclear fragments (high LET) to the dose should be kept as low as possible in the valley region. The results presented in this section show that the use of high-Z ions allow to limit the high contribution (dominant) of nuclear fragments to the valley dose at a deeper point.

4.2.2 Type of nuclear fragments and their yield

This section reports the type and yield of secondary fragments created in both peaks and valleys. For the sake of simplicity, the type and proportion of secondary fragments were assessed considering one single minibeam (700 μm $\times$ 2 cm). Figures 4.19 and 4.20 show the evolution of nuclear fragments' yield as a function of depth in peak and valley regions, respectively. As for the electron spectra presented in section 4.2.1.2, nuclear fragment yields in valley were assessed 1750 μm away from the minibeam's centre (assuming a c-t-c of 3500 μm).

In general, the yield and multiplicity of fragments increase with the atomic number of the projectile, being the yields more important in the peak than in the valley. The lightest products, protons and neutrons, are the dominant contributions in both peak and valley regions, with yields going from 0.15 (neon) to 0.48 (iron)

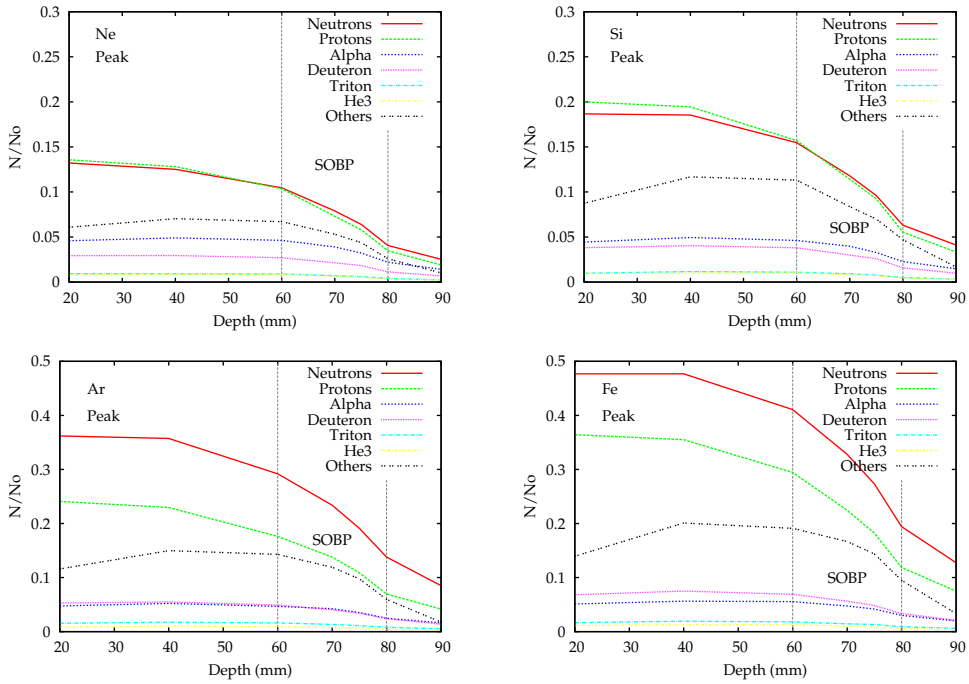

Figure 4.19: *Nuclear fragments yields as a function of depth in the minibeam path (peak) for the four considered ions. Data are normalised with respect to the number of primaries.*

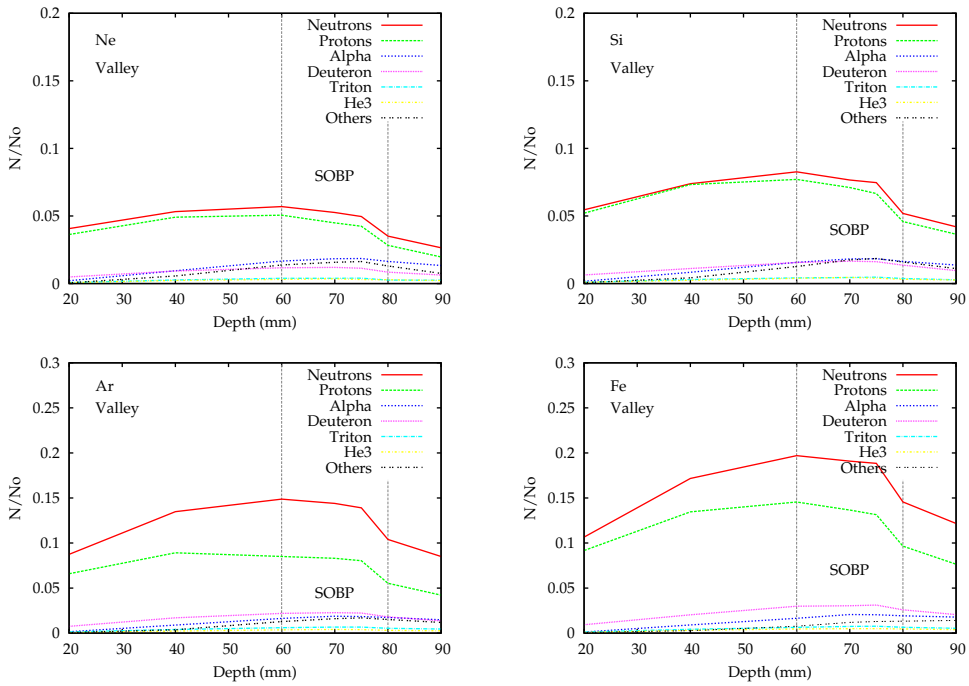

Figure 4.20: *Nuclear fragments yields as a function of depth in the valley for the four considered ions. Data are normalised with respect to the number of primaries.*

per primary particle in the peak, and from 0.05 (neon) to 0.2 (iron) in the valley. Other light fragments like deuterons, tritons, ^{3}He and alpha particles are also represented, however their yield is reduced at least by a factor 2 with respect to protons and neutrons. Heavier fragments (Z>2) constitute only a low proportion of the total fragmentation products, being in addition very reduced in valleys with respect to the peaks. In the peak, a slow decrease of the yields as a function of depth is observed, especially concerning light species (see figure 4.19). These light fragments (protons and neutrons) are directed with larger angles with respect to the beam size, and are able to escape towards the adjacent valley, which consequently results in an increase of the yields in the valley region (see figure 4.20). In contrast, heavier fragments like alpha particles are mainly forward directed and are more concentrated in peaks, while their contribution in valley is very low.

Concerning the lateral distribution of nuclear fragments, figure 4.21 shows the yields of secondary products at several lateral distances from the peak, at a depth of 4 cm in the water phantom. As one can see, the secondary species contribution expands in the penumbras and lateral tails of the minibeam. However, as we move away from the peak centre, the secondary products yield diminishes, being this reduction a factor around 2 at 700 μm, and a factor close to 4 at 1750 μm from the peak. At the latter distance (corresponding to the centre of the valley when a c-t-c

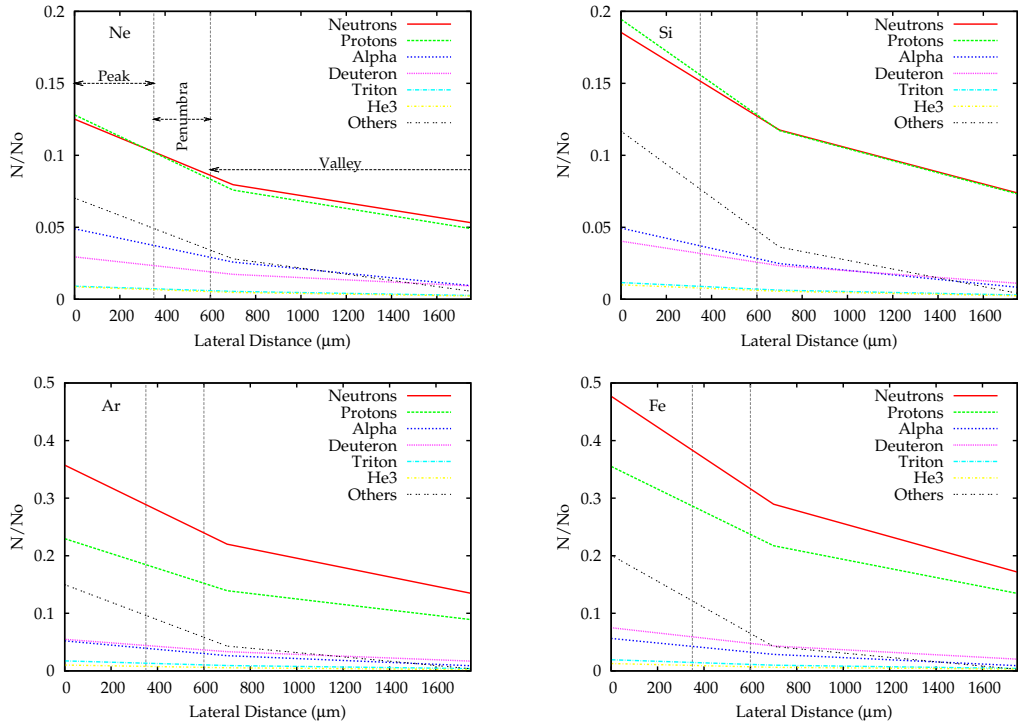

Figure 4.21: *Lateral distribution of the most frequent fragmentation products at 4 cm-depth considering a c-t-c distance of 3500 µm. Data are normalised with respect to the number of primaries. Three regions corresponding to the peak, penumbra and valley are represented.*

of 3500 μm is used), the contribution of secondary heavy fragments is remarkably reduced. This is due to the fact that, for the same velocity, heavier fragments have a shorter range than lighter ones that may travel towards the centre of the valley.

Neutrons are among the most abundant fragments. In conventional RT the neutron qualitative weight, *i.e.* the radiation weighting factor (w_R), is a function of the neutron energy, varying from 5 to 25 depending on neutron energy. As previously mentioned, biological quantities such as RBE that applies in conventional charged particle therapy are expected to not be applicable here. The neutron spectra, that could be correlated with biological observations when available, have been assessed in the valley region at several depths in the water phantom (see figure 4.22) for both neon and iron minibeams. In the normal tissues (2 and 4 cm-depth) and SOBP regions, two peaks are visible: one being around 1 MeV, and a second one at higher energies, depending on the depth. As the depth increases, the most probable energies in the spectra are shifted towards lower energies due to neutron thermalisation. The neutron contribution to the dose in the normal tissues have been assessed to be 7 orders of magnitude lower in average than the total dose. This implies that, even considering the most conservative case (highest radiation weighting factor (25)), the biologic neutron doses would be lower than 0.00025% of the SOBP dose in the valley.

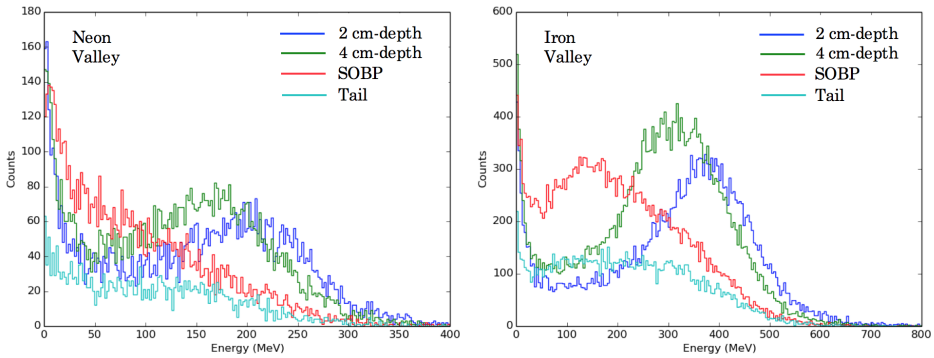

Figure 4.22: *Neutron spectra evaluated at several depths with an irradiation of for neon (left) and iron (right) minibeams. The spectra have been determined 1750 μm away from the minibeam centre, which corresponds to the centre of the valley region if an array with a c-t-c 3500 μm has been used.*

In summary, the proportion of lighter fragments is much more important than the heavier ones, in both peak and valley regions. Besides, the contribution of high-LET heavy fragments is confined in the central part and penumbra of the minibeam, while protons and neutrons are able to reach the centre of valleys, being the neutron contribution to the dose extremely small. While high-LET fragments contribution to peaks might not be critical, and could potentially constitute an advantage at the tumour position, their contribution to valleys should preferably be kept as low as possible. The results presented above thus suggest that large c-t-c distances should be favoured in very heavy ion MBRT, in order to reduce the proportion of heavy fragments in the valley region.

4.3 Summary and discussion

Despite recent advancements in RT, important issues remain in the management of hypoxic tumours that conventional RT (photons) cannot effectively treat, due to a high dependency of tumour oxygenation. Very heavy ions offer a reduced OER, meaning that they are able to induce important DNA damages even in hypoxic conditions. However they exhibit much high RBE values in the normal tissues that make them non-suitable for conventional RT (broad beam). Combining them to the normal tissue sparing of spatially fractionated technique could be one solution to profit from the reduced OER while avoiding their side effects in the normal tissues.

As a part of my *Ph.D.* I have explored this new strategy from a physics point of view (MC simulations). The study has been restricted to physical quantities due to the fact that the biological mechanisms involved in spatially fractionated irradiations are expected to greatly differ from those of conventional charged particle therapy (broad beam). The established RBE are thus likely not to be valid. In contrast, LET is a physical quantity that could be correlated to biological observations, when available, although some phenomena such as non-targeted ones will not be included. While in the peak the contribution of high LET components might not be "prejudicial", and could even be advantageous in the tumour region, it should preferably be minimised in the valleys which are known to be the main responsible for tissue sparing [Dilmanian 2002]. Although LET maps have not been directly assessed in this first proof of concept, the results allowed to draw a first estimation of the proportion of lower and higher LET secondary products contributing in peaks and valleys. The main results of this work have been compiled in an article published in *Medical Physics* [Peucelle 2015b]. See *Chapter 6*. A summary is also reported in table 4.5.

Total dose distributions					
	Valley dose	PVDR	Penumbra	Proportion of primaries	Proportion of secondaries
↗ c-t-c	↘	↗	-	*Peak:* contribution ≃ *Valley:* contribution ↘, from deeper point	*Peak:* contribution ≃ *Valley:* contribution ↗
↗ Z	↘	↗	↘	*Peak:* contribution ≃ *Valley:* contribution ↘, from deeper point	*Peak:* contribution ≃ *Valley:* contribution ↗

Secondary dose distributions			
		δ-rays	Nuclear fragments
↗ c-t-c	Peak	contribution ≃	contribution ≃
	Valley	dominant until shallower depth	dominant from shallower depth
↗ Z	Peak	dominant until shallower depth	↗ gradient, dominant from shallower depth
	Valley	↗ energy, dominant until deeper depth	dominant from deeper depth

Fragments type and yield			
	Fragments yield	Presence of light (lower LET) species	Presence of heavy (higher LET) species
Peak	↗ when Z ↗	+++	+
Valley	↗ when Z ↗ ↘ when c-t-c ↗	+	-

Table 4.5: *Summary of the relevant results obtained in this work.*

In this work, the very small beam widths and penumbras, remarkably smaller for the heaviest ions, allowed to maintain a spatial fractionation of the dose (pattern of peaks and valleys) in normal tissues for all c-t-c and projectile ions considered. Low valley doses were obtained in normal tissues, including the tail region, where the doses were lower than 8% of the prescription dose for any primary ion. A significant reduction ($< 2.5\%$) was observed when the c-t-c was enlarged. In addition, extremely high PVDR values (> 100), much superior that those observed in x-rays MBRT [Prezado 2009b], for which the sparing effect has already been proven, and than in pMBRT [Prezado 2013], were found. In general terms, the higher the Z, the lower the valley dose, thus the higher the PVDR. In the same manner, the larger the c-t-c distance was, the lower the valley dose and therefore, the higher the PVDR values. Although the spatial fractionation was also kept in the tumour (SOBP), several studies have observed a preferential damaging effect in tumour with spatially fractionated techniques, even with highly inhomogeneous dose distributions. However, if needed, a homogeneous dose distribution can be achieved by interlacing several arrays (*e.g.* two with a c-t-c of 1400 μm) in the tumour [Serduc 2010, Prezado 2012b, Prezado 2013].

A special attention was given to the secondaries distribution and nuclear fragments yields, especially in valleys. It was found that the peak dose was mainly due to the contribution of primaries, while, in contrast, the valley dose was mostly fed by secondaries (gammas, δ-rays and nuclear fragments). Although the yields of secondary nuclear fragments (high LET) were more important with higher-Z projectiles, the dose being deposited by the nuclear fragments in the valleys started to be the dominant contribution over δ-rays at deeper points, thus helping in the sparing of proximal normal tissues. Among the nuclear fragments, the lightest species (neutrons and protons) were the most abundant in both peak and valley regions. The neutron contribution to the dose in the normal tissues was found to be very low. In addition, according to the spectra, the neutron biological dose should not exceed 0.00025% of the SOBP dose in the valley. They should not be an issue in such irradiations, although this has to be confirmed by experiments. The heavier fragments, less numerous, were found to be more concentrated in the peak, and their yield reached very low values when moving away from the peak centre. The above mentioned observations, associated to higher PVDR values, might suggest a preferential use of larger c-t-c distances (3500 μm) in order to minimise the contribution of heavier fragments (higher LET) in valleys, and thus to favour tissue sparing.

In conclusion, the use of spatially fractionated very heavy ion beams seems to offer several dosimetric advantages over x-rays and proton MBRT, although only biological experiments should confirm the shifting of the normal tissue complication probability curves. The results presented in this section thus support a further exploration of this avenue. In order to be able to correlate dosimetric features with biological observations, an evaluation of the LET maps both with MC calculations and experimental measurements could be of particular interest. Consuelo Guardiola (post-doctoral researcher in the NARA team) and collaborators have developed a silicon-based three-dimensional microdosimeter that could be suitable for such eva-

luations. It consists of an array of micro-sensors that have 3D cylindrical electrodes of 15 μm diameter and a depth of 5 μm within a silicon membrane, resulting in a well-defined micrometric radiation sensitive volume [Guardiola 2015]. The performances of these microdetectors have been characterised in a high-LET environment, and have demonstrated the capability to measure dose and LET at charged particle therapy facilities.

Moreover, one strategy to further enhance this novel approach would be the exploration of thinner beams, in order to enhance the dose-volume effect. Indeed, this work only explored 700 μm-wide minibeams. In contrast to pMBRT, the Bragg peak was not significantly reduced with such beam sizes, thanks to the low Coulomb scattering of very heavy ions. This means that the use of thinner beams would be conceivable. Evaluation of this aspect is currently ongoing by Wilfredo Gonzales-Infantes, post-doctoral researcher within the NARA team. The primary results have shown that a reduction of the beam size would be possible, however it would be inadequate to use beams thinner than 300 μm, even with the reduced lateral scattering of such ions.

Chapter 5

Final Discussion & Conclusions

Since its birth in 1895, RT has continuously evolved until becoming an efficient treatment option for a large number of cancers. At the very beginning of RT, the best hope for a patient receiving a treatment was a shrinkage of the tumour size and pain relief. Since then, higher dose conformality can be achieved thanks to cutting-edge technologies such as the integration of 4D-CT for planning, IMRT and IGRT. These advances have allowed to reduce side effects in normal tissues and to escalate the dose in the tumour, making RT curative in a large number of cases. In charged particle therapy, evolutions appeared more slowly due to the costly requirements of the technique, but the current developments are following the same trend, with the advent of IMPT, imaging in the treatment room and on-line monitoring of treatment delivery thanks to prompt-gamma imaging [Min 2006], *in vivo* PET imaging [Parodi 2007] or even the "ionoacoustic" approach [Assmann 2015]. Techniques for the management of organ motions in particle therapy also start to be investigated at hospitals [De Ruysscher 2015]. In addition, inaccuracies linked to the determination of stopping powers in patient needed for dose planning could be overstepped by the use of particle-CT (preliminary developments for proton-CT nowadays) instead of x-rays CT [Hansen 2015]. When such techniques and verification approaches will be fully implemented at clinical facilities, they will further improve the accuracy of particle therapy treatments.

In the history of RT, the major evolutions have been mostly guided by technological advances, leaving biology in the background. However, they have reached a kind of plateau today, and further technical developments are expected to increase only slightly the therapeutic index of RT, but not to radically change the outcome for difficult cases like radio-resistant tumours. As today, RT treatments have been mainly restricted to an empirical delivery scheme that has been established at the inception of the technique. Indeed, RT mainly employs a temporal fractionation scheme of 2 Gy/fraction, with a delivery dose-rate of 2–6 Gy/min, using homogeneous irradiation fields of several squared centimetres. The influence of these parameters has started to be explored only recently, triggered by the recent radiobiological discoveries shaking up, even contradicting, the established concepts. The radiation-induced bystander effects or abscopal effects that include additional death, mutation and radio-adaptation in non-irradiated cells, are one example. We know today that radiation physics and biology are closely intertwined, and that the biological response to RT should be significantly modulated by the variation of one of the aforementioned physical parameters. By exploring new irradiation paradigms,

it could thus be possible to enhance the therapeutic index of RT for diseases with poor prognosis.

This *Ph.D.* thesis started in this context, at a time when new irradiation approaches that break the established paradigms of RT are emerging, in order to optimise physics-related parameters of RT to take full advantages of the underlying biology. The goal of this work was to probe the dosimetric advantages of two innovative avenues: proton and very heavy ion MBRT. They combine the more selective energy deposition of charged particles (and their biological effectiveness) to the well-established normal tissue sparing of MBRT, as a mean to further reduce the side effects of radiations. Although this exploratory work is at present not so close from future clinical implementations, it gives, along with other pioneer studies, a new direction for the evolution of RT that could certainly modify the clinical practice in the near future.

Along this line, my *Ph.D.* thesis was devoted to the evaluation of the two aforementioned innovative RT techniques. The first objective was the realisation of the experimental proof of concept of proton MBRT (pMBRT) by means of a mechanical collimation at a clinical facility (ICPO). This allowed validating the theoretical predictions [Prezado 2013]. In addition, possible optimisations of the technique, both in terms of irradiation setup and minibeam generation were evaluated in a MC study. In particular, the possible advantages of the second possible strategy for minibeams generation in pMBRT, the use of a magnetic collimation, were investigated. In the second part of this *Ph.D.* work, a potential renewed use of neon and heavier ions (Si, Ar and Fe) in therapy was explored by means of MC simulations. A particular attention was given to the possible contamination of valleys by the high-LET secondary fragments produced in nuclear reactions. These studies, carried out in *Chapters 3 & 4*, have shown promising dose distributions for both proton and heavy ion MBRT: PVDR values higher or in the same order as x-rays MBRT, low valley doses and narrow penumbras (from 50 to 1500 μm in normal tissues) were obtained. In this work, only physical evaluations of the techniques were performed. Indeed, the biological responses of tissues to both techniques might significantly differ from those of conventional charged particle therapy. For example, non-targeted effects such as cohort effects might play a significant role in spatially fractionated techniques. Hence, the commonly employed quantities describing the biological response of a tissue exposed to radiations with respect to standard conditions, such as RBE or OER, are thus likely not to be valid anymore. These quantities would need to be re-evaluated in the particular case of spatially fractionated techniques.

The different properties of protons and heavier ions will lead to different types of dose distributions and also probably different biological outcomes. Each type of therapy has its advantages and disadvantages compared to each other. An overview is given in table 5.1. In the light of their own specificities, proton and very heavy ion MBRT have to be addressed in distinct ways as for a potential forthcoming clinical implementation at hospitals. The differences will be discussed hereafter.

The first difference between the two techniques concerns the dose distribution

Strengths and weaknesses of the two techniques	
pMBRT	Very heavy ion MBRT
✓ Homogenisation at the target with one array	X Fractionation at the target (may need interlacing)
X Bragg peak reduction (700 μm)	✓ Bragg peak preservation (700 μm)
✓ No projectile fragmentation	X Projectile fragmentation (high-LET fragments)
≃ Potential enhanced biological properties/x-rays	✓ High RBE & low OER at the target
✓ Protons available in several clinical facilities	X Heavy ions available in few facilities for reasearch
✓ Mechanical & magnetic collimations conceivable	X Magnetic collimation preferable

Table 5.1: *Overview of advantages and drawbacks of pMBRT and very heavy ion MBRT.*

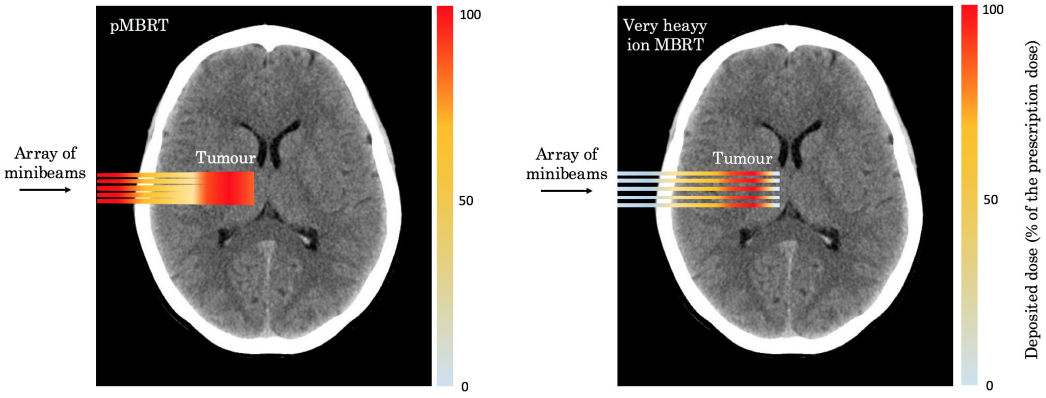

Figure 5.1: *Schematic representation of the dose distributions obtained after an irradiation with one array of protons (left) and very heavy ions (right) sub-millimetric minibeams.*

at the target, as schematically depicted in figure 5.1. With protons, only one single array of minibeams is sufficient to obtain a homogeneous dose distribution at the target position while ensuring at the same time a spatial fractionation in the normal tissues. In contrast, with very heavy ions, the spatial fractionation is maintained at all depths, even at the target level, thanks to their reduced Coulomb scattering. It must be highlighted that PVDR in the normal tissues are higher than those in pMBRT. The use of several arrays of minibeams, interlacing at the target position with the aim of obtaining a more uniform dose distribution, might be needed for tumour control. Although previous works have demonstrated some tumour control with inhomogeneous dose distributions in x-rays MBRT (for example in [Prezado 2012b]), only biological experiments could confirm similar results with charged particles. An interlaced geometry requires a high micrometric precision to position the arrays [Serduc 2010, Prezado 2012b], thus making the implementation more complex. In that sense, the use of one unique array in pMBRT simplifies the technical issues.

Another difference comes from the depth dose distribution in the peak region, also depicted in figure 5.1. With protons, the Bragg peak is reduced due to the important ratio of scattered protons with respect to the beam dimension. In order to minimise this effect and profit from the large energy deposition at the end of the

protons range, the use of larger beams (few millimetres) was evoked in *Chapter 3*. It was theoretically shown that it would be possible to obtain a similar dose distribution (spatial fractionation plus homogenisation in depth) with such larger beams. A first hint of a maintain of a sparing effect with supra-millimetric minibeams has already been observed during the first pMBRT biological experiments, where the irradiation setup employed provided beams widths comprised between 1 and 1.2 mm within the rats' head. A gain in tissue sparing was observed with such a minibeam pattern with respect to broad beam irradiations. Concerning heavy ions, the depth dose curves obtained when using 700 μm-minibeams does not significantly differ from the standard (conventional charged particle therapy) shape, thanks to the reduced Coulomb scattering. In contrast to protons, a reduction of the minibeam size could still be conceivable with heavy ions, further enhancing the dose-volume effect. The first tests carried out by a post-doctoral researcher of the team suggest that very heavy ion beams narrower than 300 μm lead to a significant reduction of the Bragg peak intensity.

Besides, one disadvantage of heavy ions over protons is the fragmentation of the projectile ions producing, among others, high-LET heavy secondary fragments that could contaminate the valley region. However, their contribution might be minimised by favouring the use of heavier ions and larger c-t-c, as explained in *Chapter 4*. In addition, some of the fragments are responsible for the fragmentation tail extending beyond the Bragg peak, delivering an undesired dose to the distal normal tissues. Hopefully, the tails were very low with respect to the SOBP dose in the theoretical study. This has to be confirmed with experimental measurements. In contrast, with proton beams, only target fragmentation can occur. The main participant to the valleys were found to be primary protons, and secondary protons coming from target fragmentation. No significant variations of LET (RBE) are thus expected between peaks and valleys in pMBRT, in contrast to very heavy ions.

Finally, one major advantage of pMBRT is the existence of more accessible proton therapy facilities around the world. According to the PTCOG, as today there are 60 facilities in operation, 31 under construction and 17 under planning stage [PTCOG 2016]. In contrast, few installations in the world allow the production of ions heavier than oxygen, which limit an extended exploration at the moment. However, in-depth studies such as the one performed in this *Ph.D.* might potentially trigger the developments of very heavy ion beamlines in existing structures.

As already discussed along the manuscript, two collimation methods may be considered to generate charged particles minibeams: a mechanical collimation method, or a magnetic focusing method that would consist in collimating the beam thanks to quadrupole magnets (with or without the need for additional beam shapers). The mechanical method has been selected for the first technical implementation of pMBRT at a clinical facility. As presented in *Chapter 3*, even with a first setup using prototypes of multislit collimators, a combination of spatial fractionation in normal tissues and dose homogenisation at the Bragg peak was obtained. Further optimisations of the irradiation setup might lead to significant increase of PVDR values as well as reduction of the FWHM [Guardiola 2016], thus increasing the dose-volume

effect. Concerning very heavy ions, only a magnetic collimation was assessed in the theoretical proof of concept proposed in *Chapter 4*. Indeed, a mechanical collimation will not be suitable with such heavy ions: an important thickness of absorber material would be certainly needed, which would significantly reduce the OF and consequently increase the irradiation time. In addition, it may also lead to a high production of secondaries that might contaminate the valleys (and maybe reduce the PVDR values) and cause radioprotection issues.

To conclude, I demonstrated in this work that the upkeep of a spatial fractionation of the dose is possible with charged particles, even with protons that are subject to important lateral scattering. This latter has been experimentally proven thanks to the first technical implementation of pMBRT at a clinical facility in the world [Peucelle 2015a]. The high PVDR values obtained, along with low valley doses, would allow keeping the dose under the tolerances for broad beam in both pMBRT and very heavy ion MBRT even with a high prescription dose (50 Gy in 1 fraction). Dose homogenisation is either possible with one single array, when a correct beams arrangement is employed, or by interlacing several arrays. To preserve a reasonable Bragg peak-to-entrance dose ratio in the depth dose distribution, the ideal minimum beam width to be used differs from one technique to another: sub-millimetric beams can still be used with very heavy ions, while supra-millimetric beams are needed in pMBRT. However, even with such larger fields, a gain in tissue sparing was already emphasised in the first biological experiments, as explained in section 3.2.5. Further optimisations of these techniques are possible in terms of irradiation setup, for instance larger c-t-c values could be explored in very heavy ions MBRT, in order to avoid the participation of high-LET components to the valleys.

The main results of this work have been compiled in two articles in the *Medical Physics* journal [Peucelle 2015a, Peucelle 2015b] and presented in several international conferences. The related scientific production is reported in *Chapter 6*.

As perspectives of this work, many steps forward remain to be taken in the development of charged particle MBRT. Further optimisations of the minibeams generation have to be pursued, from both theoretical and technical points of view. In particular, the use of a magnetic focusing of the beam seems promising. The development of such a method for both proton and very heavy ions has to be promoted. A study is currently ongoing for proton beams at ICPO, in collaboration with our team. As previously mentioned, a first evaluation showed that the existing beamline in PBS configuration was not able to provide sub-millimetric beams, and some modifications of the nozzle need to be done to reach such small field sizes. Work is on progress on this point, with a planned patent. The mechanical collimation method for pMBRT, more simple but which demonstrated interesting results, also deserves further explorations. Optimisations are currently under consideration, in particular with the work of Consuelo Guardiola. In addition, an experimental assessment of the neutron yields would allow to confirm that neutron contamination should not be an issue, as stated in the MC optimisation study [Guardiola 2016].

Besides, the development of a dedicated planning system is absolutely needed for

further improvements of pMBRT, especially to guide a second series of biological experiments. This system will have to accurately model the multiple Coulomb scattering suffered by the minibeams, as it strongly impacts the ratio between the entrance and Bragg peak dose. At present, MC physics models remain limited by the lack of cross sections data, especially for very heavy ion beams. These parameters are nonetheless a key factor in dosimetric studies. Improvements are thus needed in this domain in order to enhance the accuracy of predictive MC calculations. The development of a first MC calculation engine for pMBRT applications has already started within the team, in which I participated during my *Ph.D.* thesis. Eventually, the best way to proceed with clinical implementation of pMBRT will be the conception of an inverse planning system that will be able to describe the optimised collimator (in the case of a mechanical collimation) or beams arrangement (for a magnetic collimation) starting from objectives such as PVDR values at the target and at several points in the normal tissues.

In any case, the development of charged particle MBRT absolutely needs to be associated with biological experiments that will confirm or invalidate the gain in terms of normal tissue sparing. They have already started with a first series of normal rats irradiated (whole brain) both in pMBRT and broad beam conditions with a same average dose of 25 Gy (peak dose of 58 Gy). The irradiations were performed in one single fraction. A confirmation of the gain in normal tissue sparing with pMBRT has been already obtained at the end of this experiment. A second series of experimentations, with tumour-bearing rats, is now under planning in order to prove the effectiveness of pMBRT for tumour control. Concerning very heavy ions, no biological experiments have been performed nor are planned at present. The HIMAC facility in Japan is as today one of the very few facilities providing neon and heavier ion beams with clinically relevant energies where animal irradiations are possible. As a middle-term goal, we plan to perform biological experiments at that facility.

To correlate the biological observations with dosimetry, a first step would be the assessment of the LET quantity, which is known to be closely related to the biological effectiveness of radiations. This could be done thanks to a silicon-based three-dimensional microdosimeter that have demonstrated the capability to measure dose and LET at charged particle therapy centres [Guardiola 2015], and preliminary measurements are already planned at ICPO. A high gain in biological efficiency might be expected from minibeams of very heavy ions, that have large LET at the end of their range. This could be an asset if high-LET components are minimised in the valley region. The best case would be a high differential in the mean LET value between the peaks and the valleys. The use of proton minibeams (considered as low-LET radiations) will probably not enhance the biological efficiency as much as heavy ions, however, recent studies in conventional proton therapy have showed RBE greater than 1.1 in the distal part of the Bragg peak due to LET increase. In addition, there are emerging evidences that proton radiations might have distinct biological properties with respect to other low-LET radiations (x-rays), such as complex DNA damage-inducing capacity, enhanced ability to inhibit tumour invasion

and angiogenesis, and modulation of inflammation [Girdhani 2013], thus probably impacting their biological effectiveness. These hypotheses have to be investigated in MBRT configuration.

Finally, in the long term, reflections should be carried out about the future medical practice of charged particle MBRT. In particular, the questions of the need for new recommendations for the definition of target volumes for spatially fractionated techniques, or for dose prescription (in terms of peak dose or average dose), will have to be addressed.

As a final conclusion, both techniques exhibit favourable dosimetric characteristics that deserve to be further exploited. These pioneer projects will help in the elimination of the main barrier in RT treatments: the tolerance doses of normal tissues. They can open the door to an efficient treatment of very radio-resistant tumours, like gliomas. In addition, they can specially benefit paediatric oncology (brain and central nervous system). As previously mentioned, the main targets of charged particle MBRT will be likely neurological cases in a first phase. In other locations that are subject to (even small) movements during an irradiation course, there is a risk for blurring the minibeams pattern in the normal tissues. For the same reason, such treatments will be likely given in one single fraction, to avoid any risk of array misplacement when re-irradiating at the same entrance, that would make the spatial fractionation degrade or vanish. If a high biological effectiveness is demonstrated, very heavy ion MBRT could be a valuable tool for the treatment of hypoxic radio-resistant tumours for which other conventional treatments have failed. The possible targets of pMBRT also include the treatment of radio-resistant tumours. Thanks to the homogenisation reached at the Bragg peak with only one array, possible applications in radiosurgery for treatment of arteriovenous malformations, vestibular schwannomas or meningiomas, to cite a few, are also conceivable. Also, the reduced penumbras make it a promising candidate for use for the treatment brain disorders, like trigeminal neuralgia or epilepsy.

If the effectiveness of pMBRT is confirmed in tumour experiments, such a technique would be more accessible due to lower costs of proton beams. Nevertheless, if very heavy ion MBRT is proven to be efficient, it will be a huge breakthrough for the treatment of very radio-resistant (hypoxic) tumours. Moreover, results from the basic and preclinical RT research carried out within these projects will have a direct relevance not only for MBRT but for standard proton therapy and x-rays RT: the radiobiological knowledge acquired about spatial fractionation will certainly serve other forms of RT. Furthermore, the results of charged particle MBRT are predicted to make hadron therapy in general more amenable to administration in either a single dose fraction or in a very small number of fractions, which would significantly reduce the costs.

This exploratory study gives new insights for the evolution of RT. Continuous efforts should be provided in that direction, in order to make RT become an even more powerful and efficient treatment against cancer.

Chapter 6

Scientific Production

Articles in peer-reviewed international journals

C. Peucelle, I. Martínez-Rovira and Y. Prezado. Spatial fractionation of the dose using neon and heavier ions. *Med. Phy.* 42 (10), 2015.

C. Peucelle, C. Nauraye, A. Patriarca, E. Hierso, N. Fournier-Bidoz, I. Martínez-Rovira and Y. Prezado. Proton minibeam radiation therapy: experimental dosimetry evaluation *Med. Phy.* 42 (12), 2015.

C. Guardiola, **C. Peucelle** and Y. Prezado, Optimization of minibeam generation in proton minibeam radiation therapy by means of a mechanical collimation, *submitted to Med. Phys., on June 2016.*

Oral presentations in international conferences

C. Peucelle, I. Martínez-Rovira and Y. Prezado. Exploring new paths in particle therapy: a Monte Carlo study on the use of spatial fractionation of the dose, September 2014, 8th European Conference on Medical Physics, Athens, Greece.

C. Peucelle, I. Martínez-Rovira and Y. Prezado, Spatial fractionation of the dose in heavy ion therapy: a Monte Carlo study, April 2015, 3rd forum of European Society for Radiotherapy and Oncology, Barcelona, Spain.

C. Peucelle, C. Nauraye, A. Patriarca, E. Hierso, N. Fournier-Bidoz, I. Martínez-Rovira and Y. Prezado, Proton Minibeam Radiation Therapy (pMBRT): implementation at a clinical center, June 2015, World Congress on Medical Physics and Biomedical Engineering, Toronto, Canada.

C. Peucelle, C. Nauraye, A. Patriarca, L. de Marzi, E. Hierso, N. Fournier-Bidoz, I. Martínez-Rovira and Y. Prezado, Proton Minibeam Radiation Therapy (pMBRT): implementation at a clinical center, February 2016, International Conference on Translational Research in Radio-Oncology - Physics for Health in Europe, Geneva, Switzerland.

Chapter 7

Résumé du travail de thèse en français

Contents

7.1 Contexte du projet de thèse 147
7.2 Principaux résultats 151
7.2.1 Implémentation de la pMBRT dans un centre clinique 151
7.2.2 Impact de divers paramètres d'irradiation en pMBRT 155
7.2.3 Fractionnement spatial avec des ions plus lourds 158
7.3 Discussion & Conclusions 161

7.1 Contexte du projet de thèse

Le terme "cancer" concerne un grand groupe de maladies caractérisées par une prolifération rapide de cellules anormales qui peuvent envahir des parties adjacentes de l'organisme, puis essaimer dans d'autres organes par la circulation sanguine ou les voies lymphatiques [WHO 2015]. La radiothérapie (RT) est, avec la chimiothérapie et la chirurgie, l'un des traitements les plus efficaces et répandus contre le cancer de nos jours. Son objectif est de délivrer une dose curative de rayonnements ionisants ciblés dans la tumeur à traiter, tout en préservant l'intégrité des tissus sains environnants. Malgré de constants progrès, cette modalité reste aujourd'hui insatisfaisante lorsque l'administration d'une dose thérapeutique à la tumeur est limitée par la tolérance des tissus sains avoisinants. C'est le cas de certaines tumeurs radiorésistantes, proches d'organes sensibles, et certains cancers pédiatriques. Parmi les voies explorées pour améliorer l'issue d'un traitement, l'hadronthérapie qui utilise des faisceaux de particules chargées (protons et ions plus lourds) à la place des faisceaux de rayons X (RX) classiques, trouve son intérêt dans un ciblage plus précis de la tumeur. Contrairement aux RX dont le dépôt maximal d'énergie est atteint dès les premiers centimètres de matière traversée puis s'atténue en profondeur, les particules chargées présentent la particularité d'être stoppées dans la matière à une profondeur connue, déposant la plus grande partie de leur énergie en fin de parcours, dans une zone appelée pic de Bragg. Un second avantage se trouve dans leur efficacité biologique accrue. Pour une même dose absorbée par les tissus, les

particules chargées induisent des effets biologiques plus importants que des RX, du fait de l'initiation d'une plus importante densité d'ionisations sur leur parcours.

Mon projet de thèse s'inscrit dans un contexte d'amélioration de l'efficacité de l'hadronthérapie, en y associant une innovation permettant de minimiser les dommages aux tissus sains: un fractionnement spatial de la dose. Cette particularité a notamment été développée pour la Minibeam Radiation Therapy (MBRT) [Dilmanian 2006], technique utilisant originellement des rayonnements synchrotron (RX de faible énergie). Avec cette technique, le faisceau d'irradiation est segmenté en franges de dimensions submillimétriques (dits mini-faisceaux), à la manière d'un peigne. En résulte une irradiation inhomogène, présentant des zones de doses élevées (pics) suivant la trajectoire des mini-faisceaux et de faibles doses (vallées) dans l'espace entre deux mini-faisceaux, comme illustré en figure 7.1. Ces irradiations segmentées sont en rupture avec les paradigmes actuels de la radiothérapie pour laquelle des champs "pleins" sont utilisés. De récentes études menées avec des faisceaux de RX ont prouvé que cette technique permet une meilleure préservation des tissus sains [Deman 2012, Prezado 2015], tandis qu'un retard dans la croissance de tumeurs agressives a été observé [Prezado 2012b]. La distance séparant le centre de deux mini-faisceaux est usuellement nommée "centre-to-centre distance" et est notée "c-t-c". Le rapport des doses dans le pic et dans la vallée est appelé "peak-to-valley dose ratio" (PVDR). Le PVDR dépend de l'énergie du faisceau incident, de sa largeur, ainsi que l'espacement des mini-faisceaux, de la dimension du champ d'irradiation et de la composition des tissus. Il a été démontré que la préservation des tissus sains requiert des PVDR élevés associés à de faibles doses dans les vallées [Dilmanian 2002].

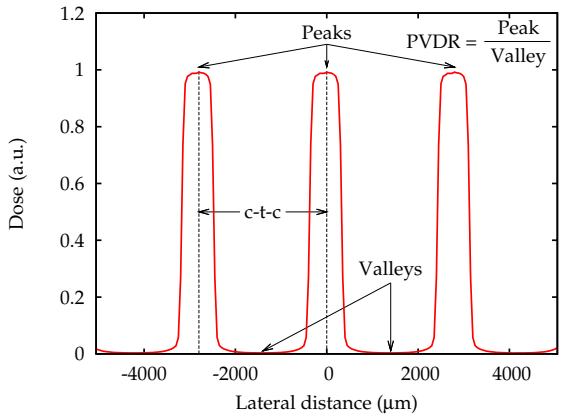

Figure 7.1: *Exemple d'un profil latéral de dose obtenu en MBRT. Plusieurs paramètres dosimétriques pertinents pour les techniques de fractionnement spatial sont représentés. Le rapport des doses dans le pic et dans la vallée est appelé "peak-to-valley dose ratio" (PVDR). La distance séparant le centre de deux mini-faisceaux est appelée "centre-to-centre distance" et est notée "c-t-c".*

Les mécanismes biologiques qui entrent en jeu lors d'une irradiation par MBRT

ne sont pas encore totalement compris à ce jour. Un des principaux acteurs favorisant la préservation des tissus sains serait l'effet "dose-volume": plus la dimension du faisceau de rayonnement est réduite, plus la dose tolérée par un tissu sain est importante [Hopewell 2000]. Un autre effet pourrait être lié à la migration des cellules endothéliales et gliales des vallées (zones de faible dose) vers les pics (zones fortement irradiées) dans le but d'y réparer le tissu endommagé [Dilmanian 2002]. D'autres effets dits "non-ciblés" tels que l'effet abscopal [Siva 2015, Fernandez-Palomo 2015], ou l'effet de cohorte [Marín 2015] pourraient également jouer un rôle.

Mon travail de thèse a consisté à évaluer le potentiel du fractionnement spatial dans le cadre de l'hadronthérapie, aux moyens de simulations Monte Carlo (MC) et de travaux expérimentaux. Il s'articule en deux axes:

- **Proton Minibeam Radiation Therapy (pMBRT)**: contrairement aux autres techniques de fractionnement spatial où la segmentation des mini-faisceaux est maintenue jusqu'au niveau de la tumeur, lors d'une irradiation avec un peigne de mini-faisceaux de protons, une distribution quasi-homogène est obtenue au niveau du pic de Bragg. Lors d'un traitement, les tissus sains situés avant le pic de Bragg pourraient alors être épargnés par le fractionnement spatial, tandis que la tumeur serait couverte de façon homogène. Cette propriété est due aux diffusions latérales multiples subies par les protons lors de leurs interactions avec la matière.

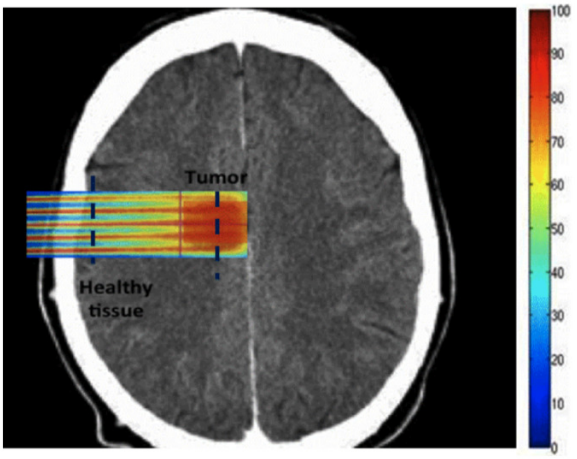

Figure 7.2: *Illustration de la distribution de dose obtenue après une irradiation d'un crâne par pMBRT. Tandis que les tissus sains bénéficient d'un fractionnement spatial de la dose, la tumeur reçoit une dose quasi-homogène. Extrait du travail de Martínez-Rovira et al. [Martínez-Rovira 2015].*

Les bases physiques de la technique pMBRT ont déjà été établies lors de travaux antérieurs [Prezado 2013]. Dans ce contexte, les objectifs de ma thèse furent les suivants: (i) mener à bien la première implémentation tech-

nique et l'évaluation expérimentale de la pMBRT dans un centre clinique (Institut Curie - Centre de Protonthérapie d'Orsay) au moyen d'une collimation mécanique et (ii) évaluer le potentiel d'une collimation magnétique au moyen de simulations MC, ainsi que d'évaluer l'impact de différents paramètres d'irradiation sur les distributions de dose.

- **Fractionnement spatial avec des faisceaux d'ions très lourds**: le traitement des tumeurs radiorésistantes, et en particulier des tumeurs hypoxiques, reste l'un des défis majeurs en RT. En effet, l'hypoxie tumorale conduit à une résistance à la RT conventionnelle ainsi qu'à la chimiothérapie, et prédispose à l'apparition de métastases [Brown 2007]. Les tumeurs hypoxiques sont moins sensibles aux RX que les tumeurs avec un niveau normal d'oxygénation. Avec des ions lourds en revanche, cette dépendance à la concentration en oxygène est beaucoup moins marquée (on parle alors de faible "Oxygen Enhancement Ratio", ou OER). Ceci est dû à la création d'une colonne d'ionisation suffisamment dense pour induire des nombreuses cassures directes des brins d'ADN, conduisant ainsi à des dommages souvent non-réparables par les mécanismes cellulaires habituels (voir la figure 7.3 à droite). Malheureusement, la région biologiquement plus efficace ("Efficacité Biologique Relative", ou EBR, élevée) de ces ions très lourds s'étend également dans les tissus normaux situés avant la tumeur (voir figure 7.3 gauche), provoquant d'importants effets délétaires.

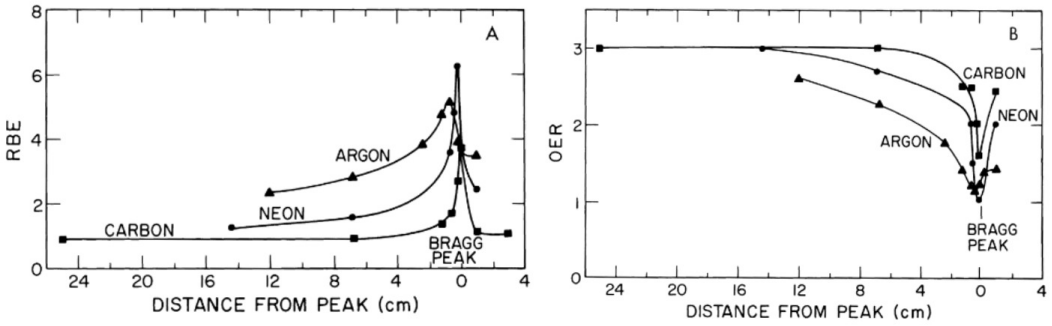

Figure 7.3: *Valeurs d'EBR (A) et d'OER (B) obtenues sur des cellules humaines mises en culture, considérant un niveau de survie de 10%, tracées en fonction de la distance à la position du pic de Bragg. Tandis que l'EBR pour les ions carbone est proche de 1 dans les tissus proximaux, puis augmentent fortement à l'approche du pic de Bragg, avec des ions plus lourds l'EBR est déjà élevé et n'augmente que peu au niveau du pic de Bragg. Les valeurs d'OER sont très faibles (proches ou égales à 1) au niveau du pic de Bragg avec des ions très lourds, tandis qu'elles restent élevées avec des ions carbone, pour lesquels un effet oxygène est maintenu. Adapté du travail de Tobias et al. [Tobias 1977].*

De tels faisceaux ont été utilisés par le passé pour traiter certains patients atteints de tumeurs hypoxiques, mais les traitements ont dû être rapidement abandonnés suite aux sévères effets secondaires observés. La remarquable préservation des tissus sains observée en MBRT par RX pourrait permettre

de profiter de la capacité tumoricide élevée de ces ions très lourds, tout en réduisant au maximum leurs effets secondaires. Cette stratégie pourrait ouvrir la porte à une nouvelle utilisation des ions très lourds en RT. Le travail que j'ai effectué durant ma thèse constitue la première exploration d'une telle stratégie avec des ions néon et plus lourds (Si, Ar et Fe), exploitant le gain de tolérance des tissus sains offert par des mini-faisceaux segmentés spatialement. En particulier, cette étude visait à effectuer une étude physique (dosimétrique) avancée afin de déterminer si un avantage peut être attendu d'une telle nouvelle approche pour laquelle les grandeurs radiobiologiques pourrait certainement dévier des valeurs standards.

Les principaux résultats obtenus pendant cette thèse seront présentés dans la section suivante.

7.2 Principaux résultats

7.2.1 Implémentation de la pMBRT dans un centre clinique

La première implémentation technique de la pMBRT a été réalisée au Centre de Protonthérapie d'Orsay (ICPO) sur l'une des lignes de faisceaux utilisées en clinique pour les traitements ophtalmiques (protons de 100 MeV). Celle-ci a été réalisée à l'aide d'une collimation mécanique: le faisceau de protons est segmenté en un (mono-fente) ou plusieurs (multi-fentes) mini-faisceaux au moyen de collimateurs en laiton (5 cm d'épaisseur) spécialement conçus pour la pMBRT, comme illustré en figure 7.4. Quatre prototypes munis de différentes dimensions de fentes et de différents c-t-c ont été testés (voir tableau 7.1). Un collimateur additionnel de 2×2 cm^2, correspondant à la dimension d'un cerveau de rat (animal choisi pour les premières expérimentations biologiques) était positionné après le collimateur à fentes. Une étude dosimétrique a été réalisée grâce à deux types de détecteurs à haute résolution spatiale: des films Gafchromic© EBT3 et un détecteur PTW microDiamond©, dans un fantôme d'eau et un fantôme de plaques (matériau "solid water"). La réalisation de mesures expérimentales dans des tailles de champs si réduites constitue en elle-même un défi.

Caractéristiques des collimateurs			
Collimateur	Largeur des fentes	Nombre de fentes	c-t-c
Multi1	700 μm	5	3500 μm
Multi2	700 μm	5	2700 μm
Multi3	400 μm	5	3200 μm
Single	700 μm	1	N.A.

Table 7.1: *Caractéristiques des quatres prototypes de collimateurs à fentes étudiés durant ce travail.*

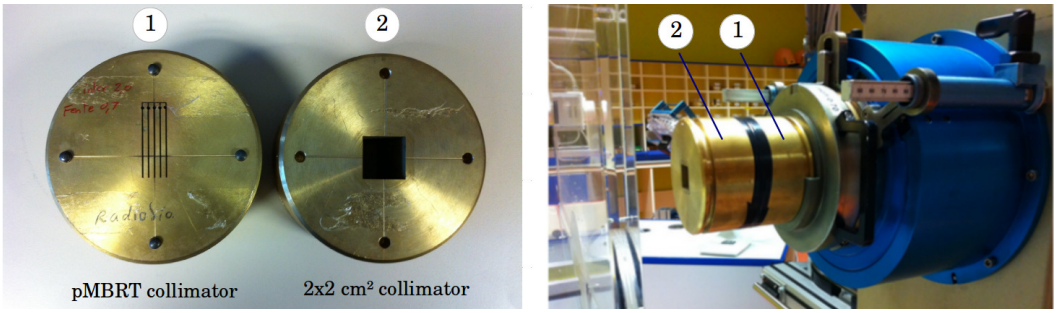

Figure 7.4: *Collimateurs multi-fentes et 2×2 cm^2 (à gauche). Le processus d'usinage utilisé crée des fentes de 3.5 cm de long. Afin d'obtenir le champ d'irradiation désiré (2 × 2 cm^2), un collimateur de section carrée doit être ajouté après le collimateur multi-fentes (à droite).*

Ce travail a confirmé que la distribution de dose produite par un peigne de mini-faisceaux de protons de 100 MeV pourrait permettre le traitement d'une lésion localisée au centre du cerveau (7.5 cm de profondeur, le pire cas pouvant être considéré) avec une dose homogène, tandis que les tissus sains dans la trajectoire des faisceaux pourraient bénéficier d'un fractionnement spatial, et ceci avec les deux types de détecteurs utilisés (voir figures 7.5 et 7.6). D'autre part, comme cela est présenté en figure 7.7, l'étude a montré que les courbes de rendement en profondeur au centre du pic central d'un peigne diffèrent d'une courbe de Bragg habituellement observée en protonthérapie. En effet, le pic de Bragg est réduit en raison de la proportion importante de protons diffusés par rapport à la dimension du faisceau.

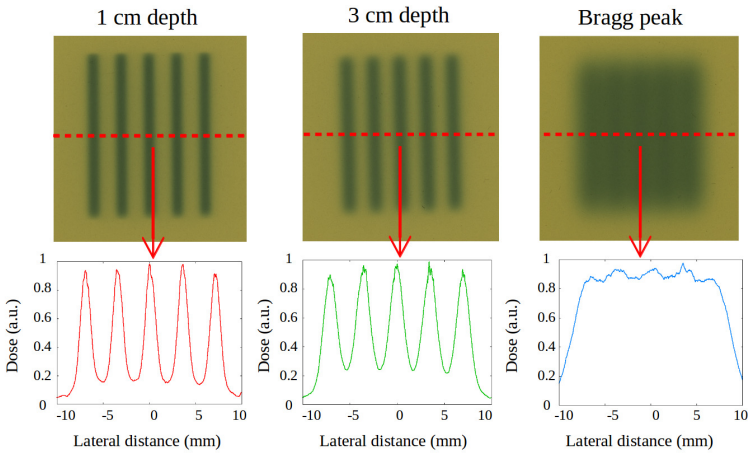

Figure 7.5: *Cette série de film irradiés à différentes profondeurs dans le fantôme de "solid water" (collimateur 700 µm/c-t-c 3500 µm) montre que le fractionnement spatial est maintenu dans les tissus sains, tandis qu'une distribution de dose quasi-homogène est obtenue au niveau du volume cible (pic de Bragg).*

Parmi les trois collimateurs multi-fentes étudiés, le collimateur 700 μm/c-t-c 2700 μm présentait les plus faibles valeurs de PVDR (maximum de 5.4 à l'entrée

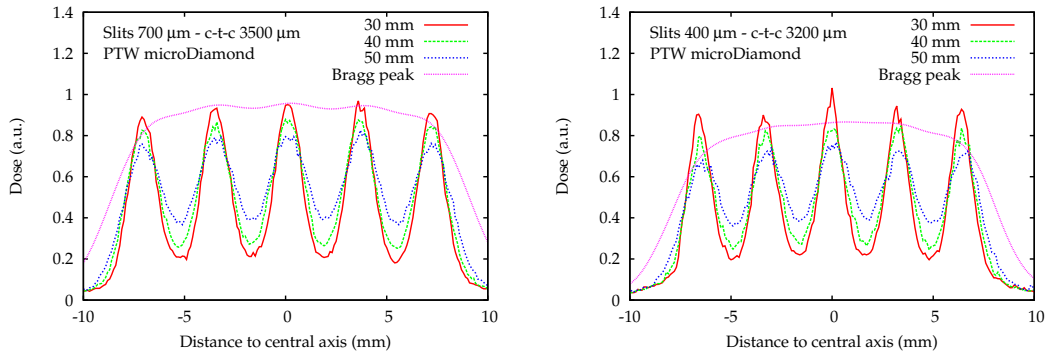

Figure 7.6: *Profils latéraux de dose obtenus à différentes profondeurs dans l'eau avec le détecteur PTW microDiamond© pour les collimateurs 700 µm/c-t-c 3500 µm (à gauche) et 400 µm/c-t-c 3200 µm (à droite).*

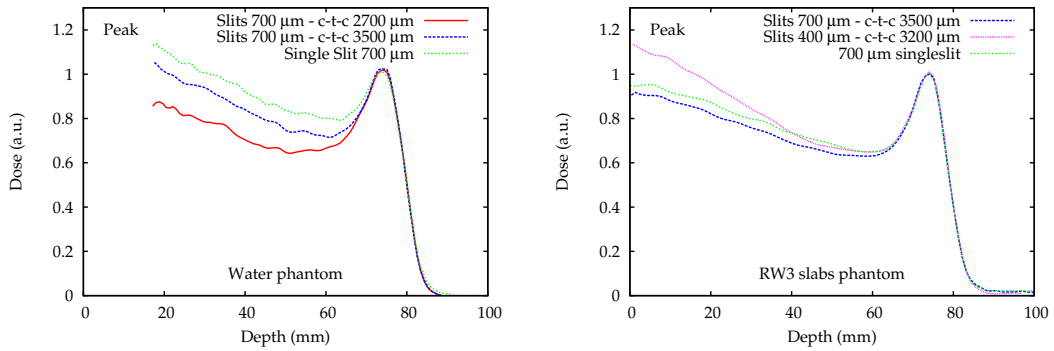

Figure 7.7: *Courbes de rendement en profondeur dans le pic central d'un peigne de mini-faisceaux obtenues dans l'eau (à gauche) et dans le matériau "solid water" (à droite). Chaque courbe est normalisée par rapport à la dose au pic de Bragg. Chaque couleur correspond à un collimateur.*

fantôme), et ne permettait pas de maintenir un fractionnement spatial jusqu'à la profondeur de pic de Bragg, en raison d'un c-t-c trop réduit (voir figure 7.8). Il a donc été jugé non approprié pour des applications en pMBRT. Les deux autres collimateurs Multi1 (700 μm/c-t-c 3500 μm) et Multi3 (400 μm/c-t-c 3200 μm) ont permis d'obtenir des PVDR plus élevés dans les tissus normaux (valeurs maximales autour de 8 à l'entrée fantôme), tout en permettant une homogénéisation de la dose au pic de Bragg. Ces valeurs sont malgré tout inférieures à celles obtenues en MBRT avec des RX, où ils atteignent environ 20 dans les tissus normaux [Prezado 2009b]. Malgré cela, un gain dans la préservation des tissus sains pourrait déjà être obtenu avec de tels PVDR, comme cela a déjà été confirmé dans une première étude biologique décrite ci-après. En outre, de futures optimisations de la technique (optimisation du collimateur, introduction d'une collimation magnétique) pourraient permettre d'obtenir des valeurs de PVDR supérieures.

Bien qu'une importante réduction du débit de dose fut observée avec les plus petites fentes (400 μm), celles-ci menèrent également à des dimensions de faisceaux

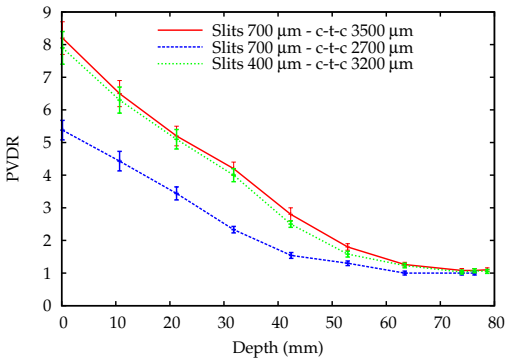

Figure 7.8: *PVDR en fonction de la profondeur mesurés avec des films EBT3 dans des plaques de "solid water" pour les trois collimateurs multi-fentes considérés.*

réduites dans le fantôme (déterminées à partir des "Full-Width at Half Maximum" ou FWHM). En ce sens, ce collimateur pourrait augmenter l'effet de volume de dose dans les tissus normaux. Le collimateur Multi3 est donc celui à privilégier parmi les trois prototypes présentés dans cette étude. Cependant, ce travail a également montré qu'une dimension de 400 μm constituait la limite inférieure en termes de largeur de fente avec ce setup expérimental, en raison d'une réduction significative de l'intensité du pic de Bragg (voir figure 7.7). Cette dimension constitue également une limitation technique en termes d'usinage.

Pour les raisons mentionnées ci-dessus, le collimateur Multi3 a été retenu pour la première étude pré-clinique sur des rats, qui a démarré à l'automne 2015. Mes travaux de thèse ont permis de fournir les connaissances dosimétriques nécessaires à la réalisation de cette première étude biologique. Des cerveaux des rats normaux ont été irradiés dans leur ensemble en protonthérapie classique (faisceau large) et en pMBRT avec une même dose moyenne de 25 Gy délivrée en une unique fraction, correspondant à une dose-pic maximale de 58 Gy en pMBRT. Le suivi des animaux a duré 7 mois, pendant lesquels des images IRM ont été acquises et des études histologiques ont été réalisées. D'importants dommages cérébraux et cutanés ont été observés chez les rats irradiés par protonthérapie conventionelle, tandis que, dans le groupe pMBRT, seule une épilation réversible s'est produite, et aucun dommage au cerveau n'a été observé.

Cette étude a donc permis de valider expérimentalement le concept de génération des mini-faisceaux au moyen d'une collimation mécanique. Malgré les défis dosimétriques imposés par cette technique (petites tailles de champ, variations du Transfert d'Energie Linéaire (TEL) du faisceau en fonction de la profondeur), des mesures ont été réalisées avec deux types de détecteurs: Gafchromic films © (EBT3) et un détecteur PTW microdiamond©. A notre connaissance, ces mesures sont les premières à avoir été effectuées dans de telles petites tailles de champ (submillimétriques) avec des faisceaux de protons. Les deux détecteurs étudiés ont montré des caractéristiques appropriées à la dosimétrie en pMBRT, et ont conduit à des résultats équivalents dans les barres d'incertitudes. Les principaux résultats de cette étude ont été publiés dans la revue scientifique *Medical Physics* [Peucelle 2015a].

7.2.2 Evaluation de l'impact de divers paramètres d'irradiation en pMBRT

Comme cela a été précédemment présenté, la première évaluation expérimentale de la pMBRT a été effectuée en utilisant une collimation mécanique. Bien que cette étude ait montré des résultats prometteurs, le potentiel de cette technique pourrait être encore mieux exploité en utilisant une génération magnétique des faisceaux. Une telle méthode pourrait être adaptée à partir des quadrupoles utilisés pour focaliser le faisceau de protons lorsqu'un balayage actif est utilisé. Les possibles avantages d'une collimation magnétique par rapport à une collimation mécanique sont les suivants: (i) une augmentation du débit de dose utilisable, (ii) une réduction du taux de création de neutrons secondaires grâce à l'élimination des éléments métalliques, (iii) une réduction des rayonnements diffusés qui alimentent les vallées (permettant donc d'obtenir des valeurs de PVDR plus élevées), et (iv) une implémentation plus flexible de la pMBRT, sans qu'il soit nécessaire de produire et d'optimiser des collimateurs individualisés pour chaque patient.

Cette seconde étude visait à explorer le potentiel d'une collimation magnétique, ainsi qu'à évaluer l'influence de différents paramètres d'irradiation sur les distributions de dose. Elle a été réalisée grâce à des simulations MC en utilisant le code Geant4/GATE. Les principales cibles de la technique pMBRT seront probablement des cas neurologiques pour lesquels les mouvements liés aux cycles cardiaques et respiratoires peuvent être facilement compensés. Dans cette étude, un fantôme cylindrique de dimensions proches d'une tête humaine (16 cm de longueur et 16 cm de diamètre) a donc été considéré. La direction du faisceau correspond à l'axe longitudinal du cylindre. Le fractionnement spatial a été réalisé dans la direction transversale. La carte de dose a été enregistrée dans un parallélépipède de dimension 4 cm × 5 mm × 16 cm situé au centre du fantôme d'eau. Une vue schématique de la géométrie simulée est représentée en figure 7.9. Pour simuler une collimation magnétique, un unique mini-faisceau a été simulé, puis un peigne fut créé en sommant la contribution de plusieurs mini-faisceaux en différentes localisations spatiales, afin de couvrir le champ d'irradiation désiré (2×2 cm^2).

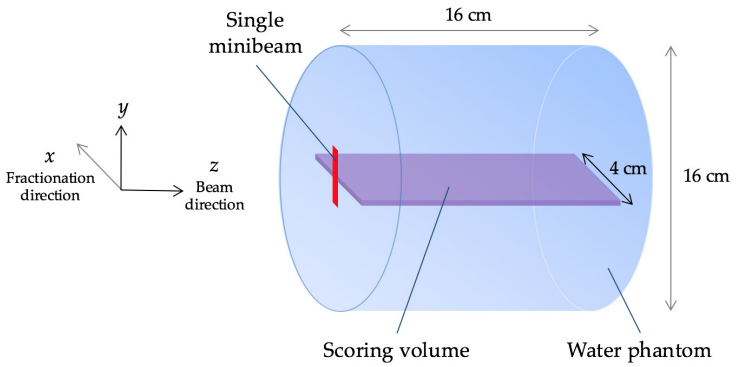

Figure 7.9: *Illustration de la géométrie simulée.*

Afin de confronter les distributions de dose en collimations magnétique et mécanique, des mini-faisceaux collimatés magnétiquement ont été simulés dans la même configuration que celle utilisée lors de l'évaluation expérimentale (*i.e.* même distance entre la naissance des mini-faisceaux et l'entrée du fantôme). Cette étude a souligné la forte contamination des vallées par les rayonnements diffusés quand une collimation mécanique est utilisée (voir figure 7.10). Ceci entraîne une diminution significative des valeurs de PVDR dans les premiers centimètres avec une collimation mécanique, comme visible sur la figure 7.11. L'utilisation d'une collimation magnétique a donc le potentiel d'offrir des PVDR plus élevés dans les tissus sains, bien que ceci devra être confirmé par des mesures expérimentales lorsqu'une telle méthode de collimation sera disponible.

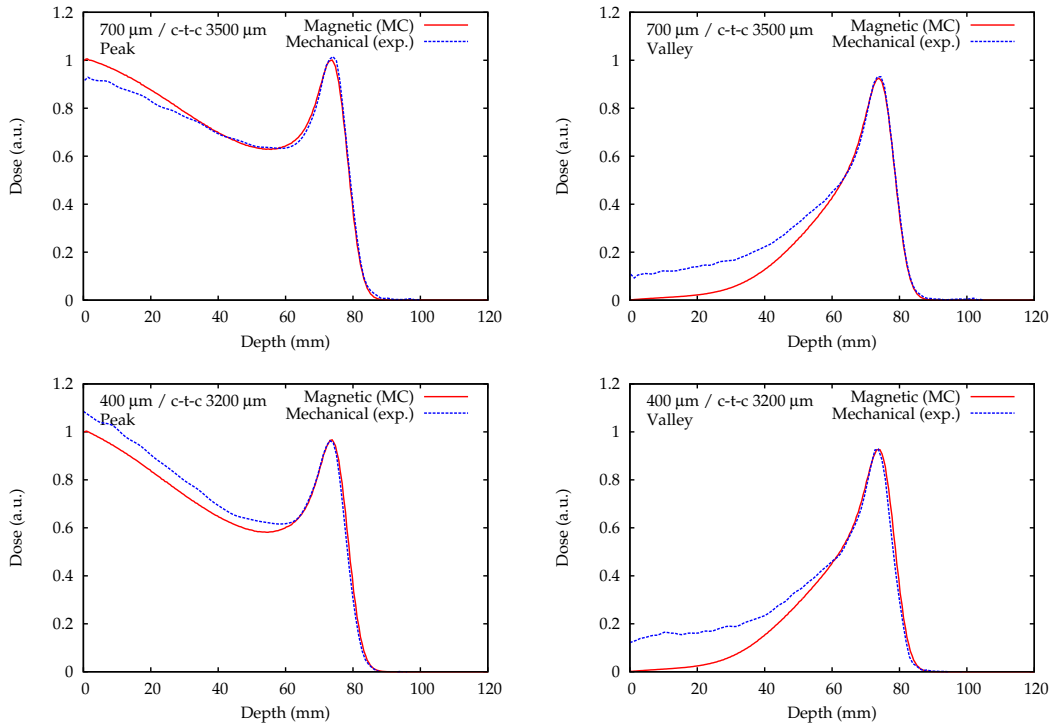

Figure 7.10: *Courbes de rendement en profondeur dans le pic (à gauche) et la vallée (à droite) pour les configurations 700 µm/c-t-c 3500 µm (en haut) et 400 µm/c-t-c 3200 µm (en bas), considérant une collimation magnétique (données MC) et mécanique (données experimentales).*

De plus, l'impact de différents paramètres d'irradiation sur les distributions de doses a été étudié afin de guider les prochaines optimisations du setup expérimental pour la pMBRT. La meilleure configuration d'irradiation serait celle offrant les FWHM les plus étroites dans les tissus normaux (afin de favoriser l'effet dose-volume), le rapport des doses pic de Bragg-entrée le plus élevé, les PVDR les plus importants dans les tissus normaux, et le plus haut degré d'homogénéisation au niveau du volume cible. Cette étude a montré que la réduction de l'air gap entre la

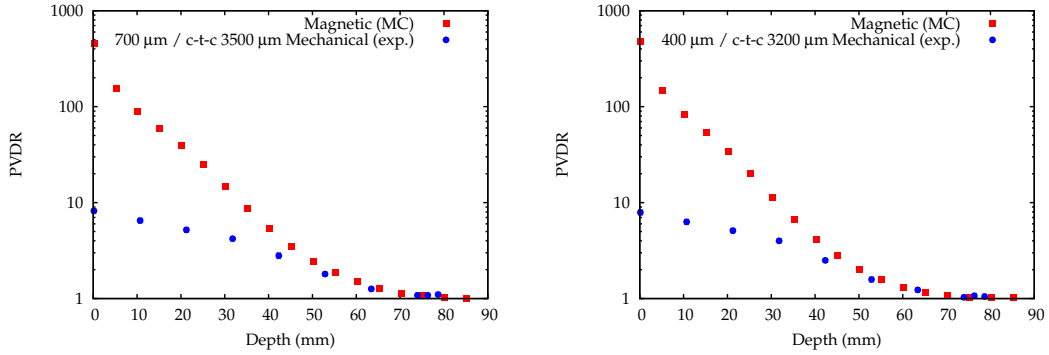

Figure 7.11: *Valeurs de PVDR en fonction de la profondeur pour les configurations 700 µm/c-t-c 3500 µm et 400 µm/c-t-c 3200 µm. Les barres d'incertitudes sont plus petites que la dimension des symboles pour les données MC.*

collimation du mini-faisceau et le fantôme/patient, une faible divergence du faisceau et une faible dispersion en énergie favorisait l'obtention de petites tailles de faisceau à l'entrée du fantôme.

Toutefois, le fait de pouvoir maintenir un dépôt de dose plus élevé en fin de parcours des protons (pic de Bragg) offrirait un avantage supplémentaire à la technique pMBRT. L'utilisation de faisceaux plus larges (3 mm) pour créer un peigne a été étudiée dans cette étude théorique, ceux-ci étants plus avantageux en termes de ratio pic de Bragg-entrée. Bien que l'effet dose-volume serait moins important dans ce cas, un gain dans la préservation des tissus sains pourrait être tout de même maintenu. Les résultats obtenus dans ce travail ont montré qu'il devrait être possible de maintenir un fractionnement spatial de la dose dans les tissus normaux avec ce type de peigne, mais seules des études biologiques pourraient démontrer le maintien d'une préservation des tissus.

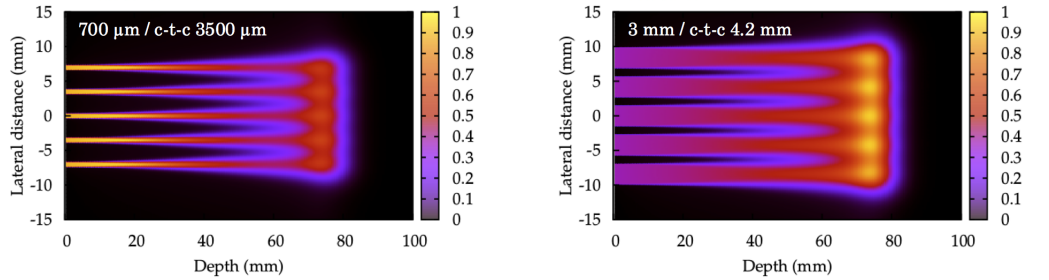

Figure 7.12: *Distributions de dose 2D dans le fantôme d'eau obtenues après irradiation avec un peigne de mini-faisceaux de 700 µm (c-t-c 3500 µm) (à gauche) et de 3 mm (c-t-c 4.2 mm) de largeur (à droite). Un fractionnement spatial de la dose est également maintenu avec des faisceaux plus larges, tout en offrant un maximum de dose au niveau du pic de Bragg, tandis qu'il se trouve en entrée pour un peigne de 700 µm.*

En résumé, le meilleur compromis serait l'utilisation de mini-faisceaux collimatés aussi près que possible du patient, avec une dimension, une dispersion en énergie

et une divergence permettant de préserver un rapport de dose pic de Bragg-entrée raisonnable (facteur d'environ 1), afin d'assurer un dépôt de dose élevé au niveau du volume cible.

Comme cela a été précédemment expliqué, une collimation magnétique pour la pMBRT pourrait être basée sur la modification d'un système existant de balayage actif des faisceaux, aussi appelé "Pencil Beam Scanning" (PBS). Une première évaluation effectuée à l'ICPO par Tim Schneider et Annalisa Patriarca (en collaboration avec notre équipe) a montré que la ligne de faisceau actuelle (avec la configuration existante du PBS) ne permet pas de fournir des faisceaux de dimension submillimétrique [Schneider 2016]. Pour obtenir de telles tailles de champs, des modifications devront être apportées au niveau du nez de traitement. En vue de la protection d'un futur brevet en préparation, aucun détail supplémentaire ne sera fourni.

7.2.3 Exploration du concept de fractionnement spatial avec des faisceaux d'ions plus lourds

Dans cette troisième étude dosimétrique, la potentielle ré-utilisation des ions très lourds en RT a été explorée, ceux-ci ayant été abandonnés par le passé. Grâce à des simulations MC (Geant4/GATE), j'ai donc étudié la faisabilité d'irradiation d'une tumeur profonde (7 cm) au moyen de peignes de faisceaux d'ions lourds, allant du néon (Z=10) au fer (Z=26). La géométrie présentée en figure 7.9 a été utilisée pour cette étude, et une collimation magnétique a été également considérée ici. Des mini-faisceaux de dimension 700 μm $\times$ 2 cm ont ainsi été simulés, considérant plusieurs distances c-t-c allant de 1400 à 3500 μm.

Malgré l'utilisation de tailles de champ submillimétriques, la faible diffusion latérale des ions lourds permet de maintenir une forme standard de pic de Bragg, contrairement à ce qui était observé en pMBRT [Prezado 2013]. Un exemple est donné dans la figure 7.13 à gauche pour un unique mini-faisceau d'argon monoénergétique (700 μm $\times$ 2 cm) simulé dans un fantôme d'eau. Dans cette étude, un SOBP de 2 cm centré à 7 cm en profondeur a été considéré pour chaque ion. La figure 7.13 à droite présente le SOBP (entre 60 et 80 mm) obtenu avec un seul mini-faisceau d'argon.

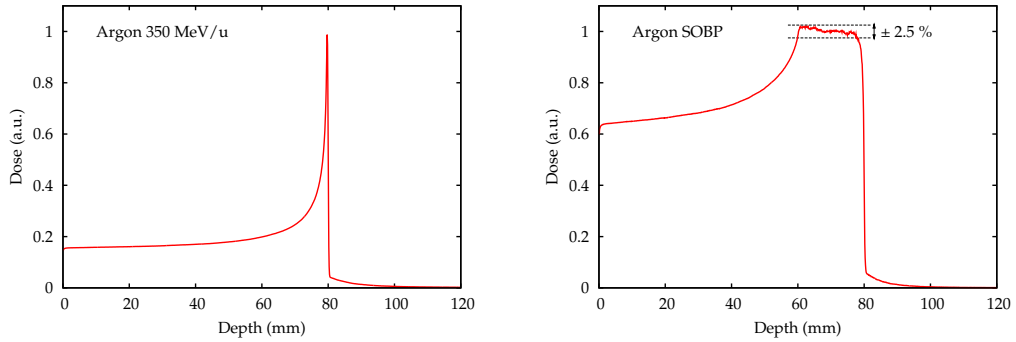

Figure 7.13: *Rendements en profondeur obtenus avec un unique mini-faisceau monoénergétique d'argon (351 MeV/u) (à gauche) et avec un SOBP (à droite) dans l'eau.*

Dans cette étude, de très petites largeurs de faisceau (FWHM) et des pénombres très faibles ont été obtenues, s'élevant respectivement à 700–800 μm et 50–300 μm dans les tissus sains. Ceci a permis de maintenir un fractionnement spatial de la dose (alternance de pics et de vallées) dans les tissus normaux pour tous les c-t-c et les ions considérés. Un exemple est présenté en figure 7.14.

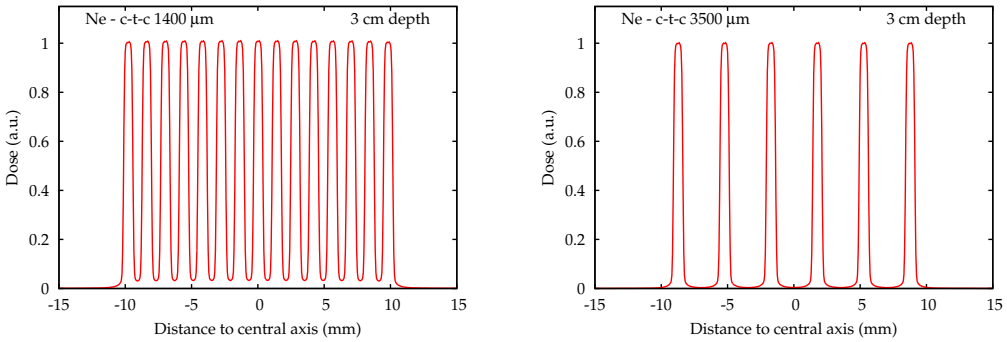

Figure 7.14: *Profils latéraux de dose obtenus à 3 cm de profondeur avec un peigne de mini-faisceaux de néon, avec un c-t-c de 1400 μm (à gauche) et de 3500 μm (à droite).*

De très faibles doses ont été obtenues dans les vallées dans les tissus normaux, y compris dans la région de la queue de fragmentation, où les doses étaient inférieures à 8% de la dose prescrite (SOBP) dans tous les cas considérés. Une réduction significative de la queue de fragmentation dans les vallées a été observée avec un c-t-c plus large ($< 2{,}5\%$). De plus, des valeurs extrêmement élevées de PVDR (> 100) ont été observées. Ces valeurs sont bien supérieures à celles observées en MBRT par RX [Prezado 2009b], pour laquelle la préservation des tissus a déjà été prouvée, ainsi qu'en pMBRT [Prezado 2013]. D'une manière générale, plus le Z de l'ion est grand, plus faible est la dose dans les vallées, et donc plus les PVDR sont élevés (voir figure 7.15). De la même manière, plus le c-t-c est large, plus faibles sont les doses dans les vallées et, par conséquent, plus les valeurs de PVDR augmentent. Bien que le fractionnement spatial soit également maintenu dans la tumeur (SOBP), plusieurs études ont observé l'induction d'un effet préférentiellement délétaire dans la tumeur, même avec des distributions de dose très inhomogènes. Cependant, si cela est nécessaire, une distribution de dose homogène peut être obtenue en entrelaçant plusieurs peignes (*e.g.* deux avec un c-t-c de 1400 μm) dans la tumeur [Serduc 2010, Prezado 2012b, Prezado 2013].

Dans un second temps, une attention particulière a été accordée aux distribution de dose des produits secondaires, ainsi qu'aux taux de production des fragments nucléaires dans les vallées. Nous avons constaté que la dose dans la région du pic est principalement attribuable à la contribution des primaires, tandis que les vallées sont principalement alimentées par les produits secondaires (gammas, electrons δ et autres fragments nucléaires). Bien que les taux de production des fragments nucléaires secondaires (TEL élevé) soient plus importants avec les projectiles de Z

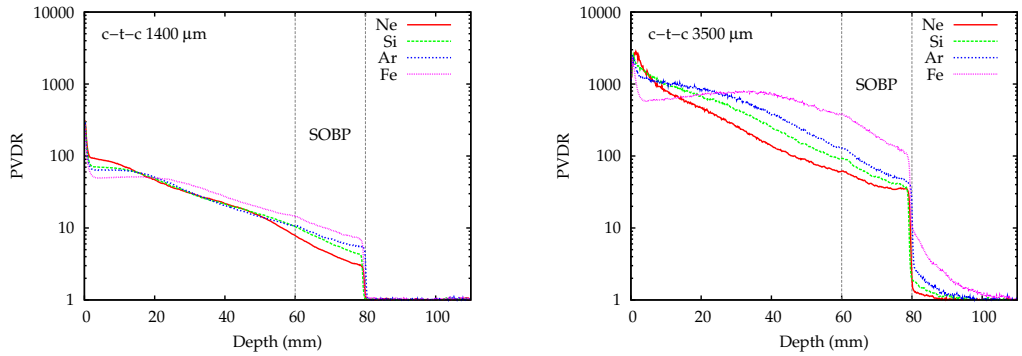

Figure 7.15: *PVDR en fonction de la profondeur obtenus avec tous les c-t-c considérés. De manière générale, plus l'ion est lourd, plus les valeurs de PVDR sont élevées du fait d'une production plus importante de fragments lourds, plus dirigés vers l'avant, et donc contribuant moins aux vallées.*

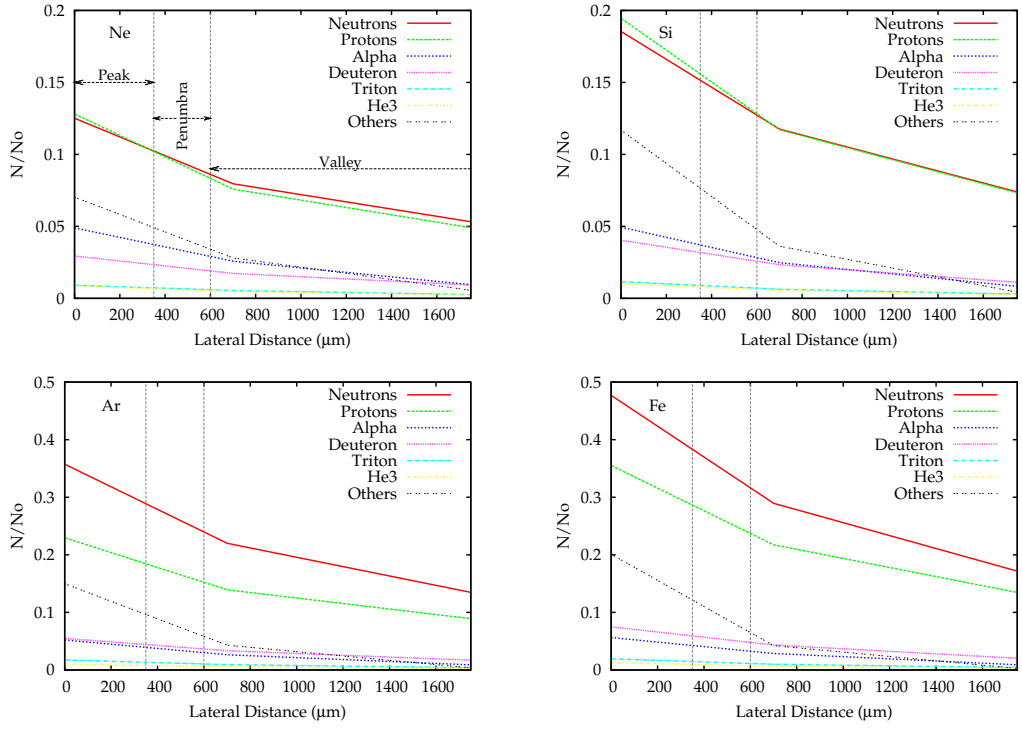

Figure 7.16: *Distribution latérale des produits de fragmentation les plus fréquents à une profondeur de 4 cm, considérant un c-t-c de 3500 µm. Les données sont normalisées par rapport au nombre de particules primaires simulées. Trois régions correspondant au pic, à la zone de pénombre et à la vallée, sont représentées.*

élevé, la dose déposée par les fragments nucléaires dans les vallées devient la contribution dominante à des profondeurs plus élevées, contribuant ainsi à la préservation

des tissus normaux proximaux. Parmi les fragments nucléaires, les espèces les plus légères (neutrons et protons) sont les plus abondantes, à la fois dans les pics et les vallées, comme illustré en figure 7.16. La contribution des neutrons à la dose dans les tissus normaux a été estimée très faible. De plus, selon les spectres, la dose biologique des neutrons dans les vallées ne devrait pas dépasser 0,00025% de la dose au SOBP. Les neutrons ne devraient donc pas constituer un problème pour ce type d'irradiations, bien que ceci devra être confirmé par des études expérimentales. Les fragments les plus lourds, moins nombreux, se sont révélés être plus concentré dans la région du pic, et leur taux atteint des valeurs très faibles lorsque l'on s'éloigne du centre des pics. Les observations mentionnées ci-dessus, associés à des valeurs de PVDR plus élevés, pourraient suggérer une utilisation préférentielle de c-t-c plus larges (3500 μm) afin de minimiser la contribution des fragments plus lourds (TEL élevé) dans les vallées, et donc de favoriser la préservation des tissus normaux.

En conclusion, d'un point de vue dosimétrique, l'utilisation de peignes de faisceaux d'ions très lourds semble être plus avantageuse que l'utilisation des RX ou des protons, bien que ces avantages devront être confirmés par les expérimentations biologiques. Les résultats présentés dans cette section sont donc en faveur d'une poursuite de l'exploration de cette nouvelle piste. Ce travail a également été publié dans le journal *Medical Physics* [Peucelle 2015b].

7.3 Discussion & Conclusions

Cette thèse s'inscrit dans une nouvelle dynamique d'amélioration de la RT, qui passe par l'exploration de nouvelles approches allant à l'encontre des paradigmes usuels de la RT, ceci dans le but d'optimiser les paramètres liés à la physique pour profiter pleinement des avantages de la biologie sous-jacente. Le but de ce travail était de d'évaluer les avantages dosimétriques de deux approches innovantes: la MBRT par mini-faisceaux de protons et d'ions très lourds. Bien que ce travail exploratoire demeure à l'heure actuelle encore loin de futures implémentations cliniques, il propose, au même titre que d'autres études pionnières, une nouvelle direction pour l'évolution de la RT qui pourrait certainement modifier la pratique clinique dans un avenir proche.

Dans ce travail, nous avons mis en évidence les propriétés propres aux mini-faisceaux de protons et d'ions plus lourds, conduisant à différents types de distributions de dose, et probablement aussi à différentes conséquences biologiques. Les deux techniques explorées dans ce travail présentent donc chacune des avantages et des inconvénients par rapport à l'autre. Une vue d'ensemble est donnée dans le tableau 7.2, et ces différences seront discutées ci-après.

La première différence entre les deux techniques concerne la distribution de dose au niveau de la cible, comme cela est représenté schématiquement sur la figure 7.17. Avec des protons, un unique peigne de mini-faisceaux est suffisant pour obtenir une distribution de dose homogène à la tumeur, tout en assurant un fractionnement spatial dans les tissus normaux. En revanche, avec des ions très lourds, le fraction-

Forces et faiblesses des deux techniques	
pMBRT	MBRT par ions très lourds
✓ Homogénéisation à la tumeur avec un seul peigne	X Fractionnement à la tumeur (plusieurs peignes à envisager)
X Réduction de l'intensité du pic de Bragg (700 μm)	✓ Préservation du pic de Bragg (700 μm)
✓ Pas de fragmentation du projectile	X Fragmentation du projectile (TEL élevé)
≃ Possibles meilleures propriétés biologiques/RX	✓ EBR élevé & OER faible à la tumeur
✓ Protons disponibles dans plusieurs centres cliniques	X Ions lourds peu disponibles, lignes de recherche
✓ Collimations mécanique & magnétique envisageables	X Collimation magnétique préférable

Table 7.2: *Vue d'ensemble des avantages et inconvénients de la pMBRT et de la MBRT par faisceaux d'ions très lourds.*

nement spatial est maintenu à toutes les profondeurs, même au niveau du volume cible, grâce à leur diffusion latérale réduite. Il est important de souligner que, dans ce cas, les PVDR dans les tissus normaux sont supérieurs à ceux obtenus en pMBRT. Afin d'obtenir un contrôle tumoral acceptable, il pourrait être nécessaire d'utiliser plusieurs peignes de mini-faisceaux entrelacés à la position du volume cible, afin d'obtenir une distribution de dose uniforme. Bien que des travaux antérieurs ont démontré la possibilité d'un contrôle tumoral avec des distributions de dose inhomogènes en MBRT par RX (par exemple dans [Prezado 2012b]), seules les expérimentations biologiques pourront confirmer des résultats similaires avec des particules chargées. Une géométrie entrelacée nécessite une grande précision micrométrique pour positionner les peignes [Serduc 2010, Prezado 2012b], ce qui rend la mise en oeuvre plus complexe. En ce sens, l'utilisation d'un unique peigne en pMBRT pourrait simplifier les éventuels problèmes techniques.

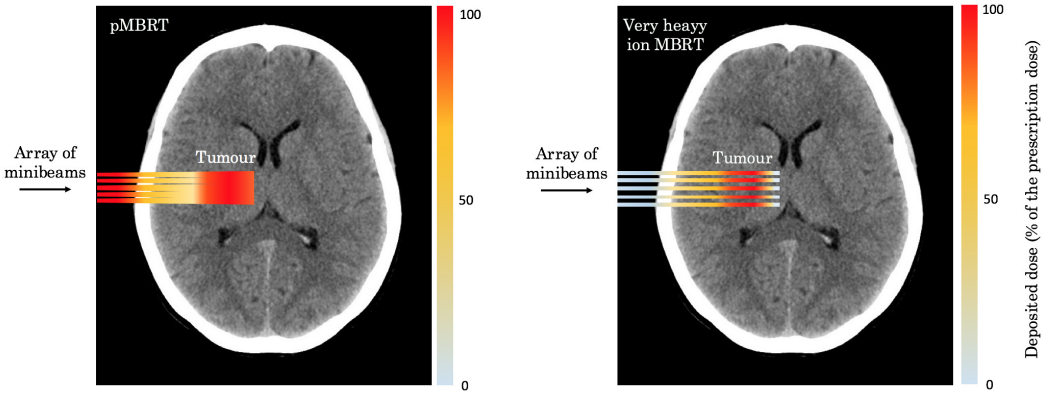

Figure 7.17: *Représentation schématique des distributions de dose obtenues après irradiation avec un peigne de faisceaux submillimétriques de protons (à gauche) et d'ions très lourds (à droite).*

Une autre différence provient de la forme des rendements en profondeur dans la région du pic, également représentée en figure 7.17. Avec des protons, le pic de Bragg est réduit en raison de la proportion importante de protons diffusés par rapport à la dimension du faisceau. Afin de minimiser cet effet et de tirer profit d'un dépôt

d'énergie important en fin de parcours des protons, l'utilisation de faisceaux plus larges (quelques millimètres) a été évoqué. Il a été démontré théoriquement qu'il serait possible d'obtenir une distribution de dose similaire (fractionnement spatial associé à une homogénéisation en profondeur) avec de tels faisceaux. Un premier indice montrant un maintien d'un effet de préservation des tissus avec des mini-faisceaux de dimension supramillimétrique a déjà été observé pendant les premières expériences biologiques en pMBRT. En effet, le setup expérimental imposait des faisceaux d'environ 1–1.2 mm dans les cerveaux des rats irradiés. Dans ce cas, un gain dans la préservation des tissus sains a été observé en comparaison avec les rats irradiés en conditions de champ large. En ce qui concerne les ions plus lourds, les rendements en profondeur obtenus en utilisant des mini-faisceaux de 700 μm sont proches de la forme des rendements en profondeur classiques, grâce à la diffusion latérale réduite. Dans ce cas, et contrairement au cas des protons, une réduction de la taille de mini-faisceaux pourrait encore être envisageable avec des ions lourds, ce qui augmenterait encore l'effet dose-volume. Cependant, les premiers tests effectués par un chercheur post-doctoral de l'équipe suggèrent que des faisceaux de dimension inférieure à 300 μm conduisent déjà à une réduction significative de l'intensité du pic de Bragg.

De plus, un inconvénient des ions lourds par rapport aux protons est le phénomène de fragmentation des ions projectiles produisant, entre autres, des fragments secondaires lourds (TEL élevé) qui pourraient contaminer la région de la vallée. Cependant, leur contribution dans cette région pourrait être minimisée en favorisant l'utilisation d'ions plus lourds et de c-t-c plus larges. Certains des fragments sont également responsables de la queue de fragmentation s'étendant au-delà du pic de Bragg, délivrant une dose indésirable aux tissus normaux distaux. Heureusement, l'étude théorique réalisée a montré que ces queues de dose étaient très faibles par rapport à la dose au SOBP. Ceci doit évidemment être confirmé par des mesures expérimentales. Avec des faisceaux de protons, seule la fragmentation de la cible peut se produire. L'étude MC menée a montré que les principaux participants de la dose aux vallées sont les protons primaires et secondaires provenant de la fragmentation de la cible. Il est donc possible d'envisager qu'aucune variation significative du TEL moyen (et donc de l'EBR) ne devrait être obervée entre les régions des pics et des vallées en pMBRT, contrairement à ce qui est attendu avec des ions très lourds.

Enfin, l'existence de nombreuses installations de protonthérapie dans le monde constitue un avantage majeur en faveur de la pMBRT. Selon le PTCOG, on compte à ce jour 60 installations en fonctionnement, 31 en cours de construction et 17 en prévision [PTCOG 2016]. En revanche, peu d'installations dans le monde permettent la production d'ions plus lourds que l'oxygène, ce qui limite l'exploration de la technique pour le moment. Cependant, des études approfondies comme celle réalisée dans cette thèse pourraient potentiellement catalyser le développement de lignes de faisceau d'ions très lourds dans les structures déjà existantes.

A l'issue de ces travaux de thèse, de nombreuses étapes restent à suivre dans le développement de ces deux techniques, comme par exemple le développement d'un

moteur de calcul dédié à la planification du traitement en pMBRT, l'optimisation de la méthode de collimation magnétique, ou encore la multiplication des études biologiques. Si l'efficacité de la pMBRT est confirmée du point de vue biologique, une telle technique serait plus accessible en raison des coûts inférieurs des faisceaux de protons par rapport à ceux d'ions plus lourds. Néanmoins, si la MBRT par faisceaux d'ions lourds se révèle efficace, ce serait une avancée des plus significatives pour le traitement de tumeurs hypoxiques et radiorésistantes. De plus, les résultats des recherches fondamentale et préclinique menées pour ces projets pourront avoir un fort intérêt non seulement pour la MBRT mais également pour les techniques plus conventionnelles de RT.

Bibliography

[AAPM-41 1993] AAPM-41. *Remote afterloading technology.* American Association of Physicist in Medicine, Madison, United States of America, 1993.

[AAPM-76 2006] AAPM-76. *The Management of Respiratory Motion in Radiation Oncology.* American Association of Physicists in Medicine, Madison, United States of America, 2006.

[AAPM-TG-51 1999] AAPM-TG-51. *AAPM's TG-51 protocol for clinical reference dosimetry of high-energy photon and electron beams.* Med. Phys., vol. 26, pp. 1847–1870, 1999.

[ACS 2015] ACS. *Cancer facts and figures 2015.* Technical report of American Cancer Society, 2015.

[Agostinelli 2003] S. Agostinelli, J. Allison, K. Amako, J. Apostolakis, H. Araujo, P. Arce, M. Asai, D. Axen, S. Banerjee, G. Barrand *et al. Geant4 – a simulation toolkit.* IEEE Transactions on Nuclear Science, vol. 506, pp. 250–303, 2003.

[Alfonso 2008] R. Alfonso, P. Andreo, R. Capote, M. Saiful Huq, W. Kilby, P. Kjäll, T.R. Mackie, H. Palmans, K. Rosser *et al. A new formalism for reference dosimetry of small and nonstandard fields.* Med. Phys., vol. 35, pp. 5179–5186, 2008.

[Amaldi 2010] U. Amaldi, R. Bonomi, S. Braccini, M. Crescenti, A. Degiovanni, M. Garlasché, A. Garonna, G. Magrin, C. Mellace, P. Pearce *et al. Accelerators for hadrontherapy: from Lawrence cyclotrons to linacs.* IEEE Transactions on Nuclear Science, vol. 620, pp. 563–577, 2010.

[Arce 2008] P. Arce, P. Rato, M. Canadas and J.I. Lagares. *GAMOS: A Geant4-based easy and flexible framework for nuclear medicine applications.* In 2008 IEEE Nuclear Science Symposium Conference Record, pp. 3162–3168. Institute of Electrical and Electronics Engineers, 2008.

[Aspradakis 2010] M.M. Aspradakis, J.P. Byrne, H. Palmans, J. Conway, K. Rosser, A.P. Warrington and S. Duane. *Small Field MV Photon Dosimetry.* Report 103 - Institute of Physics and Engineering in Medicine, vol. 978, 2010.

[Assmann 2015] W. Assmann, S. Kellnberger, S. Reinhardt, S. Lehrack, A. Edlich, P.G. Thirolf, M. Moser, G. Dollinger, M. Omar, V. Ntziachristos *et al. Ionoacoustic characterization of the proton Bragg peak with submillimeter accuracy.* Med. Phys., vol. 42, pp. 567–574, 2015.

[ASTRO 2014] ASTRO. *Proton Beam Therapy Model Policy issued by ASTRO.* American Society for Radiation Oncology, 2014.

[Barkas 1963] H. Barkas. Nuclear research emulsions, volume 1. Academic, New York, 1963.

[Bassinet 2013] C. Bassinet, C. Huet, S. Derreumaux, G. Brunet, M. Chéa, M. Baumann, T. Lacornerie, S. Gaudaire-Josset, F. Trompier, P. Roch *et al. Small fields output factors measurements and correction factors determination for several detectors for a CyberKnife® and linear accelerators equipped with microMLC and circular cones.* Med. Phys., vol. 40, p. 071725, 2013.

[Baumann 2016] M. Baumann, M. Krause, J. Overgaard, J. Debus, S. M. Bentzen, J. Daartz, C. Richter, D. Zips and T. Bortfeld. *Radiation oncology in the era of precision medicine.* Nat. Rev. Cancer, 2016.

[Berger 1975] M.J. Berger, S.M. Seltzer, S.R. Domen and P.J. Lamperti. Stopping-power ratios for electron dosimetry with ionization chambers. International Atomic Energy Agency, Vienna, Austria, 1975.

[Bethe 1930] H. Bethe. *Zur theorie des durchgangs schneller korpuskularstrahlen durch materie.* Annalen der Physik, vol. 397, pp. 325–400, 1930.

[Beyzadeoglu 2010] M. Beyzadeoglu, G. Ozyigit and C. Ebruli. Radiobiology. Basic Radiation Oncology, Springer, Berlin, Germany, 2010.

[Blakely 2004] E.A. Blakely and P.Y. Chang. *Late effects from hadron therapy.* Radiother. Oncol., vol. 73, pp. S134–S140, 2004.

[Bleeker 2012] F. Bleeker, R. Molenaar and S. Leenstra. *Recent advances in the molecular understanding of glioblastoma.* J. Neurooncol., vol. 108, pp. 11–27, 2012.

[Bloch 1933] F. Bloch. *Zur bremsung rasch bewegter teilchen beim durchgang durch materie.* Annalen der Physik, vol. 408, pp. 285–320, 1933.

[Böhlen 2010] T.T. Böhlen, F. Cerutti, M. Dosanjh, A. Ferrari, I. Gudowska, A. Mairani, J.M. Quesada *et al. Benchmarking nuclear models of FLUKA and GEANT4 for carbon ion therapy.* Phys. Med. Biol., vol. 55, p. 5833, 2010.

[Böhlen 2014] T.T. Böhlen, F. Cerutti, M.P.W. Chin, A. Fassò, A. Ferrari, P.G. Ortega, A. Mairani, P.R. Sala, G. Smirnov and V. Vlachoudis. *The FLUKA code: developments and challenges for high energy and medical applications.* Nucl. Data Sheets, vol. 120, pp. 211–214, 2014.

[Bouchet 2010] A. Bouchet, B.Lemasson, G.Le Duc, C. Maisin, E. Bräuer-Krisch, E. A. Siegbahn, L. Renaud, E. Khalil, C. Rémy, C. Poillot *et al. Preferential effect of synchrotron microbeam radiation therapy on intracerebral 9L gliosarcoma vascular networks.* Int. J. Radiat. Oncol., Biol., vol. Phys. 78, pp. 1503–1512, 2010.

[Bouchet 2013] A. Bouchet, B. Lemasson, T. Christen, M. Potez, C. Rome, N. Coquery, C. Le Clec'H, A. Moisan, E. Bräuer-Krisch, G. Leduc *et al.* *Synchrotron microbeam radiation therapy induces hypoxia in intracerebral gliosarcoma but not in the normal brain.* Radiother. Oncol., vol. 108, pp. 143–148, 2013.

[Bouchet 2015a] A. Bouchet, N. Sakakini, M. El Atifi, C. Le Clec'h, E. Bräuer-Krisch, L. Rogalev, J.A. Laissue, P. Rihet, G. Le Duc and L. Pelletier. *Identification of AREG and PLK1 pathway modulation as a potential key of the response of intracranial 9L tumor to microbeam radiation therapy.* Int. J. Cancer, vol. 136, pp. 2705–2716, 2015.

[Bouchet 2015b] A. Bouchet, Raphäel Serduc, Jean Albert Laissue and Valentin Djonov. *Effects of microbeam radiation therapy on normal and tumoral blood vessels.* Phys. Med., vol. 31, pp. 634–641, 2015.

[Bouchet 2016] A. Bouchet, E. Bräuer-Krisch, Y. Prezado, M. El Atifi, L. Rogalev, C. Le Clec'h, J.A. Laissue, L. Pelletier and G. Le Duc. *Better efficacy of synchrotron spatially micro-fractionated radiotherapy than uniform radiotherapy on glioma.* Int. J. Radiat. Oncol. Biol. Phy., 2016.

[Bouillhol 2013] G. Bouillhol. *Uncertainties and motion management in lung radiotherapy: from photons to ions.* PhD thesis, Institut National des Sciences Appliquées de Lyon, 2013.

[Brahme 2001] A. Brahme, R. Lowensohn, U. Ringborg, U. Amaldi, F. Gerardi and S. Rossi. *Design of a centre for biologically optimised light ion in therapy in Stockholm.* Nucl. Instrum. Methods Phys. Res. B, vol. B 184, pp. 569–588, 2001.

[Bräuer-Krisch 2010] E. Bräuer-Krisch, A.B. Rosenfeld, M.L. Lerch, M. Petasecca, M. Akselrod, J. Sykora, J. Bartz, M. Ptaszkiewicz, P. Olko, A. Berg *et al.* *Potential high resolution dosimeters for MRT.* AIP Conf. Proc., vol. 1269, 2010.

[Braunn 2013] B. Braunn, A. Boudard, J. Colin, J. Cugnon, D. Cussol, J.C. David, P. Kaitaniemi, M. Labalme, S. Leray and D. Mancusi. *Comparisons of hadrontherapy-relevant data to nuclear interaction codes in the Geant4 toolkit.* J. Phys.: Conference Series, 2013.

[Brenner 2008] D.J. Brenner. *The linear-quadratic model is an appropriate methodology for determining isoeffective doses at large doses per fraction.* Semin. Radiat. Oncol., vol. 18, pp. 234–239, 2008.

[Brown 2007] J.M. Brown. *Tumor hypoxia in cancer therapy.* Methods Enzymol., vol. 435, pp. 297–321, 2007.

[Bucci 2005] K. Bucci, A. Bevan and M. Roach. *Advances in radiation therapy: conventional to 3D, to IMRT, to 4D, and beyond.* Cancer J. Clin., 2005.

[Buckey 2010] C. Buckey, S. Stathakis, K. Cashon, A. Gutierrez, C. Esquivel, C. Shi and N. Papanikolaou. *Evaluation of a commercially-available block for spatially fractionated radiation therapy.* J. Appl. Clin. Med. Phys., vol. 11, 2010.

[Burlin 1966] T.E. Burlin. *A general theory of cavity ionisation.* Br. J. Radiol., vol. 39, no. 466, pp. 727–734, 1966.

[Bush 2013] D.A. Bush, G. Cheek, S. Zaheer, J. Wallen, H. Mirshahidi, A. Katerelos, R. Grove and J.D. Slater. *High-dose hypofractionated proton beam radiation therapy is safe and effective for central and peripheral early-stage non-small cell lung cancer: results of a 12-year experience at Loma Linda University Medical Center.* Int. J. Radiat. Oncol. Biol. Phys., vol. 86, pp. 964–968, 2013.

[Carrier 2004] J-F. Carrier, L. Archambault, L. Beaulieu and R. Roy. *Validation of GEANT4, an object-oriented Monte Carlo toolkit, for simulations in medical physics.* Med. Phys., vol. 31, pp. 484–492, 2004.

[Castro 1978] J.R. Castro and J. Lawrence. Recent advances in nuclear medicine. Lawrence J and Budingers (eds.), New York, 1978.

[Castro 1994] J.R. Castro, D.E. Linstadt, J-P. Bahary, P.L. Petti, I. Daftari, J.M. Collier, P.H. Gutin, G. Gauger and J.L. Phillips. *Experience in charged particle irradiation of tumors of the skull base: 1977-1992.* Int. J. Radiat. Oncol. Biol. Phys., 1994.

[Castro 1995] J.R. Castro. *Results of heavy ion radiotherapy.* Radiat. Environ. Biophys., vol. 34, pp. 45–48, 1995.

[Chen 2009] Y. Chen and S. Ahmad. *Evaluation of inelastic hadronic processes for 250 MeV proton interactions in tissue and iron using GEANT4.* Radiation Protection Dosimetry, vol. 136, pp. 11–16, 2009.

[Chetty 2006] I.J. Chetty, M. Rosu, M.L. Kessler, B.A. Fraass, R.K. Ten Haken, D.L. McShan *et al. Reporting and analyzing statistical uncertainties in Monte Carlo–based treatment planning.* Int. J. Radiat. Oncol. Biol. Phys., vol. 65, pp. 1249–1259, 2006.

[Chetty 2007] I.J. Chetty, B. Curran, J.E. Cygler, J.J. DeMarco, G. Ezzell, B.A. Faddegon, I. Kawrakow, P.J. Keall, H. Liu, C-M.C. Ma *et al. Report of the AAPM Task Group No. 105: Issues associated with clinical implementation of Monte Carlo-based photon and electron external beam treatment planning.* Med. Phys., vol. 34, pp. 4818–4853, 2007.

[Ciancaglioni 2012] I. Ciancaglioni, M. Marinelli, E. Milani, G. Prestopino, C. Verona, G. Verona-Rinati, R. Consorti, A. Petrucci and F. De Notaristefani. *Dosimetric characterization of a synthetic single crystal diamond detector in clinical radiation therapy small photon beams.* Med. Phys., vol. 39, pp. 4493–4501, 2012.

[Cirrone 2005] G.A.P. Cirrone, G. Cuttone, S. Guatelli, S.L. Nigro, B. Mascialino, M.G. Pia, L. Raffaele, G. Russo and MG. Sabini. *Implementation of a new Monte Carlo-GEANT4 simulation tool for the development of a proton therapy beam line and verification of the related dose distributions.* IEEE Transactions on Nuclear Science, vol. 52, pp. 262–265, 2005.

[Cirrone 2011] G.A.P. Cirrone, G. Cuttone, S.E. Mazzaglia, F. Romano, D. Sardina, C. Agodi, A. Attili, A.A. Blancato, M. De Napoli, F. Di Rosa *et al. Hadrontherapy: a Geant4-based tool for proton/ion-therapy studies.* Prog. Nucl. Sci. Technol., vol. 2, pp. 207–212, 2011.

[Colli 2001] B.O. Colli and O. Al-Mefty. *Chordomas of the craniocervical junction: follow-up review and prognostic factors.* J. Neurosurg., vol. 95, pp. 933–943, 2001.

[Combs 2012] S.E. Combs. *Chapter: Clinical Indications for Carbon Ion Radiotherapy and Radiation Therapy with Other Heavier Ions.* In Ion Beam Therapy, volume 320 of the series Biological and Medical Physics, Biomedical Engineering, pp. 179–192. Springer, Berlin, Germany, 2012.

[Crosbie 2010] J. C. Crosbie, R. L. Anderson, K. Rothkamm, C. M. Restall, L. Cann, S. Ruwanpura, S. Meachem, N. Yagi, I. Svalbe, R. A. Lewis, B. R. Williams and P. A. Rogers. *Tumor cell response to synchrotron microbeam radiation therapy differs markedly from cells in normal tissues.* Int. J. Radiat. Oncol., Biol., vol. Phys. 77, pp. 886–894, 2010.

[Curtis 1967] H.J. Curtis. *The use of a deuteron microbeam for simulating the biological effects of heavy cosmic-ray particles.* Radiat. Res., vol. 7, 1967.

[Cussol 2011] D. Cussol. *Nuclear physics and hadrontherapy*, 2011.

[Das 2008] Indra J Das, George X Ding and Anders Ahnesjö. *Small fields: nonequilibrium radiation dosimetry.* Med. Phys., vol. 35, pp. 206–215, 2008.

[De Angelis 2002] C. De Angelis, S. Onori, M. Pacilio, G.A.P. Cirrone, G. Cuttone, M. Raffaele L .and Bucciolini and S. Mazzocchi. *An investigation of the operating characteristics of two PTW diamond detectors in photon and electron beams.* Med. Phys., vol. 29, pp. 248–254, 2002.

[De Ruysscher 2015] D. De Ruysscher, E. Sterpin, K. Haustermans and T. Depuydt. *Tumour Movement in Proton Therapy: Solutions and Remaining Questions: A Review.* Cancers, vol. 7, pp. 1143–1153, 2015.

[Degiovanni 2014] A. Degiovanni and U. Amaldi. *History of hadron therapy accelerators.* Phys. Med., 2014.

[Deman 2011] P. Deman, M. Vautrin, V. Stupar, E.L. Barbier, H. Elleaume, F. Esteve and J.F. Adam. *Monochromatic minibeam radiotherapy: theoretical and experimental dosimetry for preclinical treatment plans.* Phys. Med. Biol., vol. 56, p. 4465, 2011.

[Deman 2012] P. Deman, M. Vautrin, M. Edouard, V. Stupar, L. Bobyk, R. Farion, H. Elleaume, C. Rémy, E.L. Barbier, F. Esteve and J.F. Adam. *Monochromatic minibeams radiotherapy: From healthy tissue-sparing effect studies toward first experimental glioma bearing rats therapy.* Int. J. Radiat. Oncol., Biol., Phys., vol. 82, pp. e693–e702, 2012.

[Dendale 2006] R. Dendale, L. L-L. Rouic, G. Noel, L. Feuvret, C. Levy, S. Delacroix, A. Meyer, C. Nauraye, H. Mammar, P. Garcia *et al. Proton beam radiotherapy for uveal melanoma : Results of Curie Institut-Orsay proton therapy center (ICPO).* Int. J. Radiat. Oncol., Biol., Phys., vol. 65, pp. 780–787, 2006.

[Despeignes 1896] V. Despeignes. *Observation concernant un cas de cancer de l'estomac traité par les rayons Roentgen.* Lyon Méd., vol. 82, pp. 428–430, 1896.

[Devic 2005] S. Devic, J. Seuntjens, E. Sham, E.B. Podgorsak, C.R. Schmidtlein, A.S. Kirov and C.G. Soares. *Precise radiochromic film dosimetry using a flat-bed document scanner.* Med. Phys., vol. 32, pp. 2245–2253, 2005.

[Dilmanian 2001] F. A. Dilmanian, G. M. Morris, G. Le Duc, X. Huang, B. Ren, T. Bacarian, J. C. Allen, J. Kalef-Ezra, I. Orion, E. M. Rosen *et al. Response of avian embryonic brain to spatially segmented x-ray microbeams.* Cell. Mol. Biol., vol. 47, pp. 485–493, 2001.

[Dilmanian 2002] F.A. Dilmanian, T. M. Button, G. Le Duc, N. Zhong, L. A. Pe na, J. A. L. Smith, S. R. Martinez, T. Bacarian, J. Tammam, B. Ren *et al. Response of rat intracranial 9L gliosarcoma to microbeam radiation therapy.* Neurooncol., vol. 4, pp. 26–38, 2002.

[Dilmanian 2003] F. A. Dilmanian, G. M. Morris, N. Zhong, T. Bacarian, J.F. Hainfeld, J. Kalef-Ezra, L.J. Brewington, J. Tammam and E. M. Rosen. *Murine emt-6 carcinoma: high therapeutic efficacy of microbeam radiation therapy.* Radiat. Res., vol. 159, 2003.

[Dilmanian 2005] F. A. Dilmanian, Y. Qu, S. Liu, C. D. Cool, J. Gilbert, J. F. Hainfeld, C.A. Kruse, J. Laterra, D. Lenihan, M.M. Nawrocky *et al. X-ray microbeams: tumor therapy and central nervous system research.* Nucl. Instr. Methods Phys. Res., vol. A 548, pp. 30–37, 2005.

[Dilmanian 2006] F. A. Dilmanian, Z. Zhong, T. Bacarian, H. Benveniste, P. Romanelli, R. Wang, J. Welwart, T. Yuasa, E. M. Rosen and D. J. Anschel. *Interlaced x-ray microplanar beams: A radiosurgery approach with clinical potential.* Proc. Natl. Acad. Sci. U.S.A., vol. 103, pp. 9709–9714, 2006.

[Dilmanian 2007] F.A. Dilmanian, Y. Qu, L.E. Feinendegen, L.A. Peña, T. Bacarian, F.A. Henn, J. Kalef-Ezra, S. Liu, Z. Zhong and J.W. McDonald. *Tissue-sparing effect of x-ray microplanar beams particularly in the CNS: is a bystander effect involved?* Exp. Hematol., vol. 35, pp. 69–77, 2007.

[Dilmanian 2008] F.A. Dilmanian, P. Romanelli, Z. Zhong, R. Wang, M.E. Wagshul, J. Kalef-Ezra, M.J. Maryanski, E.M. Rosen and D.J. Anschel. *Microbeam radiation therapy: Tissue dose penetration and BANG-gel dosimetry of thick-beams' array interlacing.* Eur. J. Radiol., vol. 68, pp. S129–S136, 2008.

[Dilmanian 2012] F. A. Dilmanian, A. Rusek, G.R. Fois, J. Olschowka, N.R. Desnoyers, J.Y. Park, I. Dioszegi, B. Dane, R. Wang, D. Tomasi *et al. Interleaved carbon minibeams: an experimental radiosurgery method with clinical potential.* Int. J. Radiat. Oncol. Biol. Phys., vol. 84, pp. 514–519, 2012.

[Dilmanian 2015] F. A. Dilmanian, J.G. Eley and S. Krishnan. *Minibeam therapy with protons and light ions: Physical feasibility and potential to reduce radiation side effects and to facilitate hypofractionation.* Int. J. Radiat. Oncol. Biol. Phys., vol. 92, pp. 469–474, 2015.

[Dudouet 2014] J. Dudouet, D. Cussol, D. Durand and M. Labalme. *Benchmarking Geant4 nuclear models for hadron therapy with 95 MeV/nucleon carbon ions.* Phys. Rev. Lett. C, vol. 89, p. 054616, 2014.

[Durante 2010] M. Durante and J.S. Loeffler. *Charged particles in radiation oncology.* Nat. Rev. Clin. Oncol., vol. 7, pp. 37–43, 2010.

[Dutreix 1990] J. Dutreix and A. Wambersie. Introduction to radiobiology. CRC Press, 1990.

[Elekta 2016] Elekta. *GammaKnife© Icon.* https://www.careforthebrain.com/, 2016.

[Faddegon 2008] B.A. Faddegon, M. Asai, J. Perl, C. Ross, J. Sempau, J. Tinslay and F. Salvat. *Benchmarking of Monte Carlo simulation of bremsstrahlung from thick targets at radiotherapy energies.* Med. Phys., vol. 35, pp. 4308–4317, 2008.

[Fano 1963] U. Fano. *Penetration of protons, alpha particles, and mesons.* Ann. Rev. Nucl. Sci., vol. 13, pp. 1–66, 1963.

[Fernandez-Palomo 2015] C. Fernandez-Palomo, E. Bräuer-Krisch, J.A. Laissue, D. Vukmirovic, H. Blattmann, C. Seymour, E. Schültke and C. Mothersill.

Use of synchrotron medical microbeam irradiation to investigate radiation-induced bystander and abscopal effects in vivo. Phys. Med., vol. 31, pp. 584–595, 2015.

[Flickinger 1990] J.C. Flickinger and A. Kalend. *Use of normalized total dose to represent the biological effect of fractionated radiotherapy.* Radiother. Oncol., vol. 17, pp. 339–347, 1990.

[Fois 2013] G.R. Fois. *Monte Carlo simulation studies for spatially fractionated radiation therapy.* PhD thesis, Univ. Cagliari, 2013.

[Folger 2004] G. Folger, V.N. Ivanchenko and J.P. Wellisch. *The binary cascade.* Eur. Phys. J. A, vol. 21, pp. 407–417, 2004.

[Gafchromic© 2016] Gafchromic©. *EBT3 dosimetry media.* www.ashland.com, 2016.

[García-Garduño 2008] A. García-Garduño, M.Á. Celis, J.M. Lárraga-Gutiérrez, S. Moreno-Jiménez, A. Martínez-Dávalos and M. Rodríguez-Villafuerte. *Radiation transmission, leakage and beam penumbra measurements of a micro-multileaf collimator using GafChromic EBT film.* J. Appl. Clin. Med. Phys., vol. 9, 2008.

[Geant4-Collaboration 2012] Geant4-Collaboration. *Geant4 User's Guide for Application Developers*, 2012.

[Geant4-Physics-Manual 2007] Geant4-Physics-Manual. *Physics reference manual.* Geant4 Collaboration, vol. 9, 2007.

[Geant4-Tutorial 2014] Geant4-Tutorial. *Geant4 Tutorial - Hadronic Physics I.* http://geant4.slac.stanford.edu/SLACTutorial14/HadronicPhysicsI.pdf, 2014.

[Gerber 2008] D.E. Gerber and T.A. Chan. *Recent advances in radiation therapy.* Am. Fam. Physician, 2008.

[Giantsoudi 2013] D. Giantsoudi, C. Grassberger, D. Craft, A. Niemierko, A. Trofimov and H. Paganetti. *Linear Energy Transfer-Guided Optimization in Intensity Modulated Proton Therapy: Feasibility Study and Clinical Potential.* Int. J. Radiat. Oncol. Biol., Phys., vol. 87, pp. 216–222,, 2013.

[Ginot 2010] A Ginot, J Doyen, J-M Hannoun-Lévi and A Courdi. *Dose de tolérance des tissus sains: la peau et les phanères.* Cancer Radiother., vol. 14, pp. 379–385, 2010.

[Girdhani 2013] S. Girdhani, R. Sachs and L. Hlatky. *Biological Effects of Proton Radiation: What We Know and Don't Know.* Radiat. Res., vol. 179, pp. 257–272, 2013.

[Girst 2015] S. Girst, C. Greubel, Reindl, C. Siebenwirth, O. Zlobinskaya, G. Dollinger and T.E. Schmid. *The influence of the channel size on the reduction of side effects in microchannel proton therapy.* Radiat. Environ. Biophys., vol. 54, pp. 335–342, 2015.

[Gottschalk 2004] B. Gottschalk. Passive beam spreading in proton radiation therapy. Harvard High Energy Physics Laboratory, Cambridge, United States of America, 2004.

[Grevillot 2010] L. Grevillot, T. Frisson, N. Zahra, D. Bertrand, F. Stichelbaut, N. Freud and D. Sarrut. *Optimization of GEANT4 settings for proton pencil beam scanning simulations using GATE.* Nucl. Instr. Meth. Phys. Res. B, vol. 268, pp. 3295–3305, 2010.

[Grevillot 2011] L. Grevillot, D. Bertrand, F. Dessy, N. Freud and D. Sarrut. *A Monte Carlo pencil beam scanning model for proton treatment plan simulation using GATE/GEANT4.* Phys. Med. Biol., vol. 56, pp. 5203–5219, 2011.

[Grevillot 2015] L. Grevillot, M. Stock and S. Vatnitsky. *Evaluation of beam delivery and ripple filter design for non-isocentric proton and carbon ion therapy.* Phys. Med. Biol., vol. 60, pp. 7985–8005, 2015.

[Guardiola 2015] C. Guardiola, D. Quirion, G. Pellegrini, C. Fleta, S. Esteban, M.A. Cortés-Giraldo, F. Gómez, T. Solberg, A. Carabe and M. Lozano. *Silicon-based three-dimensional microstructures for radiation dosimetry in hadron-therapy.* Appl. Phys. Lett., vol. 107, 2015.

[Guardiola 2016] C. Guardiola, C. Peucelle and Y. Prezado. *Optimization of minibeam generation in Proton MiniBeam Radiation Therapy by means of mechanical collimation.* Submitted, 2016.

[Guedea 2009] A. Guedea, M. Ferrer, J. Pera, F. Aguilo, A. Boladeras, J. Suarez, O. Cunillera, F. Ferrer, Y. Pardo, E. Martinez *et al. Quality of life two years after radical prostatectomy, prostate brachytherapy or external beam radiotherapy for clinically localised prostate cancer: the Catalan Institute of Oncology/Bellvitge Hospital experience.* Clin. Transl. Oncol., vol. 11, pp. 470–478, 2009.

[Guerrero 2003] M. Guerrero, X. Allen Li and L. Ma. *A technique to sharpen the beam penumbra for Gamma Knife radiosurgery.* Phys. Med. Biol., vol. 48, pp. 1843–1853, 2003.

[Haberer 2004] Th. Haberer, J. Debus, H. Eickhoff, O. Jakel, D. Schultz-Ertner and U. Weber. *The Heidelberg Ion Therapy Center.* Radiother. Oncol., vol. 73 Suppl. 2, pp. S186–190, 2004.

[Habrand 2009] J.-L. Habrand, S. Bolle, J. Datchary, C. Alapetite, S. Petras, S. Helfre, L. Feuvret, V. Calugaru, L. De Marzi, A. Bouyon-Monteau, R. Dendale,

C. Kalifa, J. Grill and F. Doz. *La protonthérapie en radiothérapie pédiatrique.* Cancer Radiother., vol. 13, pp. 550–555, 2009.

[Haettner 2006] Emma Haettner, Hiroshi Iwase and Dieter Schardt. *Experimental fragmentation studies with 12C therapy beams.* Radiat. Prot. Dosimetry, vol. 122, pp. 485–487, 2006.

[Hansen 2015] D.C. Hansen, J. Seco, Thomas S. Sørensen, J.B.B. Petersen, J.E. Wildberger, F. Verhaegen and G. Landry. *A simulation study on proton computed tomography (CT) stopping power accuracy using dual energy CT scans as benchmark.* Acta Oncol., vol. 54, pp. 1638–1642, 2015.

[Harrison 1997] L.B. Harrison. *Applications of brachytherapy in head and neck cancer.* Semin. Surg. Oncol., 1997.

[Highland 1975] V. Highland. *Some practical remarks on multiple scattering.* Nucl. Instrum. Meth., vol. 129, pp. 497–499, 1975.

[Hopewell 2000] J.W. Hopewell and K.R. Trott. *Volume effects in radiobiology as applied to radiotherapy.* Radiother. Oncol., vol. 56, pp. 283–288, 2000.

[Horowitz 2006] Y. Horowitz. Microdosimetric response of physical and biological systems to low-and high-let radiations: theory and applications to dosimetry. Elsevier, 2006.

[Hranitzky 2006] C. Hranitzky, H. Stadtmann and P. Olko. *Determination of LiF: Mg, Ti and LiF: Mg, Cu, P TL efficiency for X-rays and their application to Monte Carlo simulations of dosemeter response.* Radiat. Prot. Dosimetry, vol. 119, pp. 483–486, 2006.

[Hug 2000] E.B. Hug, L.N. Loredo, J.D Slater, A. Devries, R.I. Grove, R.A. Schaefer, A.E. Rosenberg and J.M. Slater. *Proton radiation therapy for chordomas and chondrosarcomas of the skull base.* J. Neurosurg., vol. 91, pp. 432–439, 2000.

[IAEA-TRS-398 2001] IAEA-TRS-398. *Absorbed dose determination in external beam radiotherapy: An international code of practice for dosimetry based on standards of absorbed dose to water; technical reports series No. 398*, 2001.

[IAEA-TRS-461 2008] IAEA-TRS-461. *TRS 461 - Relative biological effectiveness in ion beam therapy.* Technical Report - International Atomic Energy Agency, Vienna, Austria, 2008.

[IBA 2016] IBA. http://www.iba-dosimetry.com/, 2016.

[ICRU-1560 2007] ICRU-1560. *Dose reporting in ion beam therapy.* Technical report, International Commission on Radiation Units and Measurements, Bethesda, United States of America, 2007.

[ICRU-38 1985] ICRU-38. *Dose and volume specification for reporting intracavitary therapy in gynecology.* Technical report, International Commission on Radiation Units and Measurements, Bethesda, United States of America, 1985.

[ICRU-63 2000] ICRU-63. *Nuclear data for neutron and proton radiotherapy and for radiation protection.* Technical report, International Commission on Radiation Units and Measurements, Bethesda, United States of America, 2000.

[ICRU-78 2007] ICRU-78. *Prescribing, Recording, and Reporting Proton-Beam Therapy.* Technical report, International Commission on Radiation Units and Measurements, Bethesda, United States of America, 2007.

[IMRT-Group 2001] IMRT-Group. *Intensity-modulated radiotherapy: current status and issues of interest.* Int. J. Radiat. Oncol. Biol., Phys., vol. 51, pp. 880–914, 2001.

[Institut-Curie 2016] Institut-Curie. *La protonthérapie.* http://protontherapie.curie.fr/fr/la-protontherapie/systemes-conformation-faisceau, 2016.

[ISFPM-Task-group 2008] ISFPM-Task-group. *Mesure de la dose absorbée dans les faisceaux de photons de très petites dimensions utilisés en radiothérapie stéréotaxique.* Rapport DRPH/SER, no. 18, 2008.

[Jalota 2012] S. Jalota and A. Kumar. *Validation of Geant4 physics models for 56 Fe ion beam in various media.* Nucl. Instr. Meth. Phys. Res. B, vol. 291, pp. 7–11, 2012.

[Jan 2011] S. Jan, D. Benoit, E. Becheva, T. Carlier, F. Cassol, P. Descourt, T. Frisson, L. Grevillot, L. Guigues, L. Maigne *et al. GATE V6: a major enhancement of the GATE simulation platform enabling modelling of CT and radiotherapy.* Phys. Med. Biol., vol. 56, pp. 881–901, 2011.

[Jarlskog 2008] C. Z. Jarlskog and H. Paganetti. *Physics settings for using the Geant4 toolkit in proton therapy.* IEEE Transactions on Nuclear Science, vol. 55, pp. 1018–1025, 2008.

[Jermann 2015] M. Jermann. *Particle Therapy statistics in 2014.* Int. J. of Particle Ther., vol. 2, pp. 50–54, 2015.

[Jette 2011] D. Jette and W. Chen. *Creating a spread-out Bragg peak in proton beams.* Phys. Med. Biol., vol. 56, pp. N131–N138, 2011.

[Joiner 2009] M. Joiner and A. van der Kodel. Basic clinical radiobiology. Hodder Harold, London, United Kingdom, 2009.

[Kamada 2002] T. Kamada, H. Tsujii, H. Tsuji, T. Yanagi, J-E. Mizoe, T. Miyamoto, H. Kato, S. Yamada, S. Morita, K. Yoshikawa *et al. Efficacy and safety of carbon ion radiotherapy in bone and soft tissue sarcomas.* J. Clin. Oncol., vol. 20, pp. 4466–4471, 2002.

[Kamada 2012] T. Kamada. *Clinical evidence of particle beam therapy (carbon).* Int. J. Clin. Oncol., vol. 17, pp. 85–88, 2012.

[Kashino 2009] G. Kashino, T. Kondoh, N. Nariyama, K. Umetani, T. Ohigashi, K. Shinohara, A. Kurihara, M. Fukumoto, H. Tanaka, A. Maruhashi *et al. Induction of DNA double-strand breaks an d cellular migration through bystander effects in cells irradiated with the slit-type microplanar beam of the Spring-8 synchrotron.* Int. J. Radiat. Oncol. Biol. Phys., vol. 74, pp. 229–236, 2009.

[Kato 2004] H. Kato, H. Tsujii, T. Miyamoto, J-E. Mizoe, T. Kamada, H. Tsuji, S. Yamada, S. Kandatsu, K. Yoshikawa, T. Obata *et al. Results of the first prospective study of carbon ion radiotherapy for hepatocellular carcinoma with liver cirrhosis.* Int. J. Radiat. Oncol. Biol. Phys., vol. 59, pp. 1468–1476, 2004.

[Kawrakow 2000] I. Kawrakow and D. Rogers. *The EGSnrc code system: Monte Carlo simulation of electron and photon transport.* NRCC Report, vol. PIRS-701, 2000.

[Kirby 2009] D. Kirby, S. Green, H. Palmans, R. Hugtenburg, C. Wojnecki and D. Parker. *LET dependence of GafChromic films and an ion chamber in low-energy proton dosimetry.* Phys. Med. Biol., vol. 55, pp. 417–433, 2009.

[Klodowska 2015] M. Klodowska, P. Olko and M.P.R. Waligorski. *Proton microbeam radiotherapy with scanned pencil-beamse Monte Carlo simulations.* Phys. Med., vol. 31, pp. 621–626, 2015.

[Köhler 1909] A. Köhler. *Zur Röntgentiefentherapie mit Massendosen.* Med. Wochenschr., vol. 56, pp. 2314–2316, 1909.

[Koi 2010] T. Koi. *New native QMD code in Geant4.* In Proceedings of the MC2010 Monte Carlo Conference, 2010.

[Kooy 2015] H. M. Kooy and C. Grassberger. *Intensity modulated proton therapy.* Br. J. Radiol., vol. 88, 20150195, pp. 1–16, 2015.

[Kraft 2009] G. Kraft and S.D. Kraft. *Research needed for improving heavy-ion therapy.* New J. Phys., vol. 11, 025001, pp. 1–16, 2009.

[Kraus-Tiefenbacher 2007] U. Kraus-Tiefenbacher, L. Bauer, A. Scheda, C. Schoeber, J. Schaefer, V. Steil and F. Wenz. *Intraoperative radiotherapy (IORT) is an option for patients with localized breast recurrences after previous external-beam radiotherapy.* BMC Cancer, vol. 7, 178, pp. 1–7, 2007.

[Krengli 2004] M. Krengli, L. Masini and D. Beldi. *IORT: clinical indications.* Oncologia, vol. 37, pp. 364–370, 2004.

[Lafond 2015] C. Lafond, A. Simon, O. Henry, N. Périchon, J. Castelli, O. Acosta and R. de Crevoisier. *Adaptive radiotherapy in routine use? State of the art: The medical physicist's point of view.* Cancer Radiother., vol. 19, pp. 450–457, 2015.

[Laissue 1998] J. A. Laissue, G. Geiser, P. O. Spanne, F. A. Dilmanian, J. O. Gebbers, M. Geiser, X. Y. Wul, M.S. Makar, P. L. Micca, M. M. Nawrocky *et al. Neuropathology of ablation of rat gliosarcomas and con-tiguous brain tissues using a microplanar beam of synchrotro wiggler-generated x-rays.* Int. J. Cancer, vol. 78, pp. 654–660, 1998.

[Laissue 1999] J.A. Laissue, N. Lyubimova, H-P. Wagner, D.W. Archer, D.N. Slatkin, M. Di Michiel, C. Nemoz, M. Renier, E. Bräuer, P.O. Spanne *et al. Microbeam radiation therapy.* In SPIE's International Symposium on Optical Science, Engineering, and Instrumentation, pp. 38–45. International Society for Optics and Photonics, 1999.

[Laissue 2001] J. A. Laissue, H. Blattmann, M. Di Michiel, D. N. Slatkin, N. Lyubimova, R. Guzman, W. Zimmermann, S. Birrer, T. Bley, P. Kircher *et al. Weanling piglet cerebellum: a surrogate for tolerance to mrt (microbeam radiation therapy) in pediatric neuro-oncology.* Proc. SPIE, vol. 4508, pp. 65–73, 2001.

[Laissue 2007] J. A. Laissue, H. Blattmann, H.P. Wagner, M.A. Grotzer and D. N. Slatkin. *Prospects for microbeam radiation therapy of brain tumours in children to reduce neurological sequelae.* Dev. Med. Child. Neurol., vol. 49, pp. 577–581, 2007.

[Laissue 2013] J. A. Laissue, S. Bartzsch, H. Blattmann, E. Bräuer-Krisch, A. Bravin, A. Dallery, V. Djonov, A.L. Hanson, J.W. Hopewell, B. Kaser-Hotz *et al. Response of the rat spinal cord to x-ray microbeams.* Radiother. Oncol., vol. 106, pp. 106–111, 2013.

[Lawrence 2010] R. Lawrence, X.Q. Li, I. El Naqa, C.A. Hahn, L.B. Marks, T.E. Merchant and A.P. Dicker. *Radiation dose-volume effects in the brain.* Int. J. Radiat. Oncol. Biol. Phys., vol. 76, pp. S20–S27, 2010.

[Ling 2012] T.C. Ling, J.I. Kang, D.A. Bush, J.D. Slater and G.Y. Yang. *Proton therapy for hepatocellular carcinoma.* Chin. J. Cancer Res., vol. 24, pp. 361–367, 2012.

[Linstadt 1991] D.E. Linstadt, J.R. Castro and T.L. Phillips. *Neon ion radiotherapy: results of the phase I/II clinical trial.* Int. J. Radiat. Oncol. Biol. Phys., vol. 20, pp. 761–769, 1991.

[Livingstone 2016] J. Livingstone, A.W. Stevenson, D.J. Butler, D. Häusermann and J-F. Adam. *Characterization of a synthetic single crystal diamond de-*

tector for dosimetry in spatially fractionated synchrotron x-ray fields. Med. Phys., vol. 43, pp. 4283–4293, 2016.

[Lomax 1999] A. Lomax. *Intensity modulation methods for proton radiotherapy.* Phys. Med. Biol., vol. 44, pp. 185–205, 1999.

[Ma 1999] C-M. Ma and S.B. Jiang. *Monte Carlo modelling of electron beams from medical accelerators.* Phys. Med. Biol., vol. 44, pp. R157–R189, 1999.

[Ma 2013] C.-M. C. Ma and A. Lomax. Proton and carbon ion therapy. Imaging in medical diagnosis and therapy, 2013.

[Mandapaka 2013] A.K. Mandapaka, A. Ghebremedhin, B. Patyal, M. Marinelli, G. Prestopino, C. Verona and G. Verona-Rinati. *Evaluation of the dosimetric properties of a synthetic single crystal diamond detector in high energy clinical proton beams.* Med. Phys., vol. 40, 121702, pp. 1–9, 2013.

[Marín 2015] A. Marín, M. Martín, O. Li nán, F. Alvarenga, M. López, L. Fernández, D. Büchser and L. Cerezo. *Bystander effects and radiotherapy.* Rep. Prac. Oncol. Radiother., vol. 20, pp. 12–21, 2015.

[Marinelli 2014] M. Marinelli, F. Pompili, G. Prestopino, C. Verona, G. Verona-Rinati, G.A.P. Cirrone, G. Cuttone, R.M. La Rosa, L. Raffaele, F. Romano *et al. Dosimetric characterization of a synthetic single crystal diamond detector in a clinical 62MeV ocular therapy proton beam.* Nucl. Instrum. Methods Phys. Res. A, vol. 767, pp. 310–317, 2014.

[Marsolat 2013] F. Marsolat, D. Tromson, N. Tranchant, M. Pomorski, M. Le Roy, M. Donois, F. Moignau, A. Ostrowsky, L. De Carlan, C. Bassinet *et al. A new single crystal diamond dosimeter for small beam: comparison with different commercial active detectors.* Phys. Med. Biol., vol. 58, pp. 7647–7660, 2013.

[Martínez-Rovira 2010] Imma Martínez-Rovira, J Sempau, Jose Maria Fernández-Varea, A Bravin and Y Prezado. *Monte Carlo dosimetry for forthcoming clinical trials in x-ray microbeam radiation therapy.* Phys. Med. Biol., vol. 55, pp. 4375–4388, 2010.

[Martínez-Rovira 2012] I Martínez-Rovira, J Sempau and Y Prezado. *Development and commissioning of a Monte Carlo photon beam model for the forthcoming clinical trials in microbeam radiation therapy.* Med. Phys., vol. 39, pp. 119–131, 2012.

[Martínez-Rovira 2014] Immaculada Martínez-Rovira, J Sempau and Yolanda Prezado. *Monte Carlo-based dose calculation engine for minibeam radiation therapy.* Med. Phys., vol. 30, pp. 57–62, 2014.

[Martínez-Rovira 2015] I. Martínez-Rovira, G. Fois and Y. Prezado. *Dosimetric evaluation of new approaches in GRID therapy using nonconventional radiation sources.* Med. Phys., vol. 42, pp. 685–693, 2015.

[Martínez-Rovira 2016] I. Martínez-Rovira, W. Gonzales-Infantes, S. Brons and Y. Prezado. *Carbon and oxygen minibeam radiation therapy: experimental dosimetric evaluation.* Submitted, 2016.

[Martišíková 2010] M. Martišíková and O. Jäkel. *Dosimetric properties of Gafchromic® EBT films in medical carbon ion beams.* Phys. Med. Biol., vol. 55, pp. 5557–5567, 2010.

[Matsufuji 2005] N. Matsufuji, M. Komori, H. Sasaki, M. Ogawa K. Akiu, A. Fukumura, E. Urakabe, T. Inaniwa, T. Nishio, T. Kohno *et al. Spatial fragment distribution from a therapeutic pencil-like carbon beam in water.* Phys. Med. Biol., vol. 50, pp. 3393–3403, 2005.

[Mayles 2007] P. Mayles, A. Nahum and J-C. Rosenwald. Handbook of radiotherapy physics: theory and practice. CRC Press, 2007.

[McKinney 2012] G.W. McKinney. *Physics and Algorithm Enhancements for a Validated MCNP/X Monte Carlo Simulation Tool, Phase VII.* Technical report, Los Alamos National Laboratory, United States of America, 2012.

[Metropolis 1949] N. Metropolis and S. Ulam. *The monte carlo method.* J. Am. Stat. Assoc., vol. 44, pp. 335–341, 1949.

[Micke 2011] A. Micke, D.F. Lewis and X. Yu. *Multichannel film dosimetry with nonuniformity correction.* Med. Phys., vol. 38, pp. 2523–2534, 2011.

[Min 2006] C-H. Min, C.H. Kim, M-Y. Youn and J-W. Kim. *Prompt gamma measurements for locating the dose falloff region in the proton therapy.* Appl. Phys. Lett., vol. 89, 183517, 2006.

[Miyamoto 2007] T. Miyamoto, M. Baba, T. Sugane, M. Nakajima, T. Yashiro, K. Kagei, N. Hirasawa, T. Sugawara, N. Yamamoto, M. Koto *et al. Carbon ion radiotherapy for stage I non-small cell lung cancer using a regimen of four fractions during 1 week.* J. Thorac. Oncol., vol. 2, pp. 916–926, 2007.

[Mizoe 2004] J-E. Mizoe, H. Tsujii, T. Kamada, Y. Matsuoka, H. Tsuji, Y. Osaka, A. Hasegawa, N. Yamamoto, S. Ebihara, A. Konno *et al. Dose escalation study of carbon ion radiotherapy for locally advanced head-and-neck cancer.* Int. J. Radiat. Oncol. Biol. Phys., vol. 60, pp. 358–364, 2004.

[Mizumoto 2010] M. Mizumoto, K. Tsuboi, H. Igaki, T. Yamamoto, S. Takano, Y. Oshiro, Y. Hayashi, H. Hashii, A. Kanemoto, H. Nakayama *et al. Phase I/II trial of hyperfractionated concomitant boost proton radiotherapy for supratentorial glioblastoma multiforme.* Int. J. Radiat. Oncol. Biol. Phys., vol. 77, pp. 98–105, 2010.

[Mohiuddin 1990] M. Mohiuddin, D.L. Curtis, W.T Grizos and L. Komarnicky. *Palliative treatment of advanced cancer using multiple nonconfluent pencil beam radiation.* Cancer, vol. 66, pp. 114–118, 1990.

[Mohiuddin 1999] M. Mohiuddin, M. Fujita, W.F. Regine, A.S. Megooni, G.S. Ibbott and M.M. Ahmed. *High-dose spatially-fractionated radiation (GRID): a new paradigm in the management of advanced cancers.* Int. J. Radiat. Oncol. Biol. Phys., vol. 45, pp. 721–727, 1999.

[Nahum 1978] A.E. Nahum. *Water/air mass stopping power ratios for megavoltage photon and electron beams.* Phys. Med. Biol., vol. 23, pp. 24–39, 1978.

[Nath 1981] R. Nath and R.J. Schulz. *Calculated response and wall correction factors for ionization chambers exposed to 60Co gamma-rays.* Med. Phys., vol. 8, pp. 85–93, 1981.

[Newhauser 2015] W.D. Newhauser and R. Zhang. *The physics of proton therapy.* Phys. Med. Biol., vol. 60, pp. R155–R209, 2015.

[Nikoghosyan 2010] A.V. Nikoghosyan, I. Karapanagiotou-Schenkel, M.W. Münter, A.D. Jensen, S.E. Combs and J. Debus. *Randomised trial of proton vs. carbon ion radiation therapy in patients with chordoma of the skull base, clinical phase III study HIT-1-Study.* BMC cancer, vol. 10, 2010.

[Niroomand-Rad 1998] A. Niroomand-Rad, C.R. Blackwell, B.M. Coursey, K.P. Gall, J.M. Galvin, W.L. McLaughlin, A.S. Meigooni, R. Nath, J.E. Rodgers, C.G. Soares *et al. Radiochromic film dosimetry: recommendations of AAPM radiation therapy committee task group 55.* Med. Phys., vol. 25, pp. 2093–2115, 1998.

[NIST-ESTAR 2016] NIST-ESTAR. *Stopping power and range tables for electrons.* National Institute of Standards and Technology http://physics.nist.gov/PhysRefData/Star/Text/ESTAR.html, 2016.

[NIST-PSTAR 2016] NIST-PSTAR. *Stopping power and range tables for protons.* National Institute of Standards and Technology http://physics.nist.gov/PhysRefData/Star/Text/PSTAR.html, 2016.

[Open-Gate 2016] Open-Gate. http://www.opengatecollaboration.org/, 2016.

[Paganetti 2002] H. Paganetti, A. Niemierko, M. Ancukiewicz, L.E. Gerweck, M. Goitein, J.S Loeffler and H.D Suit. *Relative biological effectiveness (RBE) values for proton beam therapy.* Int. J. Radiat. Oncol. Biol. Phys., vol. 53, pp. 407–421, 2002.

[Paganetti 2005] H. Paganetti and T. Bortfeld. *Proton beam radiotherapy - The state of the art.* New Technologies in Radiation Oncology (Medical Radiology Series), Springer Verlag, Heidelberg, Germany, pp. 3–540, 2005.

[Paganetti 2012] H. Paganetti. Proton therapy physics - series in medical physics and biomedical engineering. CRC Press, 2012.

[Palmer 2015] A.L. Palmer, A. Dimitriadis, A. Nisbet and C.H. Clark. *Evaluation of Gafchromic EBT-XD film, with comparison to EBT3 film, and application in high dose radiotherapy verification.* Physics in medicine and biology, no. 22, pp. 8741–8752, 2015.

[Parodi 2007] K. Parodi, H. Paganetti, H.A. Shih, S. Michaud, J.S. Loeffler, T.F. DeLaney, N.J. Liebsch, J.E. Munzenrider, A.J. Fischman, A. Knopf *et al. Patient study of in vivo verification of beam delivery and range, using positron emission tomography and computed tomography imaging after proton therapy.* Int. J. Radiat. Oncol. Biol. Phys., vol. 68, pp. 920–934, 2007.

[Penn-Medicine 2016] Penn-Medicine. University of Pennsylvania http://www.oncolink.org/, 2016.

[Perl 2012] J. Perl, J. Shin, J. Schümann, B. Faddegon and H. Paganetti. *TOPAS: an innovative proton Monte Carlo platform for research and clinical applications.* Med. Phys., vol. 39, pp. 6818–6837, 2012.

[Peucelle 2015a] C. Peucelle, C. Nauraye, A. Patriarca, E. Hierso, N. Fournier-Bidoz, I. Martínez-Rovira and Y. Prezado. *Proton minibeam radiation therapy: Experimental dosimetry evaluation.* Med. Phys., vol. 42, pp. 7108–7113, 2015.

[Peucelle 2015b] C. Peucelle, I. Martínez Rovira and Y. Prezado. *Spatial fractionation of the dose using neon and heavier ions: A Monte Carlo study.* Med. Phys., vol. 42, pp. 5928–5936, 2015.

[Pinto 2016] M. Pinto, D. Dauvergne, N. Freud, J. Krimmer, J-M. Létang and E. Testa. *Assessment of Geant4 Prompt-Gamma Emission Yields in the Context of Proton Therapy Monitoring.* Front. Oncol., vol. 6:10, pp. 1–7, 2016.

[Podgorsak 2005] E.B. Podgorsak. Radiation oncology physics: A handbook for teachers and students. International Atomic Energy Agency, Vienna, Austria, 2005.

[Pommier 2006] P. Pommier, N. J Liebsch, D.G. Deschler, D.T. Lin, J.F. McIntyre, F.G. Barker, J.A. Adams, V.V. Lopes, M. Varvares, J.S. Loeffler *et al. Proton beam radiation therapy for skull base adenoid cystic carcinoma.* Arch. Otolaryngol. Head Neck Surg., vol. 132, pp. 1242–1249, 2006.

[Prezado 2009a] Y. Prezado, M. Renier and A. Bravin. *A new method of creating minibeam patterns for synchrotron radiation therapy: a feasibility study.* J. Synchrotron Radiat., vol. 16, pp. 582–586, 2009.

[Prezado 2009b] Y. Prezado, S. Thengumpallil, M. Renier and A. Bravin. *X-ray energy optimization in minibeam radiation therapy.* Med. Phys., vol. 36, pp. 4897–4902, 2009.

[Prezado 2011] Y. Prezado, I. Martinez-Rovira, S. Thengumpallil and P. Deman. *Dosimetry protocol for the preclinical trials in white-beam minibeam radiation therapy.* Med. Phys., vol. 38, pp. 5012–5020, 2011.

[Prezado 2012a] Y Prezado, I Martínez-Rovira and M Sánchez. *Scatter factors assessment in microbeam radiation therapy.* Med. Phys., vol. 39, pp. 1234–1238, 2012.

[Prezado 2012b] Y. Prezado, S. Sarun, S. Gil, P. Deman, A. Bouchet and G. Le Duc. *Increase of lifespan for glioma-bearing rats by using minibeam radiation therapy.* J. Synchrotron Radiat., vol. 19, pp. 60–65, 2012.

[Prezado 2013] Y. Prezado and G. Fois. *Proton Minibeam Radiation Therapy: a proof of concept.* Med. Phys., vol. 40, 031712, pp. 1–8, 2013.

[Prezado 2015] Y. Prezado, P. Deman, P. Varlet, G. Jouvion, S. Gil, C. LeClec'h, H. Bernard, G. Le Duc, and S. Sarun. *Tolerance to dose escalation in minibeam radiation therapy applied to normal rat brain: Long-term clinical, radiological and histopathological analysis.* Radiat. Res., vol. 184, pp. 314–321, 2015.

[PTCOG 2016] PTCOG. *Particle Therapy Co-Operative Group.* www.ptcog.ch, 2016.

[PTW 2016] PTW. *microDiamond© - Synthetic Diamond Detector specifications.* www.ptw.de, 2016.

[Regnard 2008] P. Regnard, G. Le Duc, E. Bräuer-Krisch, I. Troprès, E. A. Siegbahn, A. Kusak, C. Clair, H. Bernard, D. Dallery, J. A. Laissue and A. Bravin. *Irradiation of intracerebral 9L gliosarcoma by a single array of microplanar x-ray beams from a synchrotron: balance between curing and sparing.* Phys. Med. Biol., vol. 53, pp. 861–878, 2008.

[Romanelli 2013] P. Romanelli, G. Fardone, G. Battaglia, E. Bräuer-Krisch, Y. Prezado, H. Requardt, G. Le Duc, C. Nemoz, D.J. Anschel, J. Spiga *et al. Synchrotron-generated microbeam sensorimotor cortex transections induce seizure control withour disruption of neurological functions.* PLoS ONE, 2013.

[Rossomme 2016] S. Rossomme, J.M. Denis, K. Souris, A. Delor, F. Bartier, D. Dumont, S. Vynckier and H. Palmans. *LET dependence of the response of a PTW-60019 microDiamond detector in a 62MeV proton beam.* Phys. Med., 2016.

[Salvat 2011] F. Salvat, J.M. Fernández-Varea and J. Sempau. *PENELOPE2011: A code system for Monte Carlo simulation of electron and photon transport.* In Workshop Proceedings, 2011.

[Schardt 2010] D. Schardt, T. Elsässer and D. Schulz-Ertner:. *Heavy-ion tumor therapy: Physical and radiobiological benefits.* Rev. Mod. Phys., vol. 82, pp. 383–425, 2010.

[Schneider 2016] T. Schneider. *Master thesis - Proton minibeam radiation therapy using the pencil beam scanning technique.* PhD thesis, Ecole Polytechnique, Palaiseau / Eidgen Össiche Technische Hochschule, Zurich, 2016.

[Scott 2012] A.J.D. Scott, S. Kumar, A.E. Nahum and J.D. Fenwick. *Characterizing the influence of detector density on dosimeter response in non-equilibrium small photon fields.* Phys. Med. Biol., vol. 57, pp. 4461–4476, 2012.

[Seco 2013] J. Seco and F. Verhaegen. Monte carlo techniques in radiation therapy. CRC press, 2013.

[Serduc 2006] R. Serduc, P. Vérant, J. C. Vial, R. Farion, L. Roca, C. Rémy, T. Fadlallah, E. Bräuer-Krisch, A. Bravin *et al. In vivo two-photon microscopy study of short-term effects of microbeam irradiation on normal mouse brain microvasculature.* Int. J. Radiat. Oncol. Biol. Phys., vol. 64, pp. 1519–1527, 2006.

[Serduc 2010] R. Serduc, E. Bräuer-Krisch, E.A. Siegbahn, A. Bouchet, B. Pouyatos, R. Carron, N. Pannetier, L. Renaud, G. Berruyer, C. Nemoz *et al. High-precision radiosurgical dose delivery by interlaced microbeam arrays of high-flux low-energy synchrotron X-rays.* PLoS one, vol. 5, pp. 1–12, 2010.

[Siegbahn 2006] E.A. Siegbahn, J. Stepanek, E. Bräuer-Krisch and A. Bravin. *Determination of dosimetrical quantities used in microbeam radiation therapy (MRT) with Monte Carlo simulations.* Med. Phys., vol. 33, pp. 3248–3259, 2006.

[Sihver 1998] L. Sihver, D. Schardt and T. Kanai. *Depth-dose distributions of high-energy carbon, oxygen and neon beams in water.* Jpn. J. Med. Physics, vol. 18, pp. 1–21, 1998.

[Siva 2015] S. Siva, M.P. MacManus, R.F. Martin and O.A. Martin. *Abscopal effects of radiation therapy: A clinical review for the radiobiologist.* Cancer Lett., vol. 356, pp. 82–90, 2015.

[Slater 1992] J.M. Slater, J.O. Archambeau, D.W. Miller, M.I. Notarus, W. Preston and J.D. Slater. *The proton treatment center at Loma Linda University Medical Center: rationale for and description of its development.* Int. J. Radiat. Oncol. Biol. Phys., vol. 22, pp. 383–389, 1992.

[Slatkin 1992] D.N. Slatkin, P.O. Spanne, F.A Dilmanian and M. Sandborg. *Microbeam radiation therapy.* Med. Phys., vol. 19, pp. 1395–1400, 1992.

[Slatkin 1995] D.N. Slatkin, P.O. Spanne, J.O. Gebbers and J.A. Laissue. *Subacute neuropathological effects of microplanar beams of x-rays from a synchrotron wiggler.* Proc. Natl. Acad. Sci. U.S.A., vol. 92, pp. 8783–8787, 1995.

[Sorriaux 2013] J. Sorriaux, A. Kacperek, S. Rossomme, J.A. Lee, D. Bertrand, S. Vynckier and E. Sterpin. *Evaluation of Gafchromic® EBT3 films characteristics in therapy photon, electron and proton beams.* Phys. Med., vol. 29, pp. 599–606, 2013.

[Spiga 2007] J. Spiga, E.A. Siegbahn, E. Bräuer-Krisch, P. Randaccio and A. Bravin. *The GEANT4 toolkit for microdosimetry calculations: Application to microbeam radiation therapy (MRT).* Med. Phys., vol. 34, pp. 4322–4330, 2007.

[Strulab 2003] D. Strulab, G. Santin, D. Lazaro, V. Breton and C. Morel. *GATE (Geant4 Application for Tomographic Emission): a PET/SPECT general-purpose simulation platform.* Nucl. Phys. B, vol. 125, pp. 75–79, 2003.

[Tanaka 2005] M. Tanaka, Y. Ino, K. Nakagawa, M. Tago and T. Todo. *High-dose conformal radiotherapy for supratentorial malignant glioma: a historical comparison.* Lancet Oncol., vol. 6, pp. 953–960, 2005.

[Timmerman 2005] R.D. Timmerman, K.M. Forster and C.L. Chinsoo. *Extracranial stereotactic radiation delivery.* Semin. Radiat. Oncol., 2005.

[Tobias 1958] C.A. Tobias, J.H. Lawrence, J.L. Born, R.K. McCombs, J.E. Roberts JE and H.O. Anger. *Pituitary irradiation with high-energy proton beams: a preliminary report.* Cancer Res., 1958.

[Tobias 1977] C.A. Tobias, E.A. Blakely and R.J. Roots. Cellular and molecular radiobiology of heavy ions. Biological and medical research with accelerated heavy ions at the BEVALAC, 1974–1977. Lawrence Berkeley Laboratory report LBL-6510, 1977.

[Tsuji 2005] H. Tsuji, T. Yanagi, H. Ishikawa, T. Kamada, J-E. Mizoe, T. Kanai, S. Morita, H. Tsujii *et al. Hypofractionated radiotherapy with carbon ion beams for prostate cancer.* Int. J. Radiat. Oncol. Biol. Phys., vol. 63, pp. 1153–1160, 2005.

[Turesson 1989] I. Turesson and H.D. Thames. *Repair capacity and kinetics of human skin during fractionated radiotherapy: erythema, desquamation, and telangiectasia after 3 and 5 year's follow-up.* Radiother. Oncol., vol. 15, pp. 169–188, 1989.

[Vatnitsky 1993] S. Vatnitsky and H. Jarvinen. *Application of a natural diamond detector for the measurement of relative dose distributions in radiotherapy.* Phys. Med. Biol., vol. 38, pp. 173–184, 1993.

[Vatnitsky 1997] S.M. Vatnitsky, Reinhard W.M. Schulte, R. Galindo, H.J. Meinass and D.W. Miller. *Radiochromic film dosimetry for verification of dose distributions delivered with proton-beam radiosurgery.* Phys. Med. Biol., vol. 42, pp. 1887–1898, 1997.

[Verhaegen 2003] F. Verhaegen and J. Seuntjens. *Monte Carlo modelling of external radiotherapy photon beams.* Phys. Med. Biol., vol. 48, pp. R107–R164, 2003.

[Vuillez 2005] J.P. Vuillez. *Radiothérapie métabolique: état et perspectives.* Médecine nucléaire - Imagerie fonctionnelle et métabolique, vol. 29, 2005.

[Vujosevic 2010] Bozica Vujosevic and Bojana Bokorov. *Radiotherapy: past and present.* Arch. Oncol., 2010.

[Washington 2015] C.M. Washington and D.T. Leaver. Principles and practice of radiation therapy (fourth edition). Elsevier, 2015.

[WCRF 2015] WCRF. *Cancer facts and figures - Worldwide data.* World Cancer Research Fund International, 2015.

[WHO 2015] WHO. *Key facts of cancer.* World Health Organization's Media center, Fact sheet No 297, 2015.

[Yaes 1988] R. J. Yaes and A. Kalend. *Local stem cell depletion model for radiation myelitis.* Int. J. Radiat. Oncol. Biol. Phys., vol. 14, 1988.

[Yamada 2011] S. Yamada, M. Shinoto, S. Endo, S. Yasuda, H. Imada, T. Kamada and H. Tsujii. *Carbon ion radiotherapy for patients with locally recurrent rectal cancer.* Proceedings of NIRS-ETOILE, 2nd Joint Symposium on Carbon Ion Radiotherapy, NIRS-M-243, pp. 54–59, 2011.

[Yan 1997] D. Yan, F. Vicini, J. Wong and A. Martinez. *Adaptive radiation therapy.* Phys. Med. Biol., vol. 42, pp. 123–132, 1997.

[Yu 2011] C.X. Yu and G. Tang. *Intensity-modulated arc therapy: principles, technologies and clinical implementations.* Phys. Med. Biol., vol. 56, 2011.

[Zaidi 1999] H. Zaidi. *Relevance of accurate Monte Carlo modeling in nuclear medical imaging.* Med. Phys., vol. 26, pp. 574–608, 1999.

[Zeiss 2016] Zeiss. *Intrabeam© System from ZEISS.* http://www.zeiss.com/meditec/, 2016.

[Zeman 1959] W. Zeman, H.J. Curtis, E.L. Gebhard and W. Haymaker. *Tolerance of mouse brain tissue to high-energy deuterons.* Science, vol. 130, pp. 1760–1761, 1959.

[Zeman 1961] W. Zeman, H.J. Curtis and C.P. Baker. *Histopathologic effect of high-energy-particle microbeams on the visual cortex of the mouse brain.* Radiat. Res., vol. 15, pp. 496–514, 1961.

[Zeman 2015] E.M. Zeman, E. C. Schreiber and J. E. Tepper. *Basics of Radiation Therapy*. http://clinicalgate.com/basics-of-radiation-therapy-2/, 2015.

[Zhao 2010] L. Zhao and I.J. Das. *Gafchromic© EBT film dosimetry in proton beams*. Phys. Med. Biol., vol. 55, pp. N291–N301, 2010.

[Zhong 2003] N. Zhong, G. M. Morris, T. Bacarian, E. M. Rosen and F. A. Dilmanian. *Response of rat skin to high-dose unidirectional x-ray microbeams: a histological study*. Radiat. Res., vol. 160, pp. 133–142, 2003.

[Zlobinskaya 2013] O. Zlobinskaya, S. Girst, C. Greubel, V. Hable, C. Siebenwirth, D. W. Walsh, G. Multhoff, J. J. Wilkens, T. E. Schmid and G. Dollinger. *Reduced side effects by proton microchannel radiotherapy: Study in a human skin model*. Environ. Biophys., vol. 52, pp. 123–133, 2013.

List of Abbreviations

AAPM	American Association of Physicists in Medicine
AG	Air Gap
ART	Adaptive RadioTherapy
ASTRO	American Society for Radiation Oncology
BIC	Binary Intra-nuclear Cascade
cema	Converted Energy per unit MAss
CK	CyberKnife©
CPE	Charged Particle Equilibrium
CRT	Conformal RadioTherapy
CT	Computed Tomography
c-t-c	centre-to-centre
DNA	DeoxyriboNucleic Acid
DS	Double Scattering
EBRT	External Beam RadioTherapy
EM	ElectroMagnetic
ESRF	European Synchrotron Radiation Facility
FWHM	Full Width at Half Maximum
GK	Gamma Knife©
GPS	General Particle Source
HDR	High-Dose Rate
HIMAC	Heavy Ion Medical Accelerator in Chiba
HIT	Heidelberg Ion Therapy facility
IAEA	International Atomic Energy Agency
IC	Ionisation Chamber
ICPO	Institut Curie - Centre of Proton therapy in Orsay
ICRU	International Commission on Radiations and Units
IORT	IntraOperative RadioTherapy
IGRT	Image Guided RadioTherapy
IMAT	Intensity Modulated Arc Therapy
IMNC	Imagerie et Modelisation en Neurobiologie et Cancerologie
IMPT	Intensity Modulated Particle Therapy
IMRT	Intensity Modulated RadioTherapy
ITV	Internal Target Volume
kerma	Kinetic Energy Released per unit MAss
LDR	Low-Dose Rate
LET	Linear Energy Transfer
linac	LINear ACcelerator
LQ	Linear Quadratic
MBRT	MiniBeam Radiation Therapy
MC	Monte Carlo

MDR	Medium-Dose Rate
MOSFET	Metal Oxide Semiconductor Field Effect Transistor
MRI	Magnetic Resonance Imaging
MRT	Microbeam Radiation Therapy
NARA	New Approaches in RAdiotherapy
NIST	National Institute of Standards and Technology
NTCP	Normal Tissue Complication Probability
NTD	Normalised Total Dose
OD	Optical Density
OER	Oxygen Enhancement Ratio
OF	Output Factor
PBS	Pencil Beam Scanning
PCD	Phantom-to-Collimator Distance
PDR	Pulsed-Dose Rate
PDD	Percentage Depth Dose
PET	Positron Emission Tomography
PSF	Phase Space File
pMBRT	proton MiniBeam Radiation Therapy
PMMA	PolyMethylMethAcrylate
PTCOG	Particle Therapy Co-Operative Group
PVDR	Peak-to-Valley Dose Ratio
RBE	Relative Biological Effectiveness
RF	Radio-Frequency
RGB	Red-Green-Blue
RMT	RadioMetabolic Therapy
RT	RadioTherapy
SCDD	Single-Crystal Diamond Detector
SFRT	Spatially Fractionated RadioTherapy
SI	Stereotactic Irradiations
SOBP	Spread-Out Bragg Peak
SPECT	Single Photon Emission Computed Tomography
SRS	Stereotactic RadioSurgery
SRT	Stereotactic RadioTherapy
TLD	ThermoLuminescent Dosimeter
TPS	Treatment Planning System
TRS	Technical Report Series
US	Uniform Scanning
WET	Water Equivalent Thickness
QCF	Quenching Correction Factor
QMD	Quantum Molecular Dynamics

List of Figures

1.1 *Illustration of the concept of therapeutic window. A tumour can be effectively treated with RT if the range of doses D_{min}–D_{max}, or therapeutic window, is wide enough.* 3

1.2 *Left: Intrabeam© system with applicator dedicated to breast treatment. Right: example of applicator insertion during a breast cancer IORT treatment. Taken from the Zeiss Website [Zeiss 2016].* 6

1.3 *Schematic view of the head of a modern linac operating in x-ray (left) or electron (right) irradiation modes. The beam traverses several modifiers before reaching the patient in order to conform the radiation field to the tumour, such as collimators, flattening filters (x-ray mode) or scattering foils (electron mode). Taken from the work of Zeman et al. [Zeman 2015].* 7

1.4 *Percentage depth dose distribution of a 6 MV-photon beam (solid line), compared to the sharp fall-off distribution at the end of the range for two electron beams of different energies (6 MeV and 15 MeV).* 7

1.5 *Comparison of the depth-dose profiles of x-rays and mono-energetic ions. While x-rays exhibit an exponential decrease of the absorbed dose as a function of depth, charged particles deposit most of their energy at the end of their path, in the so-called Bragg peak, while sparing both proximal and distal located normal tissues. Taken from the work of Durante and Loeffler [Durante 2010].* 10

1.6 *Dose plans for a high-grade glioma in proton therapy using Pencil Beam Scanning delivery method (left) and in photon RT delivered with a IMAT (centre). On the right picture, the statistical variations of the dose distributions between the two techniques are shown. A significant dose bath (low doses) in IMAT technique with respect to proton therapy is observed. This can cause an increased risk of secondary cancers. Taken from the work of Baumann et al. [Baumann 2016].* 11

1.7 *Electronic and nuclear stopping power curves of ^{12}C ions and protons in water. Inelastic collisions with atomic electrons are the dominant process for all energies for proton interactions. The same situation is observed for ^{12}C ions where this process is also dominant except for the last few micrometres of path where the nuclear stopping power becomes dominant. The range of ^{12}C ions in water corresponding to their specific energy is indicated at the top. Taken from the work of Schardt et al. [Schardt 2010].* 13

1.8 *Experimental depth dose curves of protons and carbon ions having the same mean range in water. Due to the higher relative range straggling with protons, the Bragg peak width is enlarged for this particle type with respect to the carbon ions distribution. Taken from the work of Schardt et al. [Schardt 2010].* 14

1.9 *Two-dimensional view of the depth dose distribution of a proton beam. The multiple Coulomb scattering process results in a lateral spread of the beam in depth, which increases with the slowing down of the particles. This results in a maximum enlargement of the beam at the Bragg peak.* 14

1.10 *Comparison of the production yields of several secondary fragments resulting from irradiation of a water phantom with a 400 MeV/u carbon ion beam. The contributions of Li, B and Be are magnified by a factor 10. The amount of fragments reaches a maximum at the Bragg peak, then diminishes. The most frequent fragments are H and He. Taken from the work of Haettner et al. [Haettner 2006].* 15

1.11 *Experimental attenuation of the primary beam in depth due to nuclear reactions for 200 and 400 MeV/u carbon beams (top), and related depth dose curves (bottom). The ratio of Bragg peak-to-entrance dose gets reduced as a function of the projectile's energy due to a greater beam attenuation. Taken from the work of Haettner et al. [Haettner 2006].* 16

1.12 *Experimental depth dose curves of 330 MeV/u carbon ions in water, and calculated contributions of primary projectiles, secondary and tertiary fragments to the total dose. The dose tail extending beyond the Bragg peak is due to projectile fragments having a longer range than the projectiles in the medium. Taken from the work of Sihver et al. [Sihver 1998].* 17

1.13 *Schematic drawing of a cyclotron. Charged particles are accelerated by means of an electric field applied between the dees. The particles keep moving in a spiral path thanks to a strong magnetic field applied by the magnets that curve their trajectories. Taken from the work of Paganetti [Paganetti 2012].* 18

1.14 *Schematic drawing of a synchrotron. After being pre-accelerated, particles are injected in the storage ring where they are accelerated passing through RF cavities. Bending magnets deflect the particle trajectory around a circular path. Taken from the work of Ma and Lomax [Ma 2013].* 19

1.15 *Scheme of beam shaping method in a double scattering system consisting in a modulation wheel (a), a double diffusion system (b), a range shifter (c), an individualised collimator (d) and a range compensator (e). Taken and modified from the Ph.D. thesis of G. Bouillhol [Bouillhol 2013].* 20

1.16 *A spread-out Bragg peak (SOBP) is created by superimposing the contribution of several Bragg peak curves of particles with different energies thus different ranges in the medium [ICRU-78 2007].* 21

1.17 *Left: Individualised patient brass collimator (bottom) and lucite range compensator (top), taken from the Pennsylvania University website [Penn-Medicine 2016]. Right: The same elements are placed at the end of the beamline for patient treatment, taken from the Institut Curie website [Institut-Curie 2016].* . . . 21

1.18 *Illustration of an active beam delivery method. Taken and modified from the Ph.D. thesis of G. Bouillhol [Bouillhol 2013]* 22

1.19 *Illustration of the dependence of RBE as a function of LET. RBE has been estimated at different dose levels (different cell survival fractions) of human kidney cells exposed in vitro to radiations. As one can see, there is an optimum LET for which RBE reaches a maximum. Greater LET radiations produce more damages than actually required for cell inactivation, resulting in a decrease of RBE values. This is known as the "overkill effect". Taken from the work of Joiner and van der Kogel [Joiner 2009].* 23

1.20 *RBE as a function of penetration depth for several ions. RBE values for carbon ions are kept close to 1 in the proximal normal tissues, while they significantly increase in the Bragg peak. In contrast, heavier ions such as argon exhibit high RBE values already in the proximal region. Taken from the work of Kraft et al. [Kraft 2009].* 24

1.21 *Relative physical and radiobiological properties of different radiations and charged particles. Carbon ions and protons provide interesting dose distributions. Carbon ions have also higher LET and RBE in the Bragg peak which might confer an additional radiobiological advantage. With heavier ions like argon, silicon or neon, LET and RBE values are enhanced but the dose distributions are degraded due to the secondary fragments. Taken from the work of Joiner et al. [Joiner 2009].* 25

1.22 *Grid collimator used with megavoltage x-ray beams. Taken from the work of Buckey et al. [Buckey 2010].* 28

1.23 *Example of a MBRT dose profile pattern. Some relevant dosimetric parameters of spatially fractionated irradiations are depicted. The ratio of the peak dose over the valley dose is called the peak-to-valley dose ratio (PVDR). The distance separating two minibeams centers is known as the centre-to-centre distance (c-t-c).* 28

1.24 *Reconstruction of the results obtained by Zeman et al. showing the tolerance doses of mice brains to irradiation with 22.5 MeV deuteron beams of several widths [Zeman 1959]. There is an inverse relationship between radio-sensitivity and volume of tissue exposed for small volumes. This is known as the dose-volume effect.* 30

1.25 *Histology images of mice brains illustrating the dose-volume effect. On the left, complete tissue destruction is observed after irradiation with a 22.5 MeV deuteron beam of 1 mm diameter and an entrance dose of 280 Gy. On the right, an entrance dose of 4000 Gy is necessary to achieve similar results with a 25 µm-wide beam. Taken from the work of Zeman et al. [Zeman 1961].* 30

1.26 *Illustration of a dose distribution following a pMBRT irradiation of the brain. While normal tissues in the beam path benefit from a spatial fractionation of the dose, the tumour receives a quasi-homogeneous dose distribution. Taken from the work of Martínez-Rovira et al. [Martínez-Rovira 2015].* 35

1.27 *Gafchromic© film irradiated in the longitudinal direction with oxygen minibeams. The minibeams are coming from the right. Taken from the work of Martínez-Rovira et al. [Martínez-Rovira 2016].* 37

1.28 *RBE (A) and OER (B) in cultured human cells calculated at the 10% survival level, plotted as a function of distance in water from the Bragg peak position. While RBE values for carbon ions are kept close to 1 in the proximal normal tissues and then dramatically increase in the Bragg peak vicinity, with heavier ions they are already high in the proximal region and do not increase much at the end of the range. Concerning OER, the values are very low (close or equal to 1) with very heavy ions in the Bragg peak, in contrast with carbon ions where an oxygen effect is maintained. Adapted from the work of Tobias et al. [Tobias 1977].* 38

2.1 *Pictures of the three treatment rooms of ICPO. Y1 and Y2 rooms have horizontal fixed beamlines that use DS delivery method. In the third room, the isocentric gantry allows the beam to be rotated around the patient. The gantry nozzle permits both passive and active beam delivery.* 42

2.2 *Left: ICPO horizontal Y1 proton therapy treatment room. At the of the beamline is positioned the treatment couch. Right: The patient is positioned on the chair treatment.* 42

2.3 *pMBRT multislit and 2×2 cm^2 collimators (left). The machining process created 3.5 cm-long slits. To achieve the desired irradiation area (2 × 2 cm^2), an additional square collimator was added after the pMBRT collimator on the beamline nozzle (right).* 43

2.4 *Schematic view of the Y1 beamline (not to scale).* 44

2.5 *Scheme illustrating the general situation of a measurement by means of a detector introduced into a medium (left). For a given exposure to radiations of quality Q, it leads to the D_{det} quantity. To convert it into the dose D_{med} in the medium in the absence of the detector (right), one has to multiply by f_Q.* 47

2.6 *Illustration of secondary electron tracks in (A) a small cavity, (B) an intermediate cavity, and (C) a large cavity. Taken from the work of Horowitz et al. [Horowitz 2006].* 48

2.7 *Top: parallel plane chamber (PPC05 from IBA). Bottom: cylindrical chamber (CC13 from IBA). Taken from the IBA website [IBA 2016].* 51

2.8 *Illustration of the detector field of view of the source. On the left, the field size is large enough to allow a full view of the beam source from the detector's point of view, while on the right the small field size leads to a partial occlusion of the source, resulting in penumbras overlap and drop in output. The eyes represent the detector's point of view. Modified from the work of Aspradakis et al. [Aspradakis 2010].* 53

2.9 *OF measured with different active and passive dosimeters for a Novalis© system equipped with microMLC. Taken from the work of Bassinet et al. [Bassinet 2013].* 55

2.10 *Experimental setup for absolute dose determination in reference conditions (broad beam). The water tank is located after the nozzle with a 5×5 cm^2 collimator.* 57

2.11 *Red channel dose calibration curve for EBT3 films.* 59
2.12 *Experimental setups for Gafchromic© films irradiations for relative dosimetry. The red arrows show the direction of the proton minibeams.* 60
2.13 *Home-made support dedicated to irradiation of EBT3 films in the longitudinal direction in water, i.e. configuration (ii) (left). The support was maintained in a fixed position using the remote-controlled part of the water tank (right).* 60
2.14 *Pieces of Gafchromic© films irradiated in the transversal (left) and longitudinal directions (right) with a multislits collimator (not to scale).* 61
2.15 *Left: Depth dose curves measured with the IC and Gafchromic© films in the water tank. An under-estimation of the dose is observed in the film at the Bragg peak. Right: Quenching correction factors to be applied to the films measurements. Values of QCF for depths inferior to 2 cm were extrapolated to 1, as direct measurements were not possible due to the thickness of the water tank wall.* 62
2.16 *The microDiamond© detector was positioned inside the BluePhantom^2 scanning system (left). In order to take advantage from the 1 µm dimension of the active volume, the detector was oriented perpendicular to the beam direction (right).* 63
2.17 *If the diamond detector had been positioned in parallel direction for PDD acquisition, an averaging effect would have occurred in the fractionation direction.* 64
2.18 *Available hadronic models in Geant4. Taken from the Geant4 tutorial presentations [Geant4-Tutorial 2014].* 67
2.19 *Illustration of the simulated geometry. The parallelepiped scoring region is placed inside the cylindrical water phantom whose dimensions mimic a human head.* 69
2.20 *Schematic view of the simulation setup with very heavy ions. A SOBP extends from 6 to 8 cm in the longitudinal direction in order to cover a virtual tumour located at the centre of the water phantom.* 71
2.21 *Depth dose distribution for one single mono-energetic silicon minibeam (319 MeV/u) in the water phantom obtained with several voxel dimension(200 µm, 500 µm and 1 mm) in the beam direction. An averaging effect was observed when voxel dimensions below 200 µm were employed (for Si), leading to an under-estimation of the Bragg peak intensity.* 73

3.1 *Contribution to the peak and valley dose distributions of primary projectiles and secondary products for an array of proton minibeams in a water phantom. The distributions are normalised to the maximum normal dose in peak (left) and in valley (right).* 76
3.2 *Contribution of the different species of secondary particles to the peak (left) and valley (right) depth dose curves. The dose was normalised to the maximum of the total sum of secondary products. "Secondaries tot." and "nuclear fragm." refer to "secondaries total" and "nuclear fragments", respectively.* . 77

3.3 *Contribution of the different species of secondary particles to the peak (left) and valley (right) depth dose curves. The dose was normalised to the maximum of the total sum of secondary products."Sec. protons" refer to "secondary protons".* 77
3.4 *Gafchromic© films irradiated longitudinally in the RW3 phantom with one minibeam (top) and with an array of 5 minibeams with the 700 µm-slits/c-t-c 3500 µm collimator (bottom).* 79
3.5 *Evolution of the full-width at half maximum (FWHM) as a function of depth for the single slit (left) and multislit collimators (right) in the solid water phantom. Beyond 30 mm (700 µm/c-t-c 2700 µm) and 40 mm (other collimators), FWHM values were not measurable in the central peak due to the increase of the valley dose.* 79
3.6 *The FWHM is directly measurable at shallow depths in the phantom using the 700 µm-slits/2700 µm collimator (left). From 40 mm in depth (right) the valley dose is so high that the determination of FWHM is no longer possible.* 80
3.7 *Depth dose curves in the central peak of minibeams arrays obtained in water (left) and solid water (right). Each curve is normalised with respect to the Bragg peak dose. Each colour corresponds to one collimator.* 81
3.8 *Depth dose curves in valley obtained in water (left) and solid water (right). Each curve is normalised with respect to the Bragg peak dose in the peak. Each colour corresponds to one collimator.* 81
3.9 *This series of films irradiated at different depths in the solid water phantom (700 µm-slits/c-t-c 3500 µm collimator) shows how the spatial fractionation is maintained in the normal tissues while a (quasi) homogeneous dose distribution is reached in the target.* 84
3.10 *Lateral dose profiles at several water-equivalent depths in the slabs phantom obtained with EBT3 films with the single slit (left) and the Multi3 (400 µm/c-t-c 3200 µm) collimators.* 84
3.11 *Lateral dose profiles at several depths in water obtained with the PTW microDiamond© detector. Both 700 µm-slits/c-t-c 3500 µm (left) and 400 µm-slits/c-t-c 3200 µm (right) collimators were tested.* 85
3.12 *Comparison of PVDR values obtained for 700 µm-slits/c-t-c 3500 µm (left) and 700 µm-slits/c-t-c 2700 µm (right) collimators with EBT3 films in water and solid water phantom. The two data sets are in agreement within the uncertainty bars.* 85
3.13 *PVDR values as a function of depth measured with EBT3 films in solid water for the three multislit collimators.* 86
3.14 *Comparison of PVDR values obtained for 700 µm-slits/c-t-c 3500 µm (left) and 400 µm-slits/c-t-c 3200 µm (right) collimators with EBT3 films and the PTW microDiamond© detector. The two data sets are in agreement within the uncertainty bars.* 87
3.15 *Penumbras as a function of depth measured with EBT3 films in solid water for the different pMBRT collimators.* 87

3.16 *Comparison of penumbras obtained for the 700 µm/c-t-c 3500 µm (left) and 400 µm/c-t-c 3200 µm (right) collimators with EBT3 films and the PTW microDiamond©.* 88

3.17 *OF as a function of depth determined with EBT3 films in solid water.* . . . 89

3.18 *Simulated FWHM (left) and PVDR values (right) as a function of depth using a brass collimator for several PCD. A decrease of the PCD from 7 to 2 cm reduces the FWHM by a factor 1.5, and increases the PVDR values by a factor 10. Taken from the work of Guardiola et al. [Guardiola 2016].* . 91

3.19 *Schematic view of an equipment used to deflect the beam in PBS mode. Taken from the work of Paganetti [Paganetti 2012].* 92

3.20 *Left: four bar-magnets arranged to form a quadrupole magnet. Right: magnetic field lines of an idealised quadrupole field in the plane transverse to the nominal beam direction.* 93

3.21 *PDD curves in the peak (left) and valley (right) with a 700 µm/c-t-c 3500 µm (top) and 400 µm/c-t-c 3200 µm (bottom) configuration, for both magnetic (MC) and mechanical (experimental) collimations.* 94

3.22 *FWHM values as a function of depth for the 700 µm/c-t-c 3500 µm (left) and 400 µm/c-t-c 3200 µm (right) c-t-c configurations. The uncertainty bars for the MC data were smaller than the symbols.* 95

3.23 *Penumbra values as a function of depth for the 700 µm/c-t-c 3500 µm (left) and 400 µm/c-t-c 3200 µm (right) c-t-c configurations. The uncertainty bars for the MC data were smaller than the symbols.* 95

3.24 *PVDR values as a function of depth for the 700 µm/c-t-c 3500 µm and 400 µm/c-t-c 3200 µm configurations. The uncertainty bars for the MC data were smaller than the symbols.* 96

3.25 *PDD curves related to different sub-millimetric (left) and supra-millimetric beam widths (right). Data are normalised to the entrance dose of each PDD curve.* 97

3.26 *2D distributions in the water phantom obtained by the irradiation with of one single 700 µm (left) and 5 mm-wide minibeam (right). The white lines demarcate the minibeam dimension. For the smallest beam, at the Bragg peak, the ratio of scattered protons due to multiple Coulomb scattering is high with respect to the beam dimension.* 98

3.27 *2D distributions in the water phantom obtained by the irradiation with an array of 700 µm (c-t-c 3500 µm) (left) and 3 mm (c-t-c 4.2 mm) minibeams (right). In both cases, an homogenisation is reached at the Bragg peak. However, the maximum dose is delivered at the Bragg peak with the 3 mm-minibeams array.* 98

3.28 *Lateral dose profiles in the water phantom at 3 cm-depth (top) and at the Bragg peak (bottom) obtained with irradiation with arrays of 700 µm/c-t-c 3500 µm (left) and 3 mm/c-t-c 4.2 mm (right).* 99

3.29 *PVDR values as a function of depth for several configurations. Left: to achieve a same homogenisation at the Bragg peak, low PVDR values are found with the 3 mm-beams array. Right: with a larger c-t-c, comparable PVDR values are observed in the proximal normal tissues, while the homogenisation is lost at the Bragg peak.* 99
3.30 *Lateral dose profiles (left) and PDD curves (right) obtained with one single minibeam (700 µm × 2 cm) related to different AG. Data are normalised to the entrance dose of each curve.* 100
3.31 *PDD curves obtained with one single minibeam (700 µm × 2 cm) with several angular divergences considering no AG. Data are normalised to the entrance dose of each curve.* 101
3.32 *2D distributions in the water phantom obtained by the irradiation with of one single 700 µm-beam with an angular divergence of 1 mrad (left) and 7 mrad (right). The source was located at the phantom entrance. The white lines demarcate the minibeam dimension.* 102
3.33 *Lateral dose profiles at the phantom surface (left) and at a depth in water of 3 cm (right) considering several beam divergences with the minibeams collimated at the phantom surface. The data are normalised with respect to the entrance dose.* 102
3.34 *PVDR values as a function of depth for an array of minibeams (700 µm / c-t-c 3500 µm) generated at the phantom surface, and several beam divergences.* 103
3.35 *Lateral dose profiles at the phantom surface (left) and at a depth in water of 3 cm (right) for 700 µm beams considering several beam divergences. An AG of 7 cm was assumed. The data are normalised with respect to the entrance dose.* 103
3.36 *PDD curves obtained with one single minibeam (700 µm × 2 cm) with several angular divergences at 7 cm from the phantom surface. Data are normalised to the entrance dose of each curve.* 104
3.37 *PVDR values as a function of depth for an array of minibeams (700 µm / c-t-c 3500 µm) and several beam divergences. An AG of 7 cm was considered.* 104
3.38 *PDD curves obtained with one single minibeam (700 µm × 2 cm) with several mean proton energy, considering fixed energy spread of 2.5 MeV.* . 105
3.39 *FWHM values obtained one single 700 µm-wide minibeam of different mean energies. The black arrows indicate the Bragg peak (BP) for each energy considered.* 105
3.40 *2D distributions in the water phantom obtained by the irradiation with an array of 700 µm minibeams (c-t-c 3500 µm) with a mean proton energy of 80 MeV (left) and 110 MeV (right).* 106
3.41 *Lateral dose profiles at the Bragg peak location obtained with the 80 MeV (left) and 110 MeV-proton (right) arrays of 700 µm minibeams (c-t-c 3500 µm).* 106
3.42 *Left: PVDR values as a function of depth for the 700 µm/c-t-c 3500 µm configuration with several mean proton energies. Right: PVDR values as a function of depth for 80 MeV proton minibeams with several c-t-c distances.* 106

3.43 *Left: PDD curves obtained with one single minibeam (700 μm × 2 cm) with several energy spread with a fixed mean proton energy of 100 MeV. Right: PVDR values as a function of depth considering an array of 700 μm-minibeams with a c-t-c of 3500 μm.* 107

3.44 *Comparison of PVDR values in water as a function of depth considering an array of 700 μm-minibeams with a c-t-c of 3500 μm (left) and 3 mm-minibeams with a 4.2 mm c-t-c necessary to cover 2×2 cm^2 and 5×5 cm^2 areas.* 108

3.45 *An array of minibeams (grey) is made from the superposition of several individual minibeams. The peak indicated with the black arrow is mainly fed by the red minibeam, and also by the lateral tails of the green and blue minibeams. The purple one does not significantly contribute to the designed peak.* 108

4.1 *PDD of one single mono-energetic (351 MeV/u) (left) and SOBP (right) argon minibeam in the water phantom. The SOBP flatness meets the ±2.5% criterion.* 113

4.2 *2D distributions in the water phantom obtained after irradiation with one single minibeam of neon Z=10 (left) and iron Z=26 (right). The lateral spread due to elastic Coulomb scattering in the SOBP is much more reduced with a higher Z-particle.* 113

4.3 *2D dose distribution obtained with an array of neon minibeams (700 μm) spaced with a 1400 μm (left) and 3500 μm c-t-c distance (right). Due to the lateral spread of the minibeams, one part of the dose feeds the spaces between the minibeams, i.e. the valleys.* 114

4.4 *Depth dose distributions obtained in both peak and valley region with an array of neon minibeams for c-t-c distances of 1400 μm (left) and 3500 μm (right), normalised with respect to the SOBP maximum dose for each considered ion. The larger the c-t-c distance, the lower the valley dose, due to a lower proportion of secondary species reaching the centre of the valley region. Also, in general terms, the heavier the ion is, the lower the valley dose. This is related to a higher production of forward directed heavy fragments with high-Z projectiles, contributing less to the valley region.* . . 115

4.5 *Valley doses as a function of depth normalised with respect to the SOBP maximum dose for each considered ion, for all the c-t-c distances investigated.* 116

4.6 *Influence of the c-t-c: Dose tails in peak (left) and valley (right) regions for arrays of argon minibeams. Data are normalised with respect to the SOBP maximum dose.* 117

4.7 *Influence of the ion type: Dose tails in the valley region with a c-t-c distance of 1400 μm (left) and 3500 μm (right). The dose is normalised with respect to the SOBP maximum dose of each considered ion.* 118

4.8 *Full width at half maximum (left) and 80-20% penumbra width (right) as a function of depth assessed on one single minibeam. Both FWHM and penumbras increase as a function of depth because of multiple Coulomb scattering. FWHM values show a moderate increase until the SOBP and then a rapid widening from the target position, still being one order of magnitude narrower than in conventional radiosurgery.* 119

4.9 *Lateral dose profiles at 3 cm resulting from a neon MBRT irradiation. The left figure corresponds to a c-t-c distance of 1400 µm, while a c-t-c of 3500 µm was used in the right one.* 120

4.10 *Influence of the c-t-c distance: PVDR values as a function of depth obtained with an array of silicon (left) and argon minibeams (right). The higher the c-t-c distance is, the lower the valley doses, and therefore the higher the PVDR values.* 120

4.11 *Influence of the Z: PVDR values as a function of depth for all the considered c-t-c distances. In general terms, the heavier the ion is, the higher the PVDR values are, due to a higher production of forward directed heavier fragments with high-Z projectiles, thus less contributing to the valley dose.* 121

4.12 *Contribution to the peak and valley dose distributions of primary projectiles and secondary products for arrays of several ions (c-t-c of 1400 µm). The distributions are normalised to the maximum normal dose in peak (left) and in valley (right). In valleys, the contribution of primaries only appears in the vicinity of the SOBP, and is higher for low Z ions.* 124

4.13 *Contribution of the different species of secondary particles to the peak depth dose curve as a function of primary ion. The dose was normalised to the maximum of the total sum of secondary products. A c-t-c distance of 3500 µm was considered. "Secondaries tot." and "nuclear fragm." refer to "secondaries total" and "nuclear fragments", respectively.* 125

4.14 *Contribution of the different species of secondary particles to the valley depth dose curves as a function of primary ion, with a c-t-c distance of 1400 µm.* 126

4.15 *Contribution of the different species of secondary particles to the valley depth dose curves as a function of primary ion, with a c-t-c distance of 2100 µm.* 126

4.16 *Contribution of the different species of secondary particles to the valley depth dose curves as a function of primary ion with a c-t-c distance of 2800 µm.* 127

4.17 *Contribution of the different species of secondary particles to the valley depth dose curves as a function of primary ion, with a c-t-c distance of 3500 µm.* 127

4.18 *Electron spectra in peak (left) and valley region (right) at several depths for an irradiation with one single neon minibeam. The spectra in valley were assessed 1750 µm away from the minibeam's centre.* 128

4.19 *Nuclear fragments yields as a function of depth in the minibeam path (peak) for the four considered ions. Data are normalised with respect to the number of primaries.* 130

4.20 *Nuclear fragments yields as a function of depth in the valley for the four considered ions. Data are normalised with respect to the number of primaries.* 130

4.21 *Lateral distribution of the most frequent fragmentation products at 4 cm-depth considering a c-t-c distance of 3500 µm. Data are normalised with respect to the number of primaries. Three regions corresponding to the peak, penumbra and valley are represented.* 131

4.22 *Neutron spectra evaluated at several depths with an irradiation of for neon (left) and iron (right) minibeams. The spectra have been determined 1750 µm away from the minibeam centre, which corresponds to the centre of the valley region if an array with a c-t-c 3500 µm has been used.* 132

5.1 *Schematic representation of the dose distributions obtained after an irradiation with one array of protons (left) and very heavy ions (right) submillimetric minibeams.* 139

7.1 *Exemple d'un profil latéral de dose obtenu en MBRT. Plusieurs paramètres dosimétriques pertinents pour les techniques de fractionnement spatial sont représentés. Le rapport des doses dans le pic et dans la vallée est appelé "peak-to-valley dose ratio" (PVDR). La distance séparant le centre de deux mini-faisceaux est appelée "centre-to-centre distance" et est notée "c-t-c".* . 148

7.2 *Illustration de la distribution de dose obtenue après une irradiation d'un crâne par pMBRT. Tandis que les tissus sains bénéficient d'un fractionnement spatial de la dose, la tumeur reçoit une dose quasi-homogène. Extrait du travail de Martínez-Rovira et al. [Martínez-Rovira 2015].* 149

7.3 *Valeurs d'EBR (A) et d'OER (B) obtenues sur des cellules humaines mises en culture, considérant un niveau de survie de 10%, tracées en fonction de la distance à la position du pic de Bragg. Tandis que l'EBR pour les ions carbone est proche de 1 dans les tissus proximaux, puis augmentent fortement à l'approche du pic de Bragg, avec des ions plus lourds l'EBR est déjà élevé et n'augmente que peu au niveau du pic de Bragg. Les valeurs d'OER sont très faibles (proches ou égales à 1) au niveau du pic de Bragg avec des ions très lourds, tandis qu'elles restent élevées avec des ions carbone, pour lesquels un effet oxygène est maintenu. Adapté du travail de Tobias et al. [Tobias 1977].* 150

7.4 *Collimateurs multi-fentes et 2×2 cm^2 (à gauche). Le processus d'usinage utilisé crée des fentes de 3.5 cm de long. Afin d'obtenir le champ d'irradiation désiré (2 × 2 cm^2), un collimateur de section carrée doit être ajouté après le collimateur multi-fentes (à droite).* 152

7.5 *Cette série de film irradiés à différentes profondeurs dans le fantôme de "solid water" (collimateur 700 µm/c-t-c 3500 µm) montre que le fractionnement spatial est maintenu dans les tissus sains, tandis qu'une distribution de dose quasi-homogène est obtenue au niveau du volume cible (pic de Bragg).* 152
7.6 *Profils latéraux de dose obtenus à différentes profondeurs dans l'eau avec le détecteur PTW microDiamond© pour les collimateurs 700 µm/c-t-c 3500 µm (à gauche) et 400 µm/c-t-c 3200 µm (à droite).* 153
7.7 *Courbes de rendement en profondeur dans le pic central d'un peigne de mini-faisceaux obtenues dans l'eau (à gauche) et dans le matériau "solid water" (à droite). Chaque courbe est normalisée par rapport à la dose au pic de Bragg. Chaque couleur correspond à un collimateur.* 153
7.8 *PVDR en fonction de la profondeur mesurés avec des films EBT3 dans des plaques de "solid water" pour les trois collimateurs multi-fentes considérés.* 154
7.9 *Illustration de la géométrie simulée.* 155
7.10 *Courbes de rendement en profondeur dans le pic (à gauche) et la vallée (à droite) pour les configurations 700 µm/c-t-c 3500 µm (en haut) et 400 µm/c-t-c 3200 µm (en bas), considérant une collimation magnétique (données MC) et mécanique (données experimentales).* 156
7.11 *Valeurs de PVDR en fonction de la profondeur pour les configurations 700 µm/c-t-c 3500 µm et 400 µm/c-t-c 3200 µm. Les barres d'incertitudes sont plus petites que la dimension des symboles pour les données MC.* . . . 157
7.12 *Distributions de dose 2D dans le fantôme d'eau obtenues après irradiation avec un peigne de mini-faisceaux de 700 µm (c-t-c 3500 µm) (à gauche) et de 3 mm (c-t-c 4.2 mm) de largeur (à droite). Un fractionnement spatial de la dose est également maintenu avec des faisceaux plus larges, tout en offrant un maximum de dose au niveau du pic de Bragg, tandis qu'il se trouve en entrée pour un peigne de 700 µm.* 157
7.13 *Rendements en profondeur obtenus avec un unique mini-faisceau monoénergétique d'argon (351 MeV/u) (à gauche) et avec un SOBP (à droite) dans l'eau.* 158
7.14 *Profils latéraux de dose obtenus à 3 cm de profondeur avec un peigne de mini-faisceaux de néon, avec un c-t-c de 1400 µm (à gauche) et de 3500 µm (à droite).* 159
7.15 *PVDR en fonction de la profondeur obtenus avec tous les c-t-c considérés. De manière générale, plus l'ion est lourd, plus les valeurs de PVDR sont élevées du fait d'une production plus importante de fragments lourds, plus dirigés vers l'avant, et donc contribuant moins aux vallées.* 160
7.16 *Distribution latérale des produits de fragmentation les plus fréquents à une profondeur de 4 cm, considérant un c-t-c de 3500 µm. Les données sont normalisées par rapport au nombre de particules primaires simulées. Trois régions correspondant au pic, à la zone de pénombre et à la vallée, sont représentées.* 160

7.17 *Représentation schématique des distributions de dose obtenues après irradiation avec un peigne de faisceaux submillimétriques de protons (à gauche) et d'ions très lourds (à droite).* 162

List of Tables

2.1 *Specifications of the four pMBRT collimator prototypes investigated in this work.* . . . 43
2.2 *Beam characteristics at the Y1 room entrance (680 cm away from the isocentre).* . . . 44
2.3 *Composition and density of SP34 IBA solid plate phantom [IBA 2016].* . . . 58
2.4 *Densities, mass stopping powers (S) and depth scaling factors for 100 MeV protons for water-equivalent depth calculation.* . . . 61
2.5 *Geant4 hadronic processes and associated models used in this study.* . . . 71
2.6 *Minimum and maximum energies employed in the simulations to create the 2 cm-long SOBP for each type of charged particle for 8 cm maximum depth.* 72
2.7 *Number of minibeams needed to cover a 2×2 cm^2 field size as function of the c-t-c distance.* . . . 72

3.1 *Estimation of valley and average doses received at different points in the normal tissues considering pMBRT irradiations with the Multi1 (700 µm-slits/c-t-c 3500 µm) and Multi3 (400 µm-slits/c-t-c 3200 µm) collimators in solid water. The data are expressed as a percentage of the Bragg peak dose.* . . . 82
3.2 *Estimation of $NTD_{2.0}$ in the valley considering a prescription dose of 50 Gy at the Bragg peak for irradiations with the Multi1 (700 µm-slits/c-t-c 3500 µm) and Multi3 (400 µm-slits/c-t-c 3200 µm) collimators in solid water.* . . . 83
3.3 *FWHM at the phantom entrance obtained with a 700 µm × 2 cm minibeam collimated at different distances from the phantom.* . . . 100
3.4 *Summary of the influence of irradiation parameters on the dose distributions. "NT" and "hom." respectively stand for "normal tissues" and "homogenisation".* . . . 109

4.1 *Overview of the heavy ion beam facilities that produce or have produced the ions investigated in this study.* . . . 112
4.2 *Valley doses expressed as a percentage of the maximum SOBP dose as a function of depth in the normal proximal tissues.* . . . 117
4.3 *PVDR values obtained at several depths with the four c-t-c distances and ions.* . . . 122
4.4 *Electrons maximum energies and ranges in liquid water at 4 cm-depth in the peak region. The electron ranges were estimated thanks to the NIST database [NIST-ESTAR 2016].* . . . 128
4.5 *Summary of the relevant results obtained in this work.* . . . 133

5.1 *Overview of advantages and drawbacks of pMBRT and very heavy ion MBRT.* 139

7.1 *Caractéristiques des quatres prototypes de collimateurs à fentes étudiés durant ce travail.* 151
7.2 *Vue d'ensemble des avantages et inconvénients de la pMBRT et de la MBRT par faisceaux d'ions très lourds.* 162

université PARIS-SACLAY | ÉCOLE DOCTORALE PHENIICS

Titre : Fractionnement spatial de la dose en radiothérapie par particules chargées

Mots clés : fractionnement spatial, radiothérapie par particules chargées, dosimétrie, Monte Carlo

Résumé : Malgré de récentes avancées, les traitements par radiothérapie (RT) demeurent insatisfaisants : la tolérance des tissus sains aux rayonnements limite la délivrance de fortes doses (potentiellement curatives) à la tumeur. Pour remédier à ce problème, de nouvelles approches basées sur des modes de dépôt de dose innovants sont aujourd'hui à l'étude. Parmi ces approches, la technique synchrotron *"Minibeam Radiation Therapy"* (MBRT) a démontré sa capacité à élever la résistance des tissus sains aux rayonnements, ainsi qu'à induire un important retard de croissance tumorale. La MBRT combine des faisceaux submillimétriques à un fractionnement spatial de la dose. Dans ce contexte, l'alliance de la balistique plus avantageuse des particules chargées (et leur sélectivité biologique) à la préservation des tissus sains observée en MBRT permettrait de préserver d'avantage les tissus sains. Cette stratégie innovante a été explorée durant ce travail de thèse. Deux voies ont notamment été étudiées : la MBRT par faisceaux de protons (pMBRT) et d'ions très lourds. Premièrement, la preuve de concept expérimentale de la pMBRT a été réalisée dans un centre clinique (Institut Curie, Centre de Protonthérapie d'Orsay). De plus, l'évaluation de potentielles optimisations de la pMBRT, à la fois en termes de configuration d'irradiation et de génération des minifaisceaux, a été menée dans une étude Monte Carlo (MC). Dans la seconde partie de ce travail, un nouvel usage potentiel des ions très lourds (néon et plus lourds) en radiothérapie a été évalué dans une étude MC. Les combiner à un fractionnement spatial permettrait de tirer profit de leur efficacité dans le traitement de tumeurs radiorésistantes (hypoxiques), un des principaux défis de la RT, tout en minimisant leurs effets secondaires. Les résultats obtenus au terme de ce travail sont favorables à une exploration approfondie de ces deux approches innovantes. Les données dosimétriques compilées dans ce manuscrit serviront à guider les prochaines expérimentations biologiques.

Title : Spatial fractionation of the dose in charged particle therapy

Keywords : spatial fractionation, charged particle therapy, dosimetry, Monte Carlo simulations

Abstract: Despite recent breakthroughs, radiotherapy (RT) treatments remain unsatisfactory : the tolerance of normal tissues to radiations still limits the possibility of delivering high (potentially curative) doses in the tumour. To overcome these difficulties, new RT approaches using distinct dose delivery methods are being explored. Among them, the synchrotron minibeam radiation therapy (MBRT) technique has been shown to lead to a remarkable normal tissue resistance to very high doses, and a significant tumour growth delay. MBRT allies sub-millimetric beams to a spatial fractionation of the dose. The combination of the more selective energy deposition of charged particles (and their biological selectivity) to the well-established normal tissue sparing of MBRT could lead to a further gain in normal tissue sparing. This innovative strategy was explored in this Ph.D. thesis. In particular, two new avenues were studied: proton MBRT (pMBRT) and very heavy ion MBRT. First, the experimental proof of concept of pMBRT was performed at a clinical facility (Institut Curie, Orsay, France). In addition, pMBRT setup and minibeam generation were optimized by means of Monte Carlo (MC) simulations. In the second part of this work, a potential renewed use of very heavy ions (neon and heavier) for therapy was evaluated in a MC study. Combining such ions to a spatial fractionation could allow profiting from their high efficiency in the treatment of hypoxic radioresistant tumours, one of the main challenges in RT, while reducing at maximum their side effects. The promising results obtained in this thesis support further explorations of these two novel avenues. The dosimetry knowledge acquired will serve to guide the biological experiments.